Coordination Chemistry Reviews 254 (2010) 2703–2754

Contents lists available at ScienceDirect

Coordination Chemistry Reviews

journal homepage: www.elsevier.com/locate/ccr

Review

Jahn–Teller coupling and the influence of strain in T_g and E_g ground and excited states – A ligand field and DFT study on halide $M^{III}X_6$ model complexes [M = Ti^{III}–Cu^{III}; X = F^-, Cl^-]

D. Reinen [a,*], M. Atanasov [a,b], P. Köhler [a], D. Babel [a]

[a] Chemistry Department, Philipps-University, Hans-Meerwein-Strasse, 35043 Marburg, Hessen, Germany
[b] Institute of General and Inorganic Chemistry, Academy of Sciences, 1113 Sofia, Bulgaria

Contents

* Corresponding author.
E-mail address: reinen@chemie.uni-marburg.de (D. Reinen).

0010-8545/$ – see front matter © 2010 Published by Elsevier B.V.
doi:10.1016/j.ccr.2010.04.015

ARTICLE INFO

Article history:
Received 22 December 2009
Accepted 20 April 2010
Available online 29 June 2010

Keywords:
Jahn–Teller coupling
T and E ground states
Density-functional calculations
Strain effects
$3d^n$–M^{III} cations
Halide ligands
Ligand field theory

ABSTRACT

In contrast to well established experimental results of vibronic coupling effects in octahedral d^n complexes with E_g ground states (Cu^{2+}, Ag^{2+}; Cr^{2+}, Mn^{3+} etc.), not much useful material is available for the Jahn–Teller (JT) effect in orbital triplet ground states. The present study is concerned with this deficiency, providing data for octahedral halide model complexes with $3d^n$ cations – in particular for Ti^{III}, V^{III} and high-spin Co^{III}, Ni^{III} with T_{2g} and T_{1g} ground states, which involve, to first-order, solely splitting of the π-antibonding t_{2g} MOs. Besides experimental results – structural and spectroscopic, mainly from d–d spectra – data from computations are needed for a quantitative treatment of the $T_g\otimes(\varepsilon_g+\tau_{2g})$ vibronic interaction as well as in the $E_g\otimes\varepsilon_g$ coupling case (Mn^{III}, low-spin Ni^{III}); DFT was the method of choice, if only critically selected outcomes are utilised. The theoretical bases of the treatment are the d^n ligand field matrices in O_h, extended by the inclusion of lower-symmetry distortion parameters, and the conventional theory of vibronic coupling. Caution is needed when classifying the effects of interelectronic repulsion; DFT does not reproduce the magnitudes of the Racah parameters *B*, *C*, as deduced from the d–d spectra, properly – the presumed reasons are analysed. DFT even allows one to deduce reliable vibronic coupling constants via the analysis of orbitally degenerate excited states (Cr^{III}, $^4A_{2g}$ ground state). The group-theoretical analysis of the interaction with the JT-active ε_g and τ_{2g} modes yields D_{4h}, D_{3d} and D_{2h} as the possible distortion symmetries in the case of a T_g ground state. The DFT-calculations give clear evidence, that the D_{4h} stationary points represent the absolute minima in the $T_g\otimes(\varepsilon_g+\tau_{2g})$ potential surface – in agreement with experiment, where available. For the first time, vibronic coupling constants, characterising JT splitting of ground and excited T_g states, can be presented for trivalent $3d^n$ cations in octahedral halide ligand fields. They turn out to be smaller by a factor of almost 3 in comparison to those, which determine the coupling in σ-antibonding e_g MOs.

The tetragonal splitting of T_g states is typically only small, around 0.1 eV, and suggests that strain influences from a specific ligand arrangement and/or the presence of different ligands may modify the potential surface considerably. We have studied such effects via compounds $A^IM^{III}F_4$, where an *elastic* strain induced by the host structure, and a *binding* strain, due to the simultaneous existence of (largely) terminal and of bridging ligands, are active. A novel strain model, in its interplay with JT coupling, is proposed and applied – using energies from the d–d spectra, structural results and data from DFT.

Chloride complexes are only known for Ti^{III} to Fe^{III}; the rather small electronegativity already of Co^{III} suggests a reducing ligand-to-metal ($3d^n$) electron transfer for $n\geq 6$. Similarly, the low-lying ligand-to-metal charge transfer bands in the d–d spectra of the $Cu^{III}F_6^{3-}$ complex and the reduced $T_g\otimes\varepsilon_g$ coupling strength suggest a pronounced covalency of the Cu^{III}–F, and, even more distinctly, of the Cu^{III}–O bond, which is of interest for superconductivity. The $Ni^{III}F_6^{3-}$ polyhedron possesses a low-spin configuration in the elpasolite structure. The spectroscopic evidence and the DFT data indicate, that the minimum positions of the alternative $_a{}^2A_{1g}(_a{}^2E_g)$ and $_a{}^4A_{2g}$ ($_a{}^4T_{1g}$) potential curves are only ≤0.02 eV apart, giving rise to interesting high-spin/low-spin phenomena. It is the strong $E_g\otimes\varepsilon_g$ as compared to the $T_{1g}\otimes\varepsilon_g$ coupling, which finally stabilises a spin-doublet ground state in D_{4h}.

We think, that the selected class of solids is unique particularly for the study of Jahn–Teller coupling in T ground states, with model character for other systems. In our overview a procedure is sketched, which uses reliable computational results (here from DFT) for supplementing incomplete experimental data, and presents – on a semiquantitative scale – convincing statements, consistent with chemical intuition. It is also a pleading for ligand field theory, which rationalises d-d spectra in terms of chemical bonding; though the latter spectra provide frequently only rather coarse information, their assistance in the energy analysis is crucial.

1. Introduction and outline

The structural and energy properties and implications, which accompany the Jahn–Teller effect of d^n cations with E_g ground states in octahedral coordination, have been thoroughly studied and are rather well understood [1–3] – in particular for Cu^{2+},[1] but also in the case of various other transition metal ions [1–6]:

d^4 ^5E_g ($t_{2g}^3e_g^1$)	Cr^{2+}, Mn^{3+}	d^9 ^2E_g ($t_{2g}^6e_g^3$)	Cu^{2+}, Ag^{2+}
d^7 ^2E_g ($t_{2g}^6e_g^1$)	Co^{2+}, Ni^{3+} (low-spin)		

The vibronic interaction of the $E\otimes\varepsilon$ type, involving the Jahn–Teller active ε_g vibration, is very pronounced, due to the σ-antibonding character of the e_g MOs. Even, if the parent octahedron is not of O_h symmetry – because of the presence of different ligands, of multidentate ligands with angular constraints, or of host site distortions induced by the crystal structure, for example – the action of the vibronic coupling usually dominates and is mostly clearly recognisable. Octahedral T_g ($\equiv T_{2g}$, T_{1g}) ground states are much less sensitive in respect to site distortions and energetic splitting effects, as we will show, because the antibonding t_{2g} MOs involved are of only π-nature ($T_g\otimes(\varepsilon_g+\tau_{2g})$ interaction)):

d^1 $^2T_{2g}$ (t_{2g}^1)	Ti^{3+}	d^6 $^5T_{2g}$ ($t_{2g}^4e_g^2$)	Fe^{2+}, Co^{3+}
d^2 $^3T_{1g}$ (t_{2g}^2)	V^{3+}	d^7 $^4T_{1g}$ ($t_{2g}^5e_g^2$)	Co^{2+}

In the cases listed there is mostly only indirect experimental evidence for Jahn–Teller distortions, and furthermore one has to carefully select examples, where *strain effects* definitely do not play a decisive part. Before we turn to Jahn–Teller systems of such a kind we shortly mention d^n cations in tetrahedral coordination, which possess doubly (left) and triply (right) orbitally degenerate ground states, with rather different binding properties in comparison to the octahedral coordination:

d^1 ^2E (e^1)	V^{IV}, Cr^V, Mn^{VI}	d^4 $^5T_2$ ($e^2t_2^2$)	Cr^{2+}	d^9 $^2T_2$ ($e^4t_2^5$)	Cu^{2+}
d^6 ^5E ($e^3t_2^3$)	Fe^{2+}	d^8 $^3T_1$ ($e^4t_2^4$)	Ni^{2+}		

d^8 and, in particular, d^9 complexes with ($\sigma+\pi$) antibonding T ground states undergo significant Jahn–Teller distortion of the $T\otimes\varepsilon$ type [6], while for the d^4 case unambiguous evidence is scarce. One of the rare examples is Cr^{2+}, isomorphously substituted into the tetrahedral Zn^{2+} site of Cs_2ZnCl_4. The d–d spectrum at 4 K clearly reveals two transitions at 5900 and 8600 cm^{-1}, and additionally the most intense band of a contamination due to Cs_2CrCl_4, where Cr^{2+} is octahedrally coordinated (Fig. 1). The two mentioned bands have to be assigned either to the $^5B_2\rightarrow{}^5E$; $^5A_1$ transitions in D_{2d}, compressed – here the $^5B_2\rightarrow{}^5B_1$ transition is symmetry forbidden – or to the $^5A_1\rightarrow{}^5E(T_2)$; $^5E(E)$ transitions in C_{3v}, compressed. Independent of whether the Jahn–Teller distortion is tetragonal ($T\otimes\varepsilon$ coupling) or trigonal ($T\otimes\tau_2$ coupling), the ground state splitting is considerable, 0.73 eV. In contrast, for example in the case of d^1 cations in tetrahedral ligand fields, where the ground state is purely π-antibonding, the experimental evidence, so far, is ambiguous [8].

In this contribution we investigate $M^{III}F_6^{3-}$ (M^{III} = Ti–Cu) complexes – for a preliminary report see Ref. [7] – and the corresponding chloride polyhedra, as far as they exist. In the d^1, d^2 and d^6 cases they possess orbitally degenerate T ground states. We use available structural and spectroscopic results, but need additional support by *reliable* calculational methods. As we could show in a study of Mn^{III} in fluoride environment, DFT is the method of choice as long as interelectronic repulsion is not considered [9]. It furthermore turns out that the fluoride ligands involved are rather variable in their binding behaviour, depending on whether they are terminal (t) in the solid considered or found in bridging (b) function. As a bridging ligand, fluoride possesses a distinctly larger overlap covalency (see below) than in a terminal position; in the case of the Mn^{III}–F bond for example, the energy variation in the 3d(M^{III})–s,p(F) overlap on changing the metal-ligand distance is 30% larger, if a bridging fluoride is involved. On the other hand, the total bond covalency toward F_b and F_t is about equal, because the *central field* covalency [10] – the ligand-to-metal charge transfer within the bond – is more pronounced in the latter case with the larger formal negative charge. Concerning the total bond strength, F_t is the stronger ligand in respect to F_b because of the larger ionic bond increment [9]. In the following we choose *isolated* $M^{III}(X_t)_6^{3-}$ polyhedra as initial complexes, which are found in cubic elpasolite compounds with the composition $A'^I{}_2A^IM^{III}X_6$ (X = F, Cl) in good approximation (Fig. 2a). Here, A'^I and A^I are large, low-charged 12- and 6-coordinated alkaline cations, respectively, whose contrapolarising power toward the halogen ligator atoms is very weak. This binding situation can be nicely simulated by DFT, *if the calculations on the MX_6^{3-} polyhedra are performed in a polarizable solvent continuum*. Such a procedure reproduces, rather reliably, experimental d–d transition energies and structural data in the case of Mn^{III} [9].

The model structure, which defines $M^{III}(F_b)_6$ polyhedra with bridging ligands, is of the VF_3-type, a perovskite-related (distorted) ReO_3-variant (Fig. 2b and c); here, the F_b ligands (non-linearly) bridge two M^{III} cations. This necessarily implies an elastic coupling between the polyhedra throughout the lattice, which is accounted for in the derived parameters in an effective way (but see Section 4).

Before turning to our actual subject, it may be useful to sketch the difficulties which are met, if one analyses structural and spectroscopic results for T ground states with respect to underlying Jahn–Teller contributions, because these are usually small. For this purpose we shortly consider the hexafluoro-Fe^{II}-octahedra, present in the cubic perovskite $KFeF_3$, in compounds $Fe^{II}M^{IV}F_6$ (M^{IV}: Zr, Hf), which crystallise at 298 K in the ordered ReO_3 type (Fig. 2b) [11,12], and in FeF_2 with the rutile structure, where experimental evidence for a ground state splitting is available. In the mentioned compounds fluoride is bridging between either two (perovskite) or three (rutile) Fe^{2+} cations, or between one Fe^{2+} and one M^{IV} cation. The d–d spectra exhibit – as one might argue (see below) – a splitting of the excited ^5E_g state, which is ≅2400 and ≅1800 cm^{-1} at 298 K (Fig. 3) for the perovskite and the $FeM^{IV}F_6$ solids, respectively [12]. The lifting of the degeneracy of the ^5E_g state suggests a splitting of the $^5T_{2g}$ ground state as well, as the consequence of a tetragonal $T_{2g}\otimes\varepsilon_g$ Jahn–Teller coupling. Because the Fe^{II}-octahedra are regular at 298 K, however, the vibronic interaction is dynamic[2] at this temperature. $FeZrF_6$ has been investigated by Mößbauer spectroscopy down to 4 K [12]. Below 208 K a quadrupole splitting of the signal develops, which increases with decreasing temperature. This originates from a *trigonal* elongation of the hexafluoro-Fe^{II}-complex due to a structural

[1] We recall here the possible role of the Jahn–Teller coupling in the oxidic mixed valence Cu^{2+}/Cu^{3+} high-temperature superconductors. Some solid-state chemists believe that an electron flow within the narrow $b_{1g}(d_{x^2-y^2})$ band – in D_{4h} (elongated), singly occupied and empty for Cu^{2+} and (low-spin) Cu^{3+}, respectively – is of crucial importance in the superconductivity mechanism [4–6].

[2] The designation *dynamic* is normally used by chemists in the sense, that a thermal bond length equilibration occurs, which may be frozen in at low temperatures; we follow here this convention.

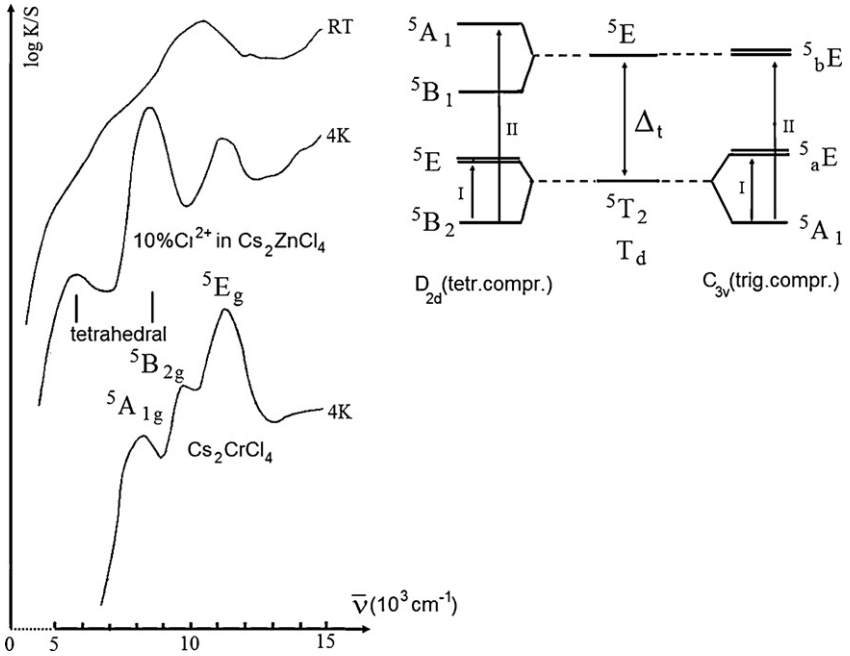

Fig. 1. The d–d spectra of Cr^{2+} (powder reflection; arbitrary intensity scale) in the tetrachloro-coordination of Cs_2ZnCl_4, with contributions from Cs_2CrCl_4 contamination – originating from D_{4h} – elongated $Cr^{II}Cl_6$ octahedra (see text). Alternative assignments according to $T\otimes\varepsilon$ and $T\otimes\tau_2$ vibronic coupling (both compressed tetrahedra), respectively, are shown in the state diagram.

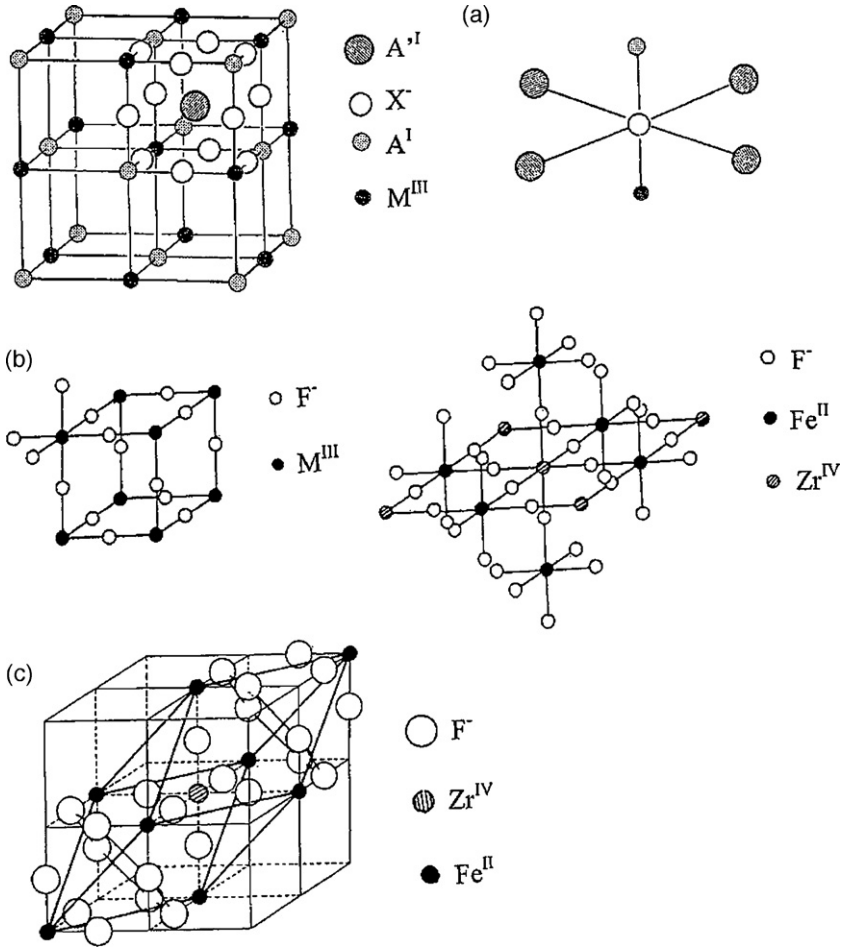

Fig. 2. The elpasolite structure of solids $A'_2{}^{I}A^{I}M^{III}X_6$ and the cationic coordination of the X^- anions (a); the ReO_3 structure [cubic parent structure of FeF_3] and its ordered variant [$FeZr(Hf)F_6$] are also shown (b); in (c) we depict the low-temperature (rhombohedral) unit cell of $FeZrF_6$ with the $LiSbF_6$ structure (ordered VF_3 type).

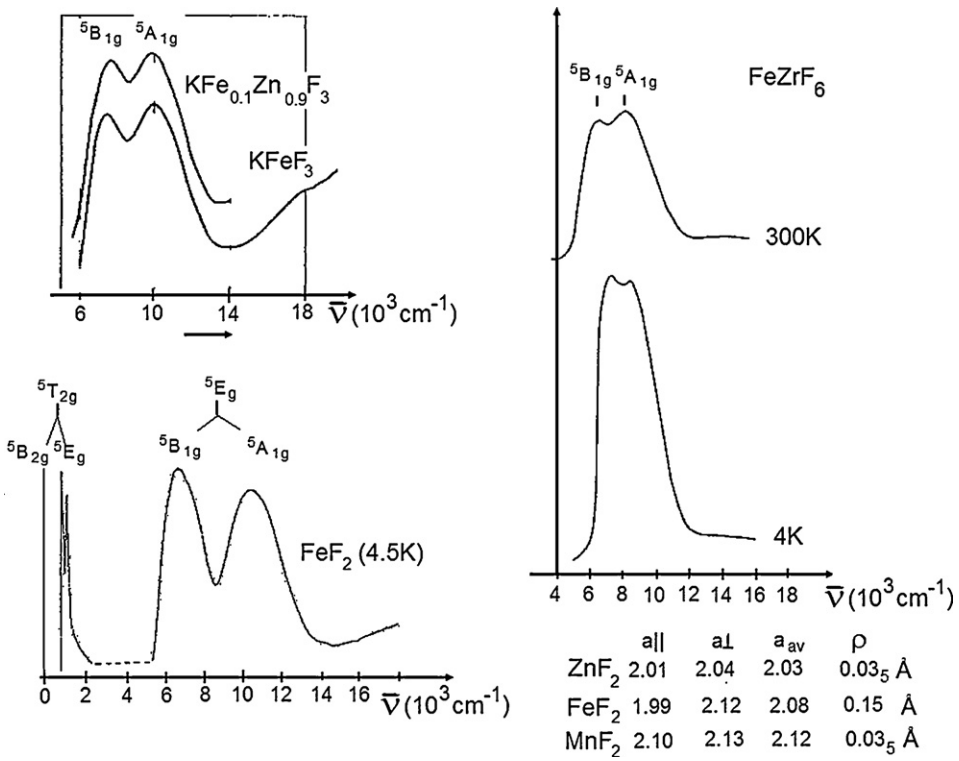

Fig. 3. d–d spectra (powder reflection; arbitrary intensity scale) of the $Fe^{II}F_6$ polyhedra in perovskite- and ordered ReO_3-type solids (top left and right), and in FeF_2 with the rutile structure (bottom left) – assignments according to D_{4h}, compression (adopted from [14]). Structural data for various MF_2 compounds are also given (for the definition of ρ see Eq. (4)).

phase transition to the low-temperature $LiSbF_6$ structure (ordered VF_3 type; see Fig. 2c). A possible tetragonal distortion induced by vibronic coupling to the ε_g mode is not seen within the time frame [13] of the Mößbauer method ($\approx 10^{-11}$ s); it is clearly visible in optical spectroscopy, however, where the time of excitation is shorter by four magnitudes of order. A structural distortion effect is not expected to be seen, because X ray and neutron diffraction methods are based on cumulative data collections within longer time periods; here, only an analysis of the temperature ellipsoids may give information. Thus, in the case of $FeZrF_6$, we are left with the situation of an apparently orthorhombic polyhedron distortion, which is caused by a very small structurally induced and static trigonal, and a superimposed tetragonal distortion component, which splits the excited ^5E_g state, but appears as a dynamic effect in methods with longer time frames. The excited state splitting of FeF_2 is, with $4\delta_1 = 3700\,cm^{-1}$ (0.46 eV), much larger than in the just discussed cases [14], and the splitting of the ground state, $3\delta_2 \cong 1100\,cm^{-1}$ (0.14 eV), has been measured by electronic Raman spectroscopy [15] (Fig. 3); the δ_1/δ_2 ratio (see the definitions in Section 2 and in Fig. 4b) is about 2.3. The structural data indicate a static distortion already at 298 K; the octahedra are tetragonally compressed – and hence the orbital singlet $^5B_{2g}$ ($^5T_{2g}$) is the ground state. The distortion is *strain-supported*, however, because already the octahedra of $3d^n$ cations with non-degenerate ground states, as in MnF_2 and ZnF_2, are compressed, though only with a difference of 0.03 Å between the long and short bond lengths.

The arguments, used for hexafluoro-Fe^{II}-octahedra, for example, to analyse a possible ground state splitting due to $^5T_{2g} \otimes \varepsilon_g$ coupling, need some closer consideration. They are based on the static theory, used throughout this contribution, without including vibrational effects. The energy diagram in Fig. 7 for the $T_{2g} \rightarrow E_g$ Franck–Condon transitions in the presence of $T_{2g} \otimes \varepsilon_g$ coupling for an octahedral d^1 (or high-spin d^6) complex illustrates, how an excited state splitting in the d–d spectrum is related to a Jahn–Teller distortion in the ground state. While this procedure can be considered as being close to physical reality in the case of strong vibronic coupling, it may lead to incorrect results, if this interaction is (very) weak. Here, the band shape – which is the envelope of numerous transitions between vibronic states – might show structures, which are sometimes far off the location of the electronic split states [16]. We will hence in the following examine in each specific

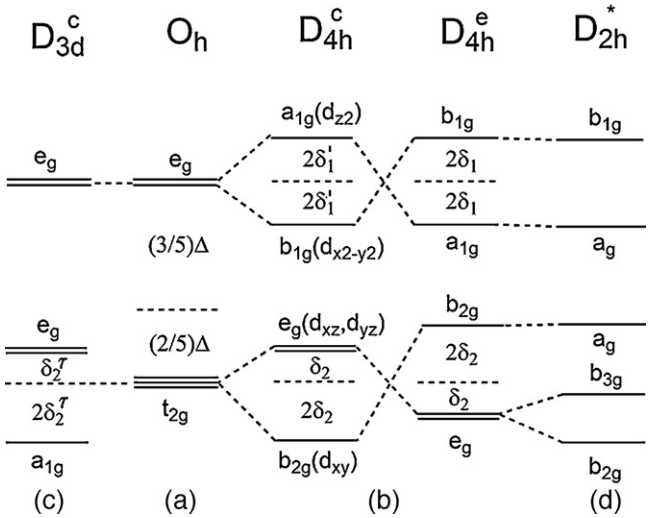

Fig. 4. Schematic MO energy diagrams for octahedrally coordinated d^1 cations (a), under the influence of $T \otimes \varepsilon$ (b) and $T \otimes \tau_2$ (c) coupling; the splitting scheme for orthorhombic $T \otimes (\varepsilon + \tau_2)$ coupling of $D_{2h}{}^*$ symmetry (see text) is depicted in (d). Energetic shifts due to the $3d_{z^2}$–4s interaction between a_{1g} ($4s^1$) and a_{1g} ($3d_{z^2}$) in (b) and between a_g ($4s^1$) and a_g ($3d_{z^2}$) in (d) are effectively included in the diagrams; the splitting parameters δ_1 and δ'_1 refer to a tetragonal elongation and compression [$2\delta_1$ ($2\delta'_1$) $\equiv A_1\rho + (-)A_2\rho^2$], respectively. Other mutual symmetry-induced interactions between 4 s and split-terms of t_{2g} (3d) are of σ- versus π-character and hence very small. The upper indices c, e refer to designations compressed and elongated, respectively.

vibronic coupling case, whether the ratio between the respective Jahn–Teller energy E_{JT} and the zero-point energy of the involved vibronic energy is large (≥ 1) or small ($\ll 1$) – according to the strong and weak coupling limit, respectively. The given examples of Fe^{2+} halides also illustrate, that it is not a simple task to elucidate the vibronic coupling symmetry – whether it is of tetragonal $T_g \otimes \varepsilon_g$ or of trigonal $T_g \otimes \tau_{2g}$ or of even orthorhombic $T_g \otimes (\varepsilon_g + \tau_{2g})$ nature (see Section 2) – and furthermore to trace out whether the distortion is dynamic or static. On the other hand, the presence of *host site strains*, structural ones and such ones, which are induced by (as here) fluoride ligands in different binding states (terminal or bridging), is crucial in cases, where the Jahn–Teller coupling is weak (see Section 4). Binding strains, induced by the impact of the cationic second-sphere environment on the binding properties of a ligator atom in a solid, are particularly significant for oxygen as the ligand, which – dissimilar to halide ions – can usually not be observed in terminal positions, due to its larger anionic (2−) formal charge [17]. In the following, we will for the chosen model halide complexes with trivalent 3d cations derive the vibronic coupling constants by employing ligand field theory and the appropriate vibronic coupling expressions. As data sources we use mainly the d–d spectra, besides other experimental evidence, and carefully selected DFT results; the latter are particularly valuable in cases, where experimental outcomes are scarce. The basic theory is presented in Section 2. We further investigate cases, in which strain effects superimpose the vibronic interactions of the Jahn–Teller type. A specific strain model within the vibronic coupling concept is developed, and outlined in Section 4. In Sections 3, 5–7 and 9–11 the halide complexes of Ti^{III}, V^{III}, Cr^{III}, Mn^{III}, Co^{III}, Ni^{III} and Cu^{III} are treated. Here, it is shown, that even coupling constants for central cations with non-degenerate ground states can be estimated. Section 8 presents a discussion of the stability of the chloride complexes on the basis of respective optical electronegativities. In Section 12, conceptional and computational implications of the DFT results in relation to ligand field and vibronic coupling theory are analysed. Section 13 summarises and supplements the obtained results, and also presents an outlook toward new developments in the field of vibronic JT coupling. The equations, derived in Section 2, refer to a d^1 (or high-spin d^6) cation in octahedral coordination, possessing a T_{2g} ground state and an E_g excited state (Fig. 4).

2. The vibronic theory

2.1. General: $T_g \otimes (\varepsilon_g + \tau_{2g})$ coupling

The general matrix (adiabatic approximation) describing the coupling of an octahedral T_{2g} (or T_{1g}) ground state with Jahn–Teller (JT) active ε_g and τ_{2g} modes (Fig. 5) and quantised along a 4-fold symmetry axis, is – in first-order – given in Eq. (1) [16,18]. While the former mode induces a tetragonal distortion along one of the three C_4 axes, the latter leads to a deformation along one of the four trigonal axes of the octahedron – see Figs. 5 and 9 (linear coupling constants V_ε and V_τ; Q_θ, Q_ε and Q_ζ, Q_η, Q_ξ are the components of the ε_g and τ_{2g} vibrations, respectively). The basis of the matrix representation is the components of an electronic T_{2g} (or T_{1g}) state. All linear and higher-order coupling constants, used in this contribution, are defined as positive quantities. Matrix (1) is easily reproduced from the system of equations in Appendix A.1 – but with a sign change for the diagonal energies, in order to keep V_ε as a positive quantity in the case of $^2B_{2g}$ ground state and a tetragonally compressed octahedron:

d_{yz}	d_{xz}	d_{xy}
$-1/2\,(Q_\theta - \sqrt{3}\,Q_\varepsilon)V_\varepsilon$	$-1/2\,Q_\zeta V_\tau$	$-1/2\,Q_\eta V_\tau$
$-1/2\,Q_\zeta V_\tau$	$-\tfrac{1}{2}\,(Q_\theta + \sqrt{3}\,Q_\varepsilon)V_\varepsilon$	$-1/2\,Q_\xi V_\tau$
$-1/2\,Q_\eta V_\tau$	$-1/2\,Q_\xi V_\tau$	$Q_\theta V_\varepsilon$

(1)

The diagonal energies have to be supplemented by the restoring energies in Eq. (2), with the force constants K_ε and K_τ, respectively:

$$E_{pot} = \tfrac{1}{2}\{K_\varepsilon(Q_\theta^2 + Q_\varepsilon^2) + K_\tau(Q_\zeta^2 + Q_\eta^2 + Q_\xi^2)\} \quad (2)$$

The solutions are computationally complex; however, some general statements can be made [18]:

(a) If the stabilisation energy of either of the three conformers, distorted along a 4-fold axis, is $-E_{JT}(D_{4h}{}^c)$ with respect to the regular octahedron, and the corresponding energy of the conformers, distorted along one of the four 3-fold axes, is $-E_{JT}(D_{3d}{}^c)$, the absolute minima of the six-dimensional potential surface are either those with $D_{4h}{}^c$- or $D_{3d}{}^c$-type distortions (see Fig. 4) – depending on whether $E_{JT}(D_{4h}{}^c)$ is larger or smaller than $E_{JT}(D_{3d}{}^c)$. If the absolute value of the former is larger, the trigonal extrema are only saddlepoints, and in the reverse case this holds for the tetragonal extrema. Upper indices c and e refer to compressed and elongated conformations, respectively.

(b) The six extremum points with orthorhombic symmetry, comprising simultaneous distortions of the ε_g and τ_{2g} type (vide infra), can never be absolute minima in the linear approximation but only saddlepoints, energetically located between the tetragonal and trigonal extrema. In the case of $E_{JT}(D_{4h}{}^c) = E_{JT}(D_{3d}{}^c)$ a continuous distribution of minima with

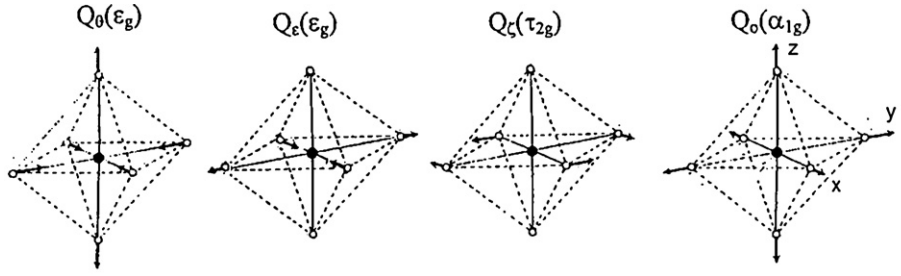

$$Q_\theta = \frac{1}{2\sqrt{3}}\{2\Delta a_z + 2\Delta a_{-z} - \Delta a_x - \Delta a_{-x} - \Delta a_y - \Delta a_{-y}\} \qquad Q_\varepsilon = \frac{1}{2}\{\Delta a_x + \Delta a_{-x} - \Delta a_y - \Delta a_{-y}\}$$

$$Q_\zeta = \frac{1}{2}a\{\Delta\alpha_x + \Delta\alpha_{-x} - \Delta\alpha_y - \Delta\alpha_{-y}\}$$

Fig. 5. The symmetrized components of the vibronically active ε_g and τ_{2g} modes in O_h and their analytical forms (Q_ξ, Q_η analogous to Q_ζ; for the latter quantity the relation: $|\Delta\alpha_x| = |\Delta\alpha_x| = |\Delta\alpha_y| = |\Delta\alpha_{-y}| = |\Delta\alpha|$ holds and a is the metal ligand distance); the totally symmetric α_{1g} vibration is also shown.

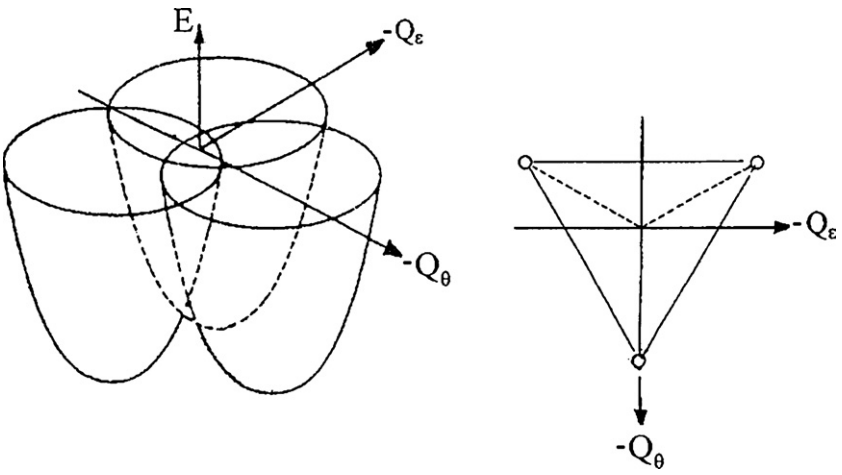

Fig. 6. The two-dimensional potential energy surface, describing the vibronic coupling between an octahedral T_g ground state and the ε_g vibrational mode. The projection of the minimum positions at D_{4h}, compressed, onto the Q_θ–Q_ε plane is also shown.

the same energy for trigonal, tetragonal or orthorhombic distortions should be observed [16].

(c) If higher-order coupling terms are included in the calculations, however, situations may arise, in which the absolute minima of the ground state potential surface are of o-rhombic nature. We will critically inspect the possibility of such cases, and consider the influence of spin–orbit coupling as well, in the next sections.

The Hamiltonian matrix, including all quadratic terms [19,6] is given in Appendix A.1.

2.2. The $T_g \otimes \varepsilon_g$ vibronic interaction in O_h

Leaving the coupling to the τ_{2g} modes aside, matrix (1) is diagonal with respect to the tetragonal V_ε coupling energies. The potential energy surface is sketched in Fig. 6. Setting:

$$Q_\theta = \rho_\varepsilon \cos\varphi; \quad Q_\varepsilon = \rho_\varepsilon \sin\varphi \tag{3}$$

the minima of the three parabolic constituents occur at values of the angular distortion parameter of $\varphi = 180°, 300°, 60°$ – corresponding to d_{xy}, d_{yz} or d_{xz} ground states of the symmetry b_{2g}, and a vibronic coupling energy of $-V_\varepsilon\rho_\varepsilon$. Having the relation $Q_\theta^2 + Q_\varepsilon^2 = \rho_\varepsilon^2$ in mind (Eq. (2)), and utilising the analytical forms of the Q_θ, Q_ε distortion paths (Fig. 5), one easily defines the radial distortion parameter:

$$\rho_\varepsilon = \{\Delta a_z^2 + \Delta a_{-z}^2 + \Delta a_y^2 + \Delta a_{-y}^2 + \Delta a_x^2 + \Delta a_{-x}^2\}^{1/2} \tag{4a}$$

where the Δa_i are the bond length changes by the induced distortion with respect to the octahedral distance a. In the case of a tetragonal compression or elongation (D_{4h} point group; $|\Delta a_z| = 2|\Delta a_{x(y)}| \equiv 2/3\Delta_d$). Eq. (4a) simplifies to (Δ_d: difference between long and short bond lengths):

$$\rho_\varepsilon = \frac{2}{\sqrt{3}}\Delta_d \tag{4b}$$

Inspecting the (E versus Q_θ) cross section of the two-dimensional curve in Fig. 6, left, the total adiabatic energy along the two branches is:

$$E(b_{2g}) = \frac{1}{2}K_\varepsilon\rho_\varepsilon^2 + V_\varepsilon\rho_\varepsilon\cos\varphi + \frac{1}{2}L_\varepsilon\rho_\varepsilon^2 \tag{5a}$$

$$E(e_g) = \frac{1}{2}K_\varepsilon\rho_\varepsilon^2 - \frac{1}{2}V_\varepsilon\rho_\varepsilon\cos\varphi - \frac{1}{4}L_\varepsilon\rho_\varepsilon^2 \tag{5b}$$

where we have supplemented the energy expressions by the second-order coupling term L_ε (see Appendix A.1) and by the restoring energy. Minimising Eq. (5a) at $\varphi = 180°$ with respect to ρ yields:

$$\rho_\varepsilon^{cm} = \frac{V_\varepsilon}{K_\varepsilon + L_\varepsilon}; \quad E_1^{cm} = -E_{JT}^{c} = -\frac{1}{2}V_\varepsilon\rho_\varepsilon^{cm} \tag{6}$$

These values refer to the minimum of anyone of the three paraboloids in Fig. 6 and correspond to a tetragonal compression (upper index c). The vertical Frank-Condon transition within the T-ground state (see Fig. 7) – the difference between $E(e_g)$ and $E(b_{2g})$ at ρ^{cm} and $\varphi_m{}^c = 180°$ (or 300°, or 60°) – is accordingly:

$$E_{FC}^{c} = 3E_{JT}^{c}\left\{\frac{1 + a/2}{1 + a}\right\}, \quad \text{with } \frac{L_\varepsilon}{K_\varepsilon} = a \tag{5c}$$

and equivalent to $3\delta_2$ (Fig. 4b; $D_{4h}{}^c$). Following the distortion paths opposite to those, which meet the parabolic minima ($\varphi_m^e = 0°, 120°$ and 240°), one moves toward saddlepoints in the potential energy surface, which appear as relative minima in the (E versus Q_θ) cross section (Fig. 7). They refer to tetragonally elongated octahedra and a doubly degenerate ground state, which is seen when minimising the energy in Eq. (5b) with respect to ρ_ε at $\varphi_m^e = 0°$:

$$\rho_\varepsilon^{em} = \frac{V_\varepsilon}{2K_\varepsilon - L_\varepsilon}; \qquad E_{2,3}^{em} = -E_{JT}^{e} = -\frac{1}{4}V_\varepsilon\rho_\varepsilon^{em} \tag{7}$$

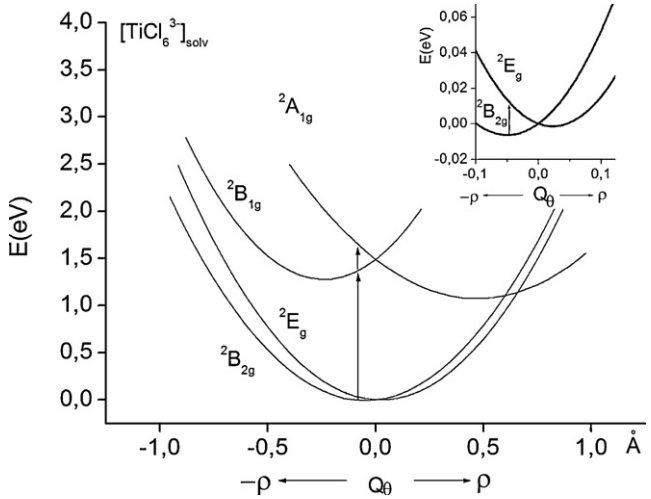

Fig. 7. The cross section of the adiabatic potential surface in Fig. 6 along the D_{4h}-path for the $^2T_{2g}$ ground state and the ^2E_g excited state of the $TiCl_6{}^{3-}$ polyhedron – as calculated by DFT (with the parameters in Tables 2 and 3). The Franck–Condon transitions within the $^2T_{2g}$ ground state and to the ^2E_g split states are indicated.

Table 1
Symmetry characteristic of the (Q_θ, Q_ε; Q_ξ, Q_η, Q_ζ) space in O_h (48 symmetry operations) under the influence of $T_g \otimes (\varepsilon_g + \tau_{2g})$ vibronic coupling (Γ_j: representation of vibrational mode; $K(O_h, \Gamma_j)$: kernel of class subdivision and H (O_h, K): the corresponding factor group; EK: epikernel; k, h, ek – the numbers in parentheses – are the respective orders). The listed groups G′ (O_h, EK) refer to those symmetry operations, which reproduce the symmetry-equivalent extrema of the considered EK; the generating displacement vector (DV) for most epikernels in (Q_θ, Q_ε; Q_ζ, Q_η, Q_ξ) space is also listed.

Γ_j	K (O_h, Γ_j)	H (O_h, K)	EK	G′ (O_h, EK)	DV
ε_g	$D_{2h}{}^{**}(8)$[a]	C_{3v} (6)	D_{4h} (16)	C_3 (3)	[ρ_ε 0, 0 0 0]
τ_{2g}	C_i (2)	T_d (24)	D_{3d} (12)	S_4 (4)	[0 0, ρ_τ ρ_τ ρ_τ]
			$D_{2h}{}^{*}$ (8)[a]	C_{3v} (6)	[0 0, 0 0 ρ_τ]
			C_{2h} (4)	T (12)	–
$\varepsilon_g + \tau_{2g}$	C_i (2)	T_d (24)	[b]		
			$D_{2h}{}^{*}$ (8)	C_{3v} (6)	[1/2 ρ_ε 0, 0 0 ρ_τ]
			C_{2h} (4)	T (12)	–

[a] The notation $D_{2h}{}^{**}$ and $D_{2h}{}^{*}$ indicates, that the distortion in the molecular x–y plane is radial ($a_x \neq a_y$; $\sphericalangle a_x$, $a_y = 90°$) and angular ($a_x = a_y$; $\sphericalangle a_x$, $a_y \neq 90°$), with the twofold axes extending along the bond lengths, and bisecting the bond length directions in one plane (Fig. 5), respectively.

[b] Epikernels resulting from either $T_g \otimes \varepsilon_g$: D_{4h}, $D_{2h}{}^{**}$ or $T_g \otimes \tau_{2g}$ coupling: D_{3d}.

The depth of these relative minima is – for small second-order coupling constants L_ε – only one quarter of that calculated for the absolute minima at D_{4h}, compressed.

A closer glance onto the symmetry of the $T_g \otimes \varepsilon_g$ interaction by group theory – we follow essentially the considerations of Murray-Rust et al. [20] – allows a better understanding of the potential energy surface in Fig. 6. Q_θ and Q_ε are the components of the ε_g representation in O_h and are both totally symmetric in the subgroup D_{2h} ($D_{2h}{}^{**}$ – for the definition see Table 1) – as is easily verified by inspecting the respective character tables. The invariant subgroup $D_{2h}{}^{**}$ is called the kernel K (O_h, ε_g) of the ε_g representation in the octahedral group and possesses the symmetry of a general point on the (E, Q_θ, Q_ε) surface. K serves as the kernel of a subdivision of the octahedral group G into classes, which are the elements of the thus defined factor group H (G, K). The order h of H is accordingly g/k (=6), where g (=48) and k (=8) are the orders of G and K, respectively. H can be considered as containing all those symmetry operations, which transfer a distortion K into equivalent ones, with different orientations. H (O_h, D_{2h}) is derived to be C_{3v}. While K defines a general point on the potential energy surface, there are other, higher-symmetry displacements, in the course of which only one component of the ε_g mode becomes totally symmetric. This condition defines a co- or epikernel. There is just one in our case, EK (O_h, ε_g), which is of D_{4h} symmetry (Table 1). The six D_{4h} extremum points at $\pm\rho_\varepsilon$ {(−1, 0), (1/2, $-1/2\sqrt{3}$), (1/2, $1/2\sqrt{3}$)} in the Q_θ–Q_ε plane subdivide into three with a positive sign, constituting the absolute minima in the potential surface (compressed octahedra) – see Fig. 6 – and three with a negative sign, corresponding to saddlepoints (elongated octahedra). Because the D_{4h} minima correspond to special positions on mirror planes, they are multiplied not according to the factor group C_{3v} but only tripled according to the C_3 subgroup (Table 1).

Very useful in this context is the epikernel principle, formulated by *A*. Ceulemans et al. [19]. It states, that extremum points prefer *epikernels* to *kernels* and *maximal epikernels* to *lower ranking epikernels*. As the authors note, it follows the more general statement (Curie, 1894 [21]), that the symmetry, characteristic of a phenomenon, is the maximal one, which is compatible with the existence of the phenomenon. Indeed, the D_{4h} distortions (Fig. 6) refer to extremum points; orthorhombic distortions can only be stabilised by applying either strains on the systems or possibly, for example, by superimposing an additional $T_g \otimes \tau_{2g}$ vibronic coupling (vide infra).

We will now shortly discuss the influence of spin–orbit coupling, looking at the interplay of energy effects induced by the linear

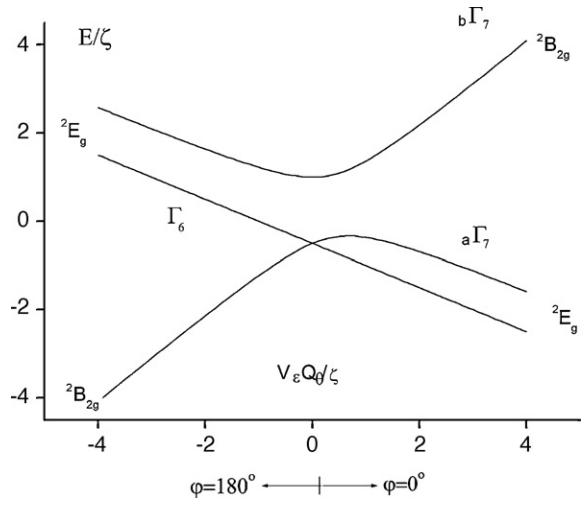

Fig. 8. The interplay between vibronic $T \otimes \varepsilon$ interaction and LS coupling for the case of a compressed and an elongated D_{4h} distortion of a six-coordinated d^1 cation, with an orbital singlet and doublet ground state, respectively.

Jahn–Teller interaction according to D_{4h} and by the LS coupling constant ζ. Matrix (8a) – the (+)/(−) signs refer to the spin orientations – considers this (for $\varphi = 0°$, 180°), and Fig. 8 pictorially shows the mutual dependence:

$$\begin{array}{ccc} d_{yz}(\pm) & d_{xz}(\pm) & d_{xy}(\mp) \\ \begin{bmatrix} -\frac{1}{2}V_\varepsilon Q_\theta & \pm\frac{i}{2}\zeta & \mp\frac{1}{2}\zeta \\ \mp\frac{i}{2}\zeta & -\frac{1}{2}V_\varepsilon Q_\theta & \frac{i}{2}\zeta \\ \mp\frac{1}{2}\zeta & -\frac{i}{2}\zeta & V_\varepsilon Q_\theta \end{bmatrix} & & \end{array} \quad (8a)$$

For a ratio between $V_\varepsilon\rho_\varepsilon$ and the effective constant ζ of about 4(or 1), for example (values approximately valid for $TiX_6{}^{3-}$ polyhedra with X = F^-(Cl^-)), the $_a\Gamma_7$ ground state at $\varphi^c = 180°$ is stabilised with respect to the $^2B_{2g}$ state by 2% (or 22%) when taking account of LS coupling. On the other hand, in the elongated case at $\varphi^e = 0°$, the Γ_6 ground state is stabilised by $\zeta/2$ in respect to the ^2E_g state, independent on the $V_\varepsilon\rho_\varepsilon/\zeta$ ratio – but never making the elongation energetically more favourable than the compression; the energy difference between $_a\Gamma_7$ and Γ_6 in the case of a compressed and an elongated octahedron, respectively, is distinct even for very small $V_\varepsilon\rho_\varepsilon/\zeta$ ratios, when recalling that ρ_ε^{cm} is by a factor of two larger than ρ_ε^{em} (Eqs. (6) and (7)). Explicitly, the energies of the ground state in $D_{4h}{}^c$ are, for very small as well as for the chosen $r = V_\varepsilon\rho_\varepsilon/\zeta$ ratios:

$$\begin{aligned} r \ll 1: &\quad E(_a\Gamma_7) = -0.50\zeta - 0.50V_\varepsilon\rho_\varepsilon \\ r \cong 1: &\quad E(_a\Gamma_7) = -0.36\zeta - 0.86V_\varepsilon\rho_\varepsilon \\ r \cong 4: &\quad E(_a\Gamma_7) = -0.15\zeta - 0.98V_\varepsilon\rho_\varepsilon \end{aligned} \quad (8b)$$

After all, LS coupling will not mislead conclusions derived from results, which are obtained without LS coupling in the case of $V_\varepsilon\rho_\varepsilon/\zeta$ ratios > 1, if the absolute minima at D_{4h}, compressed, are considered.

2.3. The $T_g \otimes \tau_{2g}$ interaction

Even when disregarding the tetragonal coupling in matrix (1), the remaining non-diagonal elements of the determinant still impede simple analytical solutions. However, as was shown by Öpik and Pryce [18], solutions are possible for certain special points in the Q_ξ–Q_η–Q_ζ space. Some introductory symmetry considera-

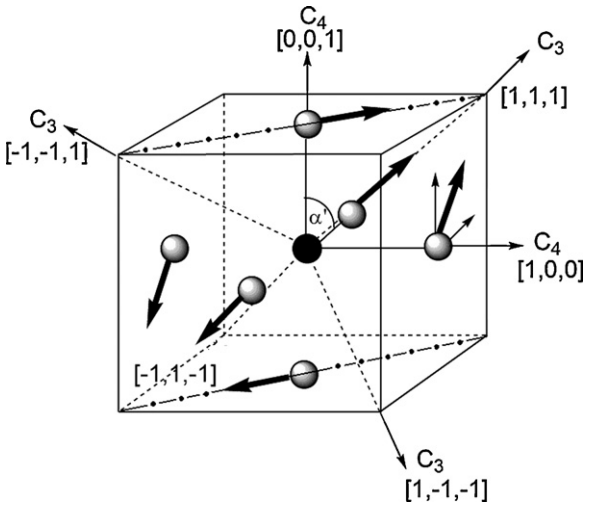

Fig. 9. The symmetry properties of the extremum points or planes on the potential energy surface according to $T_{2g} \otimes \tau_{2g}$ Jahn–Teller coupling in an octahedron (the circumambient cube has been drawn for the sake of a better geometrical illustration): The number triples at C_3 refer to the (Q_ξ, Q_η, Q_ζ) space or, alternatively, to the cartesian coordinates and denote the positions of the four D_{3d} minima (trigonal compression). The coordinates of the three octahedral axes (the one at [0,1,0] is not indicated) and their opposite directions portray the six extremum points according to the $D_{2h}{}^*$ epikernel symmetry in the (Q_ξ, Q_η, Q_ζ) space (and correlate with the six C_2 axes in Cartesian space). The faint arrows, shown for the ligand on the *x*-axis, mirror angular displacements $\Delta\alpha$ within the Q_i components ($i = \xi, \eta, \zeta$) of the τ_{2g} mode (Fig. 5), and the fat arrows angular shifts $\Delta\alpha'$ (Eq. (10b)) along the face diagonals towards the trigonal axes ($\alpha = 54{,}74^\circ$ is the angle between the central cation-ligand axes and the space-diagonal in a cube). One σ_d plane of the T_d factor group is indicated by point-dash lines.

tions may be useful again. The maximal epikernel for the $T_{2g} \otimes \tau_{2g}$ interaction in O_h is the trigonal subgroup D_{3d} (Table 1). This symmetry characterises absolute minima, which are correlated with the four C_3 axes of the octahedron and an A_{1g} ground state – recalling, that the coupling constants are defined as positive quantities. The respective displacement coordinates in the (Q_ξ, Q_η, Q_ζ) space are $+(-)\rho_\tau$ {(1 1 1), (1 −1 −1), (−1 1 −1), (−1 −1 1)}, according to the D_{3d} condition $|Q_\xi| = |Q_\eta| = |Q_\zeta|$, and correspond to a trigonal compression, if the (+) sign is chosen. The (−) sign is associated with trigonally elongated octahedra at saddlepoints and a (still Jahn–Teller unstable) E_g ground state (Fig. 9). The total-distortion parameter ρ_τ is:

$$Q_\xi^2 + Q_\eta^2 + Q_\zeta^2 = 3\rho_\tau^{*2} \equiv (\rho_\tau^t)^2 \tag{9}$$

while ρ_τ^* reflects angular motions in only *one* of the three components of the τ_{2g} modes in Fig. 5. Utilising the analytical forms of the respective distortion paths, the latter is derived to be of the magnitude:

$$\rho_\tau^* = 2a \cdot |\Delta\alpha| \tag{10a}$$

where $\Delta\alpha$ is the angular deviation from 90° according to Fig. 5 (we designate in the following all parameters, which refer to the epikernel symmetry $D_{2h}{}^*$ for $T_g \otimes \tau_{2g}$ coupling, with an upper star-index: see Table 1 and Section 2.4) and *a* the metal–ligand distance. If the distortion is trigonal, as considered so far, it is more convenient to replace $\Delta\alpha$ by the deviation $\Delta\alpha'$ from the angle of 54.74° between a C_3 axis and the three neighboured C_4 axes in an octahedron, as visualised in Fig. 9:

$$\rho_\tau = \sqrt{2}a \cdot |\Delta\alpha'| \tag{10b}$$

The kernel symmetry is C_i, and the factor group H (O_h, C_i) based on it is T_d. The latter symmetry creates for each general point C_i on the (E, Q_ζ, Q_η, Q_ξ) surface 24 equivalent ones (Table 1). The absolute D_{3d} minima correspond to special positions on the 3-fold axes of T_d (Fig. 9) and are generated from one of these by applying the four symmetry operations within the S_4 subgroup of the factor group T_d (Table 1). The epikernel next in ranking to D_{3d} possesses D_{2h} symmetry ($D_{2h}{}^*$ in Table 1). It is associated with the three C_4 axes in the (Q_ξ, Q_η, Q_ζ) space, according to the six displacement triples $\pm\{[1\,0\,0], [0\,1\,0], [0\,0\,1]\}$ (Fig. 9). The different signs distinguish, whether the angular deviations $\Delta\alpha$ are positive or negative in the respective symmetrised coordinates (Fig. 5). Anyone of the $D_{2h}{}^*$ extremum points on an S_4 axis of T_d multiplies according to the six operations of C_{3v}. The epikernel of lowest ranking possesses C_{2h} symmetry and considers all points in the (Q_ξ, Q_η, Q_ζ) space, which are located on one of the six σ_d mirror planes of T_d – excluding positions on the C_3 or C_4 axes. Explicitly, any C_{2h} point [Q_ξ, Q_η, Q_ζ] or [Q_ξ, $-Q_\eta$, Q_ζ] (with $Q_\xi = Q_\eta$ and Q_i ($i = \xi, \eta, \zeta$) $\neq 0, \pm 1$) on the tetrahedral σ_d plane indicated in Fig. 9, is multiplied according to the 12 symmetry operations of the rotation group T (Table 1). Every distortion path between $D_{2h}{}^*$ and D_{3d} has this symmetry. In all three epikernels only one of the three τ_{2g} components becomes totally symmetric.

We now proceed to calculate the structures and energies of the extremum points on the adiabatic potential energy surface according to the $T_{2g} \otimes \tau_{2g}$ coupling for an octahedrally coordinated d^1 cation. For anyone of the four D_{3d}, compressed, minima the following matrix, obtained by diagonalising matrix (1), is valid, when keeping only the V_τ terms (as positive quantities) and after having added the second-order coupling contributions according to Appendix A.1 (L_τ vanishes with the D_{3d} condition $|Q_\zeta| = |Q_\eta| = |Q_\xi| = 1$):

t_-	t_+	t_0
$\frac{1}{2}(V_\tau\rho_\tau^c + X_\tau\rho_\tau^{c2})$	0	0
0	$\frac{1}{2}(V_\tau\rho_\tau^c + X_\tau\rho_\tau^{c2})$	0
0	0	$-V_\tau\rho_\tau^c - X_\tau\rho_\tau^{c2}$

(11)

The basis wave functions, quantised along a threefold axis, are:

$$\begin{aligned} t_0 &= \frac{1}{\sqrt{3}}(d_{xy} + d_{xz} + d_{yz}) && a_{1g} \\ t_+ &= \frac{1}{\sqrt{6}}(2d_{xy} - d_{xz} - d_{yz}) && e_g \\ t_- &= \frac{1}{\sqrt{2}}(d_{xz} - d_{yz}) && e_g \end{aligned} \tag{12}$$

The A_{1g} ground state energy is – if the restoring energy from Eq. (9) is supplemented:

$$E_1^c = \frac{3}{2}K_\tau\rho_\tau^{c2} - V_\tau\rho_\tau^c - X_\tau\rho_\tau^{c2} \tag{13}$$

and after minimisation with respect to ρ_τ^c:

$$\rho_\tau^{cm} = \frac{V_\tau}{3K_\tau - 2X_\tau}, \qquad E_1^{cm} = -E_{JT}^c = -\frac{1}{2}V_\tau\rho_\tau^{cm} \tag{14}$$

The Franck–Condon transition at ρ_τ^{cm} from a_{1g} to e_g – the ground state splitting $3\delta_2^\tau$ (Fig. 4c) – correlates with $3E_{JT}^c$ in first-order and is derived from matrix (11) and Eq. (14) to be of the magnitude:

$$E_{FC}^c = 3E_{JT}^c\left\{1 + \frac{a}{1-2a}\right\}; \quad a = \frac{X_\tau}{3K_\tau} \tag{15}$$

The D_{3d} distortion path in the reverse directions (along $\rho_\tau\{(-1\,-1\,-1), (-1\,1\,1), (1\,-1\,1)$ or $(1\,1\,-1)\}$), is described via a sign change of the Q_i ($i = \zeta, \eta, \xi$) displacements on the non-diagonal positions of matrix (1) and accordingly of the V_τ contributions in matrix

Table 2
Structural and energetic DFT results for TiX_6^{3-} polyhedra (X = F^-, Cl^-) in the epikernel symmetries D_{4h}, D_{3d} and D_{2h}^* of vibronic $T_{2g} \otimes (\varepsilon_g + \tau_{2g})$ coupling, and the linear and quadratic coupling constants calculated from these data according to the equations in Section 2. The distortion parameters and JT stabilisation energies of the lowest states in each symmetry are underlined; the calculated vibrational energies (see text) are also listed.

D_{4h}	ρ_ε^{cm} (Å)	ρ_ε^{em} (Å)	a_{av} (Å)	E ($B_{2g} \rightarrow E_g$)	E_{JT}^c (eV)	E_{JT}^e (eV)	$\hbar\omega_\varepsilon$ (eV)
F^-	0.083[a]	0.041[b]	1.97_3	0.103 eV	0.034	0.008_5	0.047
Cl^-	0.050[a]	0.023[b]	2.43_5	0.020 eV	0.006_5	0.001_5	0.025_5
D_{3d}	ρ_τ^{cm} (Å)	ρ_τ^{cm} (Å)	a_{av} (Å)	E ($A_{1g} \rightarrow E_g$)	E_{JT}^c (eV)	E_{JT}^e (eV)	$\hbar\omega_\tau$ (eV)
F^-	0.094[c]	0.022[c]	1.97_3	0.082 eV	0.020	0.001_5	0.024_5
Cl^-	0.018[d]	≅0[d]	2.43_4	≈0.001 eV	<0.001	≅0	0.005
D_{2h}^*	ρ_τ^{*m} (Å)	ρ_ε^{cm} (Å)	a_{av} (Å)	E ($B_{3g} \rightarrow B_{2g}$)	E ($B_{3g} \rightarrow A_g$)	E_{JT}^* (eV)	
F^-	0.098[e]	0.039[f]	1.97_3	0.057 eV	0.080_5 eV	0.022	
Cl^-	0.023[e]	0.022[f]	2.43_3	≈0.004 eV	0.019 eV	≈0.002	
	V_ε	V_τ	K_ε	K_τ	L_ε	L_τ	X_τ	W
F^-	0.82	0.50(8)[g] eV Å^{-1}	9.9	2.9(3)[g]	≅0	≈0.5	1.7	≈0 eV Å^{-2}
Cl^-	0.27	(≈0.1)	5.4	–	≅0	–	–	≈0 eV Å^{-2}

[a] 1.997 Å (4×), 1.925 Å (2×) and 2.449 Å (4×), 2.406 Å (2×), respectively.
[b] 1.960 Å (4×), 1.995 Å (2×) and 2.428 Å (4×), 2.448 Å (2×), respectively.
[c] $|\Delta\alpha'| = 1.92°$ and 0.45°, respectively.
[d] $|\Delta\alpha'| = 0.30°$ and ≅0°, respectively.
[e] $\Delta\alpha = 1.43°$ and 0.27°, respectively.
[f] 1.961 Å (4×), 1.997 Å (2×) and 2.427 Å (4×), 2.446 Å (2×), respectively.
[g] ±0.08 eV Å^{-1} and ±0.3 eV Å^{-2}: the lower and upper limits refer to D_{3d} and D_{2h}^*, respectively.

(11). The octahedra are now trigonally elongated and the lower split-state is $E_g(t_+, t)$. We obtain:

$$E_{2,3}^e = \frac{3}{2}K_\tau\rho_\tau^{e2} - \frac{1}{2}V_\tau\rho_\tau^e + \frac{1}{2}X_\tau\rho_\tau^{e2}$$
$$\rho_\tau^{em} = \frac{1}{2}\frac{V_\tau}{3K_\tau + X_\tau} \qquad (16)$$
$$E_{2,3}^{em} = -E_{JT}^e = -\frac{1}{4}V_\tau\rho_\tau^{em}$$

LS coupling has a similar energy effect on the ground state stabilisation as the one discussed for D_{4h}. The corresponding matrix is easily constructed from those in Eqs. (1) and (8a), when keeping only the V_τ and ζ terms. In distinction to D_{4h} we note, that the lowest state in $D_{3d}{}^c$ is raised in energy by LS coupling for large $V_\tau\rho_\tau/\zeta$ ratios, while LS coupling stabilises the ground state in $D_{3d}{}^e$ (see Eq. (8b)):

$$D_{3d}{}^e: \quad E({}_a\Gamma_4) = -\frac{1}{2}V_\tau\rho_\tau^e - \frac{\zeta}{2}$$
$$D_{3d}{}^c: \quad V_\tau\rho_\tau \gg \zeta \Rightarrow \quad E({}_a\Gamma_4) = -V_\tau\rho_\tau^c + \frac{\zeta}{3} \qquad (17)$$
$$V_\tau\rho_\tau \ll \zeta \Rightarrow \quad E({}_a\Gamma_4) = -\frac{1}{6}V_\tau\rho_\tau^c - \frac{\zeta}{2}$$

However, because ρ_τ^c is much larger than ρ_ε^e (Table 2; Eqs. (14) and (16)), we may readily conclude that the lowest state is the one according to $D_{3d}{}^c$. A further inspection is not needed, for reasons discussed in the next section.

The D_{2h}^* extrema correspond to saddle points in the $T_{2g} \otimes \tau_{2g}$ potential surface in the linear approximation, with only one non-diagonal Q_i in matrix (1) different from zero. The derivation of the respective diagonalised energy matrix (Eq. (18)) is straightforward, using Appendix A.1 for the supplementary higher-order coupling contributions. The symmetry-adapted coordinate system is sketched in Fig. 10, and the accordingly quantized wave functions

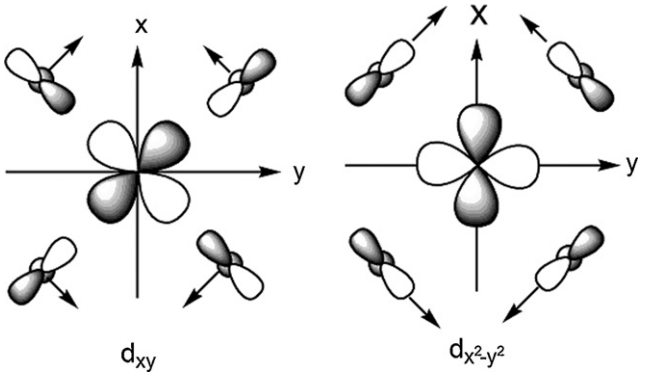

Fig. 10. The D_{2h}^* symmetry due to Q_ζ (τ_{2g})-type displacements ($T_{2g} \otimes \tau_{2g}$ coupling),with the proper choice of the Cartesian axes (matrix and wave functions (Eqs. (18) and (19)) ⇒ the degeneracy of the σ-antibonding e_g^* MO is, in first approximation, not lifted, because the overlap with the $3d_{z^2}(a_g^*)$ orbital is not influenced at all and the one with the $d_{xy}(b_{1g}^*)$ orbital – left – is (for small displacements) only affected in higher order. Also the π-overlap with the $d_{x^2-y^2}(a_g^*)$ orbital of t_{2g}^* – right – is not energetically influenced by the Q_ζ motions in first order (see matrix (18)).

are given in Eq. (19).

$d_{+1}(b_{3g})$	$d_{-1}(b_{2g})$	$d_{x^2-y^2}(a_g)$
$-1/2\ V_\tau Q_\zeta - \frac{1}{4}\ L_\tau Q_\zeta^2$	0	0
0	$+1/2\ V_\tau\ Q_\zeta - 1/4\ L_\tau\ Q_\zeta^2$	
0	0	$+1/2\ L_\tau Q_\zeta^2$

(18)

$$d_{+1(-1)} = \frac{1}{\sqrt{2}}(d_{xz} + (-)d_{yz}) \qquad (19)$$

The active vibrational z-component of τ_{2g} determines the magnitude of the radial distortion parameter in Eq. (10), with $Q_\zeta = \rho_\tau^*$.

The ground state energy is accordingly:

$$E^*(b_{3g}) = \frac{1}{2}K_\tau\rho_\tau^{*2} - \frac{1}{2}V_\tau\rho_\tau^* - \frac{1}{4}L_\tau\rho_\tau^{*2} \quad (20)$$

yielding the following radial distortion parameter and energy stabilisation, respectively:

$$\rho_\tau^{*m} = \frac{V_\tau}{2K_\tau - L_\tau}$$
$$E^{*m}(b_{3g}) = -E_{JT}^* = -\frac{1}{4}V_\tau\rho_\tau^{*m} \quad (21)$$

The same expressions result, if $Q_\zeta = -\rho_\tau^*$ is chosen – here with $d_{-1}(b_{2g})$ as the ground state wave-function (symmetry-equivalent solution). When higher-order coupling is neglected, the ratio of $E_{JT}^*(b_{3g})$ and the stabilisation energy for the D_{3d} minima E_{JT}^c (Eq. (14)) is smaller than 1 (≈0.75), as expected from the epikernel principle: $D_{2h}{}^*$ is of lower ranking than D_{3d}. This holds – as DFT shows (vide infra) – also, if derived numerical values for L_τ and X_τ (Table 2) are additionally taken into account. We finally point out, that the distortion in $D_{2h}{}^*$ is of a different quality compared to that in D_{3d}. In the latter point group it implies a *correlated* movement between the three vibrational τ_{2g} components.

We now treat the case of simultaneous coupling of ε_g- and τ_{2g}-type displacements with an electronic T ground state more closely, and consider particularly the importance of higher-order coupling terms between Q_j ($j = \theta, \varepsilon$) and Q_i ($i = \xi, \eta, \zeta$) displacements.

2.4. The $T_g \otimes (\varepsilon_g + \tau_{2g})$ Jahn–Teller interaction

The group-theoretical analysis yields, that in the five-dimensional (E, $Q_\varepsilon Q_\theta$, $Q_\xi Q_\eta Q_\zeta$) adiabatic potential energy surface the following epikernels exist (Table 1):

a. those typical for $T_{2g} \otimes \varepsilon_g$ coupling solely: D_{4h}, $D_{2h}{}^{**}$ (which was a kernel before);
b. those characteristic of $T_{2g} \otimes \tau_{2g}$ coupling solely: D_{3d};
c. those, which result from the coupling to both active vibrations: $D_{2h}{}^*$, C_{2h}; both were present already in the smaller τ_{2g} space, but have now undergone additional vibronic interactions with ε_g.

We consider first the extremum points of $D_{2h}{}^*$ symmetry, in which a displacement according to Q_i ($i = \xi$ or η or ζ) is combined with a tetragonal distortion according to $-1/2(Q_\theta - \sqrt{3}Q_\varepsilon)$, $-1/2(Q_\theta + \sqrt{3}Q_\varepsilon)$ or Q_θ, respectively. We have chosen an elongated polyhedron ($\varphi = 0$), because a compression necessarily leads into the $D_{2h}{}^{**}$ point group, lacking a coupling with τ_{2g} motions. This case is visualised in the MO diagram of Fig. 4d. The following matrix is valid for a displacement ($-1/2\ \rho_\varepsilon\ 0; 0\ 0\ \rho_\tau$) of this type (Table 1), when using matrix (1) accordingly and if second-order interaction terms (Appendix A.1) are added:

	d_{yz}	d_{xz}	d_{xy}
d_{yz}	$-1/2\ V_\varepsilon\rho_\varepsilon - 1/4\ (L_\varepsilon\rho_\varepsilon^2 + L_\tau\rho_\tau^2)$	$-1/2\ (V_\tau\rho_\tau + W\rho_\varepsilon\rho_\tau)$	0
d_{xz}	$-1/2\ (V_\tau\rho_\tau + W\rho_\varepsilon\rho_\tau)$	$-1/2\ V_\varepsilon\rho_\varepsilon - 1/4\ (L_\varepsilon\rho_\varepsilon^2 + L_\tau\rho_\tau^2)$	0
d_{xy}	0	0	$V_\varepsilon\rho_\varepsilon + 1/2\ (L_\varepsilon\rho_\varepsilon^2 + L_\tau\rho_\tau^2)$

(22)

After diagonalisation one obtains for the lowest energy component:

$$E(b_{3g}) = \frac{1}{2}\left\{K_\varepsilon\rho_\varepsilon^{e2} + K_\tau\rho_\tau^{*2} - V_\varepsilon\rho_\varepsilon^e - V_\tau\rho_\tau^* - W\rho_\varepsilon^e\rho_\tau^* - \frac{1}{2}L_\varepsilon\rho_\varepsilon^{e2} - \frac{1}{2}L_\tau\rho_\tau^{*2}\right\} \quad (23)$$

The partial differentiation with respect to ρ_ε and ρ_τ, respectively, leads to

$$\rho_\varepsilon^{em} = \frac{V_\varepsilon + W\rho_\tau^{*m}}{2K_\varepsilon - L_\varepsilon}; \qquad \rho_\tau^{*m} = \frac{V_\tau + W\rho_\varepsilon^{em}}{2K_\tau - L_\tau} \quad (24)$$

The second-order coupling parameter W arises from the simultaneous interaction with ε_g and τ_{2g} modes. From the analytical expressions for ρ_ε^{em} and ρ_τ^{*m} one can easily obtain the two quantities as functions of V_i, L_i, K_i ($i = \varepsilon, \tau$) and W solely. The JT stabilisation energy with respect to the undistorted octahedron is calculated from Eqs. (23) and (24) to be of the magnitude:

$$E^m(b_{3g}) = -E_{JT}^* = -\frac{1}{4}(V_\varepsilon\rho_\varepsilon^{em} + V_\tau\rho_\tau^{*m}) \quad (25)$$

The higher-order contribution via W may enhance $E_{JT}(D_{2h}{}^*)$ beyond the energies resulting from the linear couplings $T \otimes \varepsilon$ and $T \otimes \tau_2$, because ρ_ε^{em} and ρ_τ^{*m} might become larger with respect to the values in Eqs. (7) and (21) by the presence of a finite W parameter (Eqs. (24)). Thus, one cannot exclude with certainty that the orthorhombic D_{2h} extremum points become absolute minima in the (E, $Q_\theta Q_\varepsilon$, $Q_\xi Q_\eta Q_\zeta$) potential surface. The MO scheme in Fig. 4d displays main features of the considered vibronic interaction – the $T_{2g} \otimes \varepsilon_g$ coupling (tetragonal elongation) leads to an orbital doublet e_g as the ground state, which is further split by the coupling to the τ_{2g} mode. The Franck–Condon transition energies between the T_{2g} split-state manifold at ρ_ε^{em}, ρ_τ^{*m} and in $D_{2h}{}^*$, are from matrix (22) after diagonalisation:

$$E(b_{3g} \rightarrow b_{2g}) = V_\tau\rho_\tau^{*m} + W\rho_\varepsilon^{em}\rho_\tau^{*m} \quad (26)$$

$$E(b_{3g} \rightarrow a_g) = \frac{1}{2}\left\{(3V_\varepsilon\rho_\varepsilon^{em} + V_\tau\rho_\tau^{*m}) + W\rho_\varepsilon^{em}\rho_\tau^{*m} + \frac{3}{2}(L_\varepsilon\rho_\varepsilon^{em2} + L_\tau\rho_\tau^{*m2})\right\} \quad (27)$$

LS coupling modifies the JT energy slightly. With $1/2V_\tau\rho_\tau^{*m} \cong 1/2V_\varepsilon\rho_\varepsilon^{em} \cong 180\ cm^{-1}$ and $\zeta = 125\ cm^{-1}$ – values approximately valid for the $TiF_6{}^{3-}$ polyhedron (Table 2) – the electronic ground state is lowered by only further 40 cm^{-1}; this energy contribution is not of significance in respect to a possible stabilisation of a b_{3g} ground state as the absolute minimum, however (see Section 3).

We refrain from discussing the lower-ranking epikernel C_{2h} (in this point group three vibrational components out of five become totally symmetric, in difference to $D_{2h}{}^*$ where only two components transform as A_g) because it is not relevant in the context of this study.

2.5. $E_g \otimes \varepsilon_g$ coupling in O_h

While the Jahn–Teller splitting of octahedral 3d complexes with T_g ground states are usually rather small and difficult to analyse (see below), orbital doublets show considerably larger vibronic effects. This is so, because the former states are only π-antibonding, while E states possess σ-antibonding character. Thus, the excited ^2E_g state in the d-d spectra of the $TiX_6{}^{3-}$ complexes in elpasolites A'_2ATiX_6 undergo splitting of nearly 3000 cm^{-1} for X = F [22,23] and still of 1350 ± 150 cm^{-1} in the case of the weaker Cl^- ligand [24] (Fig. 11).

The theory of $E \otimes \varepsilon$ coupling is well available in the literature [6,18,16]. We shortly summarise the basic considerations. The vibronic Hamiltonian for a d^1 cation has the matrix form (A_1, A_2 are

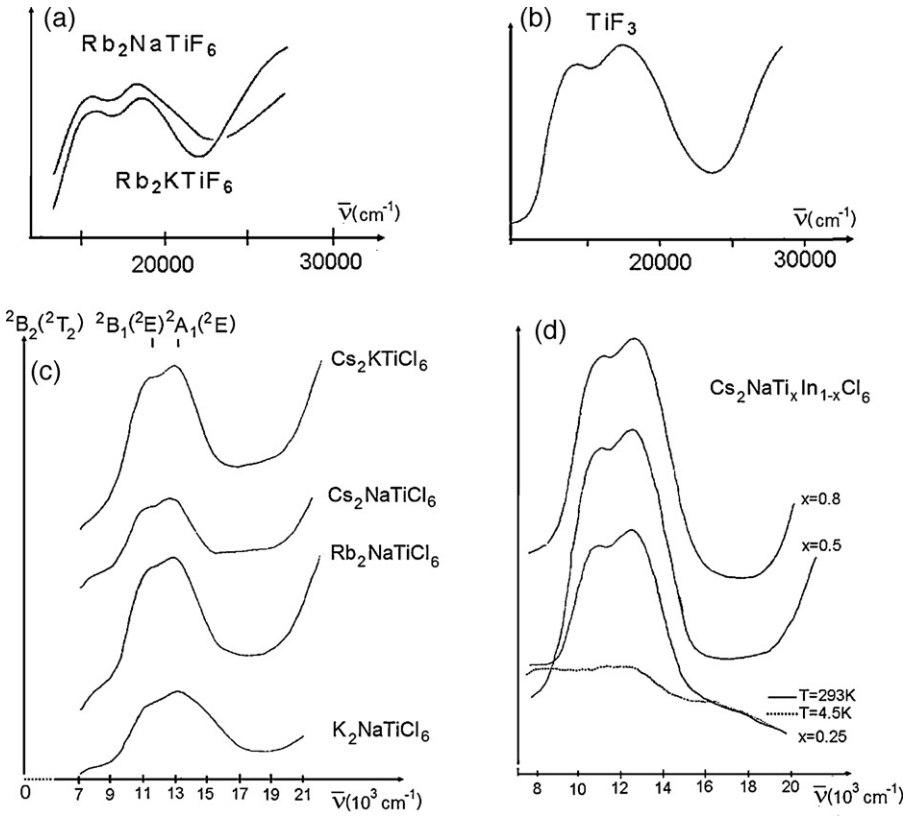

Fig. 11. The d–d spectra (powder reflection; 298 K) of elpasolites A'_2ATiX_6 ($X = F^-$, Cl^-) and of TiF_3 (top part adopted from [23]). The chloride elpasolites (bottom, left) are cubic for A′, A = Cs, K; Cs, Na; Rb, Na with the unit cell parameters $a = 10.74$; 10.39; 10.27 Å, respectively, while $K_2NaTiCl_6$ is a lower-symmetry variant. The lattice constants for the mixed crystals with In^{III} (bottom, right) decrease linearly with the Ti^{III} content from 10.53_5 to 10.39 Å.

defined as positive quantities):

$$\begin{array}{cc} d_{x^2-y^2} & d_{z^2} \\ \hline A_1Q_\theta + A_2(Q_\theta^2 - Q_\varepsilon^2) & -A_1Q_\varepsilon + 2\,A_2Q_\theta Q_\varepsilon \\ -A_1Q_\varepsilon + 2\,A_2\,Q_\theta Q_\varepsilon & -A_1Q_\theta - A_2(Q_\theta^2 - Q_\varepsilon^2) \end{array} \quad (28)$$

A_1 and A_2 are the linear and quadratic coupling constants, respectively, and Q_θ, Q_ε the components of the JT active ε_g vibration (Fig. 5). The resulting energy equation – when adding the totally symmetric restoring energy – is:

$$E_{-(+)} = \frac{1}{2}K_\varepsilon\rho_\varepsilon^2 - (+)\rho_\varepsilon\{A_1^2 + A_2^2\rho_\varepsilon^2 + 2A_1A_2\rho_\varepsilon\cos 3\varphi\}^{1/2} \quad (29)$$

The corresponding potential energy surface (leaving aside the A_2 term) is of the well-known Mexican-hat shape without preference for any value of the angular parameter φ (Fig. 12, left). If the A_2 terms are taken into account, the potential energy surface becomes structured with three absolute minima at $\varphi_m^e = 0°$, 120°, 240° and three saddle-points at $\varphi_m^c = 180°$, 300°, 60°; the cited angles refer to tetragonally elongated and compressed octahedra, respectively (Fig. 12, right).

The symmetry analysis is analogous to that for $T_g \otimes \varepsilon_g$ coupling – the only epikernel present is D_{4h}, the symmetry of the three absolute minima and of the three saddlepoints in the (E, Q_θ, Q_ε) potential surface. All other points possess the D_{2h}** kernel symmetry (Table 1). The higher-order coupling contribution comprises, above all, the nd_{z^2}–$(n+1)s$ interaction, which usually determines magnitude and sign of the A_2 increment in the $3d^n$ cases. As may be deduced from Fig. 13, the choice $\cos 3\varphi = +1$ supports an energy lowering of the $a_{1g}(d_{z^2})$ MO, due to the mentioned interaction with $a_{1g}(4s)$, and hence a tetragonal elongation. One deduces from Eq. (29), if E_- is minimised with respect to ρ_ε (for $A_1^2 \gg A_2^2\rho_\varepsilon^2$):

$$\rho_\varepsilon^m = \frac{A_1}{K_\varepsilon - 2A_2\cos 3\varphi} \quad (30a)$$
$$E_-^m = -E_{JT} = -\frac{1}{2}A_1\rho_\varepsilon^m$$

The further minimisation in respect to the angular variable yields:

$$\cos 3\varphi_m = +(-)1 \Rightarrow \varphi_m^e(\varphi_m^c) = 0°, 120°, 240°(180°, 300°, 60°) \quad (30b)$$

and as exact solutions of Eq. (29):

$$\rho_\varepsilon^{em}(\rho_\varepsilon^{cm}) = \frac{A_1}{K_\varepsilon - (+)2A_2}; \quad E_{JT}^e(E_{JT}^c) = \frac{1}{2}A_1\rho_\varepsilon^{em}(\rho_\varepsilon^{cm}) \quad (31a)$$

The E–Q_θ cross section in Fig. 13 shows the absolute minimum at $\varphi_m^e = 0°$ and the saddlepoint at $\varphi = 180°$, appearing here as a relative minimum. The Franck–Condon transition within a JT-split E_g state of a six-coordinated d^n cation in an elongated and in a compressed D_{4h}-ligand field, respectively, is derived from Eq. (29) to be of the magnitude:

$$E_{FC} = 2\rho_\varepsilon^m\{A_1 + A_2\rho_\varepsilon^m\cos 3\varphi_m\} \quad (31b)$$

Because we meet in the context of this study orbital doublets of E_g symmetry mostly as excited states, as in the d–d spectra in Fig. 11 for example, the structural properties are determined by the vibronic coupling within the T_g ground state. Here, as follows from the preceding subsections, only D_{4h}, D_{3d} or eventually D_{2h}* extremal points may occur as absolute minima. From these, the D_{3d} symmetry cannot lift the degeneracy of an $e_g(O_h)$ level (Fig. 4c), and in the case of D_{2h}* (Fig. 4d) we may hence confidently assume

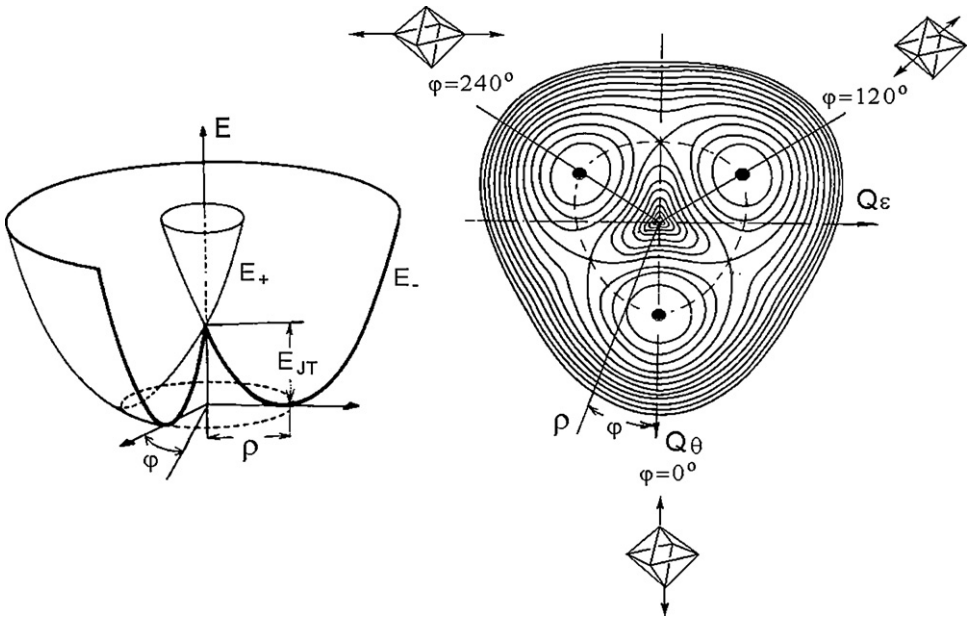

Fig. 12. The potential energy surface for linear $E \otimes \varepsilon$ coupling (left) and – in a cross section perpendicular to the energy axis – the warping due to higher order vibronic interactions (right).

that it is nearly exclusively the component due to the tetragonal elongation, which splits the orbital doublet, because τ_{2g} is not a JT active mode for an electronic E_g state. An angular displacement $\Delta\alpha$ (Eq. (10)) will slightly weaken the d_{xy}-ligand σ-overlap (Fig. 10), while the d_{z^2}-ligand overlap stays as it is – thus even diminishing the splitting of the e_g MO. An energy contribution to the splitting of an e_g^* MO (see Fig. 4c) from Q_ζ displacements may hence be neglected in first-order. We conclude, that a splitting of an excited E_g state in the d-d spectra of an octahedral d^n cation with a T_g ground state (Fig. 11) either indicates a pure $T_{2g} \otimes \varepsilon_g$ vibronic interaction according to D_{4h} compression, or eventually hints toward a $T_{2g} \otimes (\varepsilon_g + \tau_{2g})$ coupling, in which only the contribution due to the stretching mode (D_{4h} elongation) is energetically significant. The latter is much less distinct than the one in $D_{4h}{}^c$, however, due to the relation $\rho_\varepsilon^{cm} \cong 2\rho_\varepsilon^{em}$ (Eqs. (6) and (7)). DFT calculations have been performed for the three mentioned possible polyhedron symmetries in the T_{2g} ground state of a d^1-cation and in the excited E_g state as well. The results are compared with available experimental data, in particular from optical spectroscopy, in the following section.

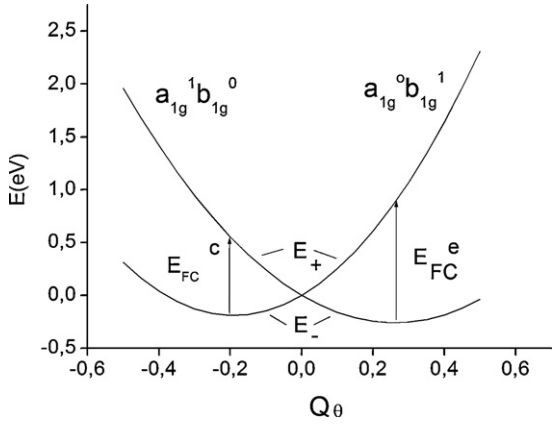

Fig. 13. Cross section of the Mexican hat potential surface along the energy axis for a cation with one electron in an excited e_g^* state; parameters are those for the MnF_6^{3-} polyhedron (DFT results): $A_1 = 2.00\,eV\,Å^{-1}$; $K_\varepsilon = 9.1$, $A_2 = 0.7\,eV\,Å^{-2}$, adopted from [9].

3. The Jahn–Teller effect in $Ti^{III}X_6{}^{3-}$ polyhedra

3.1. Introductory remarks

In a study on Mn^{III} in hexafluoro-coordination we have found, that DFT rather well reproduces available structural and energetic results, if the following restrictions are paid attention to [9]:

a. The calculations have to be performed in a *polarisable solvent continuum* for providing a charge compensation of the anionic complexes.
b. Only *energy differences*, such as the Franck–Condon transitions, *and the molecular structures at or very near to the extremum positions of the potential curves should be used*. Further away from such points, the DFT-calculated curves may deviate appreciably from those derived on the basis of the equations in Section 2. This is illustrated for MnF_6^{3-} polyhedra with an E_g ground state in Fig. 14, where the DFT curves distinctly deviate from the harmonic shape assumed here. We further mention, that the average metal–ligand bond length changes with the extent of the distortion (structural data from Cu^{2+} chemistry are in accord with such DFT results), obviously as the consequence of $E_g \otimes \alpha_{1g}$ coupling. There is no need to consider the latter effect, however, as long as we stay in the neighbourhood of extremum points.
c. The *energies* of *orbitally degenerate states* are not reliably reproduced by Kohn-Sham DFT in its present implementations because of errors due to the self-interaction of an electron [25a], when distributed over two or more orbital components ($e_g{}^1$ in $O_h \rightarrow (d_{z^2})^{0.5}(d_{x^2-y^2})^{0.5}$, for example). Such a distribution usually leads to a lower energy than that in the case of a one electron/one orbital-occupation. A smart escape from this difficulty is to choose a lower polyhedron symmetry, where the degeneracy is lifted, though the molecular structure is kept unaltered (see also Section 12.1) [25b,9].
d. Interelectronic repulsion is distinctly underestimated by DFT (see Section 12). Accordingly, in the case of d^n cations, the Racah parameters *B* and *C* should be taken from the d–d spectra.

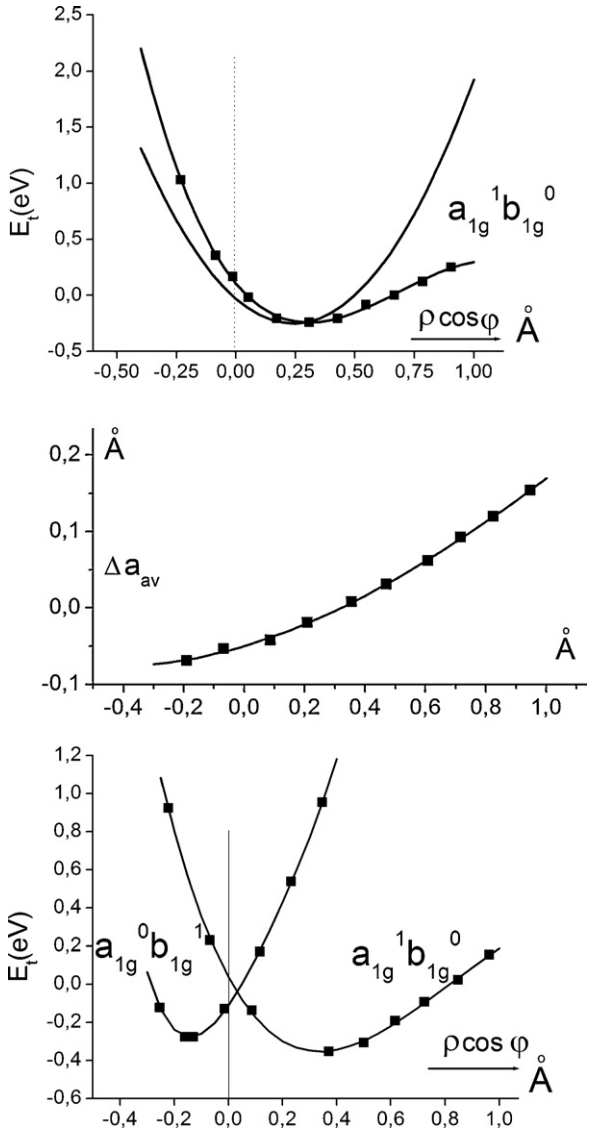

Fig. 14. Potential energy diagram for the MnF_6^{3-} polyhedron (E_g ground state in O_h–D_{4h} cross section at $\varphi = 0°$, 180°), obtained from point-by-point DFT calculations in a solvent continuum, and the alterations of the average bond length with respect to $a_{aver.} = 1.93$ Å at the minimum position for the $a_{1g}{}^1$ curve (bottom and amidst); the figure on top displays the a_{1g} potential energy branch in comparison to the harmonic curve, resulting from the here applied theory (adopted from [9]).

3.2. Energy and structural results, from DFT and experiment

Table 2 summarises the DFT results for TiX_6^{3-} polyhedra with respect to the T_{2g} ground state, and the derived parameters. We note here, that, besides eV, we use also cm^{-1} as the energy unit, because the latter is common, if optical transitions are considered; the conversion relationship is: $1\,eV \equiv 8065\,cm^{-1}$.

D_{4h}: The $T_{2g} \otimes \varepsilon_g$ parameters V_ε, K_ε and L_ε (vanishing) are calculated from the optimised radial distortion parameters ρ_ε^{cm} and ρ_ε^{em}, and by utilising the Franck–Condon transition at ρ_ε^{cm} (Eqs. (5c), (6) and (7)).

D_{3d}: Similarly, the $T_{2g} \otimes \tau_{2g}$ vibronic constants V_τ, K_τ, X_τ are obtained from the DFT values for ρ_τ^{cm}, ρ_τ^{em} and for E_{FC}^c at ρ_τ^{cm} (Eqs. (14)–(16)) – taking notice of Eqs. (9) and (10a) in addition.

$D_{2h}{}^*$: The D_{4h} coupling constants V_ε and K_ε are already known. V_τ and K_τ are not necessarily identical with the corresponding parameters in D_{3d}, because the distortion pathway in the latter point group implies three strongly correlated ligand displacements of the $D_{2h}{}^*$-type; accordingly they are treated as unknown parameters besides W and L_τ. The quantities in question are derived by a best fit to the DFT values for ρ_ε^{em}, ρ_τ^{*m} (Eq. (24)) and the two Franck–Condon transition energies between the split states of the octahedral T_{2g} parent ground state: $B_{3g} \rightarrow B_{2g}$, A_g (Eqs. (26) and (27); Fig. 4d).

Considering first the fluoride complex, the JT stabilisation energy is distinctly larger for the tetragonal ($275\,cm^{-1}$) than for the trigonal distortion ($160\,cm^{-1}$). This is in accord with d–d spectroscopy, where a splitting of the E_g excited state is observed [22,23], for which a $T_{2g} \otimes \tau_{2g}$ coupling of D_{3d} symmetry cannot be responsible (Fig. 11). In $D_{2h}{}^*$, the optimised radial distortion component ρ_ε^{em} for the $T_{2g} \otimes (\varepsilon_g + \tau_{2g})$ coupling is, within the margin of error, identical with the respective $D_{4h}{}^e$ value (Eqs. (7) and (24)), *indicating a vanishing second-order ε_g–τ_{2g} coupling constant W*. The coupling constants V_τ and K_τ in $D_{2h}{}^*$ are enhanced by $\approx 0.15\,eV\,Å^{-1}$ and $0.6\,eV\,Å^{-2}$ with respect to those in D_{3d}. The derived ground state stabilisation E_{JT}^* ($180\,cm^{-1}$) is slightly larger than the one in D_{3d} – but considerably smaller than the $D_{4h}{}^c$ energy. Even when taking the small contribution from LS coupling (vide supra) into account, the *$D_{4h}{}^c$ extremal points remain the absolute minima in the $T_{2g} \otimes (\varepsilon_g + \tau_{2g})$ potential surface*. This conclusion is confirmed by results for the excited E_g state, which we consider below. The ratio between the linear vibronic constants for $T_{2g} \otimes \varepsilon_g$ and $T_{2g} \otimes \tau_{2g}$ coupling is about $1.6_5(2_5)$, the one between the totals of the higher-order coupling and force constants in the expressions for ρ (Eqs. (7) and (14)), in $D_{4h}{}^c$ and $D_{3d}{}^c$ respectively, is: $(K_\varepsilon + L_\varepsilon)/(3K_\tau - 2X_\tau) \approx 1.9(3)$; accordingly, in spite of V_ε being larger than V_τ, even more pronounced angular distortions ρ_τ result in comparison to those (ρ_ε) induced by stretching vibrations (Table 2). The energy effect is smaller in the $T_{2g} \otimes \tau_{2g}$ case, however – τ_{2g} is a softer mode than ε_g. After all, *DFT says, that the ground state splitting and the polyhedron distortion is exclusively caused by $T_g \otimes \varepsilon_g$ coupling*. For the derivation of A_1, A_2 and K'_ε (the dashed restoring force constant refers to an excited state and is expected to be smaller than the one in Table 2 in D_{4h}) we use DFT optimised excited state value for ρ'^{cm}_ε and ρ'^{em}_ε (see Eq. (30a)) as well as the *experimental* excited state splitting in the spectra of A'_2ATiF_6 elpasolites ($2900 \pm 200\,cm^{-1}$) [22,23] – here applying Eq. (31b), but of course with the ground state distortion ρ_ε^{cm} (Table 3). Though the calculated electronic Franck–Condon transition from $^2B_{2g}$ to $^2B_{1g}$ at ρ_ε^{cm} reproduces the experimental energy within $200\,cm^{-1}$ (Fig. 11), the position of the $^2A_{1g}$ state is not properly mirrored – DFT exaggerates the energetic effect of the $a_{1g}(nd)$–$a_{1g}((n+1)s)$ interaction (see the discussion in Section 7.1). In $D_{2h}{}^*$, the $^2B_{3g} \rightarrow {}^2B_{1g}$ transition (see Fig. 4d) is calculated to appear at $18.0 \times 10^3\,cm^{-1}$, significantly lower than the experimental energy (Table 3). This observation confirms, that *a pure $T_{2g} \otimes \varepsilon_g$ coupling governs the energies and the molecular structure of the TiF_6^{3-} polyhedron*. The resulting A_1 coupling constant is considerably larger than V_ε – the latter imaging a π- and the former a σ-antibonding effect ($V_\varepsilon/A_1 \cong 0.36$). The magnitude of A_1 – and of A_2 as well – is consistent with that for Mn^{III} in the same type of solids, but with an E_g ground state (see Table 13) [9].

The DFT-calculated vibrational energy for the JT active ε_g mode is $380\,cm^{-1}$, in the range of reported experimental values for other $M^{III}F_6^{3-}$ complexes with M^{III} centres from the 3d series: Fe^{III} ($374\,cm^{-1}$) and Ga^{III} ($398\,cm^{-1}$) [26], and close to the DFT energy for CrF_6^{3-} ($417\,cm^{-1}$). The ratio λ_ε between the ($T_{2g} \otimes \varepsilon_g$)–JT energy and the zero-point energy $\hbar\omega_\varepsilon$ is near to 1 (0.73; Table 2), indicating an intermediate-type vibronic coupling effect. Apparently, the lowest vibronic level is reasonably well localised in either one of the three wells in the ground state potential surface (Figs. 6 and 7), justifying at least approximately the procedure applied for the derivation of the A_1, A_2 parameters from the apparent excited state splitting. LS coupling leaves the energy landscape nearly unchanged

Table 3
Excited state properties (estimated values in brackets) for polyhedra TiX_6 in elpasolites (X = F_t, Cl_t) and TiF_3 (X = F_b); besides the derived vibronic parameters the ligand field strength Δ is listed.

	E ($B_{2g} \rightarrow B_{1g}$[a] or $B_{3g} \rightarrow A_g$[a])	E ($B_{2g} \rightarrow A_{1g}$[a] or $B_{3g} \rightarrow B_{1g}$[a])	Δ[b]	A_1 (eV Å^{-1})	K_ε, A_2 (eV Å^{-2})	ρ'^{cm}_ε, ρ'^{em}_ε (Å)
F_t, exp.	15.9	18.8(3)[c]	16.8	–	–	–
Calc. (D_{4h}[c])	16.1[a]	–[d]	–	2.25	7.8[e] 1.1	0.222[e,f] 0.400[e,f]
Calc. (D_{2h}*)	–[d]	18.0[a]	–	–	–	–
F_b, exp.[g]	14.1	17.7(2)[c]	≅15.3	[≅2.9]	[≅12] [≅1.3]	–
Cl_t, exp.	11.4(1)[c]	12.8(2)[c]	12.0	–	–	–
Calc. (D_{4h}[c])	12.0[a]	–	–	1.80	5.0[e] 1.2	0.241[e,h] 0.685[e,h]

[a] If the (correct) assignment according to D_{4h}[c] compression, or the one in D_{2h}* (in the fluoride case) is chosen, respectively; energies in 10^3 cm^{-1}.
[b] Taking the calculated electronic ground state stabilisation energy due to the vibronic $T_{2g} \otimes \varepsilon_g$ coupling into account (see Fig. 4b); energies in 10^3 cm^{-1}.
[c] In parentheses: (±) variation width.
[d] Not correctly accessible to DFT (see text).
[e] Excited states' values (=$K_{\varepsilon'}$).
[f] 2.092 (4×), 1.900 (2×) Å (a_{av} = 2.028 Å) and 1.913 (4×), 2.259 (2×) (a_{av} = 2.028 Å), respectively.
[g] Estimated magnitudes for the $^2T_{2g}$ ground state parameters are: $V_\varepsilon \approx 1.0_0$ eV Å^{-1}; $\rho^{cm}_\varepsilon \approx 0.08_3$ Å , $E_{JT}{}^c \approx 0.04_1$ eV.
[h] 2.567 (4×), 2.358 (2×) [a_{av} = 2.497 Å] and 2.381 (4×), 2.788 (2×) [a_{av} = 2.517 Å], respectively.

due to the large $V_\varepsilon \rho_\varepsilon / \zeta$ ratio of 4.4 ($\zeta/\zeta_0 \cong 0.8$, $\zeta_0 = 155$ cm^{-1} [27]; Fig. 8, Eq. (8b)). The τ_{2g} vibrational energy is estimated by DFT to be of the magnitude 200 cm^{-1}, lower than the one reported for $GaF_6{}^{3-}$ (281 cm^{-1}) [26], but very near to the DFT value for $CrF_6{}^{3-}$ (195 cm^{-1}). The ratio λ_τ between E_{JT} and the zero-point energy is similar to λ_ε (0.80) – but bears no relevance, because the Jahn–Teller coupling via the τ_{2g} mode does not refer to absolute minima in the D_{3d} and D_{2h}* point groups. We think, that the JT interaction within the $TiF_6{}^{3-}$ polyhedron (and in D_{4h}[c]) is large enough to justify a treatment without explicitly accounting for the vibrational structure, at least in satisfactory approximation.

The elpasolite solids, whose d–d spectra are shown in Fig. 11, are cubic at 298 K, and for $Cs(Rb)_2KTiF_6$ Ti–F bond lengths of 1.962(8) Å are reported [28], in perfect agreement with the averaged distance from DFT (Table 2). Because the spectra definitely demand a distorted octahedron, the Jahn–Teller coupling is obviously dynamic at 298 K, freezing into a static distortion only at lower temperatures. The estimated ground state splitting, deduced from magnetic measurements [22] is smaller (≅400(40) cm^{-1}) than the DFT value (830 cm^{-1}; Table 2) – not unexpected in regard of the involved dynamic/static implications.

The ground state Jahn–Teller coupling in $TiCl_6{}^{3-}$ (D_{4h}[c]) is comparably much weaker. The linear coupling constant and the radial distortion parameter are smaller by a factor of 0.33 and 0.60, respectively, than in the fluoride case (Table 2), yielding a ratio of only 0.19 between the respective JT stabilization energies. The latter number reflects the considerably less pronounced energetic π-sensitivity of the larger and softer chloride ligand with respect to changes of the bond length. The D_{4h}[c] extremum points are again absolute minima in the $T_{2g} \otimes (\varepsilon_g + \tau_{2g})$ potential surface; the JT interaction in D_{3d} and also in D_{2h}* is nearly vanishing. The vibrational ε_g energy is calculated to be of the magnitude 206 cm^{-1}. It cannot be seen in the Raman spectrum, but is usually located between α_{1g} and τ_{2g}, which are observed at 310 and 133(8) cm^{-1}, respectively [24]. Unfortunately, the force constant K_τ cannot be derived from DFT with sufficiently high precision, in order to see whether the calculated τ_{2g} vibrational energy matches with the experimental value. There are only few experimental studies on the ground state properties of octahedral Ti^{III}, and only one with halide ligands [24]. From EPR and magnetic data of the elpasolites Cs_2KTiCl_6 and $Rb_2NaTiCl_6$ a ground state stabilisation by the Jahn–Teller effect between 25 cm^{-1} (static approach) and 110 cm^{-1} (dynamic treatment) is estimated. The DFT energy ($E^c_{JT} \cong 50$ cm^{-1}, Table 2) is within this range. The ratio between E^c_{JT} and $\hbar\omega_\varepsilon$ is 0.26, which is rather low and suggests a partial quenching of the JT coupling. Magnetic and EPR data [24] are in support of such a suppression, having the comparatively long time frame of these methods in mind. The scarce structural data indicate cubic lattices for the two above mentioned elpasolites at 298 K, but small distortions at lower temperatures, which are induced by strains due to structural packing effects. In view of these results it is striking in the first instance, that the optical transitions in the d–d spectra still reflect a ground state splitting of the JT type. Obviously the optical excitation is still fast enough to avoid time averaging as in the three other mentioned physical methods. Thus, at least the lowest vibronic level seems to be localised in either one of the three D_{4h}[c] wells of the ground state adiabatic potential surface. For the calculation of A_1 and A_2 we adopt, as in the fluoride case, besides the radial distortions in the $^2B_{1g}$, $^2A_{1g}$ (^2E_g) states from DFT, the observed excited state splitting in the d–d spectra (Fig. 11c) – supposing, that vibrational effects will not too significantly obscure the band shape. The splitting is 1400(200) cm^{-1} and remains unchanged, when diluting Ti^{III} on the octahedral lattice position by In^{III}; it is still recognisable in the low-temperature spectrum, where the intensity drops to nearly zero due to the centrosymmetric colour centre (Fig. 11d). When applying the same procedure for the calculation of the vibronic parameters in the σ-antibonding excited E_g state as for $TiF_6{}^{3-}$, one obtains the numerical values collected in Table 3. Very interesting is the observation, that the A_1 coupling constants do not differ too much for fluoride and chlorides as the ligand, while V_ε is only 1/3 of the fluoride value in the chloride case. Apparently, the π-covalence in transition metal–halide $M^{III(II)}$–X bonds is more distinctly enhanced, when substituting F^- by Cl^- as the ligands, than the σ-overlap; this phenomenon is well-known to experimental chemists.

A preliminary conclusion might be that the Jahn–Teller coupling in $TiX_6{}^{3-}$ (X = Cl^-, F^-) complexes is weak, and particularly in the Cl^- case not far from the limit of suppression by vibrational mechanisms. However, at least for the fluoride ligand, one can expect that *the linear coupling is large enough to cause a significant enhancement of polyhedron distortions and energy effects by vibronic interaction, if lower-symmetry elastic and binding strains in the chosen host structures are present.* We will study such phenomena in Section 4.

3.3. The presence of bridging ligands

Structural data [28] and d–d spectra [22,23] are reported for TiF_3, which crystallizes in a distorted ReO_3 lattice variant with regular $Ti(F_b)_6$ octahedra and fluoride ligands, which are bridging between two Ti^{III}-centres in the VF_3-type lattice (Fig. 2c); the bridging angle is 150° and the Ti–F_b bond length is 1.964 Å [28] – practically identical with the ones (see above) in the elpasolites (lower indices b and t: bridging and terminal, respectively). In order to obtain approximate vibronic coupling data for the $Ti(F_b)_6$ polyhedron, we consult results for the corresponding Mn^{III} complex, as it exists in MnF_3 – with an ^5E_g ground state in O_h. Here the linear coupling constant A_1 was 30% and the second-order coupling parameter A_2

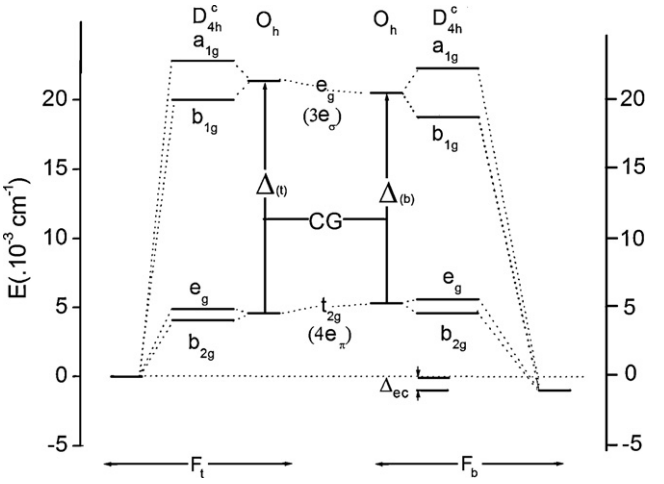

Fig. 15. Semiquantitative MO diagrams for the $Ti(F_i)_6$ polyhedra in elpasolites (i = t; left) and in TiF_3 (i = b; right). The two schemes are related to each other via the supposition that the centre of gravity of the antibonding energies (CG) is identical for F_b and F_t, (see text). The resulting Δ_{ec} energy (≅0.12 eV) originates from the different effective charge (ec) on the metal atom due to a central field covalency contribution, which is larger for the Ti–F_t than for the Ti–F_b bond [9]. The used AOM parameters are (in 10^3 cm^{-1}): $e_\pi^\perp = 1.03$, $e_\sigma^\perp = 6.67$, $e_\sigma^\parallel(\text{eff}) = 8.12$ (t), and $e_\pi^\perp \cong 1.4$, $e_\sigma^\perp \cong 6.6$, $e_\sigma^\parallel(\text{eff}) \cong 8.4$ (b); they refer to the axial (||) and equatorial (⊥) bond lengths in the D_{4h}, compressed, octahedra. The antibonding energies are estimated with the reasonable assumption: $e_\pi^\parallel/e_\pi^\perp = 1.4$; otherwise the energies in Tables 2 and 3 are used.

as well as the force constant were 20(5)% larger than in the elpasolite case. We refer to Section 7 and Table 13 for the respective reasoning and the basic experimental data. Utilising these information and the splitting energy of the excited ^2E_g state in the d-d spectrum of TiF_3 (0.45 eV [22,23] – Fig. 11b), the data in Table 3 result. From these one obtains via Eq. (31) a polyhedron distortion of $\rho_\varepsilon^{cm} \approx 0.08$ Å and via Eq. (6) a linear coupling constant of $V_\varepsilon \approx 1.0$ eV Å^{-1}, by ≈20% larger than for the complex with terminal ligands. A comparison with V_ε for the $Mn(F_b)_6$ complex and hence an analysis of the π-antibonding splitting of the excited $^5T_{2g}$ state is not possible, because the respective absorptions are obscured by quintet–triplet transitions (Fig. 29) [29]. After all, the polyhedron distortion is about equal to that in the elpasolites, while E_{JT}^c is 20% larger, in essential agreement with available magnetic data [22]. Apparently, the Jahn–Teller distortion is here also dynamic at 298 K, becoming static only at lower temperatures. The semiquantitative MO schemes in Fig. 15 model the binding properties within the hexafluoro-complexes of Ti^{III} in elpasolites and in TiF_3, as will be discussed below.

For a closer analysis of the binding properties of the fluoride ligands toward an $M^{III}(3d)$ cation the angular overlap model (AOM) [30] is the method of choice. The linear and higher-order vibronic coupling constants for ε_g-type ligand displacements can be readily expressed in terms of AOM energy parameters e_i (a: metal–ligand distance) [6]:

$$V_\varepsilon = \frac{2}{\sqrt{3}}\left(\frac{de_\pi}{da}\right) \tag{32}$$

$$A_1 = \frac{\sqrt{3}}{2}\left(\frac{de_\sigma}{da}\right); \quad A_2 \cong \frac{3}{4e_{ds}}\left(\frac{de_{sd}}{da}\right)^2$$

The latter are defined as accounting for the antibonding effect with respect to the free 3d cation:

$$e_i = k_i S_i^2 \quad (i = \sigma, \pi;\ \text{sd}) \tag{33}$$

but with an effective charge (ec) as in the complex. The charge reduction with respect to the formal oxidation state due to the electron flow from the ligand to the central cation defines a binding phenomenon, which *C.K. Jórgensen* called *central field covalency* [10]. In Eq. (33), the S_i are standard overlap integrals of the metal-3d with the s- and p-ligand orbitals, and the k_i measure, how effective this orbital overlap is energetically. The e_i energy effects originate from weak covalent bonding, and comprise metal 3d-to-ligand antibonding interactions (here specifically within the antibonding e_g^* and t_{2g}^* MO manifold), which are caused by orbital overlap effects between cation and ligands at the respective effective charges. We may conceptually relate the latter covalent bond energy increments to what *C.K. Jórgensen* defined as *symmetry-restricted* covalency [10]. In Eq. (32) it is assumed, that the higher-order coupling via A_2 is solely determined by the $nd_{z^2} - (n+1)s$ interaction; the respective AOM parameter is e_{sd} [30], which plays a dominant role in the interplay between the elongated and compressed conformations of a Jahn–Teller distorted octahedron. Considering explicitly the D_{4h} distortion of an octahedral complex, switching from the general definitions to the AOM energy parameters connected with the e_g and t_{2g} molecular orbitals and from a to the radial distortion parameter ρ, one obtains:

$$E_\sigma(b_{1g}^*) = 3e_\sigma^\perp, \qquad E_\sigma(a_{1g}^*) = 2\,e_\sigma^\parallel(\text{eff}) + e_\sigma^\perp; \quad e_\sigma^\parallel(\text{eff}) \equiv e_\sigma^\parallel - E_{ds} \tag{34}$$

$$E_\pi(b_{2g}^*) = 4e_\pi^\perp \quad \text{and} \quad E_\pi(e_g^*) = 2(e_\pi^\perp + e_\pi^\parallel) \tag{35}$$

The notations || and ⊥ refer to the z-axis and the xy-plane, respectively.

In Fig. 15 the MO diagrams of an $M^{III}(F_t)_6$ and an $M^{III}(F_b)_6$ complex are displayed side by side. The used energies are from DFT and optical spectroscopy for M^{III} = Ti (ground state splitting and optical transitions to a_{1g}^* and b_{1g}^* – see Figs. 7 and 11), which – with the arbitrary, but reasonable choice $e_\pi^\parallel/e_\pi^\perp \cong 1.4$ for the tetragonally compressed complexes – allows one to calculate the AO parameters e_i^j (j = ||, ⊥; i = σ, π). The two diagrams are related to each other via the assumption that the centres of gravity (CG) for the five MOs are identical in energy in the two cases; we base this supposition on the observation that the magnitudes of the Racah parameters of interelectronic repulsion B, C – which are probes of the total d-bond covalency (nephelauxetic effect [10]), and which can be deduced from the d–d spectra in the case of $3d^n$–M^{III} cations with $1 < n < 9$ – do not depend on whether the fluoride ligands in $M^{III}F_6$ complexes (M^{III}: V to Co) are terminal or bridging (vide infra). The derived AO parameters are listed in the caption of Fig. 15; in particular, $e_\pi^\perp$ and $e_\pi^\parallel$ are larger in the case of the $Ti(F_b)_6$ polyhedron. Accordingly, the ligand field strength is smaller (Fig. 15), when recalling that $\Delta = 3e_\sigma - 4e_\pi$. A further significant result is, that the zero-points on the energy scale are different in the two cases. The central field covalency is larger for F_t, due to a more pronounced charge flow toward the metal caused by the higher negative formal charge (−1). In the case of F_b the formal charge is less negative (−0.5), leading to an effective charge on the metal, which is less reduced in respect to (+3) than in the $M(F_t)_6$ polyhedron. The energy difference Δ_{ec} reflects this (ec: effective charge) and will be a significant quantity when treating complexes, in which F_t and F_b ligands are simultaneously present. We summarize [9]: *The total bond covalency is similar for the two kinds of ligand, while the total bond strength – and hence (mostly due to the smaller negative charge on the F_b-ligand) the ionic bond increment – is larger for the terminal ligand.* Partitioning the bond covalency into a part, which measures the *ligand-to-metal charge flow* (central field covalency [10]), and an increment stemming from *orbital overlap* (symmetry-restricted covalency [10]), *one obtains $F_t > F_b$ for the former and the reverse sequence for the latter contribution.*

We are now ready to discuss structural and spectroscopic [31,32] results for solids A^ITiF_4 (A^I: Na [33], K [34], Rb, Cs [35]) which crystallise in the $TlAlF_4$ structure (Fig. 16 top) or in lower-

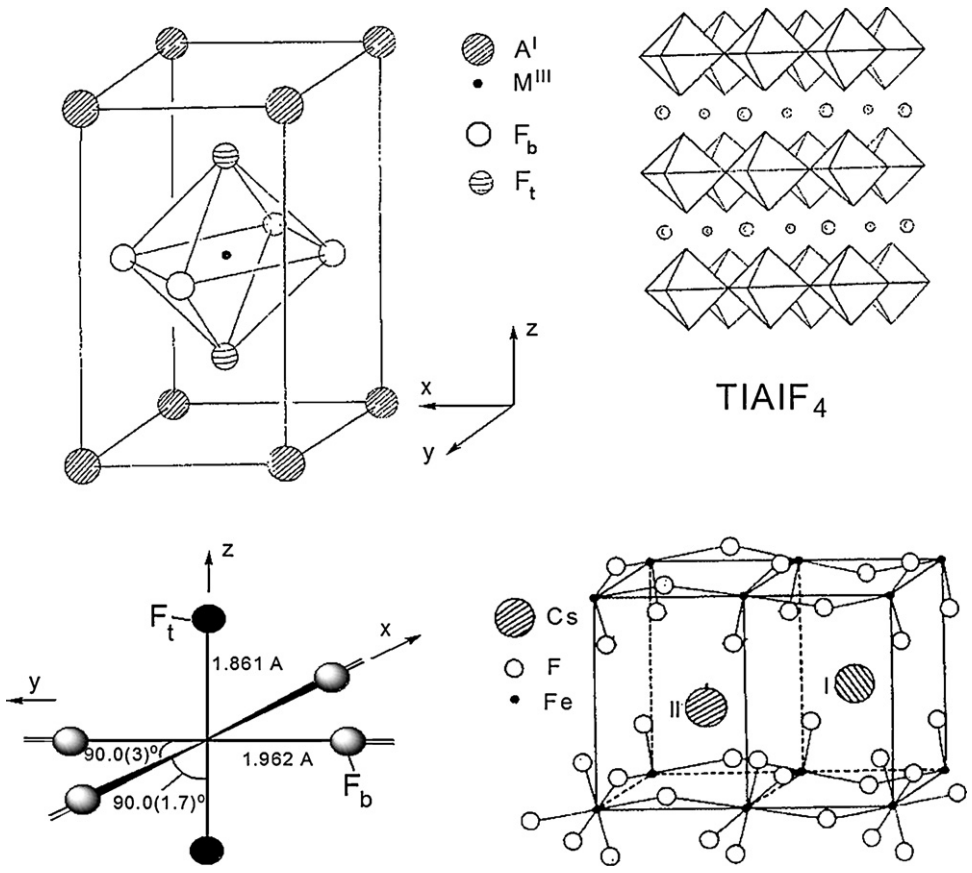

Fig. 16. The tetragonal unit cell of $TlAlF_4$ (above) and the also tetragonal $TlAlF_4$-type structure of $CsFeF_4$ [40] with puckered layers (bottom, right); bond lengths and bond angles in the trans-$Fe(F_t)_2(F_b)_4$ polyhedra (bridging angle F_b–Fe–F_b: 166.4°) are shown on the left – partly adopted from [40].

symmetry variants of this type. In the single trans-$M^{III}(F_b)_4(F_t)_2^-$ complexes, constituting the lattice, terminal and bridging ligands (perpendicular to and in the planes, respectively) are simultaneously present. The polyhedra are tetragonally compressed (Table 4), even if the ground state is vibronically stable, as in the compounds with Fe^{III} ($^6A_{1g}(d^5)$ ground state in O_h). The corresponding strain-induced bond length anisotropy – measured by $\rho_s \cong 0.10_5(1)$ Å (Eq. (4b); Table 4) – occurs, though the bond distances in the $Fe^{III}(F_t)_6^{3-}$ complexes of the elpasolite $RbNaFeF_6$ – 1.933 Å [36] – and in the $Fe^{III}(F_b)_6$ polyhedra of FeF_3 – 1.923 Å [37] – are nearly equal, and also of the same magnitude as the averaged bond length in the $TlAlF_4$-type solids $A^IFe^{III}F_4$ (A^I = K [38], Rb[39], Cs [40]; Table 4). Apparently, *different binding properties are not necessarily reflected by different bond lengths*; a pronounced distance effect occurs, however, in cases as here ($Fe(F_t)_2(F_b)_4^-$ octahedra), where the same ligand occurs partly in terminal and partly in bridging function.

Table 4
Structural data – references, see text – for the trans-$M^{III}(F_t)_2(F_b)_4^-$ octahedra (M^{III}-$F_b \equiv a_\perp$; M^{III}-$F_t \equiv a_{||}$; aver. bond length a_{av} – in Å) in $TlAlF_4$-type lattices (Fig. 16). Data, estimated from spectroscopic results, are set in brackets.

M^{III}	A^I	$a_\perp$ (4×)	$a_{||}$ (2×)	a_{av}	ρ_ε^c [a]
Fe	K[b], Rb[c,d], Cs[c]	1.963(5)	1.871(9)	1.932(4)	0.105(12)
Ti	Na[b]	2.022	1.877	1.973	0.168
	K[b]	2.009	1.887	1.968	0.141
	Cs[b]	1.998	1.877	1.958	0.140
V	K[b], Rb[c], Cs[c]	[1.97 ± 0.04][e]	[1.88]	1.94	[≅0.12_5][e]
Cr	α-Rb[d],Tl[c]	≅1.93_5	≅1.84_5[f]	1.90_5[f]	≈0.10_5[f]
Co	Cs[c]	1.969	1.812	1.917	0.181
	Li[d,g]	1.964 ± 0.034	1.827	1.919	0.173

[a] Observed distortions; induced by the structural strain solely in the case of: Fe^{III}, Cr^{III}.
[b] Orthorhombic structures, with mutual layer displacements.
[c] Tetragonal or pseudo-tetragonal structures.
[d] The β-modification of $RbCrF_4$ is reported to crystallize similar to Cs(K)CrF_4 (Table 12).
[e] The V–F_b bond lengths in the *x*–*y*-plane (Fig. 30) – 1.93 and 2.01 Å ($\varphi_m \cong 137°$ (223°)) – presumably equilibrate, either dynamically or even due to vibronic quenching, with ρ decreasing to an apparent value of ≈0.10_5 Å (see text).
[f] Adopted in comparison to Fe^{III} with an equally non-degenerate ground state.
[g] Structure description according to the topology of a dirutile-type lattice [92]; with a distinct orthorhombic component of the polyhedron distortion in the Co($F_{b(4)}$) plane.

In order to learn about the structural and electronic properties of a Jahn–Teller complex, in which part of the ligands is substituted by ligator atoms with (slightly) differing binding and elastic characteristics, a novel strain model is proposed by one of us (D.R.), which is introduced in the following section.

4. The strain model

4.1. The elastic and the binding strain

We look upon the $Ti(F_t)_6^{3-}$ octahedron, as it occurs in elpasolites, as the parent complex; the partial substitution of terminal (F_t) by bridging (F_b) ligands is considered as a non-random strain, imposed on the system. One component of this strain is surely of elastic origin, because F_b is tied up in the bulk of cooperative lattice vibrations to a much larger extent than the (approximately) terminal ligands. In the frame of our treatment we take account of this strain increment by introducing an addition: $K_s(\varphi_s)$ to the force constant, which depends on the deviation (φ–φ_s) of the angular parameter from that structural conformation, which is favoured by the elastic properties of the Ti^{III} octahedron (lower index s denotes strain). In the specific case of replacing four F_t- by F_b-ligands in one

octahedral plane, studied here, φ_s is chosen in such a way, that it eases a polyhedron distortion along the α_{1g} (ε_g) pathway toward a tetragonal compression – following the structural observation in the $Fe^{III}(F_t)_2(F_b)_4$ polyhedron:

$$\Delta E^{st} = -K_s\rho_\varepsilon^2\cos(\varphi-\varphi_s) \Rightarrow: \quad = K_s\rho_\varepsilon^2\cos\varphi, \quad \text{for } \varphi_s = 180^\circ \tag{36a}$$

The proposed expression is symmetry-related to the angular dependence of the cubic third-order diagonal term occuring in the coupling to the ε_g mode [6]:

$$A_3Q_\theta(Q_\theta^2 - 3Q_\varepsilon^2) = A_3\rho_\varepsilon^3\cos\varphi(1-4\sin^2\varphi) \tag{36b}$$

Depending on the sign of A_3, it favours or destabilises a tetragonal distortion in anyone of the three potential wells of the adiabatic potential surface (Fig. 6). If one wants to stabilise a D_{4h} distortion only in one potential well, the factor in parenthesis – which makes the three wells energy-equivalent – is omitted, leaving a linear cos-dependence as chosen in Eq. (36a). The K_s-term breaks the symmetry by the introduction of an angular term, which favours the minimum at $\varphi_s = 180^\circ$ in the present case and, in particular, destabilises an elongation along the F_t–Fe–F_t-molecular direction ($\varphi = 0$). The origin of the soft mode behaviour along the α_{1g} ($D_{4h}{}^c$)-distortion path is the larger total bond strength between Fe^{III} and $F_t{}^-$ as compared to Fe^{III}–$F_b{}^{-0.5}$, with a shorter spacing in the former case. These properties modify, in the here used model, as an *elastic strain the force constant, even if vibronic coupling increments are not present*. The tetragonally compressed $Fe^{III}[Cr^{III}](F_t)_2(Fb)_4{}^-$ octahedra in solids AFe[Cr]F_4 ($\rho_s \cong 0.105$ Å; Table 4) with orbitally non-degenerate ground states thus substantiate the necessity to account for an *elastic strain term.* However, as shown below, a second strain term is needed, if one wants to meet the requirements of available experimental (and calculated) data. The straightforward intuitive procedure is the adoption of *binding strain components* V_ε^s *and* A_1^s, *which possess the same symmetry as* V_ε *and* A_1 (see matrix (1) – the diagonal elements – and matrix (28), respectively) – the former mirroring the $T_{2g}\otimes\varepsilon_g$- and the latter the $E_g\otimes\varepsilon_g$-interaction. The angular coordinate is set constant, however, because the binding situation – created by the substitution of bridging ligands into the molecular equatorial plane – refers to d-MOs (here d_{xy}) with fixed orientations in space ($\varphi = \varphi_s'$). φ_s' is not necessarily identical with φ_s (Eq. (36a)), but in the present case, where both strain effects are (at least predominantly) caused by the F_t-by-F_b-replacements, $\varphi_s = \varphi_s' = 180^\circ$ is valid, because the tetragonally compressed octahedra in $A^IFe^{III}[Cr^{III}]F_4$ also demand this distortion angle:

$$\begin{aligned} Q_\theta^s &= \rho_\varepsilon\cos\varphi_s \Rightarrow -\rho_\varepsilon \\ Q_\varepsilon^s &= \rho_\varepsilon\sin\varphi_s \Rightarrow 0 \end{aligned} \tag{37}$$

Accounting for the elastic strain contribution via K_s and for the binding strain component via V_ε^s, one obtains the following adiabatic energies for the split states of $^2T_{2g}$, when restricting to $\varphi = 0^\circ$ and $\varphi = 180^\circ$:

$$E_1(b_{2g}) = \tfrac{1}{2}(K_\varepsilon + K_s\cos\varphi)\rho_\varepsilon^2 + (V_\varepsilon\cos\varphi - V_\varepsilon^s)\rho_\varepsilon + \tfrac{1}{2}L_\varepsilon\rho_\varepsilon^2 \tag{38a}$$

$$E_{2,3}(e_g) = \tfrac{1}{2}(K_\varepsilon + K_s\cos\varphi)\rho_\varepsilon^2 - \tfrac{1}{2}(V_\varepsilon\cos\varphi - V_\varepsilon^s)\rho_\varepsilon - \tfrac{1}{4}L_\varepsilon\rho_\varepsilon^2 \tag{38b}$$

With $\varphi_m = 180^\circ$ from experiment (and $L_\varepsilon \cong 0$) one obtains for the $^2B_{2g}$ ground state after minimisation in respect to ρ_ε:

$$\rho_\varepsilon^{sm} = \frac{V_\varepsilon + V_\varepsilon{}^s}{K_\varepsilon - K_s}; \quad E_1 = -E_{JT}^s = -\frac{1}{2}(V_\varepsilon + V_\varepsilon^s)\rho_\varepsilon^{sm} \tag{39a}$$

The index s is meant to denote, that strain effects participate; ρ_ε^{sm} is the experimentally observed distortion parameter for solids $ATiF_4$ ($0.15_5(1_5)$ Å; Table 4). The Franck–Condon transition energy within the octahedral $^2T_{2g}$ ground state at this distortion is:

$$E_{FC}^s = \tfrac{3}{2}(V_\varepsilon + V_\varepsilon^s)\rho_\varepsilon^{sm} \equiv 3E_{JT}^s \tag{39b}$$

The vibronic $T_{2g}\otimes\varepsilon_g$ coupling and both strain components favour the elongation of the (equatorial) Ti–F_b bonds, whereby the π-antibonding energy of the singly occupied d_{xy} MO is lowered in respect to the octahedral t_{2g}-parent MOs (Eqs. (38a) and (38b)), due to the action of a by V_ε^s enhanced coupling parameter and a by K_s reduced force constant. While the preference of an elongated to a compressed D_{4h} distortion – or vice versa – is a first-order effect in $T_g\otimes\varepsilon_g$ vibronic coupling, it is of only second-order in the $E_g\otimes\varepsilon_g$ case. The master equation for the excited state splitting of the compressed Ti^{III} polyhedra in solids $ATiF_4$ at the ground state distortion ρ_ε^{sm} is:

$$E'^s_{FC} = 2(A_1 - A_1^s\cos\varphi_m + A_2\rho_\varepsilon^{sm}\cos 3\varphi_m)\rho_\varepsilon^{sm} \quad (\varphi_m = 180^\circ) \tag{40}$$

Here, we have supplemented A_1 by the A_1^s contribution according to the modified binding situation with respect to the $Ti(F_t)_6{}^{3-}$ polyhedron; the second-order constant A_2 is assumed to stay approximately unchanged (Table 3). We refer to Section 7, where we explicitly consider the strain influence in the case of an E_g ground state (see Eq. (60)).

Usually, a strain model introduced by Ham [41] is applied in a case as that considered here. It is formally related to what we call a binding strain, but does not contain ρ_ε as a variable:

$$Q_\theta^s = S\cos\varphi_s; \qquad Q_\varepsilon^s = S\sin\varphi_s \tag{37a}$$

The demand for a binding strain component becomes immediately apparent, when inspecting the observed and calculated Franck–Condon energies and distortion parameters for $ATiF_4$ and the elpasolites in comparison (E'^s_{FC} at ρ_ε^{sm}, Eq. (40), as well as E'^c_{FC} at ρ_ε^{cm}, Eq. (31); numerical values in Tables 2 and 3). Already in a coarse consideration, with $A_2 \approx 0$, an increase of A_1 of about 1/3 ($A_1^s \approx (1/3)A_1$) is afforded.

We note, that the introduced semiempirical strain concept originates from the careful analysis of the structural and spectroscopic properties of the investigated model-solids and of the data base, provided by DFT. It provides to solid-state-chemists insight into the interplay between the Jahn–Teller coupling – which is defined in reference to a high-symmetry parent structure and rarely met in the chemical reality – and the structural and binding qualities of the host compound and its host sites; the latter may modify the energetic and geometric landscape essentially. The, in the first instance, merely intuitive distinction between *elastic* and *binding strain* perfectly matches with reality. As an impressive example we quote the extended range of angular distortions, between pseudo-tetrahedral and square planar, of $CuCl_4{}^{2-}$ anions (charge-compensated by large counter cations), which is caused by a variation of the force constant exclusively; here, obviously, the vibronic coupling constants remain unchanged in the vast series of compounds [44]. The analysis by the presented strain model is surely approximate in character, because we have still utilised the cubic Hamiltonian, in spite of the lower symmetry of the strain terms. Without doubt, however, the proposed discrimination between two types of strain provides more detailed experiment-related information than the exact, but rather simplistic Ham approach, which was nevertheless successfully applied to numerous solids in, particularly, Cu^{2+}-chemistry [42]. A disadvantage is, that a larger reservoir of experimental results and reliable data from calculations is needed – which is available in the case of Mn^{III}, for example (see Section 7.2).

Table 5
Vibronic coupling constants (V_ε, V_ε^s; A_1, $A_1{}^s$ in eV Å^{-1} and K_ε, K_s in eV Å^{-2})[a], Jahn–Teller energies (eV)[b] and tetragonal splitting parameters (in 10^3 cm^{-1}) [c] of the trans- and cis-configured $M(F_t)_2(F_b)_4$ polyhedra in compounds $AM^{III}F_4$ (Tables 4 and 11). The radial distortion parameters are also listed.

M^{III}	A	V_ε	V_ε^s	A_1	$A_1{}^s$	K_ε	K_s	E_{JT}	δ_2	δ_1'	ρ_ε^m
Ti	Cs, Rb	0.82	0.14	2.25	$\approx 0.5_5$	9.9	3.7	0.074	0.7_5	1.8	0.15_5
V	Cs, Rb, K	0.89	0.20	2.00	≈0.4	12.0	≈5.9	0.060[d]	0.6	1.1_5	0.12_5[d]
Cr	Rb, Tl	0.7	$\approx 0.4_5$	1.8	≈0.4	7.5	–	–	0.6_5	1.0_5	0.10_5[e]
Co	Cs	0.65	0.21	2.00	0.6_5	8.1	3.3	0.078	0.8	2.0_5	0.18_1
Cr	Cs	0.7	$\approx 0.2_5$[f]	1.8	$\approx 0.4_5$[f]	–	–	–	0.4	0.9[g]	0.09_7[e]

[a] V_ε, A_1 and K_ε, L_ε, A_2 are chosen as for the $M(F_t)_6{}^{3-}$ polyhedra in the elpasolites.
[b] For the compressed (Ti, Co) and D_{2h}-distorted (V; $\varphi_m^o = 137^\circ, 223^\circ$) polyhedra in the absolute minimum of the adiabatic ground state potential surface, respectively (Fig. 22).
[c] δ_2, $\delta_1'(\delta_1)$ are the splitting, expected or obtained from the experiment (see Fig. 4), and contain energy contributions from central field covalency, in distinction to E_{JT} (see Sections 6 and 3, for details).
[d] Data from Fig. 22; the assumption of a suppression of the possibly present orthorhombic symmetry component yields ≅0.10_5 Å (see Table 4).
[e] Strain-induced values.
[f] Calculated when using ρ_{sb} for the cis-$Cr(F_t)_2(F_b)_4$ polyhedron distortion (see text).
[g] Cis-elongated polyhedra: δ_1.

4.2. Solids $A^ITi^{III}F_4$

When analysing the structural and energetic ground state properties of the $Ti^{III}(F_b)_4(F_t)_2{}^-$-octahedra in solids $A^ITi^{III}F_4$, we meet the difficulty, that the available experimental and DFT data do not suffice to determine K_s and V_ε^s separately. One may evaluate K_s via the following approximate energy relation, however:

$$\frac{1}{2}(K_\varepsilon - K_s)\rho_s^2 - \frac{1}{2}K_\varepsilon\rho_\varepsilon^{cm2} \cong 0 \Rightarrow K_s \cong K_\varepsilon\left\{1 - \left(\frac{\rho_\varepsilon^{cm}}{\rho_s}\right)^2\right\} \qquad (41)$$

Eq. (41) reflects, that the enhancement of the local polyhedron distortion from ρ_ε^{cm} (Table 2) to ρ_s is supposed to be solely induced by the action of K_s – if only the elastic energy contributions are considered and vibronic coupling is left aside. It adopts the distortion of the $Ti(F_t)_6{}^{3-}$ polyhedron, accessible by DFT ($\rho_\varepsilon^{cm} = 0.083$ Å), and the resulting distortion, if four F_t are replaced by F_b ligands in the corresponding Fe^{III} or Cr^{III} complexes ($\rho_s = 0.10_5$ Å). V_ε^s is now also easily accessible, utilising Eq. (39a), with $\rho_\varepsilon^{sm} = 0.155$ Å . The magnitudes of K_s (derived via Eq. (41)), which mirrors the *structural-elastic strain*, and of V_ε^s, which comprises the *binding strain* induced by the larger vibronic coupling within the Ti–F_b as compared to the Ti–F_t bonds (from Eq. (39a)), are listed in Table 5. We learn, that the elastic strain enhances the radial distortion from 0.083 to 0.13 Å (Eq. (39a) with $V_\varepsilon^s = 0$), while the further increase by the binding strain amounts to 0.02_5 Å. If one factorises the increase of the JT stabilisation energy from 0.034 to 0.074 eV (Tables 2 and 5) it comes out, that the binding strain participates with a factor of $\{(V_\varepsilon + V_\varepsilon^s)/V_\varepsilon\}^2 \cong 1.4$ and the elastic force with a factor of $K_\varepsilon/(K_\varepsilon - K_s) \cong 1.6$. The distortion in compounds with non-degenerate ground states (Fe^{III} or Cr^{III}) is the result of the soft mode property of α_{1g} (ε_g) along the D_{4h} distortion path, which eases displacements toward a tetragonal compression and aggravates motions toward D_{4h}[e], for $M^{III}(F_b)_4(F_t)$ polyhedra.

When evaluating the ground state splitting in the case of $M^{III}(F_t)_2(F_b)_4$ polyhedra (Eq. (39b), one has to make allowance of an additional energy increment Δ_{ec} (≅0.12 eV) due to a different effective charge, depending on whether bridging or terminal ligands are involved. Thus, as Fig. 15 illustrates, the AOM parameters $e_i^{||}(t)$ and $e_i^{\perp}(b)$ ($i = \pi, \sigma$) refer to different reference points on the energy scale. Because, according to our vibronic model, we have chosen the parent $Ti(F_t)_6{}^{3-}$ octahedron as the zero-point of the energy scale, a correction has to be applied to the experimental splitting, in order to match with the AO and vibronic coupling energies. As we will outline in Section 6.3, the ground state splitting, as given by Eq. (39b) for the case of the $Ti^{III}(F_b)_4(F_t)_2{}^-$ octahedra, has to be enlarged by approximately 0.06 eV (see the considerations in connection with Eqs. (55a) and (55b)). Having this in mind, one obtains $3\delta_2 \cong 0.28$ eV for the expected experimental T_{2g} ground state splitting (Table 5). The potential energy diagram of Fig. 17 illustrates the strain influence. While the curves for ^2E_g ($^2T_{2g}$) do not differ too much with and without strain, this is different for the $^2B_{2g}$ ground state and a D_{4h}, compressed, structure. Here, one observes a considerable change in the shape – generating specifically a strongly flattened minimum; striking is the enhancement of the stabilisation energy and of the radial distortion parameter by the strain influence. The former does not contain the Δ_{ec} contribution, which would add an additional ≅0.02 eV to the stabilisation energy.

Fig. 18 depicts the d-d spectra of various solids $A^ITi^{III}F_4$ (A^I = Na, Rb, Cs). In particular, the excited $^2A_{1g}$ (^2E_g) split state at $\approx 20.5 \times 10^3$ cm^{-1} is very broad and intense and allows only a rough estimate of the splitting energy ($4\delta_1' \approx 7000$ cm^{-1} or 0.9 eV), which is by a factor of more than two larger than the one found in the elpasolite case (Fig. 11). Correcting the energy by $2/3\Delta_{ec} \cong 0.08$ eV (see Eqs. (55a) and (55b) and Fig. 15) and utilising $\rho_\varepsilon^{sm} = 0.155$ Å , an A_1^s parameter addition of 0.5_5 eV Å^{-1} is obtained. The enhancement of the linear vibronic coupling is about 25%, and hence smaller than the one for the full substitution of F_t by F_b ($A_2'ATi(F_t)_6 \rightarrow Ti(F_b)_3$), consistent with the underlying strain model. A short non-numerical outline of the above outlined strain model has been previously presented [7].

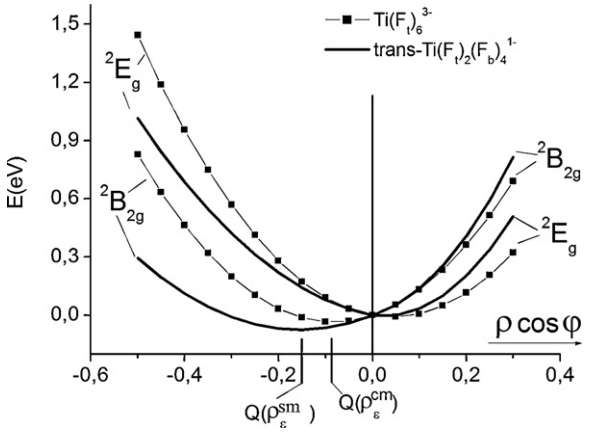

Fig. 17. Cross section of the adiabatic ground state potential surface along the energy axis at $\varphi = 180^\circ$, 0° for the $TiF_6{}^{3-}$ polyhedra in elpasolites (Eq. (5)), with the vibronic parameters from DFT in Table 2, and in solids $ATiF_4$ (Eq. (38)), using additionally the K_s and V_ε^s parameters in Table 5; the contribution from the Δ_{ec} increment is not included in the treatment. The minimum positions are indicated ($\rho_\varepsilon^{sm} = 0.15_5$ Å).

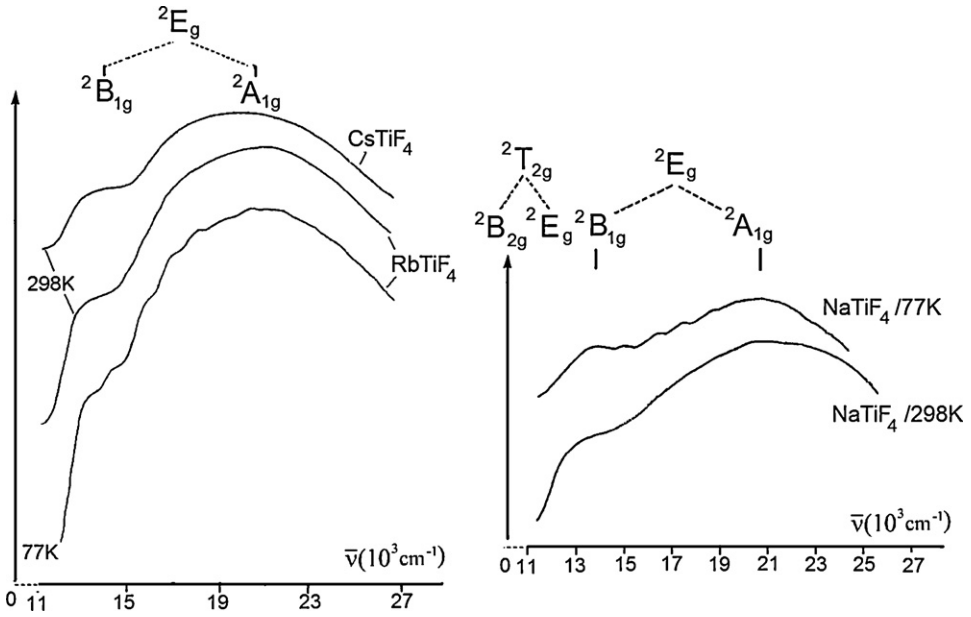

Fig. 18. d–d spectra [31,32] of solids $A^{I}Ti^{III}F_4$ crystallising in $TlAlF_4$-type lattices.

5. Vibronic coupling in $V^{III}X_6^{3-}$ polyhedra

5.1. Ground state analysis

We anticipate, that the trend for the extent of the stabilisation by vibronic coupling follows the sequence $D_{4h}{}^{c} > D_{3d}{}^{c} \approx D_{2h}{}^{*}$ not only in the case of TiX_6 octahedra, but also for VX_6 complexes, and will prove that in the end of this section. The ligand field matrices for a d^2 cation in octahedral coordination with a tetragonal distortion component (only spin-triplet states) are summarised in Eq. (42):

	$e_g^2(t_{2g}^2)$	$b_{2g}{}^1b_{1g}{}^1(t_{2g}{}^1e_g{}^1)$
$^3A_{2g}$	$-2\,\delta_2$	$-6B$
$(_{a,b}{}^3T_{1g})$	$-6B$	$\Delta + 2(\delta_1 + \delta_2) + 9B$

	$b_{2g}{}^1a_{1g}{}^1(t_{2g}{}^1e_g{}^1)$
$^3B_{2g}$ ($^3T_{2g}$)	$\Delta - 2(\delta_1 - \delta_2) - 3B$

	$e_g{}^1b_{2g}{}^1(t_{2g}{}^2))$	$e_g{}^1b_{1g}{}^1(t_{2g}{}^1e_g{}^1)$	$e_g{}^1a_{1g}{}^1(t_{2g}{}^1e_g{}^1)$
	δ_2	$3\,B$	$-3\sqrt{3}B$
^3E_g ($_a{}^3T_{1g}$,	$3\,B$	$\Delta + 2\delta_1 - \delta_2$	$-3\sqrt{3}B$
$^3T_{2g}$, $_b{}^3T_{1g}$)	$-3\sqrt{3}B$	$-3\sqrt{3}B$	$\Delta - 2\delta_1 - \delta_2 + 6B$

	$a_{1g}{}^1b_{1g}{}^1(e_g^2)$
$^3B_{1g}$ ($^3A_{2g}$)	$2\Delta - 3B$

(42)

They differ from those given by Perumareddi [45] by being fully diagonalised with respect to all ligand field parameters and by differently defined tetragonal field splitting parameters. The quantities δ_2 and δ_1, used here, refer to the undistorted octahedron as the origin, with the electronic splitting energies obeying the centre of gravity rule [46], which may be considered as appropriate as long as Δ is large with respect to δ_1, δ_2 (see Fig. 4). The chosen signs of δ_2 and δ_1 characterise a tetragonally elongated structural configuration, and the *diagonal* energy of the O_h ground state $^3T_{1g}$ $(t_{2g}{}^2)$ is set to zero.

The energy matrix for the ground state $T_{1g} \otimes \varepsilon_g$ coupling of a d^2 cation is easily constructed by employing matrix (1) – with $V_\tau = 0$ and summing up the one-electron energies. Higher-order L_ε contributions (see Appendix A.1) are omitted, because they are about vanishing (vide supra), and interactions with excited terms via the Racah parameter B are not accounted for in this instance (strong field approximation):

	$d_{yz}{}^1d_{xz}{}^1$	$d_{xy}{}^1d_{yz}{}^1$	$d_{xy}{}^1d_{xz}{}^1$
	$-V_\varepsilon\rho_\varepsilon\cos\varphi$		
		$\frac{1}{2}\,V_\varepsilon\rho_\varepsilon(\cos\varphi + \sqrt{3}\sin\varphi)$	
			$\frac{1}{2}\,V_\varepsilon\rho_\varepsilon(\cos\varphi - \sqrt{3}\sin\varphi)$

(43)

The diagonal energies have to be supplemented by the restoring force $1/2K_\varepsilon\rho_\varepsilon^2$. The absolute minimum appears at $\varphi = 0^\circ$ and the saddlepoint at $\varphi = 180^\circ$, characterised by tetragonally elongated and compressed octahedra and a many-electron $^3A_{2g}$ and ^3E_g state, respectively. Again the signs in the vibronic matrices are chosen such, that the coupling constants are always positive. The distortion parameters and JT stabilisation energies at these extremum points are as follows:

$$^3A_{2g}: \quad \rho_\varepsilon^{em} = \frac{V_\varepsilon}{K_\varepsilon}; \quad E_-^{me} = -\frac{1}{2}V_\varepsilon\rho_\varepsilon^{em} \equiv -E_{JT}^{e} \tag{44a}$$

$$^3E_g: \quad \rho_\varepsilon^{cm} = \frac{1}{2}\frac{V_\varepsilon}{K_\varepsilon}; \quad E_-^{mc} = -\frac{1}{4}V_\varepsilon\rho_\varepsilon^{cm} \equiv -E_{JT}^{c} \tag{44b}$$

The Franck–Condon transition within the ground state at ρ_ε^{em} is calculated to be of the energy:

$$E_{FC}^{e} = 3E_{JT}^{e} \tag{45}$$

From the DFT optimised values for ρ_ε^{em}, ρ_ε^{cm} and E_{FC}^{e} (Tables 6a and 6b) the coupling constants V_ε and K_ε, collected in Table 7, are calculated. We emphasize that the parameters are valid in the strong field-approximation. The $^3T_{1g}(t_{2g}{}^2)$–$^3T_{1g}(t_{2g}{}^1e_g{}^1)$ configuration interaction will be considered later.

The influence of spin-orbit interaction in D_{4h} may be taken from the diagram in Fig. 19, where the electronic energy of the $_a{}^3T_{1g}(t_{2g}{}^2)$ split states in dependence on the ratio between the first-order

Table 6a
Structural (Å) and energy (eV) data for the isolated VF_6^{3-} polyhedron in D_{4h}, resulting from spin-unrestricted DFT calculations in a solvent continuum (R_{solv} = 0.95 and 1.40 (Å); for V^{III} and F^{-I}, respectively) – total energies E_t (which include the solvent energy increments E_{solv}) in respect to the $^3A_{2g}$ (e_g^2) ground state at *−53.878* eV (E_{solv} = *−21.470* eV); optimised data in italics. Calculations refer to the diagonal energies in the matrices of Eq. (42); LS coupling is not accounted for.

	Config.	Symmetry	$a_\perp$	$a_{\|\|}$	a_{av}	E_t (E_{solv})
E_1[e]	e_g^2	D_{4h}[a] D_{4h}[b]	*1.918*[c]	*1.983*[c]	1.940	≡0
E_2[c]	$e_g^1 b_{2g}^1$	D_{4h} D_{4h}	*1.950*[c]	*1.918*[c]	1.939	*−0.007*[d] (*0.059*)
E_3[e]	$b_{2g}(e_g)^1$ $b_{1g}(b_{2g})^1$	D_{4h} D_{2h}	1.918	1.983	1.940	0.100[c] (0.016)
E_4[c]	$e_g^1 b_{1g}^1$	D_{4h} D_{4h}	*2.037*	*1.894*	1.989	*1.821*[d] (*0.358*)
E_5[e]	$e_g^1 b_{1g}^1$	D_{4h} D_{4h}	1.918	1.983	1.940	2.268[d] (0.198)
E_6[e]	$e_g^1 a_{1g}^1$	D_{4h} D_{4h}	*1.885*	*2.249*	2.006	*1.871*[d] (*0.428*)
E_7[e]	$e_g^1 a_{1g}^1$	D_{4h} D_{4h}	1.918	1.983	1.940	2.312[d] (0.276)
E_8[e]	$b_{2g}^1 b_{1g}^1$	D_{4h} D_{4h}	1.918	1.983	1.940	2.940 (0.217)
E_9[e]	$b_{2g}^1 a_{1g}^1$	D_{4h} D_{4h}	1.918	1.983	1.940	1.929 (0.182)
E_{10}[e]	t_{2g}^2 [e]	D_{4h} O_h	1.918	1.983	1.940	−0.026[d] (0.014)

[a] Nuclear arrangement.
[b] Electronic distribution.
[c] Used for the derivation of V_ε and K_ε (see text).
[d] Energies too low, caused by self-interaction (see text).
[e] $\equiv e_g^{4/3} b_{2g}^{2/3}$.

Table 6b
Structural (Å) and energy (eV) data for the isolated VCl_6^{3-} polyhedron in D_{4h}, resulting from spin-unrestricted DFT calculations in a solvent continuum (R_{solv} = 0.95 and 1.75 (Å), for V^{III} and Cl^{-I}, respectively) – total energies E_t (which include solvent energy increments E_{solv}) in respect to the $^3A_{2g}$ (e_g^2) ground state at E_t = *−42.449* eV (E_{solv} = *−17.483* eV); optimised data in italics. Results refer to the diagonal energies in the matrices (42); without LS coupling.

	Config.	Symmetry	$a_\perp$	$a_{\|\|}$	a_{av}	E_t (E_{solv})
E_1[e]	e_g^2	D_{4h}[a] D_{4h}[b]	*2.374*[c]	*2.420*[c]	2.390	0
E_2[c]	$e_g^1 b_{2g}^1$	D_{4h} D_{4h}	*2.396*[c]	*2.373*[c]	2.388	*−0.020*[d] (*0.053*)
E_3[e]	$b_{2g}(e_g)^1$ $b_{1g}(b_{2g})^1$	D_{4h} D_{2h}	2.374	2.420	2.390	0.026[c] (0.006)
E_4[c]	$e_g^1 b_{1g}^1$	D_{4h} D_{4h}	*2.505*	*2.329*	2.446	*1.460*[d] (*0.335*)
E_5[e]	$e_g^1 b_{1g}^1$	D_{4h} D_{4h}	2.374	2.420	2.390	1.652[d] (0.109)
E_6[e]	$e_g^1 a_{1g}^1$	D_{4h} D_{4h}	*2.335*	*2.741*	2.470	*1.535*[d)] (*0.251*)
E_7[e]	$e_g^1 a_{1g}^1$	D_{4h} D_{4h}	2.374	2.420	2.390	1.794[d] (0.063)
E_8[e]	$b_{2g}^1 b_{1g}^1$	D_{4h} D_{4h}	2.374	2.420	2.390	2.113 (0.080)
E_9[e]	$b_{2g}^1 a_{1g}^1$	D_{4h} D_{4h}	2.374	2.420	2.390	1.468 (0.104)
E_{11}[e]	t_{2g}^2 [e]	D_{4h} O_h	2.374	2.420	2.390	−0.049 (0.014)

[a] Nuclear arrangement.
[b] Electronic distribution.
[c] Used for the derivation of V_ε and K_ε (see text).
[d] Energies too low, caused by self-interaction (see text).
[e] $\equiv e_g^{4/3} b_{2g}^{2/3}$.

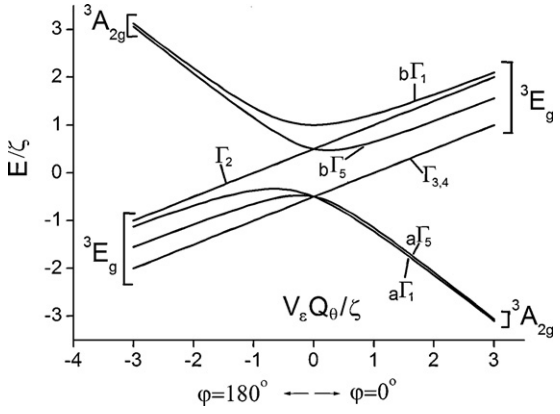

Fig. 19. The interplay between vibronic and LS-coupling in the $^3T_{1g}$ ground state of an octahedral d^2 complex.

Jahn–Teller coupling and the LS coupling constant ζ (ζ_0 = 210 cm^{-1}) is displayed. The respective equations, referring to $\varphi = 0°$ (180°), are:

$$
\begin{aligned}
E[_{a,b}\Gamma_1] &= (\mp)\tfrac{1}{4}V_\varepsilon\rho_\varepsilon + \tfrac{1}{4}\zeta \mp \tfrac{3}{4}\{V_\varepsilon^2\rho_\varepsilon^2(\pm)\tfrac{2}{3}V_\varepsilon\rho_\varepsilon\zeta + \zeta^2\}^{1/2}\\
E[_{a,b}\Gamma_5] &= (\mp)\tfrac{1}{4}V_\varepsilon\rho_\varepsilon \mp \tfrac{3}{4}\{V_\varepsilon^2\rho_\varepsilon^2 + \tfrac{4}{9}\zeta^2\}^{1/2}\\
E[\Gamma_{3,4}] &= (\pm)\tfrac{1}{2}V_\varepsilon\rho_\varepsilon - \tfrac{1}{2}\zeta\\
E[\Gamma_2] &= (\pm)\tfrac{1}{2}V_\varepsilon\rho_\varepsilon + \tfrac{1}{2}\zeta
\end{aligned}
\qquad (46)
$$

One readily sees, that – though LS coupling stabilises the tetragonal compression (by 1/2ζ) to a larger extent than the elongation – the $^3A_{2g}(e_g^2)$ state is always lowest. In the case of a very weak vibronic interaction the JT contribution to the $_a\Gamma_1$ ground state stabilisation is reduced by a factor of 1/2, while in the opposite case LS coupling is completely suppressed.

We proceed to consider a possible trigonal D_{3d}-type distortion. The relevant equations, which can be used to evaluate the respective V_τ, K_τ and X_τ parameters, are easily accessible, by summing up,

Table 7
Vibronic coupling within $V(X_t)_6^{3-}$ polyhedra (X = F, Cl): DFT results (without and with – see footnote b – configurational mixing: Tables 6a and 6b), supplemented by experimental data – $T_{1g} \otimes \varepsilon_g$ and $E_g \otimes \varepsilon_g$[a] interactions. Ground state $T_{1g} \otimes \tau_{2g}$ coupling data for trigonally distorted $V(F_t)_6^{3-}$ octahedra, as derived from DFT, are also listed.

D_{4h}	ρ_ε^{em} (Å)	ρ_ε^{cm} (Å)	a_{av} (Å)	E ($B_{2g} \rightarrow E_g$)	E_{JT}[e] (eV)	E_{JT}[c] (eV)
F^-	0.075[b]	0.037	1.939	0.100 eV	0.033_5[b]	0.008_5
Cl^-	0.053	0.027	2.389	0.025 eV	0.008	0.002

D_{4h}	V_ε	A_1 (eV Å^{-1})	K_ε (eV Å^{-2})	$K_\varepsilon{}'$[a]	A_2 (eV Å^{-2})	Δ (eV)[c]	calc.	exp.	δ_1	δ_2 (10^3 cm^{-1})
F^-	0.89[b]	2.0	11.9	≅7.6	0.9		2.12	2.01(1)	0.62	0.27
Cl^-	0.33	1.1	6.2	$\cong 3.6_5$	0.5		1.62	1.55	0.24	0.07

D_{3d}	ρ_τ^{cm} (Å)	ρ_τ^{cm} (Å)	a_{av} (Å)	E ($A_{2g} \rightarrow E_g$)
F^-	0.01_5[d]	0.02[d]	1.94	$\approx 0.01_3$ eV

[a] Excited state values, referring to an octahedral $t_{2g}^1 e_g^1$ configuration.
[b] The corresponding effective values accounting for configurational mixing are: $V_\varepsilon{}^{eff} \cong 0.84$ eV Å^{-1}, $\rho_\varepsilon^{eff} \cong 0.07_0$ Å and $E_{JT}{}^{eff} \cong 0.03_0$ eV.
[c] The calculated B ($=B_{te}$) parameters are 470 (F^-) and 350 (Cl^-) cm^{-1}, those deduced from the d–d spectra, 650 and 525 cm^{-1} for F^- and Cl^-, respectively – see text.
[d] $|\Delta\alpha'| = 0.32°$ and 0.42°, respectively.

from matrix (11) and when adding the restoring energy:

$$E_1({}^3A_{2g}\text{–}e_g{}^2) = \tfrac{3}{2}K_\tau\rho_\tau^{e2} + X_\tau\rho_\tau^{e2} - V_\tau\rho_\tau^{e}$$
$$\rho_\tau^{em} = \frac{V_\tau}{3K_\tau + 2X_\tau};\quad E_{JT}^{e} = \frac{1}{2}V_\tau\rho_\tau^{em} \tag{47a}$$

$$E_{2,3}({}^3E_g\text{–}a_{1g}{}^1e_g{}^1) = \tfrac{3}{2}K_\tau\rho_\tau^{c2} - \tfrac{1}{2}X_\tau\rho_\tau^{c2} - \tfrac{1}{2}V_\tau\rho_\tau^{c}$$
$$\rho_\tau^{cm} = \frac{1}{2}\frac{V_\tau}{3K_\tau - X_\tau};\quad E_{JT}^{c} = \frac{1}{4}V_\tau\rho_\tau^{cm} \tag{47b}$$

They are valid for octahedra, elongated and compressed along a trigonal axis, respectively, with the former referring to the minimum positions in D_{3d} symmetry. The Franck–Condon transition within the octahedral ${}_a{}^3T_{1g}(e_g{}^2)$ ground state is accordingly:

$$E_{FC}^{e}({}^3A_{2g} \rightarrow {}^3E_g) = 3E_{JT}^{e}\left\{\frac{1-a}{1+2a}\right\};\quad a = \frac{X_\tau}{3K_\tau} \tag{47c}$$

While the energy effects for the $V(Cl_t)_6{}^{3-}$ polyhedron are below numerical significance and not given, we discuss some interesting results for the fluoride complex. The calculated ρ_τ^{em} distortion at the relative $D_{3d}{}^e$ minimum is extremely small (Table 7), and accordingly also the ground state splitting of $E_{FC}^{e} \cong 105$ cm, if compared to the corresponding, by a factor of 6 larger, ρ_τ^{cm} and E_{FC}^{c} values for Ti^{III} (Table 2). We refrain from giving numbers for V_τ, K_τ and X_τ in view of the small radial distortion and energy values. It is very probably the (in relation to K_τ) large X_τ coupling constant, which mainly diminishes ρ_τ^{em} and E_{FC} in the trigonally elongated structure (Eq. (47a), V^{III}) and enlarges these quantities in the compressed case (Eq. (14), Ti^{III}). In the $D_{3d}{}^c$ conformation the $a_{1g}(t_o{}^1)$ electron cloud is subject to repulsion by the six ligands at an angle of $\geq 54.74^\circ$, while in $D_{3d}{}^e$ the d–electron distribution according to $A_{2g}(t_+{}^1t_-{}^1)$ is such, that the repulsion angle is with $\geq 35.26^\circ$ distinctly smaller, with a correspondingly more pronounced destabilising effect. In $D_{2h}{}^*$ the tetragonal distortion component is the same as in $D_{4h}{}^c$, indicating again a vanishing W contribution; $\Delta\alpha$ is only about 0.38°, yielding with $\rho_\tau^{*m} \cong 0.025$ Å an equally only tiny distortion. After all we can confidently assume, that in the d^2 case of $VX_6{}^{3-}$ (X = F^-, Cl^-) polyhedra the $T_g \otimes \varepsilon_g$ coupling clearly dominates the ground state potential energy surface – even much more pronounced than for Ti^{III}.

5.2. Excited state analysis

Inspecting the matrices of Eq. (42), the Racah parameter of interelectronic repulsion, B, comes additionally into play, when considering excited states. DFT usually underestimates this repulsion energy within open d^n shells considerably (see Section 12). We accordingly prefer to use B as calculated from the d–d spectra (Fig. 20). When translating DFT into ligand field energies, one should notice that both concepts are orbital-oriented. Accordingly, the DFT energies in Tables 6a and 6b, labelled by specific MO configurations, refer to the *diagonal energies* of the ligand field matrices. With this information at hand we can readily formulate the following master equations for the vertical transitions at the ground state distortion ρ_ε^{em}:

$$E_8^e - E_1^e = \Delta + 2\delta_1 + 4\delta_2 + 9B \quad (e_g{}^2 \rightarrow b_{2g}{}^1b_{1g}{}^1) \tag{48a}$$

$$E_9^e - E_1^e = \Delta - 2\delta_1 + 4\delta_2 - 3B \quad (e_g{}^2 \rightarrow b_{2g}{}^1a_{1g}{}^1) \tag{48b}$$

$$E_7^e - E_5^e = 6B - 4\delta_1 \quad (e_g{}^1b_{1g}{}^1 \rightarrow e_{1g}{}^1a_{1g}{}^1) \tag{48c}$$

Though in the case of Eq. (48c) the energy difference between two orbitally degenerate ${}^3E_g$ (${}^3T_{2g}$, ${}^3T_{1g}$) states is involved, it implies the excitation of an electron between orbital singlets and should hence not be falsified – see Section 3.1 – by self-interaction. From the three equations (48) the quantities Δ, δ_1 and B are accessible (Table 7), because the ground state splitting $3\delta_2$ is known

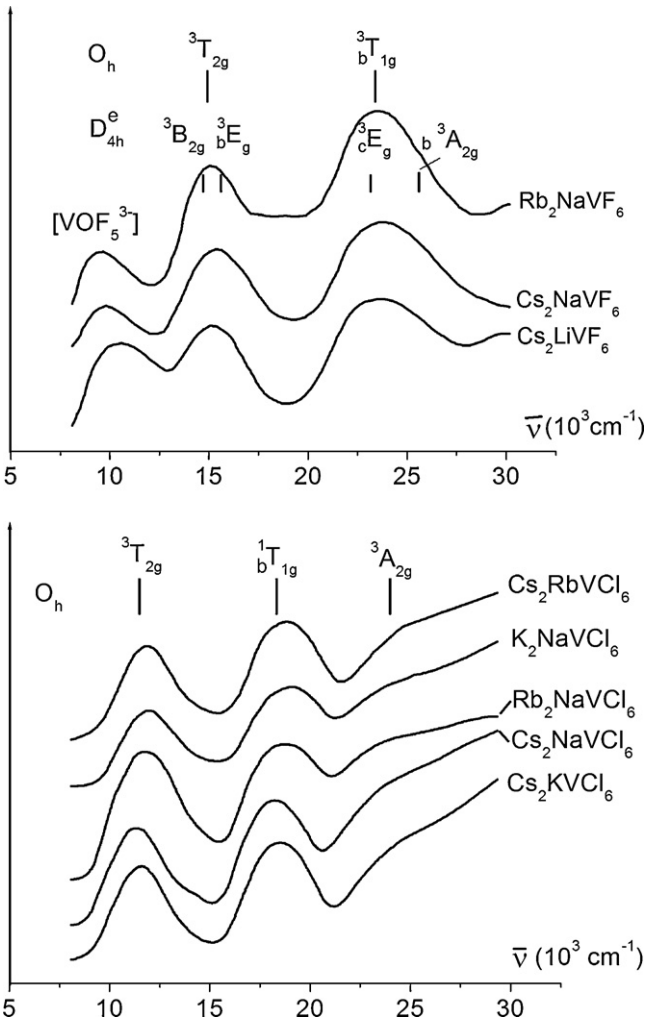

Fig. 20. d–d spectra (solid state reflection) of elpasolites $A_2'AVX_6$ (298 K; ${}_a{}^3T_{1g}$ ground state) with X = F^- (above) and Cl^- (below), respectively. The band assignment is according to the parameters Δ = 16,200 (12,500) cm^{-1} and B = 650 (525) cm^{-1} for F^- (Cl^-). In the fluoride case, a possible tetragonal ligand field component, as seen by DFT, is indicated via a $D_{4h}{}^e$ band fitting (${}_a{}^3A_{2g}$ (${}_a{}^3T_{1g}$) ground state; δ_1 = 0.62, $\delta_2 = 0.27 \times 10^3$ cm^{-1}). For the band at ≈10.000 cm^{-1} [43] see Appendix A.2.

already. Recalling that $4\delta_1$ equals $2(A_1\rho_\varepsilon^{em} + A_2\rho_\varepsilon^{em2})$ in the case of a tetragonal elongation (Eq. (31b); Fig. 4), we need further equations of condition in order to derive A_2 besides A_1. We have chosen the *optimised* excited state polyhedron distortions for $e_g{}^1b_{1g}{}^1$ (D_{4h} compressed) and $e_g{}^1a_{1g}{}^1$ (D_{4h} elongated) for the calculation; the corresponding state energies in respect to $t_{2g}{}^2$ in O_h are obtained by summation from Eqs. (5a), (5b) and (29):

$$(E_4^c)' = \Delta + \tfrac{1}{2}V_\varepsilon\rho_\varepsilon - A_1\rho_\varepsilon + A_2\rho_\varepsilon^2 + \tfrac{1}{2}K_\varepsilon'\rho_\varepsilon^2$$
$$(E_6^e)' = \Delta - \tfrac{1}{2}V_\varepsilon\rho_\varepsilon - A_1\rho_\varepsilon - A_2\rho_\varepsilon^2 + \tfrac{1}{2}K_\varepsilon'\rho_\varepsilon^2 + 6B \tag{49a}$$

Minimisation with respect to ρ_ε yields:

$$\rho'^{cm}_\varepsilon = \frac{2A_1 - V_\varepsilon}{2K_\varepsilon' + 4A_2}$$
$$\rho'^{em}_\varepsilon = \frac{2A_1 + V_\varepsilon}{2K_\varepsilon' - 4A_2} \tag{49b}$$

With these relations and with the δ_1 energy at hand, we readily calculate the excited state parameters A_1, A_2, and K_ε' (Table 7). The latter is an effective force constant, partly reflecting excited state properties, and correspondingly smaller than K_ε. The magnitude of A_2 is possibly subject to errors (too large) due to the already mentioned deficit of DFT to correctly account for the $3d_{z^2}$–4s interaction

(see Section 7.1) – without touching the gross result, however. After all, the DFT calculations allow the determination of the ligand field parameters Δ, δ_1 and δ_2 as well as the Racah parameter of interelectronic interaction B. On a finer scale, the vibronic coupling parameters A_1, A_2, V_ε and K_ε were deduced – replacing the coarser energy quantities δ_1 and δ_2. Though we do not want to stress a *fully quantitative* significance of the results too much, the obtained parameter set in Table 7 is very reasonable in relation to that for Ti^{III}. Also the calculated Δ values are consistent with those derived from the d–d spectra (see below). B is about 30% smaller than the experimental value. The JT-stabilisation energies are near to those for Ti^{III} (Tables 2 and 7). The d–d spectra in Fig. 20 do not show symmetry splitting at the first glance, thus indicating a regular O_h coordination. Possibly (vide infra), the Jahn–Teller coupling is suppressed. One reason for the absence of band splitting might be the configurational mixing of the excited state $^3A_{2g}$ ($b_{2g}{}^1b_{1g}{}^1$) state into the strong-field ground state $^3A_{2g}$ ($e_g{}^2$) via the non-diagonal matrix element $6B$ (see Eq. (42) and the following section).

The d–d spectra of the elpasolitic solids A'_2AVCl_6 in Fig. 20 have a cubic appearance, with the two broad transitions $_a{}^3T_{1g} \rightarrow {}^3T_{2g}$, $_b{}^3T_{1g}$ at 11,450(50) and 18,300(100) cm^{-1}, yielding $\Delta = 12{,}500$ and $B = 525\,cm^{-1}$. For the Cs, Na compound the band positions are slightly lower (11,100 and 17,900 cm^{-1}), with a correspondingly reduced Δ parameter of 12,300 cm^{-1}. All solids are – with the exception of Cs_2RbVCl_6 – cubic compounds with unit cell parameters 10.08 Å (K,Na), 10.20 Å (Rb,Na), 10.34 Å (Cs,Na) and 10.68 Å (Cs,K) [32]. The third transition of low intensity ($\rightarrow {}^3A_{2g}$; two-electron jump) is expected to occur at ≈24,000 cm^{-1}, where indeed a discontinuity in the intensity increase toward the charge-transfer region is observed. The spectra of the corresponding fluorides resemble those of the chlorides in appearance, showing the first two spin-allowed transitions at 14,850(50) and 23,250(50) cm^{-1}, similar to the band positions reported for Cs_2KVF_6 [47]. The (in O_h, but see Section 5.3) derived Δ and B parameters are 16,200 and 650 cm^{-1}, respectively. The third low-intensity main band should occur at ≅31,000 cm^{-1}. There was earlier [48] much discussion about the origin of the broad low-energy band appearing around 10,000 cm^{-1}, which was assigned to the lowest $_a{}^3T_{1g} \rightarrow {}^1E_g$, $^1T_{2g}$ transitions [49]. We can unambiguously show [43], however, that this absorption is caused by $V^{IV}OF_5{}^{3-}$ impurities and will give evidence for this in Appendix A.2.

5.3. The ground state properties due to configurational mixing

We shortly consider the mixing of the $e_g{}^2$ ($t_{2g}{}^2$) ground state with the $b_{2g}{}^1b_{1g}{}^1$ ($t_{2g}{}^1e_g{}^1$) excited state via interelectronic repulsion (mediated by the Racah parameter B) in order to obtain parameters and energies for the true many-electron ground state $_a{}^3A_{2g}$ ($_a{}^3T_{1g}$) (see the $^3A_{2g}$ matrix in Eq. (42)). The mixing coefficients of the respective wave functions in the O_h ground state are calculated for $VF_6{}^{3-}$ (with $\Delta = 16{,}200\,cm^{-1}$, $B = 650\,cm^{-1}$) to be of the magnitudes $c_1 \cong 0.98_5$ and $c_2 \cong 0.17$. The electronic ground state stabilisation energy ($-2\delta_2$) is accordingly reduced to $-2\delta_2^{eff} = -2\delta_2 c_1^2 + 2(\delta_1 + \delta_2)c_2^2 \cong -1.75\delta_2$ (with $\delta_1/\delta_2 \cong A_1/V_\varepsilon \cong 2.3$ from Table 7), yielding a reduced effective linear coupling constant V_ε^{eff} of 0.84 eV Å^{-1} and, in particular, a by 12% diminished E_{JT}^e energy. After all, the Jahn–Teller stabilisation energy has become smaller by less than 15%, switching from the fluoride complex of Ti^{III} ($E_{JT}^c = 0.034$ eV; Table 2) to that of V^{III} ($E_{JT}^{eff} \cong 0.030$ eV; Table 7). This reduction is most likely not the reason, why vibronic coupling might be suppressed in the case of the vanadium(III) fluoride complexes. Magnetic measurements, which we have performed with the cubic elpasolite Cs_2RbVF_6 (and with Cs_2KVCl_6 as well), suggest an only tiny ground state splitting of ≈0.02 eV; this energy is near to the margin of error of the method. Possibly, as suggested in the case of Ti^{III} already, DFT slightly overstates the vibronic coupling.

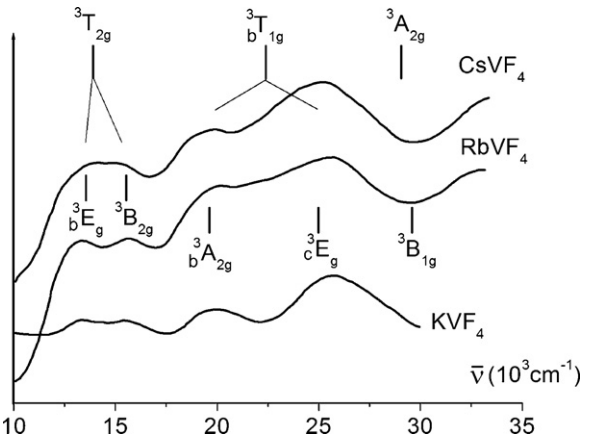

Fig. 21. The d–d spectra of solids AVF_4 (A^I = Cs, Rb, K) at 298 K. Band assignments (energies in 10^3 cm^{-1}) under the assumption of a compressed D_{4h} polyhedron symmetry ($_a{}^3E_g$ ($_a{}^3T_{1g}$)-ground state; see text), with the best-fit parameter set: $\Delta = 15150$, $B = 650$, $\delta_1' = 1150$, $\delta_2 = 600\,cm^{-1}$; the octahedral parent terms are also indicated. The $_a{}^3A_{2g}$ ($_a{}^3T_{1g}$) state is calculated at ≅1500 cm^{-1}; the transition to the $^3B_{1g}$ state (at ≅29,000 cm^{-1}) is a forbidden two-electron jump. Observed and calculated band positions are:

A^I	$_b{}^3E_g$	$^3B_{2g}$	$_b{}^3A_{2g}$	$_c{}^3E_g$
Cs	≈13.6	≈14.8	19.5	25.0
Rb	13.4	15.6	20.0	25.4
K	13.4	15.4	19.8	25.5
Calc.	13.5	15.5	19.7	25.0

The JT stabilisation energy of 240 cm^{-1} is not much smaller than the zero-point energy of the ε_g vibration (≈380 cm^{-1}, estimated from data in [26]), and the $V_\varepsilon^{eff}\rho^{eff}/\zeta$-ratio is – with $\zeta = 170\,cm^{-1}$ ($\zeta_0 = 210\,cm^{-1}$ [27] and $\zeta/\zeta_0 = 0.8$) – nearly 3. Hence, both ratios do not really support a suppression of the Jahn–Teller coupling. Experimentally, an O_h symmetry of the $VF_6{}^{3-}$ polyhedra in cubic elpasolite-type hosts is suggested by a spectroscopic study on V^{3+} doped K_2NaScF_6; the 9 K luminescence fine structure of the $_a{}^3T_{1g}$ ground state does not give any hint for the presence of a lower-symmetry crystal field component [50]. Nevertheless, we do not want to entirely exclude, that the d–d spectra in the case of the fluoridic elpasolites might mirror polyhedra with a symmetry deviating from O_h. A ligand field calculation, using the DFT energies for δ_1 and δ_2, is not in contradiction with, in particular, the broad-band character of the $_a{}^3T_{1g} \rightarrow {}_b{}^3T_{1g}$ transition and the distinct asymmetry in the high-energy descent of this band (Fig. 20).

5.4. The presence of bridging besides terminal ligands

VF_3 crystallises in an ReO_3-type lattice with almost regular $V(F_b)_6$ octahedra and bond lengths of 1.935 Å [51], perfectly matching with the (averaged) DFT value (Table 7). The reported spectrum is, again, cubic in appearance [47]. The Δ parameter (15,250 cm^{-1}) is 6% smaller than the elpasolite value, while the B parameter (650 cm^{-1}) is identical. Inspecting the d–d spectra (Fig. 21) of AVF_4 solids (A^I: K, Rb, Cs) with a $TlAlF_4$-related structure (Table 4) pronounced band splitting and intensity distributions within the considerably split $_b{}^3T_{1g}$ band occur, which are rather in favour of a compressed than of an elongated structure; also, a consistent band fitting, when using matrices (42), is only achieved under this, at least approximate, presumption.

5.5. The strain influence in solids A^IVF_4

We use an analogous procedure to that, introduced in Section 4 and applied to $ATiF_4$ solids, for the evaluation of the strain-induced parameters K_s (elastic strain) and V_ε^s, A_1^s (binding strain). The former

constant is again considered as a non-cubic correction to the force constant K_ε, which eases ligand displacements toward a tetragonal compression and aggravates displacements toward a tetragonally elongated polyhedron distortion. The latter statement holds for the binding strain parameters as well. The energy equations for a d^2 cation in the presence of an elastic and binding strain, at an arbitrary angle φ, are (see matrix (43), Eqs. (38a) and (38b); $\varphi_s = 180^\circ, L_\varepsilon = 0$)):

$$E(d_{yz}{}^1 d_{xz}{}^1) = -V_\varepsilon \rho_\varepsilon \cos\varphi + V_\varepsilon^s \rho_\varepsilon + \tfrac{1}{2}(K_\varepsilon + K_s \cos\varphi)\rho_\varepsilon^2$$
$$E(d_{yz}{}^1 d_{xy}{}^1) = \tfrac{1}{2} V_\varepsilon \rho_\varepsilon (\cos\varphi + \sqrt{3}\sin\varphi) - \tfrac{1}{2} V_\varepsilon^s \rho_\varepsilon + \tfrac{1}{2}(K_\varepsilon + K_s \cos\varphi)\rho_\varepsilon^2$$
$$E(d_{xz}{}^1 d_{xy}{}^1) = \tfrac{1}{2} V_\varepsilon \rho_\varepsilon (\cos\varphi - \sqrt{3}\sin\varphi) - \tfrac{1}{2} V_\varepsilon^s \rho_\varepsilon + \tfrac{1}{2}(K_\varepsilon + K_s \cos\varphi)\rho_\varepsilon^2 \quad (50)$$

Here, the d_{xy} orbital is stabilized by $-V_\varepsilon^s \rho_\varepsilon$ and the d_{xz}, d_{yz} MOs are raised in energy by $+1/2 V_\varepsilon^s \rho_\varepsilon$. In contrast to Ti^{III}, the d^2 cation V^{III} aims at a tetragonal elongation ($\varphi = 0^\circ$) by the V_ε-induced Jahn–Teller forces, thus in a deviating direction in space with respect to the elastic and the binding strain. Accordingly, an orthorhombic D_{2h} symmetry might result as the energetic compromise. Any angle φ between 120° (or 240°) – D_{4h} elongation along the molecular x (or y) axis – and 180° – D_{4h} compression along z – is obviously feasible. Hence both, K_s and V_ε^s, favour a $D_{4h}{}^c$ polyhedron distortion and a doubly degenerate ground state ^3E_g ($d_{xz}{}^1 d_{xy}{}^1$, $d_{yz}{}^1 d_{xy}{}^1$), while the vibronic coupling due to V_ε tends toward a $D_{4h}{}^e$ structure and an orbital singlet $^3B_{2g}$ ($d_{xz}{}^1 d_{yz}{}^1$) as the ground state. One can easily show, that an energy stabilisation along the orthorhombic distortion pathway is only feasible, if $^3B_{3g}(d_{xy}{}^1 d_{xz}{}^1)$ [or alternatively B_{2g} ($d_{xy}{}^1 d_{yz}{}^1$)] becomes the new ground state. The absolute minimum occurs at:

$$\rho_\varepsilon^{sm} = \frac{1}{2}\frac{V_\varepsilon(\sqrt{3}\sin\varphi_m - \cos\varphi_m) + V_\varepsilon{}^s}{K_\varepsilon + K_s\cos\varphi_m} \quad (51a)$$

with the energy:

$$E_- = -E_{JT}^s = -\tfrac{1}{4}\{(V_\varepsilon(\sqrt{3}\sin\varphi_m - \cos\varphi_m) + V_\varepsilon^s\}\rho_\varepsilon^{sm} \quad (51b)$$

The successive differentiation of E_{JT}^s with respect to the angular parameter allows one to fix φ by the straightforward, but rather complex expression:

$$K_s\left(\sqrt{3} - \alpha\cos\varphi_m + \frac{V_\varepsilon^s}{V_\varepsilon}\sin\varphi_m\right) = 2\alpha K_\varepsilon \quad \text{with}: \alpha \equiv -(\sin\varphi_m + \sqrt{3}\cos\varphi_m). \quad (51c)$$

The Franck–Condon transitions: $d_{xy}{}^1 d_{xz}{}^1 \rightarrow d_{xy}{}^1 d_{yz}{}^1(E_{FC}^{(1)})$ and $\rightarrow d_{xz}{}^1 d_{yz}{}^1(E_{FC}^{(2)})$ within the $^3B_{3g}$, $^3B_{2g}$, ^3A_g ($^3T_{2g}$) split-state manifold (see Fig. 4d) occur at:

$$E_{FC}^{(1)} = \sqrt{3} V_\varepsilon \rho_\varepsilon^{sm}\sin\varphi_m$$
$$E_{FC}^{(2)} = \tfrac{1}{2}\{V_\varepsilon(\sqrt{3}\sin\varphi_m - 3\cos\varphi_m) + 3V_\varepsilon^s\}\rho_\varepsilon^{sm} \quad (51d)$$

For the estimation of K_s we refer to the same consideration as employed for the $ATiF_4$ solids (Eq. (41)), namely, that the restoring energy does, approximately, not change if passing over from the $V(F_t)_6{}^{3-}$ complex ($1/2 K_\varepsilon \rho_\varepsilon^{em2}$) to the $M(F_t)_2(F_b)_4{}^-$ polyhedra in AMF_4-type compounds ($1/2(K_\varepsilon - K_s)\rho_\sigma^2$) – with the condition, that vibronic coupling is not considered. The estimated (with $\rho_\varepsilon^{em} = 0.075$ Å, $\rho_s = 0.105$ Å; Tables 4 and 7) strain correction to the force constant is rather large (Table 5). We now proceed to derive V_ε^s, ρ_ε^{sm} and φ_m from the band splitting energy δ_2, thereby utilising Eqs. (51). Because the energy δ_2 is obtained by band fitting of the d–d spectra in Fig. 21 on the (not necessarily correct – see below) assumption of a $D_{4h}{}^c$ symmetry, we approximately correlate $3\delta_2$ with $E_{FC} = E_{FC}^{(2)} - 1/2\, E_{FC}^{(1)}$, but with the correct angular parameter $\varphi_m \neq 180^\circ$ (Eq. (51d)) and after the experimental splitting (Table 5) has been reduced by a correction due to the differing central field

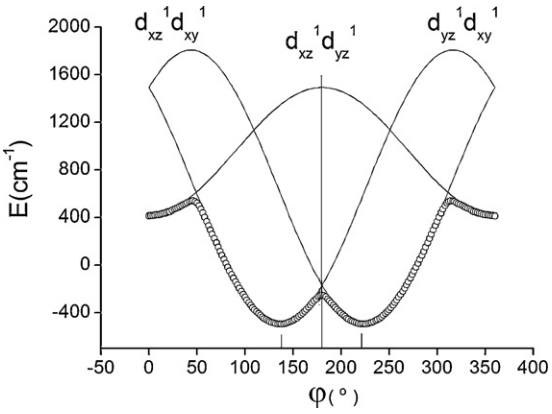

Fig. 22. Cross section of the adiabatic ground state potential surface along the energy axis and unfolded along the angular φ-path, at $\rho_\varepsilon^{sm} = 0.12_5$ Å, for the $V(F_t)_2(F_b)_4$ polyhedra in solids AVF_4 (Eq. (50), with the vibronic parameters from Table 5) – without taking account of the configuration interaction via B and of the Δ_{ec} correction. The electronic ($d_{xz}{}^1 d_{xy}{}^1$), ($d_{yz}{}^1 d_{xy}{}^1$), ($d_{xz}{}^1 d_{yz}{}^1$) configurations refer to $^3B_{3g}$, $^3B_{2g}$ and ^3A_g states in D_{2h}, respectively (see Fig. 4d); energies are in respect to O_h.

covalency of the terminal and bridging ligands (see Fig. 15 and Eq. (55a)) by $1/2\Delta_{ec} \cong 0.06$ eV ($3\delta_2 \cong 0.22$ eV $\Rightarrow E_{FC}^c \cong 0.16$ eV). The resulting V_ε^s parameter is somewhat larger in magnitude than for Ti^{III}, while the φ_m angle of 137° (223°) (Table 4) suggests a strongly orthorhombic polyhedron structure, closer to an elongation along one of the F_b–V–F_b axes than to a tetragonal compression along the F_t–V–F_t axis. The extent of the polyhedron distortion ($\rho_\varepsilon^{sm} = 0125$ Å) exceeds only slightly the strain-only value of 0.10_5 Å. Our results suggest a similar lattice as the one found for A^IMnF_4 compounds, where an antiferrodistortive order of short and long M–F_b bond lengths in the crystal planes perpendicular to the M–F_t directions is well established (Fig. 30). We will discuss this structural phenomenon in Section 7.

After all, vibronic coupling favours a tetragonal elongation via V_ε but, on the other hand, promotes a compression along the z-axis via the binding strain term V_ε^s, and the elastic strain K_s as well. The energetic landscape (without the contributions from the configuration interaction via B and the effective charge correction) is illustrated by the φ-dependence of the adiabatic ground state potential curves in a cross section parallel to the energy axis at $\rho_\varepsilon^{sm} = 0.125$ Å (Fig. 22). The absolute minima occur at $\varphi_m = 180 \pm 43^\circ$ and $E_{JT}^s = 485\,cm^{-1}$ (Table 5); from ρ_ε^{sm}, φ_m and $a_{av} = 1.94$ Å in Table 7, one estimates the bond-lengths listed in Table 4. The energy gap between the D_{2h}-distorted and the D_{4h}-compressed octahedron at $\varphi = 180^\circ$ is only $\approx 300\,cm^{-1}$. One may hence suggest, that the orthorhombic component is either dynamic – possibly down to rather low temperatures, with equilibrated V^{III}–F_b bond lengths of 1.97 Å (Table 4) – or even completely suppressed by the common action of LS coupling and vibrational quenching, with an apparent distortion parameter of $\rho_\varepsilon^{sm}(dyn.) \cong 0.105$ Å. The energy of the minimum positions is significantly affected by spin–orbit interaction; the energy barrier toward the $D_{4h}{}^c$ structure at $\varphi = 180^\circ$ is thereby lowered by $\approx 50\,cm^{-1}$. Having further in mind, that configuration interaction also reduces the JT energy, a suppression of the orthorhombic ligand field component seems feasible. The d–d spectra support this supposition – there is no obvious indication for splitting beyond those due to the tetragonal compression, as – in particular – the spectrum of KVF_4 indicates (Fig. 21). Accordingly, the extent of the distortion of the trans-$V(F_t)_2(F_b)_4{}^-$ octahedra would be about that induced solely by the elastic strain, as in $Fe(F_t)_2(F_b)_4{}^-$ ($r_\varepsilon^{sm} = 0.105$ Å $\cong \rho_s$; Tables 4 and 5). Unfortunately, no structural data for the polyhedron distortion in the $TlAlF_4$-related structures of $A^IV^{III}F_4$ solids are available, which could test the predictions.

We now turn to the estimation of A_1^s from the splitting parameter δ_1, which was obtained via band-fitting (Fig. 21) and has to be corrected with respect to central field covalency contributions by $2/3\Delta_{ec} = 0.08$ eV (Fig. 15; Eq. (55a)). Adopting the concept of a suppressed orthorhombicity ($\varphi_m = 180°$, $\rho_\varepsilon^{sm} = 0.105$ Å; Tables 4, 5 and 7), and utilising Eq. (60), which are derived in Section 7, a coupling constant A_1^s of ≈0.4 eV Å^{-1} results. Also here a significant enhancement of the $E_g \otimes \varepsilon_g$ coupling strength is indicated, when switching from the V^{III}–F_t to the V^{III}–F_b bond, which is identical with the one in the case of Ti^{III} ($A_1^s/A_1(Ti) = A_1^s/A_1(V) = 0.2$).

6. $Cr^{III}X_6^{3-}$ polyhedra

6.1. The ligand field parameters

The d^3 energy matrices for the high-spin states, including the distortion parameters δ_1, δ_2 characterising possible D_{4h} deformations, are easily derived from those for d^2 (Eq. (42)) – recalling the necessary sign switch for Δ, δ_1 and δ_2. The energies – with respect to the $^4A_{2g}(t_{2g}^3)$ [in D_{4h}: $^4B_{1g}(e_g^2b_{2g}^1)$] ground state and for a tetragonal elongation – are accordingly [52,46]:

	$e_g^2b_{1g}^1$ $(t_{2g}^2e_g^1)$	$e_g^2a_{1g}^1$ $(t_{2g}^2e_g^1)$	$b_{2g}^1a_{1g}^1b_{1g}^1$ $(t_{2g}^1e_g^2)$
$^4B_{2g}$	$\Delta + 2(\delta_1 - \delta_2)$		
$^4A_{2g}$		$\Delta - 2(\delta_1 + \delta_2) + 12B$	$-6B$
$(_{a,b}{}^4T_{1g})$		$-6B$	$2\Delta + 2\delta_2 + 3B$

	$e_g^1b_{2g}^1a_{1g}^1$ $(t_{2g}^2e_g^1)$	$e_g^1b_{2g}^1b_{1g}^1$ $(t_{2g}^2e_g^1)$	$e_g^1a_{1g}^1b_{1g}^1$ $(t_{2g}^1e_g^2)$
^4E_g	$\Delta - 2\delta_1 + \delta_2 + 3B$	$-3\sqrt{3}B$	$3B$
$(^4T_{2g},$	$-3\sqrt{3}B$	$\Delta + 2\delta_1 + \delta_2 + 9B$	$-3\sqrt{3}B$
$_{a,b}{}^4T_{1g})$	$3B$	$-3\sqrt{3}B$	$2\Delta - \delta_2 + 3B$

(52)

In Fig. 23 a series of spectra with the cubic elpasolite structure is collected, with the Cl^- ligand [32]. The derived (matrices (52) with $\delta_1 = \delta_2 = 0$) ligand field parameters Δ are smallest, if the size difference between A' and A is largest (Cs,Na) – because there is no significant compression effect on the $CrCl_6^{3-}$ octahedra in such a case. Conversely, Δ is largest for a combination K, Na (Table 8). With respect to the interelectronic repulsion parameters we follow the considerations of C.K. Jorgensen, who discriminates between B_{tt}, B_{te} and B_{ee} – depending on whether in the considered MO configuration two t_{2g}, one t_{2g} and one e_g, or two e_g electrons interact [10]. In the d^2 case of V^{III} we have dealt with one-electron excitations $t_{2g}^2 \rightarrow t_{2g}^1e_g^1$ and hence with B_{te} exclusively. The latter Racah parameter B ($t_{2g}^3 \rightarrow \cong t_{2g}^2e_g^1$) = B_{te}, derived from the chloride spectra (Table 8), does not change significantly with the A^I, A'^I-composition, though a small fluctuation occurs, due to the sensitivity to reading errors in the position of the second band. The nephelauxetic ratio $\beta = B_{te}/B_0$ ($B_0 = 920$ cm^{-1} [49] – for the free Cr^{3+} cation) is 0.60(2), practically identical with the value for VCl_6^{3-} (0.61; $B_0 = 860$ cm^{-1}) [49]; also Δ is similar for Cr^{III} and V^{III}. $Cs_2NaCrCl_6$ is a hexagonal elpasolite, presumably with the same 12-layer structure as the fluoride analogue (Fig. 26) [53]. By pressure application or by a change of the preparation conditions it can be obtained as a cubic elpasolite, however. $Rb_2LiCrCl_6$ is presumably a hexagonal elpasolite as well, but could not be transformed into the cubic structure under pressure; Δ (13,600 cm^{-1}) and B_{te} (600 cm^{-1}) are in the range of the values in Table 8. The third spin-allowed transition $^4A_{2g} \rightarrow {}_b{}^4T_{1g}$ – which is expected to occur at about 29,000 cm^{-1} as a weak band (nearly a two-electron jump) – is lost in the intensity increase toward the charge transfer region.

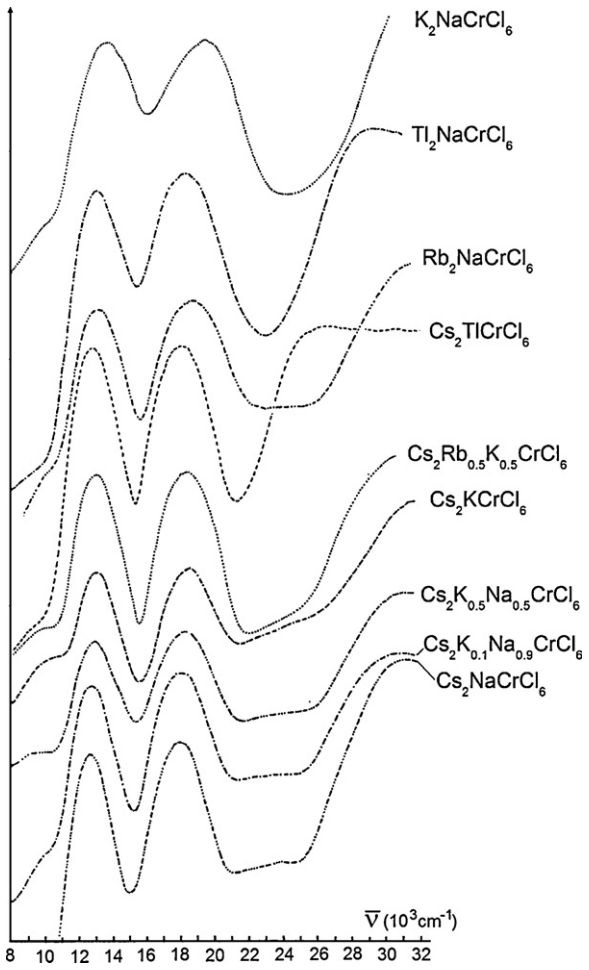

Fig. 23. d–d spectra of various cubic Cr^{III}-chloride elpasolites at 298 K; the two bands around 13 and 19×10^3 cm^{-1} are the transitions $^3A_{2g} \rightarrow {}^3T_{2g}$ and $\rightarrow {}_a{}^3T_{1g}$, respectively (see Table 8).

In Fig. 24 four high-sensitivity solid-state reflection spectra at 77 K are depicted, where various weak spin forbidden transitions are resolved. Two of them, at 14,600 and 15,200 cm^{-1} in the region of the first main transition, are sharp because they occur within the ground state t_{2g}^3 configuration (negligible Δ dependence). The energies of the respective two transitions are – for $\Delta/B_{tt} \approx 20$ [54]:

$$\rightarrow {}_a{}^2E_g: \quad 0.04\Delta + 6.4B_{tt} + 3C_{tt}; \quad \rightarrow {}_a{}^2T_{1g}: \quad 0.03\Delta + 7.6B_{tt} + 3C_{tt} \tag{53}$$

yielding a B_{tt} value of 760 cm^{-1} (with $C_{tt}/B_{tt} = 4$) corresponding to a nephelauxetic ratio of 0.85. The latter is considerably larger than the one in Table 8, because it involves repulsions within pairs of π-antibonding t_{2g} electrons only – in difference to the smaller value of $B_{te} \cong 550$ cm^{-1}, where a more covalent σ-antibonding e_g electron participates. Jørgensen has analysed these covalency effects; we refer to his work, without going into further detail [10]. The third visible quartet-doublet transition ($\rightarrow {}_a{}^2T_{2g}$) with an about 0.2Δ-dependence is observed at 20,200 cm^{-1}. The Δ independence of the two low-energy quartet-doublet transitions (Eq. (53)) can be nicely followed, when inspecting the spectrum of the cryolite Cs_3CrCl_6; here, the ligand field parameter is rather large (13,800 cm^{-1}) – due to the compression of the $CrCl_6^{3-}$ octahedron by the neighboured voluminous Cs^+ cation in the A position of this lower-symmetry variant of the elpasolite structure. A high-resolution single crystal spectrum of Cr^{3+}-doped $Cs_2NaSeCl_6$ at 15 K is reported by Wenger and Güdel [55], where the mentioned $^4A_{2g} \rightarrow {}_a{}^2E_g$, $_a{}^2T_{1g}$, $_a{}^2T_{2g}$

Table 8
Unit cell (Å) and ligand field parameters (10^3 cm^{-1}) of cubic elpasolites A'_2ACrCl_6.

A′,A	K,Na	Tl,Na	Rb,Na	Cs,Na[a]	$Cs,K_{1/2}Na_{1/2}$	Cs,K	$Cs,Rb_{1/2}K_{1/2}$[b]	Cs,Tl
Δ[c]	13.6_5 (0.60)	13.0 0.53	13.1 0.57	12.6_5 0.54	12.8_5 0.56	13.0_5 0.57	13.0 0.55	12.8 0.54
a	10.00[d]	10.06	10.14[d]	10.29	10.44	10.65[d]	10.68	10.70

[a] Preparation under pressure (50 kb) or at higher temperatures (see text).
[b] Cs,Rb: non-cubic elpasolite with $\Delta = 13{,}050$ and $B = 540$ cm^{-1}.
[c] B, as derived from the $^4A_{2g} \rightarrow {}_a{}^4T_{1g}$ transition with the excitation of (approximately) one electron from t_{2g} into $e_g(\cong B_{te})$, is in the average: 550 ± 20 cm^{-1}.
[d] Reported already in literature [58].

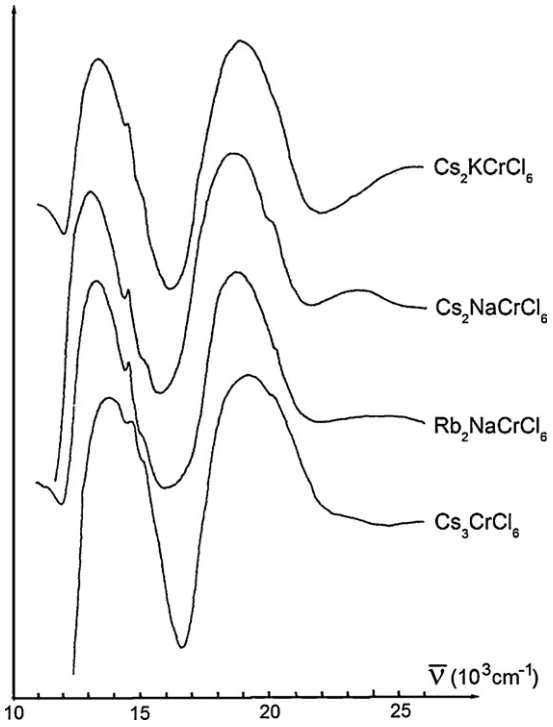

Fig. 24. d–d spectra of elpasolite-type[a] Cr^{III}-chloride elpasolites (Cs_3CrCl_6 is a distorted variant) at 77 K with resolved $^4A_{2g} \rightarrow {}_a{}^2E_g$, ${}_a{}^2T_{1g}$ and ${}_a{}^2T_{2g}$ transitions at 14,600, 15,200 and ≅20,200 cm^{-1}.

spin-flip transitions are analysed in detail. The 7*K* luminescence $^4T_{2g} \rightarrow {}^4A_{2g}$ fine structure was interpreted as originating from a (dynamical) $D_{4h}{}^c$-type distortion of the magnitude $\rho = 0.13_5$ Å in the excited state. Our DFT results indicate an only slightly larger value (0.15_3 Å) for the tetragonally compressed $Cr(Cl_t)_6{}^{3-}$ polyhedron in the $^4B_{2g}$ ($e_g{}^2b_{1g}{}^1$) MO configuration, which represents the minimum in the adiabatic potential surface of the split octahedral $^4T_{2g}$ ($t_{2g}{}^2e_g{}^1$) state (see below).

We now turn to the discussion of the corresponding fluoridic elpasolites. We have measured the spectra of a series of compounds (A′, A: Cs, Li; Cs, Na; Cs, K; Cs, Rb; Cs, Tl; K, Na; K, Li), possessing cubic structures with the exception of the first two, which crystallise with hexagonal structures (Fig. 26). There is an overlap of the two spin-forbidden ($\rightarrow {}_a{}^2E_g$, ${}_a{}^2T_{1g}$) with the first main transition ($\rightarrow {}^4T_{2g}$) – in difference to the situation for the Cl^- ligand, where they appear in the descent of the latter band; this has been the cause of some controversy in literature [49] concerning the exact assignment of the observed fine structure. Inspecting Fig. 27, we readily deduce from the spectrum of $CsCrF_4$, where the two well resolved and narrow, nearly Δ-independent (Eq. (53)) quartet-doublet transitions appear between the two $^4A_{2g} \rightarrow {}^4T_{2g}$ split bands, that they should be positioned at 15,300 and 15,800 cm^{-1}, respectively. This observation supports the assignment proposed in the single crystal study of Ferguson et al. [56] (Table 9) and contrasts other ones [57]. Our studies suggest a position of the lowest main band $^4A_{2g} \rightarrow {}^4T_{2g}$ (=Δ) slightly above the two spin-forbidden bands – though one should take into consideration that the close neighbourhood of quartet–doublet and quartet–quartet transitions may lead to an intermixing of the respective wavefunctions due to non-diagonal LS coupling matrix elements and, though to only small energetic shifts, to distinct intensity changes. The ligand field parameters, deduced from the spectra in Fig. 25 by fitting to the matrices (52), are summarised in Table 9. We have again discriminated the *B* parameters, depending on whether they originate from π-antibonding t_{2g} or σ-antibonding e_g MOs [10]. The nephelauxetic ratio B_{te}/B_o nearly equals the one for the V^{III} elpasolites ($\beta = 650/860 = 0.76$; Fig. 20) also in the case of the fluorides. Because the position of the second band ($\rightarrow {}_a{}^4T_{1g}$) in the d–d spectra, from which B_{te} is evaluated, depends only modestly on *B* in the chromium(III) case [54], this Racah parameter may be subject to larger errors, as *B* (from ${}_b{}^4T_{1g}(t_{2g}{}^1e_g{}^2)) \approx B_{ee}$ as well. The comparison of published *B* parameters is often difficult and confusing, because very frequently a single *B* value is used in the band fitting. We think, that it is necessary for a better understanding of the binding phenomenon to use the more sophisticated approach with different Racah-parameters for different MO configurations. The derived ligand field strength Δ is comparable to the value for V^{III}. The third main transition $^4A_{2g} \rightarrow {}_b{}^4T_{1g}$ of expected weaker intensity due to an approximate two-electron jump can be observed in the fluoride case, because the intensity increase toward the charge-transfer bands starts at higher energies than in the case of the chlorides. The decrease of the nephelauxetic ratio with increasing occupation of the e_g orbitals (Table 9) nicely illustrates the augmenting d-covalency in the Cr^{III}–F bond.

We shortly discuss the structures of hexagonal elpasolites (Fig. 26) with a possibly different bonding of the M^{III} cations as compared to the one in the cubic analogues [59]. In the former lattices the transition metal ions may occupy octahedral sites equivalent to those in the cubic elpasolites with linear M^{III}–F–A^I

Table 9
Spectroscopic results for solids A'_2ACrF_6 – band positions (shoulders in parentheses), assignments and derived parameters (energies in 10^3 cm^{-1}, $C/B = 4$).

$^4A_{2g} \rightarrow$	${}_a{}^2E_g$	${}_a{}^2T_{1g}$	$^4T_{2g}$	${}_a{}^2T_{2g}$	${}_a{}^4T_{1g}$	${}_b{}^4T_{1g}$	Δ	B_{tt}[c]	B_{te}[c]	B_{ee}[c]
	15.2[a]	(15.8)	16.3	(22.8)	23.6	36.0	–			
	15.3[b]	15.8	≅16.2	(22.2)	23.1	35.0	16.2[b]	0.79 (0.86)	≅0.68_5 (0.74_5)	≅0.62 (0.67)

[a] Ref. [56] (A′,A: K,Na).
[b] Own results (Fig. 25).
[c] For the nomenclature: Jørgensen [10] denotes these quantities B_{55}, B_{35} and B_{33}, respectively; nephelauxetic ratios ($B_0 = 920$ cm^{-1}) in parenthesis.

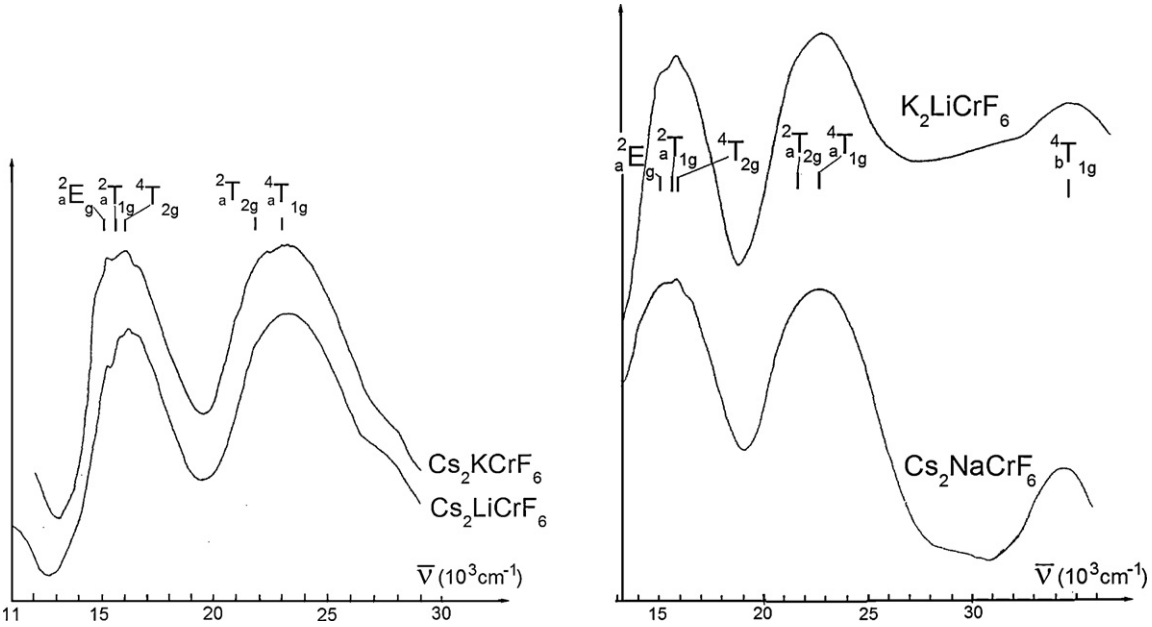

Fig. 25. d–d spectra of elpasolite-type solids $A_2'ACrF_6$ (A′, A: Cs, Li and Cs, Na hexagonal; Cs, K and K, Li cubic) at 298 K in an extended energy range (right), and at 77 K (left); assignments according to the parameter set in Table 9.

bridging or sites, in which – due to a (partly or fully) face-connection between the octahedra – all or half of these bridges are strongly bent. Because the contrapolarising A^I alkaline ions are ionic in their bonding character, if they are large, a differing binding behaviour is not expected. If only 3d cations occupy the octahedral positions and hence M^{II}–F–M^{II} bridges occur, as in compounds $A^IM^{II}F_3$, a significant weakening particularly of the π-antibonding properties is observed on diminishing the bond angles from ≈180° (in perovskite) to about 80° in the case of face connections – indicated by a distinct increase of the ligand field strength. This has been studied for the solid $CsNiF_3$, which crystallizes dimorphically in lattices of the hexagonal perovskite type (see [71]).

6.2. Vibronic coupling in excited states

We are now prepared to estimate effective linear vibronic coupling constants V_ε and A_1 also for Cr^{III}. This can be done, by performing DFT optimisations in the excited states $^4T_{2g}$, $_a{}^4T_{1g}$, resulting from the octahedral $t_{2g}{}^2e_g{}^1$ configuration (see matrix (52)). The procedure is shortly sketched and the respective equations are given in Appendix A.3. The obtained parameters are collected in Table 10 and come out to be very similar to those for Ti^{III} and V^{III} in the hexa-fluoride polyhedra (Tables 2, 3 and 7); in the chloride case, where the polyhedron distortions are larger – the distinctly smaller force constant is the main reason – and the energetic effects smaller – due to strongly reduced coupling con-

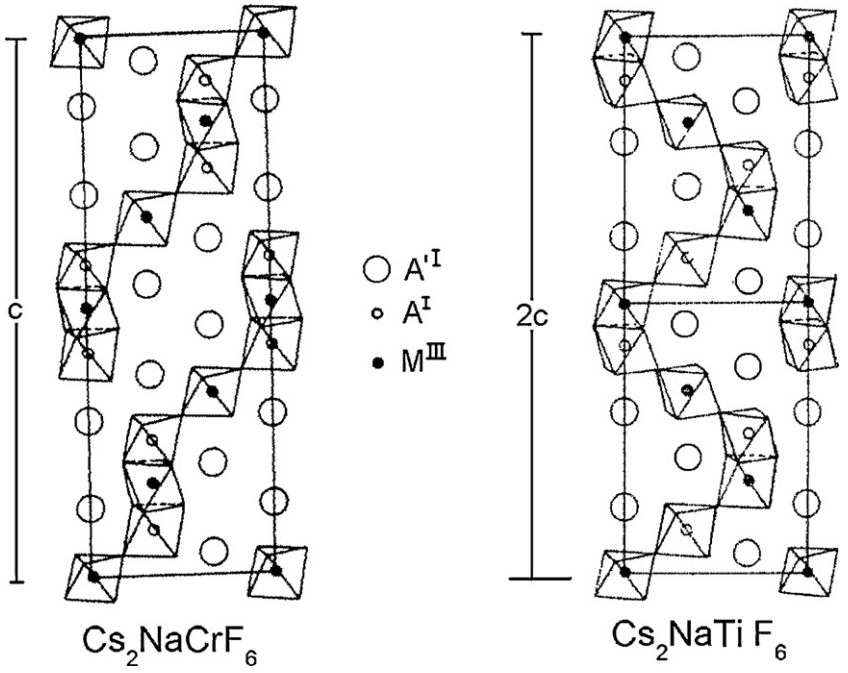

Fig. 26. Two variants of hexagonal elpasolites with the constitution $A_2'AM^{III}F_6$: the structure of Cs_2NaTiF_6 (space group $C_{3v}{}^1$) [60] and the Cs_2NaCrF_6 type (space group $D_{3d}{}^5$), adopted from [53].

Table 10
Estimated vibronic parameters for the $Cr(X_t)_6^{3-}$ octahedra (X = Cl^-, F^-), derived from DFT when using calculated polyhedron distortions and Franck–Condon transitions involved in the excited $^4T_{2g}$, $^4T_{1g}$ ($t_{2g}^2e_g^1$) states (see Appendix A.3).[a] The average Cr–F bond lengths (in parentheses) are by ≅0.06 Å larger than the ones in the ground state, due to the participation of the totally symmetric α_{1g} mode.

ρ (Å)[b] ⇒	$e_g^2b_{1g}^1$ (a_{av})[c]	$e_g^2a_{1g}^1$ (a_{av})[e]	$e_g^1b_{2g}^1b_{1g}^1$ (a_{av})[c]	$e_g^1b_{2g}^1a_{1g}^1$ (a_{av})[e]
Cl^-	0.153 (2.41_3)	0.454 (2.43_9)	0.276 (2.42_2)	0.371 (2.42_6)
F^-	0.117 (1.95_8)	0.413 (1.98_0)	0.238 (1.96_5)	0.253 (1.96_5)

E_{FC}^x (eV)	x = (a)[c]	(b)[c]	V_ε	A_1	A_2	K_ε'
Cl^-	0.848	0.584	0.2_5	1.0 eV Å^{-1}	0.4	$3._5$ eV Å^{-2}
F^-	1.186	0.949	0.7	1.8 eV Å^{-1}	0.8	$7._5$ eV Å^{-2}

[a] The calculated Racah parameters B_{te} are 360 (Cl^-) and 530 cm^{-1} (F^-) – about 30% smaller than the experimental energies (Tables 8 and 9), similar to the situation for V^{III} (Table 7).
[b] The upper indices c and e refer to compressed and elongated, respectively.
[c] The indices x refer to electronic transitions, as listed in Appendix A.3.

stants – the consistency with the vibronic parameters of Ti^{III} and V^{III} is also mostly striking. We will use the parameter set, derived for the $Cr(F_t)_6^{3-}$ parent octahedron, in the analysis of the d-d spectra of solids $ACrF_4$ with F_t/F_b-mixed ligand coordination spheres of Cr^{III}. Here, experimental information can be extracted from the d-d spectra, showing distinct splitting of orbitally degenerate excited states (Fig. 27).

6.3. The presence of bridging ligands in trans- and cis-positions

The ligand field spectrum of CrF_3, with a distorted ReO_3 structure and octahedra with exclusively bridging ligands (Cr–F_b bond lengths: 1.901 Å [61]), shows only the two broad $^4A_{2g} \rightarrow {}^4T_{2g}$, $_a{}^4T_{1g}$ transitions [56]. The derived ligand field strength of 14,800 cm^{-1} is about 9% smaller than in the case of $Cr(F_t)_6^{3-}$ entities, while the nephelauxetic effect ($B_{te} \approx 700$ cm^{-1}) is practically identical in both cases – in perfect analogy to corresponding solids with V^{III} and Ti^{III}.

The investigated compounds A^ICrF_4, whose d–d spectra are depicted in Fig. 27, possess only in the cases A^I = Rb, Tl and NH_4 (not shown) a $TlAlF_4$-related structure with tetragonally compressed trans-$Cr(F_t)_2(F_b)_4^-$ octahedra, as can be deduced from X-ray powder data (Table 4) and also from the d–d spectra (see below). The splitting parameters δ_1' and δ_2, obtained by band fitting to the experimental spectra via the matrices in Eq. (52), are near to those for AVF_4 solids of the same structural $TlAlF_4$-type (Tables 5 and 11). They are, after correction with respect to Δ_{ec} (see Eq. (55a)), transformed into the adiabatic potential analogues via the following expressions – for $\varphi = \varphi_s = 180°$ – when utilising Eqs. (39b) and (40):

$$2\delta_2 - 0.04 = 2\delta_2^{cor} = (V_\varepsilon + V_\varepsilon^s)\rho_\varepsilon^{sm}$$
$$2\delta_1' - 0.04 = 2\delta'^{cor}_1 = (A_1 + A_1^s - A_2\rho_\varepsilon^{sm})\rho_\varepsilon^{sm} \quad (54)$$

We choose the distortion parameter to be of the magnitude $\rho_s \cong 0.105$ Å from the solids $AFe^{III}F_4$; this value should approximately hold also for the compressed trans-$Cr(F_t)_2(F_b)_4$ polyhedra in the $ACr^{III}F_4$ compounds with an equally non-degenerate ground state (Table 4) and a similar metal–ligand bond length (Table 12). In contrast to Ti^{III} and V^{III} the distortion is purely due to the action of

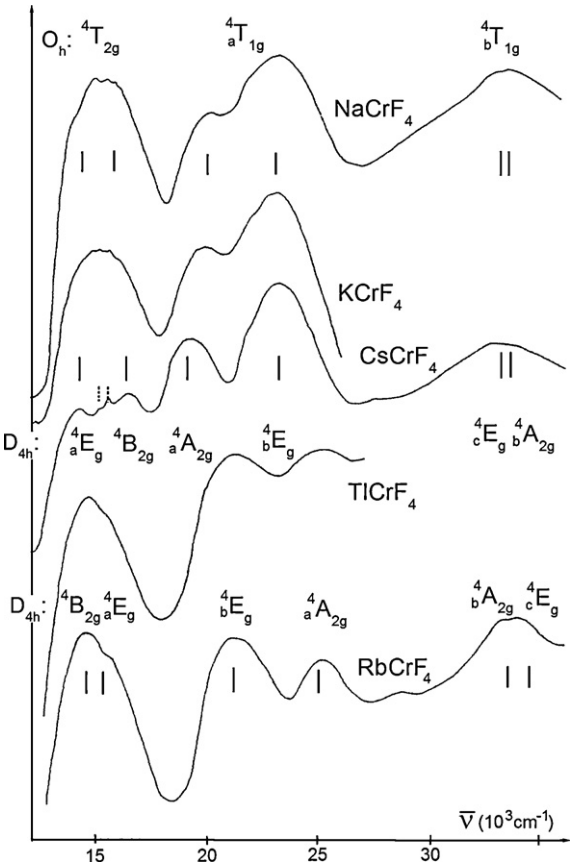

Fig. 27. The d–d spectra of solids $A^ICr^{III}F_4$ (77K). Band assignments and fitting in D_{4h} (octahedral parent term designations are indicated above) for A^I = Na, K and Cs – elongated cis-$Cr(F_t)_2(F_b)_4^-$ octahedra – and for A^I = Rb (and Tl) – compressed trans-$Cr(F_t)_2(F_b)_4^-$ octahedra; fitting parameters as in Table 11. The spin-forbidden transitions – in O_h: $^4A_{2g} \rightarrow {}_a{}^2E_g$, $_a{}^2T_{1g}$ – occur approximately within the octahedral t_{2g}^3 configuration and are indicated for $CsCrF_4$ by dotted lines (see text).

Table 11
Observed band positions (in 10^3 cm^{-1}) and assignments in the d–d spectra of solids $A^ICr^{III}F_4$ (Fig. 27), with cis-(A^I = Na, K, Cs) and trans-$Cr(F_t)_2(F_b)_4^-$ octahedra (A^I = Rb, Tl). Best-fit ligand field parameters are listed; the B_{te} and B_{ee} parameters were taken from Table 9 for reasons given in the text and in order to keep the number of unknown parameters small.

A^I	$_a{}^4E_g$	$^4B_{2g}$	$_a{}^4A_{2g}$	$_b{}^4E_g$	$_b{}^4E_g$	$_b{}^4A_{2g}$	Δ	δ_1/δ_1'	δ_2
Cs	14.4	16.5	19.4	23.3	33.2	34.0	15.3	1.0	0.4
K	≅15.5		19.9	23.0	–	–			
Na	≈14.5	≅16.0	20.4	23.2	33.5 (2)		15.3	$\approx 0.7_5$	≈0.3
Rb	≅15.5	14.7	25.0	21.2	≅33.9	≅33.3	15.6	1.0_5	0.6_5
Tl	≅15.5	14.7	25.0	21.2	–	–			

Table 12
Structural data (Å) for the cis-$M^{III}(F_t)_2(F_b)_4^-$ octahedra in solids AMF_4, which crystallise in the $NaNbO_2F_2$ lattice[a] or in a structure with columns of interconnected cis-polyhedra[b] (Fig. 28).

A^I	M^{III}	a_t (cis)	a_b (cis)	a_b (trans)	a_{av}	Ref.	ρ_{sb}*	ρ_{av}*
Na	V [a]	1.871	1.959	1.971	1.934	[62b]	0.109	0.052
Na	Fe [a]	1.874	1.956	1.955	1.928	[62d]	0.094	0.046
Na	Cr [a]	1.861	1.936	1.927	1.908	[62c]	0.082	0.033
Cs	Cr [b]	1.851	1.940	1.929	1.907	[63]	0.097	0.039
K	Cr [b]	1.860	1.943	1.926	1.910	[64]	0.088	0.028

* Calculated from the single bond distances (ρ_{sb}) and from the averaged bond lengths ($1/2\{a_t(cis)+a_b(cis)\}$) perpendicular to a_b (trans) (ρ_{av}), respectively.

an elastic strain. Utilizing the data in Table 10 (see Appendix A.3) via Eq. (54) binding strain components result, which are rather large in the $T_g \otimes \varepsilon_g$ coupling case (V_ε^s) and near to those of Ti^{III} and V^{III}, if A_1^s is considered (Table 5).

Solids A^ICrF_4 with A^I = Na, K, Cs crystallise in very interesting structural alternatives, in which the polyhedron interconnection occurs partly via fluoride anions in cis-position. In the $NaNbO_2F_2$ type [62a] (Fig. 28, Table 12) puckered layers of octahedra share two ligands in trans-position perpendicular to the paper plane and two further ligands in cis-position within this plane; solids $NaMF_4$ with M^{III} = V [62b], Cr [62c], Fe [62d] adopt this structure. If the A^I position is occupied by larger alkaline cations, a different interconnection pattern may occur (Fig. 28; $CsCrF_4$ type [63]) where columns – consisting of three chains, which are cis-connected in the paper plane – form the hexagonal lattice. The constituting octahedron in $CsCrF_4$ is depicted in Fig. 28, bottom. The bridging angles between two Cr^{III} centres in these structures are between $<(Cr–F_b–Cr) \cong 150^\circ$ and about linear. It is striking, that – choosing Fe^{III} and Cr^{III} with non-degenerate ground states – the single $M^{III}–F_b$ bond lengths are nearly equal, independent on whether they occur in cis- or trans-positions to each other (Table 12). Furthermore, they do not differ significantly from the bond lengths found in the trans-$M(F_t)_2(F_b)_4^-$ octahedra in $TlAlF_4$-type structures (Table 4). If the binding energetics of the d-orbitals is considered and, particularly, that they possess an inversion centre, the actual approximate C_{2v} symmetry of the cis-configured octahedron is regarded as being D_{4h}; the polyhedron is elongated along the $F_b–M–F_b$ axis (z), with smaller bond lengths in the cis-$(F_b)_2M(F_t)_2$ plane (xy) – obtained by averaging the respective $M–F_b$ and $M–F_t$ bond lengths trans to each other (Fig. 28). The assumption of a tetragonal elongation is confirmed by the positions of the split transitions of the octahedral $^4A_{2g} \rightarrow {}_a{}^4T_{1g}$ bands and their intensity distributions in Fig. 27, if the spectra of $CsCrF_4$ and $RbCrF_4$ are compared; the centres of gravity of the split bands possess nearly the same energetic position at $22.3(2) \times 10^3$ cm^{-1} in the chosen assignments. The shoulder, which appears at about 22.500 cm^{-1} in the ascent (A^I = Na, K, Cs) or descent (A^I = Rb) of the $^4B_{1g} \rightarrow {}_b{}^4E_g$ band, has to be assigned to the octahedral $^4A_{2g} \rightarrow {}_a{}^2T_{2g}$ transition, which is nearly Δ-independent and should not split significantly in a tetragonal field. The solid $RbCrF_4$ is reported to be dimorphic, crystallising also in a $CsCrF_4$-related structure. Structural data for solids, in which the constituting polyhedra are of a cis-$M^{III}(F_t)_2(F_b)_4^-$ configuration, are collected in Table 12. The listed distortion parameters ρ_{sb} (sb: single bond) were calculated from these data, utilising the recipe of Eq. (4a); the ρ_{av} values, which result when averaging over the a_t(cis) and a_b(cis) bond lengths, are also given. The ρ_{sb} distortions in the cases of Fe^{III} and Cr^{III} with orbital singlet ground states are smaller by about 0.01 Å than those of the compressed trans-$Fe^{III}(F_t)_2(F_b)_4^-$ species (Table 4), suggesting that this structural alternative is slightly less preferred by the elastic strain (smaller K_s force constant contribution).

The AOM energy equations for the compressed trans- and the elongated cis-$M^{III}(F_t)_2(F_b)_4^-$ octahedra in solids AMF_4 are, respectively (see the MO schemes in Fig. 15):

$$
\begin{aligned}
t_{2g}: \quad & E(e_g) = 2\{e_\pi^{\parallel}(t) + e_\pi^{\perp}(b)\} - \tfrac{1}{2}\Delta_{ec} \\
& E(b_{2g}) = 4e_\pi^{\perp}(b) - \Delta_{ec} \\
& 3\delta_2 \cong 2\{e_\pi^{\parallel}(t) - e_\pi^{\perp}(b)\} + \tfrac{1}{2}\Delta_{ec} \\
e_g: \quad & E(a_{1g}) = 2e_\sigma^{\parallel}(t) + e_\pi^{\perp}(b) - \tfrac{1}{3}\Delta_{ec} \\
& E(b_{1g}) = 3e_\sigma^{\perp}(b) - \Delta_{ec} \\
& 4\delta_1' \cong 2\{e_\sigma^{\parallel}(t) - e_\sigma^{\perp}(b)\} + \tfrac{2}{3}\Delta_{ec}
\end{aligned}
\qquad (55a)
$$

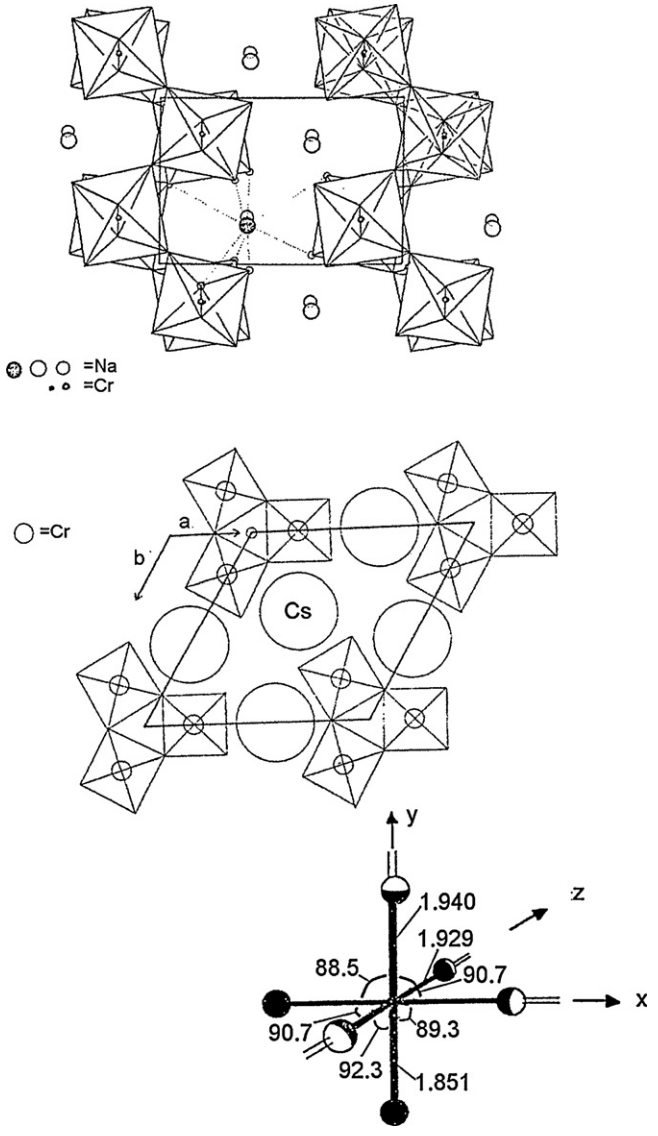

Fig. 28. The monoclinic and hexagonal structures of $NaCrF_4$ ($NaNbO_2F_2$-type – top) and $CsCrF_4$ (columns of three interconnected chains – central; adopted from [63]); the cis-$Cr(F_t)_2(F_b)_4$ octahedron in $CsCrF_4$ is shown at the bottom (the $Cr–F_b–Cr$ angles in the trans- and cis-directions are 177.9° and 149.3°, respectively; the bridging function of the F_b ligands is indicated).

$$
\begin{aligned}
t_{2g}: \quad & E(b_{2g}) = 2\{e_\pi^\perp(t) + e_\pi^\perp(b)\} - \tfrac{1}{2}\Delta_{ec} \\
& E(e_g) = 2e_\pi^{||}(b) + e_\pi^\perp(b) + e_\pi^\perp(t) - \tfrac{3}{4}\Delta_{ec} \\
& 3\delta_2 \cong e_\pi^\perp(t) + e_\pi^\perp(b) - 2e_\pi^{||}(b) + \tfrac{1}{4}\Delta_{ec} \\
e_g: \quad & E(b_{1g}) = \tfrac{3}{2}\{e_\sigma^\perp(b) + e_\sigma^\perp(t)\} - \tfrac{1}{2}\Delta_{ec} \\
& E(a_{1g}) = 2e_\sigma^{||}(b) + \tfrac{1}{2}\{e_\sigma^\perp(b) + e_\sigma^\perp(t)\} - \tfrac{5}{6}\Delta_{ec} \\
& 4\delta_1 \cong e_\sigma^\perp(b) + e_\sigma^\perp(t) - 2e_\sigma^{||}(b) + \tfrac{1}{3}\Delta_{ec}
\end{aligned}
\tag{55b}
$$

The superscripts ||, ⊥ refer to the axial direction and the equatorial plane, respectively, while (b) and (t) stand for bridging and terminal ligands. The $e_\sigma^{||}$ parameters contain, in an effective way, energy contributions from the $3d_{z^2}$–4s interaction (≡ $e_\sigma^{||}$(eff); Section 3.3, Eq. (34)); they diminish this binding increment in the compressed ($e_\sigma^{||}$(t)) and elongated case ($e_\sigma^{||}$(b)) and are the more significant, the larger the deviation of the octahedra from a regular O_h structure is. According to our model, the AOM energies are defined as referring to the $M(F_t)_6^{3-}$ parent octahedron as the zero-point of the energy scale, and hence a correction with respect to the central field covalency is necessary. It is 1/2 and 2/3Δ_{ec} for the t_{2g} end e_g splitting, respectively, in the trans-case and half in magnitude for the cis-octahedra, as one may deduce from Fig. 15. If one uses the structural result of nearly equal M–F_b bond lengths in the cis- and trans-positions in question and infers: $e_\pi^\perp(b) = e_\pi^{||}(b)$, $e_\sigma^\perp(b) = e_\sigma^{||}(b)$ – a not necessarily correct presumption (see below) – it is seen, that the π- and σ-splitting should be larger by a factor of about 2 for the trans- in comparison to the cis-configured $Cr(F_t)_2(F_b)_4^-$ octahedra; however, the δ_1'/δ_1 ratio is lowered, if the $3d_{z^2}$–4s interaction is taken into account, because δ_1' and δ_1 are reduced and enhanced in magnitude, respectively.

We now contrast the AOM expressions for the dσ and dπ splitting parameters of the cis-$Cr(F_t)_2(F_b)_4$ polyhedra with the respective adiabatic potential equations. Choosing the coordinate system as in Fig. 28 for $CsCrF_4$ and modelling the elongated (||z; φ = 0) complex by the steric mean of two trans-configured compressed polyhedra, in which the F_t–Cr–F_t axis is alternatively oriented along the x- (φ_s = 300°) and y-axis (φ_s = 60°) – both with the distortion ρ_{sb} ≅ 0.10 Å (see the definition in Table 12, footnote a), valid for each of the two component polyhedra – one obtains the following relations:

$$
\begin{aligned}
2\delta_2^{cor} &= (V_\varepsilon + \tfrac{1}{2}V_\varepsilon^s)\rho_{sb} \\
2\delta_1^{cor} &= (A_1 + \tfrac{1}{2}A_1^s + A_2\rho_{sb})\rho_{sb}
\end{aligned}
\tag{56}
$$

δ_2^{cor}, δ_1^{cor} are the experimental splitting energies δ_2, δ_1 from Table 11, obtained from band fitting (Fig. 27), but corrected (Eq. (55b)) with respect to Δ_{ec}. Eqs. (56) are derived using the diagonal energies of matrix (43) with φ = 0°, supplemented by the symmetry-equivalent V_ε^s (at φ_s = 60°, 300°) additions – for δ_2^{cor} – and adopting Eq. (59) – for δ_1^{cor}; here, we mirror the binding situation for Cr^{III} by the excited $t_{2g}^2e_g^1$ configuration in O_h, with the t_{2g}^2 and e_g^1 orbital components referring to δ_2^{cor} and δ_1^{cor}, respectively. The respective effective charge correction is (see Eq. (55b)): (1/12)Δ_{ec} = 0.01 eV. The inspection of Eq. (56) in comparison to those, valid for the trans-polyhedra (Eq. (54)), signalizes essential agreement with the experiment (Table 5, 3. and 5.line) – δ_2^{cor} should be smaller in the cis-case due to a smaller support by V_ε^s, while the δ_1^{cor} splitting might be about equal, when supposing that $1/2A_1^s \approx 2A_2\rho_\varepsilon^{sm}$. The magnitudes of V_ε^s and A_1^s (derived via Eq. (56)) are indeed near to those of the other M^{III} cations (Table 5). If one uses the by a factor of more than 2 smaller ρ_{av} distortions instead of ρ_{sb} – inconsistent with the vibronic model – there would be essential agreement with the AOM (Eq. (55b)), but generate A_1^s and V_ε^s increments of non-sensibly large magnitudes. *Apparently, the steric effect, imaged by ρ_{sb}, does not depend on, whether the M^{III}–F_b and M^{III}–F_t bonds occur in the same molecular direction* (here along the molecular x- and y-directions of the cis-configured species), *or whether they are cis-oriented to each other* (as in the trans-complexes). A thermodynamical trans-influence [65] in that the M–F_t(F_b) bonds in the molecular xy-plane impose their properties onto the M–F_b(F_t) bonds trans-oriented to them is seemingly not present. In agreement, a perceptible trans-effect on the bond lengths is also not observed. However, larger energy and bond length effects are not necessarily expected, because the total metal–ligand interactions only partly reflect the comparatively smaller contributions due to the d-orbitals.

We finally discuss some interesting structural properties in connection with the eventual stabilisation of either the trans-compressed (I) or the cis-elongated (II) species by vibronic forces (Tables 4 and 12). Compounds $NaM^{III}F_4$ give preference to the structure-type II in the absence of a Jahn–Teller instability (Fe^{III}, Cr^{III}). Ti^{III}– which aims at a compressed environment, where the vibronic energy gain is largest – avoids this structural type and prefers host lattices (I) with already (by elastic strains) tetragonally compressed sites. On the other hand, $NaV^{III}F_4$ – V^{III} aims at a tetragonal elongation – crystallises in structure II, with a slightly enhanced radial distortion in respect to that of Fe^{III} and Cr^{III} with orbital singlet ground states in the same lattice. V^{III} is also found in $TlAlF_4$-kind solids K(Rb,Cs)VF_4, however, where the elastic and binding strain act against the JT forces. Here, the distortion of the trans-$V(F_t)_2(F_b)_4^-$ octahedron (Table 4) is of a comparable magnitude to that in $NaVF_4$ (Table 12) – with a structure, which is orthorhombic, intermediate between compression and elongation (ρ_ε^{sm} ≅ 0.125 Å), or of D_{4h}[c] symmetry with vibronically suppressed orthorhombicity (ρ_ε^{sm} ≅ 0.105 Å).

7. $Mn^{III}X_6^{3-}$ polyhedra

7.1. Fluoride as the ligand

A DFT and ligand field study of the vibronic coupling in the ^5E_g ground state of $Mn(F_t)_6^{3-}$ polyhedra as they occur in elpasolites, has been published elsewhere (see also Fig. 14) [9] The results are summarised in Table 13, together with the estimated parameters for the $Mn(F_b)_6$ polyhedra in MnF_3. The latter are based on the d-d spectrum [9,29] and on the structural data of MnF_3 [66], which crystallises in a monoclinically distorted VF_3 lattice with a complex cooperative order of the antiferrodistortive type and – enforced by lattice strains – a local polyhedron distortion with a distinct orthorhombic component ($a_\perp$ = 1.82; 1.91 Å; $a_{||}$ = 2.09 Å). While the radial distortion is nearly unchanged in respect to that in the elpasolites, the ground state splitting increases by 50% (Table 13, Fig. 29), giving unambiguous evidence for a distinctly larger coupling parameter A_1 and force constant K_ε, when replacing the terminal by bridging ligands. The observed ground state splitting in the cubic elpasolites $Cs_2K(Na)MnF_6$ and in $[Co(NH_3)_6]MnF_6$ is of the magnitude $9.3(4) \times 10^3$ cm^{-1}, which value is exactly reproduced by DFT, and originates from a considerable tetragonal elongation of the MnF_6^{3-} octahedra. The splitting is by about 10% smaller, and the elongation is also perceptibly reduced [67b], in the case of the cryolite Na_3MnF_6, where packing effects in the monoclinic lattice impose strain restrictions on the extent of distortion. The splitting of the excited $^5T_{2g}(t_{2g}^2e_g^2)$ state is ≈2000 cm^{-1} (≈0.25 eV) in the elpasolitic cases, corresponding to a coupling parameter V_ε of 0.64 eV $Å^{-1}$. The experimental splitting energy is only a rough estimation, however; spectroscopic band shape simulations – a quantitative analysis is not possible because only powder-reflectance data are available – show, that the true splitting should be about 20% larger, bringing V_ε(exp.) to 0.77 eV $Å^{-1}$. A calculation of V_ε is not possible for MnF_3, because here (as in compounds $AMnF_4$) the excited state splitting is

Table 13
Vibronic coupling [9] and distortion parameters (ρ_ε in Å; A_1 in eV Å^{-1}; A_2, K_ε in eV Å^{-2}; E in eV) for the $Mn^{III}F_6$ polyhedra in elpasolites [67a] (a), MnF_3 [66] (b) and in solids $AMnF_4$ (A^I: Na [70], K [72a], Cs [72a,b]) (c). The data in brackets refer to the strain parameters $A_1{}^s$ and K_s. Underlined data are experimental.

	ρ_ε^{em}	ρ_ε^{cm}	A_1	A_2	$E_{JT}{}^e$	$E_{JT}{}^c$	$E_{FC}{}^e$	φ	K_ε
a $Mn(F_t)_6$	0.26(2)	0.19	2.00	0.70	0.26	0.19	1.15	0°(120°,240°)	9.1
b $Mn(F_b)_6$	≅0.27	–	≅2.6	≅0.8_5	≅0.36	–	1.52	≈0°(120°,240°)	≅11.5
c $Mn(F_t)_2(F_b)_4$[a]	0.38_5[b]	–	[0.35]	0.80	0.43	–	1.84[c]	128° (232°)[b]	[3.1]

[a] The listed best fit parameters A_1, $A_1{}^s$ and A_2, K_ε, K_s yield: $\rho_\varepsilon^{sm} = 0.38$ Å, $\varphi_m = 135°(225°) \Rightarrow a_z = 1.790$, $a_{x,y} = 2.025 \pm 0.135$ Å and $E_{FC}{}^s = 1.84$ eV.
[b] According to structural data from Ref. [70–72]: $a_z = 1.810(7)$, $a_y = 1.865(9)$, $a_x = 2.169(2)$ Å and $a_{av} = 1.948(2)$ Å (Fig. 30).
[c] Experimental ground state splitting $E_{FC}{}^s = 1.88$ eV [29]; Δ_{ec}-correction ≅0.04 eV (see text).

obscured by quintet–triplet transitions, which have gained intensity by M^{III}–Mn^{III} interactions via F_b bridging ligands (Fig. 29) [29]. From the spin-forbidden transitions (see the respective ligand field matrices for d^6 in D_{4h} elongation [68,46], in the supplementary material Appendix B.1) the Racah parameter B and the C/B ratio are calculated to be of the magnitudes 780 cm^{-1} and 4.6, respectively [29]. The former value corresponds to a nephelauxetic ratio ≈0.80 (using the B_0 parameter in Table 16), consistent with those for V^{III} and Cr^{III}.

The $B_{1g}(e_g{}^2b_{2g}{}^1a_{1g}{}^1)$ ground state in $D_{4h}{}^e$ is subject to a significant interaction with a higher energy state of the same symmetry, where the $3d_{z^2}$ electron is excited into the 4s-orbital. As mentioned before, this effect is accounted for by the higher-order coupling constant A_2. We can accordingly estimate the respective energy contribution to the ground state splitting via the following expression (see Eq. (31b)):

$$\Delta E_{FC}^e \equiv E_{FC}^e - E_{FC}^e(with\, A_2 = 0) = 2\{(A_1 + A_2\rho_\varepsilon^{em})\,\rho_\varepsilon^{em} - A_1(\rho_\varepsilon^{em})'\} \tag{31c}$$

where $(\rho_\varepsilon^{em})'$ is the hypothetical radial distortion with $A_2 \cong 0$. With the parameter values in Table 13 one obtains 0.27 eV – which is about 23% of the observed Franck–Condon energy (1.15 eV). Though the energy contribution is significant, it is distinctly smaller than the energy stabilisation due to the $E_g \otimes \varepsilon_g$ JT coupling. There is further convincing experimental evidence for $3d_{z^2}$–4s mixing, for example in the case of Cu^{2+} in tetragonally compressed $CuF_6{}^{4-}$ octahedra, with a ground state of B_{1g} ($b_{2g}{}^2e_g{}^4b_{1g}{}^2a_{1g}{}^1$) symmetry; here, the mixing of 4s electron density into $3d_{z^2}$ is directly seen in the EPR hyperfine splitting (see [112]). The d–s interaction was first studied by Smith, utilising the angular-overlap model [69a]; it can

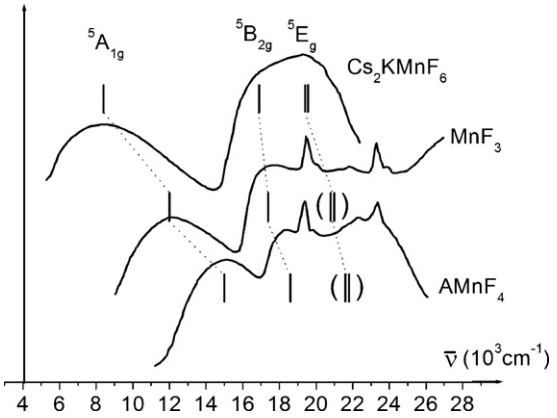

Fig. 29. d–d spectra (5 K) of the hexafluoro-manganese(III) polyhedron in the elpasolite Cs_2KMnF_6 – top – in MnF_3 –amidst – and in an $AMnF_4$-type solid – bottom. The ligand field transitions in D_{4h} nomenclature are indicated, with $^5B_{1g}$, $^5A_{1g}$ and $^5B_{2g}$, ^5E_g resulting from the octahedral E_g ground state and T_{2g} excited state, respectively (adopted from Refs. [9,29]). The ^5E_g markings for MnF_3 and $CsMnF_4$ refer to band positions, which are roughly estimated as averages over orthorhombic split terms; for a fitting within ligand field theory – also of the sharp quintet–triplet transitions, see Ref. [29] and the supplementary material B1.

be formally treated as a pseudo-JT effect ($E_g \otimes \varepsilon_g \otimes A_{1g}$ coupling) [69b], but there is no need to do so, because the first-order ($E_g \otimes \varepsilon_g$) coupling clearly dominates.

7.2. The strain in solids A^IMnF_4

We now turn to the discussion of the binding properties in the trans-$Mn(F_t)_2(F_b)_4{}^-$ octahedra, as they occur in solids $A^IMn^{III}F_4$ (A^I = Li to Cs, Tl) with a strongly JT-distorted $TlAlF_4$-type structure. As one might expect, not a tetragonal compression ($\varphi = 180°$), but a bond length anisotropy in the x–y plane, with a pronounced elongation along one of the F_b–Mn–F_b polyhedron axes is observed (Fig. 30). The cooperative order within the $\{Mn(F_b)_{4/2}\}_\infty$ layers is antiferrodistortive [1]. The average polyhedron distortion, reported for solids $AMn^{III}F_4$ ($a_z = 1.81$ Å; $a_{xy} \cong 2.02 \pm 0.15$ Å; $\rho \cong 0.39$ Å; $a_{av} \cong 1.95$ Å) corresponds to an angular parameter φ of ≅130° (Table 13, Fig. 30). The correlation between the angular parameter φ and the deviations from the average bond length within the distorted polyhedron is given by the following relations (see also Eq. (4a)) [9]:

$$\begin{aligned} &\Delta a_x + \Delta a_y + \Delta a_z = 0 \\ &\cos\varphi = \left(\frac{\sqrt{3}}{\rho}\right)\Delta a_z, \qquad \sin\varphi = \left(\frac{1}{\rho}\right)(\Delta a_x - \Delta a_y) \end{aligned} \tag{57}$$

The appropriate vibronic perturbation matrix for $E \otimes \varepsilon$ coupling in the presence of a strain at φ_s, if a $d^4(t_{2g}{}^3e_g{}^1)$ ground state, as in the case of Mn^{III} [equivalent to a $d^1(e_g{}^1)$ excited state], is considered, adopts the form – see matrix (28), supplemented by an A_1^s contribution:

$$\begin{vmatrix} A_1\rho\cos\varphi + A_1^s\rho\cos\varphi_s + A_2\rho^2\cos 2\varphi & -A_1\rho\sin\varphi - A_1^s\rho\sin\varphi_s + A_2\rho^2\sin 2\varphi \\ -A_1\rho\sin\varphi - A_1^s\rho\sin\varphi_s + A_2\rho^2\sin 2\varphi & -A_1\rho\cos\varphi - A_1^s\rho\cos\varphi_s - A_2\rho^2\cos 2\varphi \end{vmatrix} \tag{58}$$

The sign of the $A_1{}^s$ increment is chosen (according to the given experimental reality) to support a $d_{x^2-y^2}$ ground state and to destabilise a d_{z^2} ground state. The following energy equation results, if the A_1 contribution dominates:

$$E_\pm = \tfrac{1}{2}(K_\varepsilon - K_s\cos(\varphi - \varphi_s))\rho_\varepsilon^2 \pm \{(A_1 + A_1^s\cos(\varphi - \varphi_s) + A_2\rho_\varepsilon\cos 3\varphi\}\rho_\varepsilon \tag{59}$$

Here, the restoring energy and the elastic strain contribution according to Eq. (36a) have been added. Setting $\varphi_s = 180°$, the minimisation with respect to ρ yields:

$$\rho_\varepsilon^{sm} = \frac{A_1 - A_1{}^s\cos\varphi}{K_\varepsilon + K_s\cos\varphi - 2A_2\cos 3\varphi} \tag{60}$$

$$E_-^s = -\tfrac{1}{2}(A_1 - A_1^s\cos\varphi)\rho_\varepsilon^{sm} \equiv -E_{JT}^s$$

$$E_{FC}^s = 2\{(A_1 - A_1^s\cos\varphi) + A_2\rho_\varepsilon^{sm}\cos 3\varphi\}\rho_\varepsilon^{sm}$$

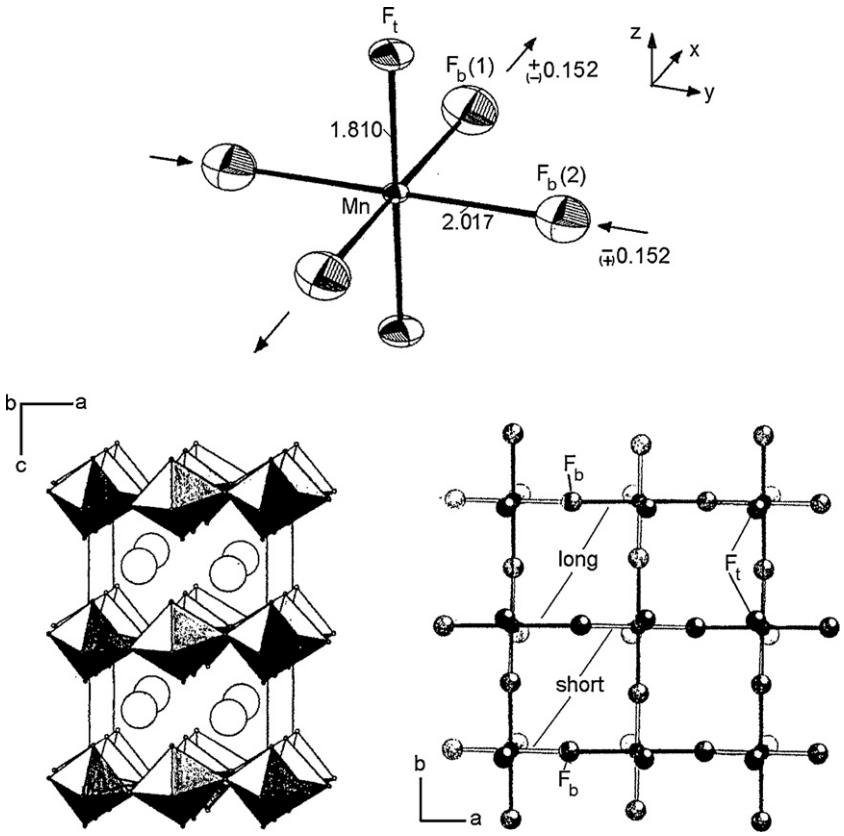

Fig. 30. The trans-$Mn(F_t)_2(F_b)_4$ polyhedron in solids with a $TlAlF_4$-related structure(in $CsMnF_4$ the $F_b(1)$–Mn–$F_b(2)$ and F_t–Mn–F_b angles are 90.0(3)° and 90.0(1.5)°, respectively, and the Mn–F_b–Mn bridging angle is 161.9°) [70–72]. The tetragonal unit cell and the antiferrodistortive order between long and short Mn–F_b bond lengths in the a–b plane (adopted from [70–72a]) are shown below.

The successive minimisation of E^s_{JT} in respect to φ yields an additional relation between K_ε, K_s, A_1, A_2, A^s_1, and φ_m, which is, though easily obtained, rather complex and not given analytically here. Utilising the experimental data, namely ρ^{sm}_ε, E^s_{FC} (the effective charge-corrected $4\delta^{cor}_1$ splitting energy) and φ_m, as listed in Table 13, A^s_1 and K_s can be derived from Eq. (60), using otherwise A_1, A_2 and K_ε from the $Mn(F_t)_6^{3-}$ parent complex. In distinction to the d^1 and d^2 cases of Ti^{III} and V^{III}, we can accordingly deduce the elastic strain contribution to the force constant, K_s, here reliably. Furthermore, assisted by the mentioned additional relation as a third equation of condition, we have adjusted the A_2 coupling constant and refined the angular parameter φ_m; the resulting parameter set is listed in Table 13. φ_m is larger than the experimental distortion angle, reflecting a more pronounced orthorhombic deformation component, while the bond lengths deviate by only about 0.01_5 Å from the range of reported values (see the best fit parameters in footnote a of Table 13). One should consider here, that the bond length difference between $a_x(a_y)$ and $a_y(a_x)$ within the antiferrodistortive order of approximately along $a_x(a_y)$ elongated octahedra in the *ab*-plane of the $TlAlF_4$-related structure (Fig. 30) is not easily revealed exactly by X-ray crystallography.

In Fig. 31 the φ dependence of the lower ground state potential surface is depicted. It is governed by the interplay between the binding and elastic strain parameters A^s_1 and K_s, favouring $\varphi = 180°$, on the one hand, and A_2, stabilising $\varphi = 120°(240°)$, on the other hand. At the latter angles there is an extension along $x(y)$ and a compression along $y(x)$, which are both F_b–Mn–F_b axes; this polyhedron structure is only partly favoured by the imposed strain, but is the ideal geometry with respect to the second-order coupling constant A_2 (see Eq. (60)). The minimum positions are calculated to occur at $\varphi^s_m = 135°$ and 225°, rather far away from the tetragonal compression at $\varphi = 180°$, and indicating that A_2 is of major importance in the interplay. Inspecting the AOM energies, we meet a *structural situation very near to the one, on which Eq. (55b) is based*; accordingly the experimental ground state splitting had to be corrected by $1/3\Delta_{ec} \cong 0.04$ eV for obtaining E^s_{FC} (Table 13). Besides the absolute minima, the potential surface possesses a high-lying minimum at 0° and a saddlepoint at 180°. The location of the latter with respect to the absolute minima is about 600 cm^{-1} and tantamount to the barrier, which tips the scales for either having a dynamically equilibrated tetragonal compression of the $Mn(F_t)_2(F_b)_4^-$ octahedron parallel to *z*, or a frozen-in structure near to D_{4h} elongation ($||x$ or $||y$). The barrier height is – in contrast to the V^{III} case (Fig. 22)

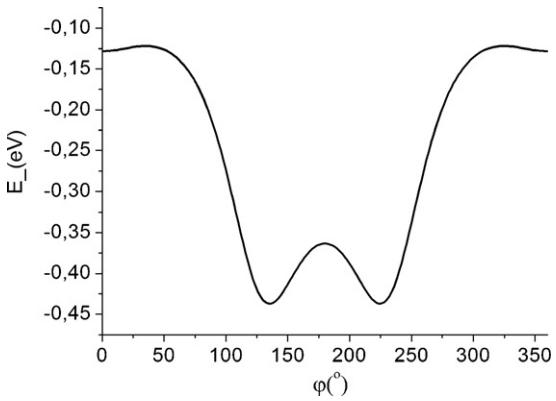

Fig. 31. The φ dependence of the ground state potential surface of the trans-$Mn(F_t)_2(F_b)_4^-$ octahedron in solids A^IMnF_4 at ρ^{sm}_ε (Eq. (60) – with the parameter set in Table 13, footnote a).

Table 14
Observed and calculated d–d transitions (in units $10^3\,cm^{-1}$) of the $MnCl_5^{2-}$ octahedron with various countercations and in solution (assignments and DFT calculations according to C_{4v} symmetry; ground state: $^5B_1$ ($e^2b_2{}^1a_1{}^1$)). The numbers in parentheses indicate the (±) variations of observed transitions.

	$\rightarrow A_1$	$\rightarrow E$[a]	$\rightarrow B_2$	C.T.	$a_{\|\|}$ (Å)	$a_\perp$ (Å)
$(NEt_4)_2$[b]	11.5	16.0	–	23.9		
$BipyH_2$; $phenH_2$	13.8(2)	17.2(3)	18.2[c]	23.9	2.583[d]	2.332(4)[d], 2.241[d]
Acetone solut.	≈13.0	17.4(2)	–	23.8(2)		
DFT	9.0	15.3	17.0	–	2.419[e]	2.292[e], 2.287[e]

[a] Strong, electronically allowed transition; no splitting due to an eventual symmetry-lowering to C_{2v} is resolved or calculated.
[b] For the pure salt (powder data), for the doped $(NEt_4)_2InCl_5$ compound (single crystal) and for the salts with $(NMe_4)^+$, $(NHMe_3)^+$ countercations (powder results).
[c] This transition is vibrationally allowed only in (⊥z) polarisation in C_{4v}, and expected to appear ||z as well, if the polyhedron symmetry is lowered to C_{2v}.
[d] Structural data [78] are for the $bipyH_2$ salt; the polyhedron structure (≅C_{2v}) only slightly deviates from C_{4v}, with bond angles between $a_{||}$ and $a_\perp$: 95.0(3.0)° and 99.4°, and in the $a_\perp$ plane: 89.2(6)°, 165.5(4.4)°.
[e] The absolute minimum is found at C_{2v} (Table 15), with a polyhedron structure very near to C_{4v}; the bond angles between $a_{||}$ and $a_\perp$ are 98.0° and 95.9°.

– out of reach of thermal energies. The derived strain parameters $A_1^s = 0.35\,eV\,Å^{-1}$ and $K_s = 3.1\,eV\,Å^{-2}$ are in full accord with those, estimated for Ti, V and Cr (Table 5).

Though a diagram similar to that in Fig. 31 was derived, using the strain formalism proposed by Ham [41] (see Fig. 11 in [9]), the approach, used here, better suffices the requirements of inorganic solid-state chemistry. It is strongly linked to the chemical reality and lends more detailed insight into the structural and energy implications of the involved aggregates of atoms in the considered solid – in particular by introducing a binding in addition to an elastic strain. The procedure, chosen here to ascertain the coupling and, specifically, the restoring energy increments, differed partly from that, applied in Sections 4 and 5.5 for $T_{2(1)g}$ ground states, because a wealth of structural data is available.

We finally shortly discuss the case of Na_2MnF_5, which crystallises in a chain structure with tetragonally elongated trans-$Mn(F_t)_4(F_b)_2^-$ octahedra ($a_{||}(F_b) = 2.109$ Å, $a_\perp(F_t) = 1.849$ Å; $a_{av} = 1.936$ Å; $\rho_\varepsilon \cong 0.30$ Å; $\sphericalangle(Mn–F_b–Mn) \cong 133°$) [69] and only two F^- ligands in bridging positions. Applying the strain model with $\varphi = \varphi_s = 0°$ and utilising the d-d spectrum with an ^5E_g ground state splitting of 12,500 cm^{-1} [73], one deduces: $A_1^s = 0.3\,eV\,Å^{-1}$, a nearly vanishing K_s contribution and a JT stabilisation energy of 0.34 eV – based otherwise on the parameter set in Table 13. The spectroscopic data from a single crystal study on $TlMnF_5{\cdot}H_2O$ with an analogous structure [74], yield a comparable result. Not unexpected (the elastic coupling via F_b is only one-dimensional), solely the binding strain has a significant influence on the extent of the tetragonal elongation.

7.3. The chloride ligand

There are only very few reports about the existence of $MnCl_6^{3-}$ complexes with the coordination number of 6, which can apparently only be stabilised by the presence of large counter cations, as in the compounds $[Co^{III}(1.2\text{-pn})_3]Mn^{III}Cl_6$ and $[Rh^{III}(C_3H_{10}N_2)_3]MnCl_6$ [75]. On the other hand, a series of salts with the $MnCl_5^{2-}$ anion has been reported, and spectroscopically characterised [76]. A break-through was the single crystal ligand field study of C. Bellitto et al., which revealed the, for a Jahn–Teller unstable species expected (see below), strongly apically elongated structure [77] – confirmed by the results of an X-ray structural analysis (Table 14) [78]. The assignment of the d–d bands (C_{4v} symmetry) in the powder spectra is straightforward; the electronically allowed (in xy) $^5B_1(e^2b_2{}^1a_1{}^1) \rightarrow {}^5E(e^1b_2{}^1a_1{}^1b_1{}^1)$ transition dominates in intensity, while the further $^5B_1 \rightarrow {}^5A_1(e^2b_2{}^1b_1{}^1)$, $^5B_2(e^2a_1{}^1b_1{}^1)$ transitions, which gain weak intensities by vibrational mechanisms, are only seen as shoulders of the former band. They are resolved and can be localised precisely in the single crystal spectra (Fig. 32) [77]. Two kinds of d–d spectra, depending on the nature of the countercation, are observed. The spectrum with the higher-energy d–d positions stems from the solid-state bipyridinium- and phenantrolinium-salts, and from the $MnCl_5^{2-}$ ion in acetone solution. We suspect, that here hydrogen-bridging and polarising solvent influences affect particularly the loosely bonded apical ligand – thus giving rise to the by 8% larger ground state splitting (Table 14). In the absence of such forces, as in the presence of spherelike and screened tetraalkylammonium countercations, also the observed energy of the $B_1 \rightarrow A_1$ transition is distinctly smaller and somewhat nearer to the DFT value in magnitude.

The reason for the mismatch between the calculated and observed transition energies is very probably the sensitivity of the position of the apical ligand toward the differing polarizing influences of the various counter cations, which are not precisely enough

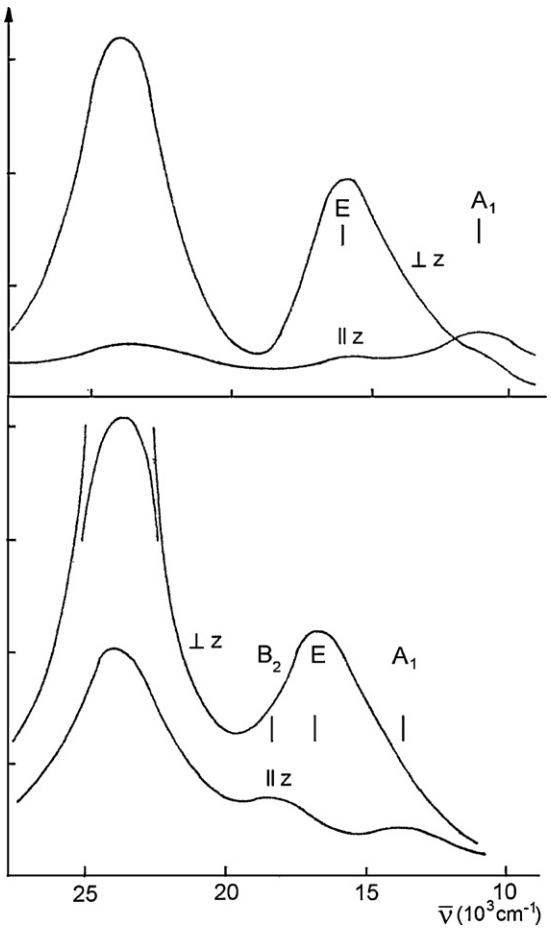

Fig. 32. Single crystal d–d spectra of Mn^{III} doped $(NEt_4)_2InCl_5$ (above) and of $(bipH_2)MnCl_5$ (below), with || and ⊥ referring to the C_4-axis of the $MnCl_5^{2-}$ square pyramid (adopted from [77]); assignment in C_{4v} ($B_1(e^2b_2{}^1a_1{}^1)$ ground state) – the band at $24 \times 10^3\,cm^{-1}$ is of charge-transfer origin.

Table 15
DFT results: The structures and energies (E_{FC}: ground state splitting) of various $[Mn^{III}Cl_{6-x}]^{(3-x)-}$-polyhedra ($x = 0, 1$). The estimated coupling and force constants for the ground state (A_1, A_2, K_ε) of the $MnCl_6^{3-}$ polyhedron are given in the last column (obtained by the fit to the calculated ρ_ε values in D_{4h}[e] and D_{4h}[c] and the experimental E_{FC}[e] energy).

		E_t (eV)	ρ_ε (Å)	a_{av} (Å)	E_{FC} (10^3 cm^{-1})	(For $MnCl_6^{3-}$)	
$MnCl_6^{3-}$	D_{4h}, elong.	−42.380	0.343[a]	2.40	6.49[b]	A_1	1.3_5 eV Å^{-1}
	D_{4h}, compr.	−42.312	0.219[a]	2.39	3.89	A_2	0.5 eV Å^{-2}
$MnCl_5^{2-}$	C_{2v} (elong.)	−35.377[c]	[d]	2.31_5	9.35	K_ε	5.0 eV Å^{-2}
	D_{3h}	−34.908	[e]	2.29_5	–		

[a] Bond lengths: 2.597 (ax), 2.300 Å (eq) and 2.262(ax), 2.451 Å (eq), respectively.
[b] The $B_{1g} \rightarrow B_{2g}$, E_g transitions are calculated at 16.25 and 16.32×10^3 cm^{-1} and observed at $\approx 17.5 \times 10^3$ cm^{-1}; the experimental energy for the $B_{1g} \rightarrow A_{1g}$ transition is 8.3×10^3 cm^{-1}.
[c] 0.031 eV below the C_{4v} optimisation.
[d] Structural data see Table 14.
[e] Bond lengths: 2.260 Å (ax); 2.315 Å (eq).

simulated by DFT (COSMO). The deviation is small for the $B_1 \rightarrow E$ band (≈5%), but considerable in the case of the $B_1 \rightarrow A_1$ transition, which might be partly caused by the before-mentioned deficiency of DFT to reproduce the $3d_{z^2}$–4s interaction exactly. Surprisingly, the single crystal study of Bellitto et al. and the DFT calculations as well indicate, that the $B_1 \rightarrow B_2$ transition is energetically positioned *above* the $B_1 \rightarrow E$ band. According to Eqs. (34) and (35) – modified from octahedral D_{4h} to C_{4v} with five-coordination – this is a quite unexpected result in view of the pretended stronger π-bonds in the equatorial plane than in the apical direction:

$$E_2(B_1 \rightarrow E) = 3e_\sigma^\perp - 2e_\pi^\perp - e_\pi^{||}$$
$$E_3(B_1 \rightarrow B_2) = 3e_\sigma^\perp - 4e_\pi^\perp \quad (61a)$$

The observation might be understood, however, when assuming that π-antibonding effects contribute only little to the Mn^{III}–Cl overlap interaction. Neglecting π-overlap completely, the AOM energies for the d–d transitions of a five-coordinated d^4 complex are as follows [30]:

$$E_1(B_1 \rightarrow A_1) = 2(1 - 3\sin^4\delta\alpha)e_\sigma^\perp - e_\sigma^{||}(\text{eff})$$
$$E_2(B_1 \rightarrow E) = 3\cos^4\delta\alpha(1 - 2\tan^2\delta\alpha)e_\sigma^\perp \quad (61b)$$
$$E_3(B_1 \rightarrow B_2) = 3\cos^4\delta\alpha e_\sigma^\perp$$

if the AOM consideration is refined by taking the deviation of the apical-to-equatorial bond angle from 90° in C_{4v}, $\delta\alpha$, into account. $e_\sigma^{||}(\text{eff})$ includes the (here rather large) d–s interaction energy – see Eqs. (32)–(35). The energy difference $E_3 - E_2$, $3/2(\sin^2 2\delta\alpha)e_\sigma^\perp$, results from the canting between the d_{xz} and d_{yz} metal orbitals and the π-orbitals of the equatorial ligands, which introduces σ-overlap components and leads to an energy relation $E_3 > E_2$, as observed. In a rough estimate one obtains (with $\delta\alpha = 8°$ and the transition energies in Table 14) AOM parameters: $e_\sigma^\perp \cong 6200$ and $e_\sigma^{||}(\text{eff}) = -1400$ cm^{-1} for the bipyH_2 or phenH_2 compounds, when neglecting π-overlap effects. The effective quantity $e_\sigma^{||}(\text{eff})$ is negative and indicates $e_\sigma^{||}/E_{ds}$ ratios < 1 – a quite common situation for polyhedron structures near to square planar [30].

We think, that the lack of π-energy contributions is caused by the large deviation of the five-coordinate complex from octahedral. While this pronounced distortion meets the strong tendency of the σ-antibonding $E \otimes \varepsilon$ vibronic effects in the ground state, the π-overlap – weak anyhow for the chloride ligand – rather opposes a distortion, if it exceeds the limit favoured by the $T \otimes \varepsilon$ coupling (minimum of the adiabatic potential curve at a much less pronounced radial distortion ρ_ε). In such cases, even vanishing energy effects for the 3d(M^{III})–3s, p(Cl^-) π-overlap may happen. We finally note that the reversed sequence of the π-antibonding d_{xy} and d_{xz}/d_{xy} energies is a more general problem, and has been particularly discussed for planar low-spin d^8 complexes. In these cases, for example [79], differential interelectronic d–d repulsion effects have been invoked in a rather sophisticated explanation.

The correct vibronic coupling treatment for a d^4-cation in five-coordination should be based on a D_{3h}-polyhedron symmetry, with an $^5A_1'(e''^2e'^2)$ ground state and a closely neighboured $^5E'(e''^2e'^1a_1'^1)$ excited state, giving rise to an $A_1' \otimes \varepsilon \otimes E'$ pseudo-JT interaction with considerable radial and angular distortions. The distortion pathway, originating from D_{3h}, possesses C_{2v}-symmetry; the minima on the adiabatic potential surface are usually located very near to the C_{4v} structure, which occur as accidental points on the ground state potential surface [80]. The DFT calculations on $MnCl_5^{2-}$ show, that – due to this vibronic interaction – the trigonal bipyramid is less stable than the very-near-to-C_{4v} polyhedron by 0.53 eV (Tables 14 (footnote e) and 15). The square-pyramid is strongly apically elongated, which is equally expected from the simple (though not strictly symmetry-conform) reasoning of a $Mn^{III}Cl_6^{3-}$ parent complex, in which the axial bonds are considerably weakened due to $E_g \otimes \varepsilon_g$ coupling – by even loosing one ligand completely.

We finally return to the above mentioned $MnCl_6^{3-}$ salts. d-d spectroscopic studies [75] report a weak band at 8300 cm^{-1} – obviously corresponding to the octahedral ^5E_g ground state splitting and found at a by 1800 cm^{-1} larger energy than obtained by DFT – and a shoulder at ≈17,500 cm^{-1} on the slope of a strong and broad band, appearing at 22,400 cm^{-1}. The shoulder is assigned to the $^5B_{1g}(^5E_g) \rightarrow {}^5B_{2g}$, $^5E_g(^5T_{2g})$ transitions, which are calculated at 16250 and 16,320 cm^{-1}, respectively – by ≈1000 cm^{-1} lower than the experimental value (Table 15). The DFT-calculated, nearly vanishing splitting of the excited $^5T_{2g}$ state confirms the absence of significant π-bonding even for polyhedra with less pronounced deviations from O_h than the $MnCl_5^{2-}$ polyhedron and indicates a very small V_ε coupling constant. As discussed above, the large distortion, imposed on the octahedron by the $E_g \otimes \varepsilon_g$ coupling, opposes the tendency of a $T_g \otimes \varepsilon_g$ interaction, which aims at a considerably smaller ρ value. The ligand field strength is $\Delta \cong 13.3 \times 10^3$ cm^{-1} – a reasonable value in comparison to those of the corresponding Ti^{III}, V^{III} and Cr^{III} complexes (Tables 3, 7 and 8) with Δ-energies of $12.5(5) \times 10^3$ cm^{-1}. In Table 15 the vibronic parameters for the ^5E_g ground state of the $Mn(Cl_t)_6^{3-}$ polyhedron are listed, as derived from DFT by a best fit to the ρ_ε^{em}, ρ_ε^{cm} distortion parameters and to the experimental E_{FC}^e energy. Their magnitudes, in comparison with those for the corresponding fluoride complexes, follow the data for the V^{III} and Ti^{III} polyhedra.

8. The ligand-to-metal charge transfer in MCl_6^{3-} polyhedra (M^{III}: Ti–Co)

We have still to comment on the strong high energy bands at 23.9 and at ≅22.4×10^3 cm^{-1}, which are observed in all spectra of the $MnCl_5^{3-}$ polyhedron [76] and in the two spectra of the $MnCl_6^{3-}$ complex [75], respectively, and which have definitely to be assigned to a chloride-to-manganese(III) charge transfer. The

Table 16a
Optical electronegativities χ_{opt} of trivalent M^{III} cations (M^{III} = Ti–Co; high-spin) in complexes MCl_6^{3-}, embedded in an elpasolite matrix, as estimated from the onset[a] of the intensity increase toward the charge-transfer region or as calculated from the position of the first parity- and spin-allowed electron-transfer band (in $10^3\,cm^{-1}$); the spin correction (SC) due to the change in the ligand field by the excitation [85] is also given.[b] E′(CT) denotes the corrected (see Eq. (62)) excitation energy. The E′(CT) energies in parentheses refer to the lowest-energy spin-allowed $t_{1u}{}^n \rightarrow t_{2g}{}^*$ transition, as calculated by DFT (spin-unrestricted, in O_h; for Mn^{III} in D_{4h}[e]), but also corrected by the empirical SC energy.

M^{III}	n	Onset at[a]	SC for d^n	$\rightarrow d^{n+1}$ [b]	E′(CT)	$\chi_{opt}(M^{III})$[c]	r (Å)[d]
Ti	1	21	−14/3 B	≈−2.5	$27._5$ (36)	2.1 (1.8)	0.67_5
V	2	20	−28/3 B	−5	29 (30)	2.0_5 (2.0)	0.64_5
Cr	3	27	+14 B	$+7._5$	$23._5$ (29)	2.2 (2.0_5)	0.61_5
Mn	4	$22._5$[e]	+49/3 B	$+9._5$	13 ($17._5$)	2.5_5 (2.4)	0.64
Fe	5	25[e]	+56/3 B	$+11._5$	$13._5$ (8)	2.5_5 (2.7_5)	0.64
Co	6	[11][f]	+14 B	+9	[6][f] (3)	[2.8] (2.9)	0.60_5

[a] Estimated maximum E(CT) of the lowest-energy electron-transfer band at ≈ onset energy ⊕ $4 \times 10^3\,cm^{-1}$ (assuming a width of the charge-transfer band of ≈$8000\,cm^{-1}$).
[b] Energies calculated with the nephelauxetic ratio $B_{te}/B_0 = 0.6$ (see Tables 7 and 8) and using the free cation B_0 values 860, 920, 970, 1020 and $1070\,cm^{-1}$ for V^{III} to Co^{III} (after Ref. [49]), respectively, and $B_0 \approx 800\,cm^{-1}$ (estimated) for Ti^{III}.
[c] Utilising Eq. (62), with $\chi_{opt}(Cl^-) = 3.0$.
[d] Effective ionic radii for the metal ions, from M^{III}–F bond lengths, with $r(F^-) = 1.29$ Å; values are nearly identical with those of Shannon and Prewitt [86].
[e] Location of lowest parity-allowed $t_{1u}{}^n \rightarrow t_{2g}{}^*$ charge-transfer transition ($MnCl_6^{3-}$ and $FeCl_6^{3-}$ – see text).
[f] Energies in brackets derived with the assumption of $\chi_{opt} = 2.8$ for Co^{III} (see text).

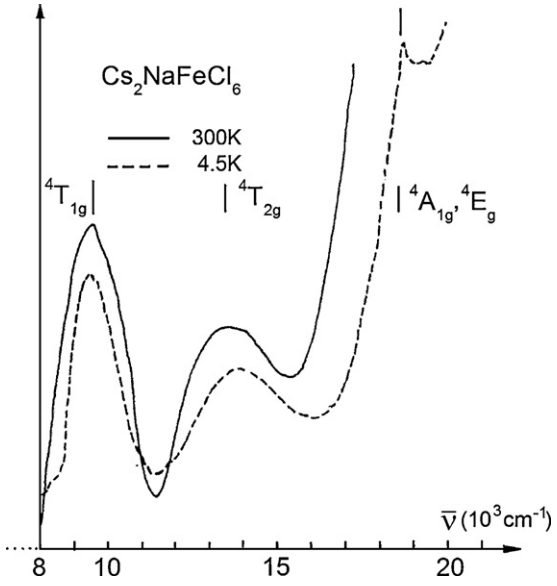

Fig. 33. Powder reflexion spectra of the $FeCl_6^{3-}$ octahedron in a cubic elpasolite matrix ($^6A_{1g}$ ground state); assignment with $\Delta = 10.65$ and $B = 0.62 \times 10^3\,cm^{-1}$, $C/B = 4.0$.

origin of the lowest energy spin- and parity-allowed transition of this kind is, in cases as those considered here, the excitation from an (approximately) non-bonding $t_{1u}{}^n$ MO into an empty or partially occupied antibonding $t_{2g}{}^*$ MO. The former is largely ligand-centred, while the latter is predominantly localised at the metal ion. One recognises the onset of the charge-transfer absorption in the spectra of the $Ti(Cl_t)_6^{3-}$ polyhedron already in the visible region, which thereafter covers the blue-violet spectroscopic range and accordingly imparts a greenish-yellow colour to the complex (Fig. 11; Table 16a). Similarly, at about $20 \times 10^3\,cm^{-1}$ occurs the intensity increase in the case of $V(Cl_t)_6^{3-}$, leaving as the colour-determining feature the narrow minimum at $\cong 21 \times 10^3\,cm^{-1}$ – the origin of the blue-violet hue of the respective compounds (Fig. 20). The dark-violet-colour of the $Cr(Cl_t)_6^{3-}$ salts results from d–d transitions exclusively, because here the charge-transfer region starts only at $27 \times 10^3\,cm^{-1}$ (Fig. 23). It is interesting to further look at the d^5 case of $Fe(Cl_t)_6^{3-}$. Fig. 33 shows the 298 and 5 K reflexion spectrum of the cubic elpasolite $Cs_2NaFeCl_6$ ($a = 10.32_5$ Å); the given ligand field parameters are evaluated following a procedure described elsewhere [81]. The increase from the very weak spin-forbidden sextet–quartet d–d transitions toward the high intensity charge-transfer region is particularly pronounced here, and occurs already around $17.0 \times 10^3\,cm^{-1}$. The colour-determining minimum appears at ≈16,000 cm^{-1}, in the orange spectroscopic region. The UV electron transfer spectrum of the Fe^{3+}-doped alpasolite Cs_2NaYCl_6 shows the first parity- and spin-allowed $t_{1u}{}^n \rightarrow t_{2g}{}^*$ charge-transfer band at $\cong 25 \times 10^3\,cm^{-1}$ [82]. The onset starts already at a rather low energy in the case of the $FeCl_6^{3-}$ octahedron, because it refers here to spin-forbidden and not to spin-allowed d–d transitions with a distinctly larger intensity, as in the case of the $M^{III}Cl_6^{3-}$ complexes considered previously.

The $MnCl_5^{2-}$ salts are green according to the narrow minimum between the d–d band at ≈20 and the charge transfer transition at $24 \times 10^3\,cm^{-1}$. The relative instability of the $MnCl_6^{3-}$ octahedron with respect to $MnCl_5^{2-}$ is documented by the red shift (by ≈$1500\,cm^{-1}$) of the ligand-to-metal charge-transfer; this is opposed to the expectation [83] when increasing the coordination number. The excited $^5B_{1g} \rightarrow {}^5B_{2g}$, ^5E_g transitions occur in the region of the $t_{1u}{}^n \rightarrow t_{2g}{}^*$ band (Table 15). Hence, only the spectroscopic region below $17{,}000\,cm^{-1}$ is transparent for the visible light, and the compounds are accordingly reddish at lower and brown at room temperature [75], due to the increase of the band-width with temperature.

Following a proposal of Jørgensen to correlate the energy of the first Laporte-allowed CT band with the electronegativity difference between the ligand and the metal ion, the following semiempirical relation was formulated [10,84]:

$$E'(\mathrm{CT};\ \mathrm{in}\ 10^3\,cm^{-1}) \cong 30\{\chi_{opt}(\mathrm{anion}) - \chi_{opt}(\mathrm{cation})\} \qquad (62)$$

where χ_{opt} are *optical electronegativities*, in distinction to other (though closely related) electronegativity scales. In order to obtain E'(CT) from the experimental charge transfer energy E(CT), a spin-correction (SC) has to be applied, which considers the change of the interelectronic repulsion (via the Racah parameter B), when exciting one electron from $t_{1u}{}^n$ into $t_{2g}{}^*$. Referring to the literature for a summarising and more basic consideration [85], we present in Table 16a these spin-corrections and the calculated optical electronegativities of the cations Ti^{III} to Co^{III} (see also Table 16b). In the cases of Ti^{III} to Cr^{III} the onset to the charge-transfer region served as the basis for the estimation of the optical electronegativity, while for Fe^{III} and Mn^{III} the experimental parity-allowed $t_{1u}{}^n \rightarrow t_{2g}{}^*$ transition energies could be directly used for the derivation of χ_{opt}. Though the numbers obtained for the former complexes are only rough estimates, there is clear evidence for an increase of $\chi(M^{III})$ with increasing nuclear charge of the cation, mirroring a stronger tendency to capture an electron from the ligands. Possibly, there is a discontinuous ascent from the $d^{1,2,3}$ – to the $d^{4,5,6}$ – electron config-

Table 16b
Optical electronegativities of complexes $M^{III}F_6^{3-}$ in elpasolites (see Table 16a), as calculated by Eq. (62) with $\chi_{opt}(F^-) = 3.9$ and after having applied the necessary correction due to B and Δ.

M^{III}	E (CT) [49]	Correct. [85]	E′(CT)	χ_{opt} (M^{III})	R (Å)[a]
Ni ($t_{2g}{}^6e_g{}^1$)	32.0	$\Delta - 35/3\ B$[b]	28.0	2.9_7	0.59
Cu ($t_{2g}{}^6e_g{}^2$)	29.5	$\Delta + 14/3\ B$[b]	11.7	3.5	0.62

[a] Effective ionic radii with $r(F^-) = 1.29$ Å (Tables 18a and 19); reported values [86] are for Ni^{III}: 0.56 Å (low-spin) and 0.60 Å (high-spin).
[b] With $B = 0.78$, $\Delta = 13.1$ (Ni^{III}) and ≈0.7, $14.5 \times 10^3\,cm^{-1}$ (Cu^{III}) ($B_0 = 1.12$ and $\cong 1.2 \times 10^3\,cm^{-1}$ [49]).

urations by about 0.4, due to the occupation of e_g^* MOs. We have also estimated the transition energies from the – with respect to the metal centre non-bonding – t_{1u}^n MO to the π-antibonding t_{2g}^* MO by DFT. Though deficient with respect to interelectronic repulsion, the sequence of the deduced E'(CT) energies roughly follows the one of the experimental estimations, with a similar gradation from Ti^{III} to Co^{III}. In the latter case, the suggested optical electronegativity of 2.8 – the small ionic radius (Table 16a) demands a high ionisation energy – predicts the $t_{1u}^n \rightarrow t_{2g}^*$ CT band to occur around 15,000 cm^{-1}. Apparently, charge transfer bands completely cover the visible region [87], and indicate an only very low energy barrier for the $Co^{3+} \rightarrow Co^{2+}$ reduction. To our best knowledge, high-spin Co^{III} complexes with chloride as the ligand are indeed not reported. Tentatively, the following decomposition redox process may be formulated, with the very stable tetrahedral $Co^{II}Cl_4^{2-}$ tetrahedron as the final product:

$$\underset{-39.08\,eV}{Co^{III}Cl_6^{3-}} \rightarrow \underset{-29.54\,eV}{Co^{II}Cl_4^{2-}} + \underset{-7.14\,eV}{Cl^-} + \underset{-1.86\,eV}{\tfrac{1}{2}\,Cl_2} - \Delta H \qquad (63)$$

DFT predicts a positive and rather large enthalpy of 0.54 eV for this reaction (and hence a somewhat smaller Gibbs energy, because entropy clearly favours the right side of the equation). Presumably, the deficiency of DFT to properly account for the involved change of interelectronic repulsion as well as uncertainties in the magnitudes of the solvent energy, when comparing complexes with different charge, are responsible for the significant mismatch.

The dependence of the hue of a solid on the, here, M–L binding properties in an $M^{III}(3d)L_6$ colour centre – which becomes apparent in the energy positions of the ligand field bands in the d–d spectrum – is a fascinating aspect of application and aesthetics in an otherwise rather formal and theoretical field of research. It is the merit of O. Schmitz-DuMont to have first systematically studied the interrelation between the colour and the constitution of solids with 3d-cations [88], which also implies the possibility to steer the hue by the aimed interference into the bonding characteristics of the colour-centre in the host solid. This aspect can be extended toward Jahn–Teller systems, where the extent of a vibronically induced polyhedron distortion can be equally controlled via the properties of the matrix. For example, if in the nearly white host $NH_4Fe^{III}P_2O_7$ manganese(III) is doped into the Fe^{III} position, a blue colour appears, due to a sharp minimum between the $^2B_{1g}$ (^2E_g) → $^2B_{2g}$, ^2E_g ($^2T_{2g}$) transitions and the charge-transfer region. The full substitution by Mn^{III} raises the local JT-distortion ρ_ε of the $Mn^{III}O_6$-octahedra, caused by a decrease of the force constant. The latter effect is the consequence of the enhancement of the cooperative-elastic interactions between the distorted octahedra. The corresponding increase of the ground state splitting 4 E_{JT} and accordingly a blue-shift of the absorption bands now generates two minima in the visible region and a reddish-violet hue of the compound (see [99]). One learns, that also an aimed variation of the JT-forces offers the possibility to steer the hue.

9. $Co^{III}X_6^{3-}$ polyhedra

9.1. The stable high-spin state

Concerning the procedure for the evaluation of the vibronic parameters from the structural data and energies derived from DFT we refer to Ti^{III} (Section 3.2). The electron configuration is high-spin d^6 – this is, what is observed [89] for CoF_6^{3-} and what should hold for hypothetical $CoCl_5^{2-}$ and $CoCl_6^{3-}$ octahedra as well – with one electron exceeding the half-filled d-shell; the treatment is hence analogous to that for Ti^{III}, as long as only the spin-quintet states are considered. With ρ_ε^{cm}, ρ_ε^{em} and the Franck–Condon transition within the ground state for D_{4h}[c], all data obtained from DFT, the vibronic constants V_ε and K_ε in Table 17 are derived. They are, in the fluoride case, distinctly – by ≈20% – smaller than those for Ti^{III} (Table 2); the instability of the hypothetical $CoCl_6^{3-}$ species is documented by very low values of the linear coupling parameter and of the force constant, which are half and only about 40% in magnitude, respectively, of the quantities derived for $TiCl_6^{3-}$. The calculated small JT energy of 210 cm^{-1} for the $Co(F_t)_6^{3-}$ octahedron, corresponding to a bond length anisotropy of only 0.07 Å, suggests a dynamic bond length equilibration at 298 K. We have also considered the extremum points corresponding to the possible $T_{2g} \otimes \tau_{2g}$ and $T_{2g} \otimes (\varepsilon_g + \tau_{2g})$ vibronic interactions. They are even smaller in relation to the E_{JT}^c energy for the $T_{2g} \otimes \varepsilon_g$ coupling than observed in the d^1 case of Ti^{III}; again, the higher order $\varepsilon_g \otimes \tau_{2g}$ coupling term W is vanishing. Accordingly, we refrain from reporting numerical data, but just cite the respective derived JT energies and the estimated V_τ and K_τ parameter values in footnote d of Table 17.

Fig. 34 shows the d–d spectrum of an elpasolitic fluoride compound with the rhombohedral Cs_2NaCrF_6 structure (Fig. 26), exhibiting a splitting of the excited ^5E_g state of 2500 cm^{-1}, in agreement with the value reported by Cotton and Meyers in 1960 for the elpasolite K_2NaCoF_6 [88]. DFT reproduces the splitting energy rather well, but the split band positions only within about 8% (Table 17); larger shortcomings due to an erroneous account of the $3d_{z^2}$–4s interaction are not recognisable in this case. We further use the experimental energies and the DFT-optimised structural distortions in the excited $^5B_{1g}$ and $^5A_{1g}$ states – in analogy to the d^1 case of Ti^{III} – for the evaluation of A_1, A_2 and K_ε'. As for the ground

Table 17
Structural and energy DFT results for the $^5T_{2g}$ ground state ($T_{2g} \otimes \varepsilon_g$ coupling) – above – and the ^5E_g excited state of CoX_6 complexes (X = F_t^-, Cl_t^-, F_b^-) – below – together with the derived coupling constants; the cubic ligand field strength is also listed. For the DFT-calculations in D_{3d} and D_{2h}* see footnote d.

	ρ_ε^{cm} (Å)	ρ_ε^{em} (Å)	a_{av} (Å)	E ($B_{2g} \rightarrow E_g$)	E_{JT}[c] (eV)	V_ε (eV Å^{-1})	K_ε (eV Å^{-2})
F_t^-	0.081[a]	0.038[b]	1.927[c]	0.078 eV	0.026[d]	0.65[d]	8.1[d]
Cl_t^-	0.068[a]	0.032[b]	2.373	0.015 eV	0.005	0.15	2.2

	ρ'^{cm}_ε (Å)	ρ'^{em}_ε (Å)	E ($B_{2g} \rightarrow B_{1g}$)[e]	E ($B_{2g} \rightarrow A_{1g}$)[e]	Δ[f] (10^3 cm^{-1})	A_1 (eV Å^{-1})	K_ε' (eV Å^{-2})	A_2
F_t^-	0.215	0.328	1.628(148) eV	1.910(179) eV	12.7	2.00	7.7	0.8
F_b	–	–	(1.38) eV	(1.82) eV	12.3	≅2.6[g]	≈0.9_2[g]	≅0.9_5[g]

[a] 1.950 Å (4×), 1.880 Å (2×) and 2.400 Å (4×), 2.341 Å (2×), respectively.
[b] 1.914 Å (4×), 1.947 Å (2×) and 2.364 Å (4×), 2.392 Å (2×), respectively; the ratio $\rho_\varepsilon^{cm}/\rho_\varepsilon^{em}$ is approximately 2, demanding $L_\varepsilon \cong 0$.
[c] Experimental: 1.890(5) Å [90b]; in CoF_3: 1.895 Å [90a].
[d] The estimated E_{JT}[c] (D_{3d}) and E_{JT}* (D_{2h}*) energies are 0.003 and 0.011 eV, respectively (see text), with $V_\tau = 0.2_5(1)$ eV Å^{-1} and $K_\tau \approx 3.5$ eV Å^{-2}.
[e] Experimental energies in parentheses.
[f] Calculated from experiment, but taking the DFT-ground state splitting due to $T_{2g} \otimes \varepsilon_g$ coupling into account.
[g] Estimated magnitudes for A_1 and A_2, K_ε' (enhancement by 30% and 20% in respect to the values of the F_t ligand, respectively – in analogy to Ti^{III}; see Tables 2 and 3) – assuming the same increase in the case of V_ε (0.8_5 eV Å^{-1}) and K_ε (9.7 eV Å^{-2}), the ground state radial distortion and Jahn–Teller stabilisation energy come out to be of the magnitude: $\rho_\varepsilon^{cm} \approx 0.08_8$ Å ; $E_{JT} \approx 0.03_7$ eV, respectively.

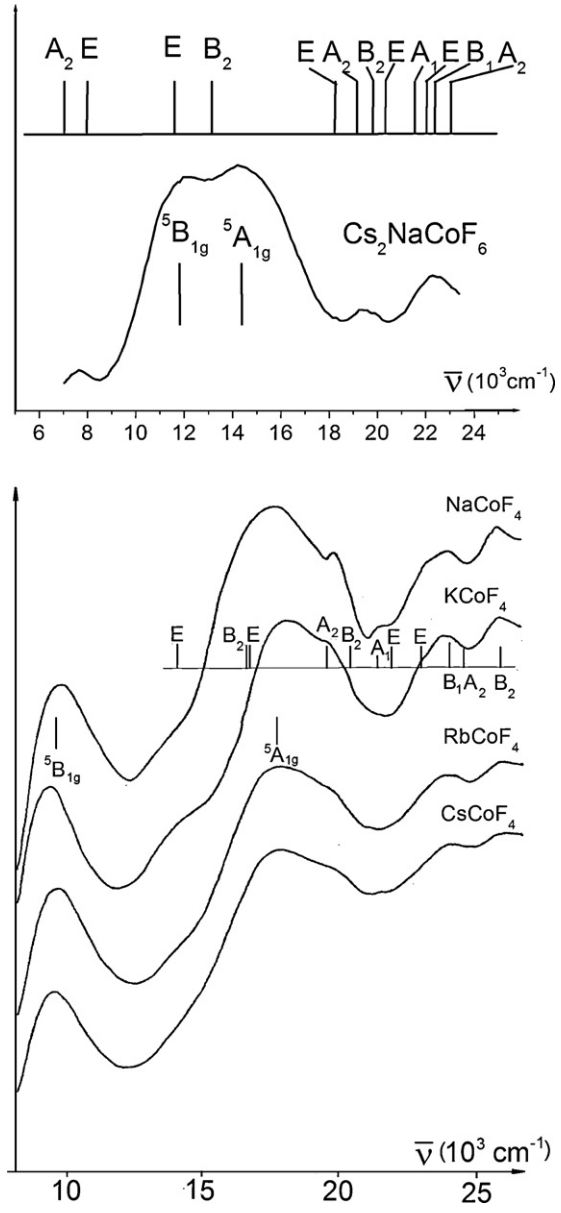

Fig. 34. The d–d spectra (T = 298 K) of hexacoordinated Co^{III} in the rhombohedral elpasolite Cs_2NaCoF_6 and in compounds $A^ICo^{III}F_4$ with $TlAlF_4$-type structures. The assignment and band fitting was performed in D_{4h}, compressed ($^5B_{2g}$ ground state), on the basis of the parameters: Δ = 12.7 and 12.0; δ_1' = 0.62_5 and 2.0; δ_2 = 0.21 and 0.8×10^3 cm^{-1} for the former compound and the latter solids, respectively. A global B was chosen as 0.825×10^3 cm^{-1} and C/B as 4.3. The calculated band positions of the spin-forbidden quintet-triplet transitions in D_{4h}[c] (see the ligand field matrices in the supplementary material B1) are indicated above in the figures (the respective octahedral parent terms are: ^3E_g (→ $^3A_{1g}$, $^3B_{1g}$); $^3T_{2g}$ (→ $^3B_{2g}$, ^3E_g); $^3T_{1g}$ (→ $^3A_{2g}$, ^3E_g)).

state, the derived coupling constants are smaller than for the TiF_6^{3-} complex (Table 3).

Analogous to the elpasolites, the $Co(F_b)_6$ octahedra in the VF_3-type structure of CoF_3 are regular at ambient temperature with a nearly identical bond length (1.895 Å) [90a]. The excited state splitting in the d–d spectrum is 0.44 eV [90b], from which – following the procedure used in the Ti^{III} case – the vibronic constants listed in Table 17 are estimated. The suggested distortion as well as the JT energy are close to the values for TiF_3 (Table 3) and also indicate dynamic behaviour, at least at 298 K. Low-temperature studies are not reported.

9.2. The strain in solids A^ICoF_4

We proceed with the discussion of the structures and d–d spectra [31,32] of various compounds $A^ICo^{III}F_4$ (Fig. 34) with a $TlAlF_4$-related structure and constituting trans-$Co(F_t)_2(F_b)_4^-$ species. Structural data are known for $CsCoF_4$ [91] (Table 4). Besides the latter solid, bond length data are only reported for $LiCoF_4$ [92], with a strongly distorted $TlAlF_4$-structure due to the small Li^+ cation, but a radial distortion of similar magnitude. The elastic strain constant K_s and the linear coupling contribution V_ε^s arising from the substitution of the four equatorial F_t by F_b ligands are derived (Table 5) by utilising the distortions of the $Co(F_t)_6^{3-}$ (from DFT), of the $Co(F_t)_2(F_b)_4^-$ (in $CsCoF_4$) and of the $Fe(F_t)_2(F_b)_4^-$ (in $AFeF_4$ solids) octahedra (Tables 4 and 17), analogous to the d^1 case via Eqs. (39)–(41). The structural strain enhances ρ_ε^{cm} from 0.081 to 0.137 Å; the binding strain causes the further increase to 0.181 Å. From the deduced JT stabilisation energy a ground state splitting of (after the Δ_{ec} correction) $3\delta_2 \cong 0.29$ eV is derived. The excited ^5E_g state splitting, with transitions at 9.5(2) and $17.7(2) \times 10^3$ cm^{-1}, allows one to calculate A_1^s, utilising Eq. (40) with $\varphi = \varphi_s = 180°$ and at $\rho_\varepsilon^{sm} = 0.181$ Å, again after having applied the Δ_{ec} correction. Though the vibronic addition A_1^s is rather large in comparison to that in the d^1 case (Table 5), it is still of a reasonable magnitude in view of particularly the broad-band character of the $^5B_{2g} \rightarrow {}^5A_{1g}$ ligand field transitions, which handicaps an exact energy reading.

The $V_\varepsilon^s/V_\varepsilon$ and $A_1{}^s/A_1$ ratios, in the case of Ti^{III}, V^{III}, Co^{III} (Table 5), are 0.25(7) and 0.26(6), respectively – an overall description of the vibronic landscape, which makes sense. Also the coarsely estimated ratios for trans- and cis-$Cr(F_t)_2(F_b)_4^-$, with non-degenerate ground states, are still of acceptable magnitude. The derived ligand field parameter for the trans $Co(F_t)_2(F_b)_4^-$ octahedron (12.0×10^3 cm^{-1}) is also of reasonable magnitude.

9.3. High-spin versus low-spin

The d–d spectra show distinct weak absorption features in addition to the dominating $^5B_{2g} \rightarrow {}^5B_{1g}$, $^5A_{1g}$ bands, which are readily assigned to spin-forbidden quintet–triplet transitions (Fig. 34). Most of these appear in the spectroscopic range between 18 and 26×10^3 cm^{-1} as transitions to the split states of the octahedral parent states $_a{}^3E_g$, $_{b,c}{}^3T_{2g}$ and $_{b,c}{}^3T_{1g}$ and are (nearly) Δ independent, hence involving the Racah parameters B_{tt} and C_{tt}. Though not completely resolved – here the spectrum of $NaCoF_4$ shows the best resolution – they can be fitted rather well with the Δ and δ_1' energies taken from the observed quintet-quintet transitions and the δ_2 value from DFT and – for the $ACoF_4$ solids – from Table 5. A B parameter of 825 cm^{-1} and a C/B ratio of 4.3 were the reasonable choice for the spectroscopic fit. The respective nephelauxetic ratio (≅0.77) is near to those involving B_{te} for V^{III} and Cr^{III}, but noticeably smaller than the B_{tt} value of Cr^{III} (Table 9). The higher intensity of the spin-forbidden transitions in the $ACoF_4$ than in the elpasolite spectra is very likely due to the presence of bridging ligands, mediating spin–spin interactions between neighboured Co^{III} cations. Such a mechanism, in the Mn^{III} case, gives rise to a dramatic intensity increase of some sextet–quartet transitions in the presence of F_b ligands (Fig. 29) [29]. For the ligand field calculation we have used the matrices given by Perumareddi for a D_{4h} symmetry [68], but, as before mentioned, modified [46] according to the nomenclature used here (see supplementary material Appendix B.1). The weak absorption at 8000 cm^{-1} in the spectrum of Cs_2NaCoF_6 seems to originate from that $_a{}^3T_{1g}$ term, which is of the lowest energy from all intermediate $t_{2g}{}^5e_g{}^1$ spin states present. The eventually stabilised low-spin $_a{}^1A_{1g}(t_{2g}{}^6)$ ground state (see the $^1A_{1g}$ matrix in the supplementary material Appendix B.1) is – in first order – calculated at an energy: $\delta E = 5B + 8C - 2\Delta + 2\delta_2$ above the

real $^5B_{2g}$ ground state, corresponding to 7.5_5 and $10.1 \times 10^3\,cm^{-1}$ for the $Co(F_t)_6^{3-}$ and the trans-$Co(F_t)_2(F_b)_4^-$ octahedron, respectively, if the ligand field parameters in Fig. 34 are used. Including configuration interaction, these energies are considerably reduced to 4.8 and $7.2 \times 10^3\,cm^{-1}$. Nevertheless, high-spin Co^{III} is clearly favoured in the interplay between Δ and interelectronic repulsion in fluoride complexes. DFT is not helpful in the calculation because of its repeatedly mentioned deficiency to reproduce interelectronic repulsion energies with the necessary precision. The high-spin/low-spin separation energy in the d^7 case (see the following section) is of comparable magnitude to that for d^6, if only the (Δ, B, C) increments are considered (Eq. (64)); in that case, it is the additional JT contribution by the $E_g \otimes \varepsilon_g$ vibronic coupling, which finally stabilises a low-spin ground state.

10. The NiF_6^{3-} polyhedron

10.1. High-spin or low-spin ground state?

Only few elpasolitic solids of the constitution A'_2ANiF_6 have been prepared and structurally characterised (A′, A: Cs, K; Rb, K; Rb, Na; Cs, Na) [93]. They crystallise in cubic structures at 298 K, with the exception of Cs_2NaNiF_6, which is a hexagonal elpasolite of the Cs_2NaCrF_6-type (Fig. 26). The d–d spectrum of K_3NiF_6 was interpreted by Allen and Warren [49], who presented evidence that the band appearing around 6500 cm^{-1} has to be ascribed to the transition within the Jahn–Teller-split ^2E_g ground state of low-spin Ni^{III}. The analysis of the d–d spectra of various solids $A_2'ANiF_6$ and, particularly, their EPR spectra and the temperature dependence of the g-values [94] have confirmed this presumption and further suggested that the spin–doublet–quartet separation (between the potential energy minima of the $_a{}^2A_{1g}$ ground state and the lowest excited spin-quartet $_a{}^4A_{2g}$ state – in D_{4h}, elongated) is very small [1]. The powder reflection d–d spectrum of the elpasolitic solid Cs_2KNiF_6 exhibits four, in particular at 5 K well resolved, bands (Fig. 35). From the underlying eight Laporte-forbidden spin-allowed transitions, expected in the energy region up to $\cong 26 \times 10^3\,cm^{-1}$, only five are also vibronically allowed, via the (octahedral) τ_{1u} vibration; these are the $_a{}^2A_{1g} \rightarrow {}_a{}^2B_{1g}$, $_{a,b,c}{}^2E_g$ and $_b{}^2A_{1g}$ transitions, from which the last one is presumably the shoulder at $\approx 25 \times 10^3\,cm^{-1}$ – appearing, where the intensity starts to rise toward the charge-transfer region. We have fitted the spectra, utilising the matrices for a d^7 cation in a tetragonally elongated octahedral ligand field with respect to a ^2E_g ($t_{2g}{}^6e_g{}^1$) ground state in O_h (see supplementary material B.2) [95,46], for obtaining reliable values for Δ, B and δ_1 ($= 1/2(A_1 + A_2\rho_\varepsilon^{em})\rho_\varepsilon^{em}$); C/B was arbitrarily set to 4.0, while δ_2 ($= 1/2V_\varepsilon\rho_\varepsilon^{em}$) was adopted from a fit to the orbital contributions to the g-values (vide infra). The essential features in the absorption spectra are rather well reproduced with the parameter set given in the caption of Fig. 35. We remark, that the band positions are not very sensitive to smaller alterations of Δ, B and C/B, as long as $\delta_{2,4}^{eff}$ (Fig. 36) remains at the same energy. The chosen global B parameter is essentially B_{te} – yielding a nephelauxetic ratio ($B_0 = 1120\,cm^{-1}$ [49]) of 0.70, perceptibly reduced with respect to the values for V^{III} and Cr^{III} (0.75_5). The (vertical) quartet–doublet separation is, in first order – as one can easily reproduce from the diagonal energies in the respective matrices (see the supplementary material B.2):

$$\delta_{2,4} = E(^4A_{2g} - e_g^4b_{2g}^1a_{1g}^1b_{1g}^1) - E(^2A_{1g} - e_g^4b_{2g}^2a_{1E}^1)$$
$$= \Delta - 4(B + C) + 2(\delta_1 - \delta_2) \quad (64)$$

and turns out to be of the magnitude of $\approx 280\,cm^{-1}$. Configuration interaction is considerable and brings this energy to $\cong 770\,cm^{-1}$ (Fig. 35). LS coupling further raises the energy of the $_a{}^4A_{2g}$ state with respect to the $_a{}^2A_{1g}$ ground state (Fig. 36).

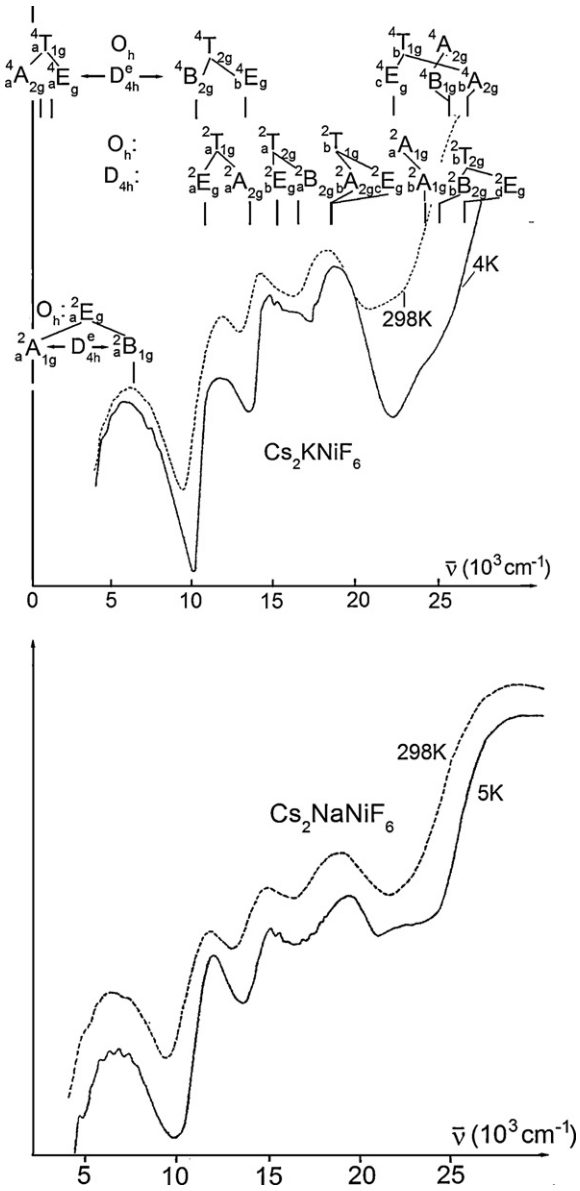

Fig. 35. The d–d spectrum of Cs_2KNiF_6 (after [94]); the band assignment (see text) and fitting procedure was performed with the parameters $\delta_1 = 1700$ and $\delta_2 = 320\,cm^{-1}$, deduced from the energy of the $_a{}^2A_{1g} \rightarrow {}_a{}^2B_{1g}$ transition and from EPR spectroscopy, respectively, with $C/B = 4.0$ and using Δ and B ($=B_{te}$) as best fit parameters ($\Rightarrow$ 13.1 and $0.78 \times 10^3\,cm^{-1}$, respectively). The spectrum of the hexagonal elpasolite Cs_2NaNiF_6, with a low-spin and a high-spin site side by side (see text), is shown below.

Before discussing the energies within the $_a{}^2E_g$–$_a{}^4T_{1g}$ split state manifold in the ground state region in greater detail, we report about the DFT results for the NiF_6^{3-} polyhedron in the low-spin and high-spin state, respectively; in both cases, vibronic coupling leads to tetragonally elongated species. The vibronic parameters A_1, A_2 and K_ε for low-spin NiF_6^{3-} were derived, using the experimental Franck–Condon transition E_{FC}^e within the ^2E_g ground state, which is larger than the DFT value by about 15%, and the ρ_ε values, at $D_{4h}{}^e$ and $D_{4h}{}^c$ (Appendix A.4; Table 18a). In order to gain some insight into the (low-spin) $t_{2g}{}^5e_g{}^2$ excited state properties as seen by DFT, we have further calculated the optimised distortion parameters for the two lowest $^2B_{2g}$ states ($e_g{}^4b_{2g}{}^1a_{1g}{}^2/b_{1g}{}^2$) and the Franck–Condon transitions in $D_{4h}{}^e$ from $^2A_{1g}$($e_g{}^4b_{2g}{}^2a_{1g}{}^1$) to these two states, in order to compute V_ε, besides Δ, B_{te} and K'_ε; the respective equations are specified in Appendix A.4. The magnitudes

Table 18a
Structural (Å) and energy (eV) results from DFT for tetragonally distorted NiF_6^{3-} polyhedra in the low-spin ^2E_g ($t_{2g}^6e_g^1$) – above – and the (hypothetical) high-spin $^4T_{1g}$ ($t_{2g}^5e_g^2$) ground state – below – in O_h. In addition, excited $t_{2g}^5e_g^2$ spin-doublet states were analysed (for the calculation procedures see text and Appendix A.4). The derived vibronic parameters and force constants A_1, V_ε, A_2, K_ε and K_ε' for low- and V_ε, K_ε for high-spin Ni^{III} are also listed. Effective distortion and energy parameters with inter-configurational mixing accounted for (see text), are additionally given in brackets (ρ_ε^{eff}, E_{JT}^{eff}) and mirror observable quantities.

ρ_ε^{em}	ρ_ε^{cm}	a_{av}	E_{FC}[e] [a]	E_{FC}[c]	E_{JT}[e]	A_1	A_2	K_ε
0.189[b] [0.183]	0.143[b]	1.881	0.726 (0.844)	0.560	0.194 [0.182]	2.05 eV Å^{-1}	0.9	12.7 eV Å^{-1}
ρ_ε^{em} ($e_g^4b_{2g}^1a_{1g}^2$)[c]	a_{av}	ρ_ε^{cm} ($b_{2g}^1e_g^4b_{1g}^2$)[c]	a_{av}	V_ε	K_ε'[d]			
0.668 (D_{4h}[e])	1.973	0.238 (D_{4h}[c])	1.928	0.68 eV Å^{-1}	10.8 eV Å^{-2}			
ρ_ε^{em}	ρ_ε^{cm}	a_{av}	E_{FC}[e]	E_{JT}[e]	V_ε	K_ε		
0.070[e] [0.060]	0.037[e]	1.915	0.064	0.021 [0.015]	0.61 eV Å^{-1}	8.6 eV Å^{-2}		

[a] In parenthesis: experimental value (6400 cm^{-1}), but corrected for interconfigurational mixing ⇒ 6800 cm^{-1}.
[b] $a_{||}$ = 1.991, $a_\perp$ = 1.827 Å [$a_{||}$ = 1.987, $a_\perp$ = 1.828 Å] and $a_{||}$ = 1.797, $a_\perp$ = 1.921 Å, respectively.
[c] The transition energies from $^2A_{1g}$ to the two $^2B_{2g}$ states with these configurations, at ρ_ε^{em}. (Appendix A.4), are calculated at: 22.14 and 22.40 × 10^3 cm^{-1}, respectively.
[d] For the excited $t_{2g}^5e_g^2$ doublet state in O_h. Δ and B come out as listed in first line of Table 18b.
[e] $a_{||}$ = 1.956, $a_\perp$ = 1.895 Å and $a_{||}$ = 1.894, $a_\perp$ = 1.926 Å, respectively.

of the ρ_ε values and of the two E_{FC} transition energies, obtained by DFT, are listed in Table 18a, together with the derived V_ε coupling and K_ε' force constant. The calculated ligand field strength perfectly matches with the one derived from the d–d spectra, while B_{te} comes out too small by 15% (Table 18b, first line, and Fig. 35). For convenience, we give also in Table 18a ρ_ε^{eff}- and E_{JT}^{eff}-values, which mirror in an effective way the reduction of the JT-coupling by configurational mixing with excited doublet states of the same symmetry. Furthermore, a DFT calculation with the complete set of 120 Slater determinants for the d^7 configuration was performed, again adjusting the obtained energies to the respective ligand field expressions; the procedure of the respective LFDFT approach is outlined elsewhere [96] (see also Section 12). The resulting ligand field and Racah parameters are confronted with the results from Table 18a in Table 18b (first two lines). The complete calculation yields an enhanced Δ parameter, far away from the experimental energy (Fig. 35).

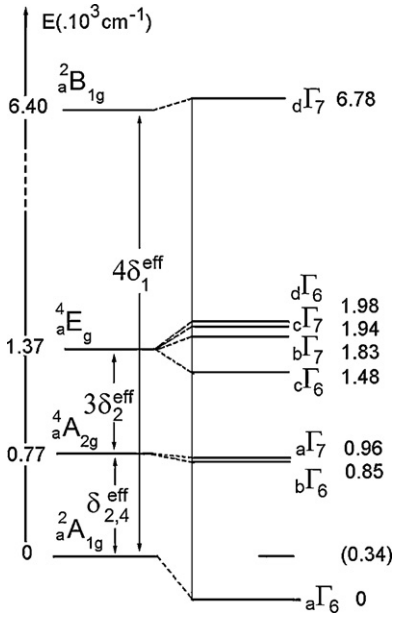

Fig. 36. Energy diagram for the NiF_6^{3-} octahedron in Cs_2KNiF_6 (adopted from [94]) in the energy region of the ground state. The ligand field calculation was performed with the parameter set, used in Fig. 35; the LS coupling constant was set to 500 cm^{-1}, according to a ξ/ξ_o ratio of 0.7 (ξ_o = 715 cm^{-1} [27]).

The calculation for the hypothetical high-spin polyhedron is based on the matrices in Eq. (42), which are valid for the d^7 configuration as well, when considering that a spherically symmetric $t_{2g}^3e_g^2$ electron shell is added to d^2. The diagonal ground state splitting $3\delta_2$ in D_{4h}[e] is:

$$\tfrac{3}{2}V_\varepsilon\rho_\varepsilon^{em} = E(^4E_g - e_g^3b_{2g}^2a_{1g}^1b_{1g}^1) - E(^4A_{2g} - e_g^4b_{2g}^1a_{1g}^1b_{1g}^1) \quad (65)$$

and directly accessible to DFT. The respective energy and the distortion parameters $\rho_\varepsilon^{em} = 2\rho_\varepsilon^{cm} \cong V_\varepsilon/K_\varepsilon(L_\varepsilon \cong 0)$ yield the vibronic constants V_ε and K_ε in Table 18a. From the three transitions from $^4A_{2g}(e_g^4b_{2g}^1a_{1g}^1b_{1g}^1)$ to the excited $^4B_{2g}$, $^4B_{1g}$ states and to the second $^4A_{2g}$ state at ρ_ε^{em} = 0.070 Å (diagonal energies in matrices (42)), calculated via DFT, Δ, δ_1 and a global B parameter are, additionally to δ_2, accessible and summarized in Table 18b (third line). δ_1 is nicely reproduced with the A_1 and A_2 parameters from low-spin Ni^{III} – a rather consistent result. V_ε is smaller by about 10% than the value, deduced from data for low-spin Ni^{III} – in view of the small δ_2 splitting a still reasonable outcome. Derived effective values ρ_ε^{eff} and E_{JT}^{eff} indicate a pronounced partial suppression of vibronic coupling, by the configuration interaction between the two $^4A_{2g}$ states. For high-spin Ni^{III} also a complete LFDFT calculation was performed. The obtained parameter set differs from the one resulting, if only quartet states are taken in account; it produces an enhanced B value – which is still too low in regard to the experiment, however.

The experimental δ_1 and δ_2 splitting parameters for low-spin Ni^{III} (Fig. 35) are not too far away from the values in Table 18b (1./2.line); there is an inconsistency in the magnitude of the ligand field strength, however. If, in a rough consideration, the mean

Table 18b
Excited state analysis by DFT for low-spin (top two lines) and high-spin NiF_6^{3-} (bottom two lines) – energies in 10^3 cm^{-1}. The first and third line refer to a ligand field calculation on the basis of the restricted set of transitions used in Table 18a, the second and the fourth line to a full LFDFT calculation (see text).

Δ	δ_1	δ_2	B	C/B	δ^{eff}[a]
13.30	1.70	0.52	0.67_5	(4.0)	2.5
14.97	1.46	0.40	0.62	4.1	4.6
13.97	0.57	0.17	0.39	(4.0)	−4.3
13.85	0.48	0.13	0.66	3.5	−2.9

[a] The doublet-quartet and quartet-doublet separations $\delta_{2,4}^{eff}$ and $\delta_{4,2}^{eff}$, respectively – first and second, and, third and fourth line. The data from the d–d and EPR spectra for low-spin Ni^{III} yield: $\delta_{2,4}^{eff}$ = 0.90 (δ_1 = 1.70, δ_2 = 0.32), and the suggested separation energy for high-spin Ni^{III} is $\delta_{4,2}^{eff}$ = 1.20 (δ_1 = 0.57, δ_2 = 0.17) × 10^3 cm^{-1} – with Δ = 13.1 and B = 0.78 × 10^3 cm^{-1} in both cases (from Fig. 35).

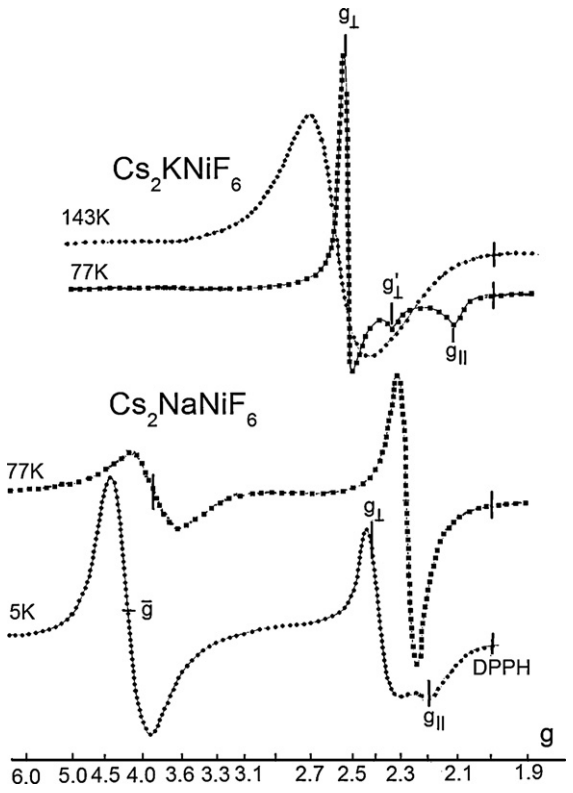

Fig. 37. The EPR spectra of the elpasolite Cs_2KNiF_6 (the signal $g_{\perp'}$ is probably due to exchange coupling between $g_{||}$ and $g_\perp$ – see text) and of Cs_2NaNiF_6 with the hexagonal Cs_2NaCrF_6 structure and two different Ni^{III} sites – adopted from [94].

of the two calculated values is taken, Δ does not differ essentially from the mean for high-spin Ni^{III} (Table 18b, 3./4.line) – 14.1(8) and $13.9 \times 10^3\,cm^{-1}$, respectively – and comes out to be about 7% larger than the experimental value in the low-spin case (Fig. 35). The occurrence of a single value for Δ is supported by the experimental data, underlying the potential surface in Fig. 40 (vide infra); it is surprising only in the first instance, when solely focusing on the by $\cong 0.03_5$ Å larger average bond length in the high-spin case (Table 18a). However, as the ground state potential curves indicate, their minima occur at nearly the same energy, and one may thus confidently suggest, that the Ni–F bond strength is comparable in the low- and high-spin case.

As has been pointed out already, the alternative $^2A_{1g}$ ($e_g^4 b_{2g}^2 a_{1g}^1$) and $^4A_{2g}$ ($e_g^4 b_{2g}^1 a_{1g}^1 b_{1g}^1$) ground state energies are subject to alterations caused by configuration interaction with excited states of the same symmetry and the same spin. These effects are small in the case of the here present low-spin ground state, but are of significant influence on the splitting of the lowest-energy $^4T_{1g}$ excited state (Table 18a). One has further to consider, however, that the low-spin $_a{}^2A_{1g}$ ground state undergoes additional mixing with the $_a{}^4A_{2g}$ and $_a{}^4E_g$ states, located in close energetic neighbourhood, via LS coupling (vide infra). This is seen by EPR spectroscopy, which is a finer probe to the energetic situation within the ground state than the d–d spectra [94]. Fig. 36 illustrates the energetic landscape of the competing octahedral $_a{}^2E_g$ and $_a{}^4T_{1g}$ states in the presence of LS coupling. The respective interaction between the $_a{}^2A_{2g}$ ground state and the $_a{}^4A_{2g}$, $_a{}^4E_g$ excited states gives rise to large orbital contributions to the g-tensor components (Fig. 37) [94], from which the energy separations $\delta_{2,4}^{eff}$ and $3\delta_2^{eff}$ (the notation: "effective" indicates, that configuration interaction has been accounted for) emerge with high precision. The, in the first instance, unexpected result is, that $3\delta_2$ (at $\rho_\varepsilon^m = 0.189$ Å) comes out smaller ($320\,cm^{-1}$) than expected by DFT ($520\,cm^{-1}$, Table 18a). The mismatch is most certainly caused by the neglect of LS-coupling in the DFT calculation and by errors introduced by the $3d_{z^2}$–4s interaction, which is not properly accounted for in DFT. Nevertheless, the magnitudes of the coupling constants $A_1(2.05)$ and V_ε ($\approx 0.6_5$ eV/Å) are well in range of those, derived for Ti^{III} to Co^{III} in fluoride ligand fields.

The EPR spectrum of the hexagonal elpasolite Cs_2NaNiF_6 is particularly interesting because it shows – in contrast to the spectra of the regular elpasolites with corner-connected octahedra exclusively – a high-spin signal around 4 in addition to the anisotropic low-spin signal (Fig. 37); it has to be ascribed to Ni^{III} in the central position of the group of three face-connected octahedra in this structure (Fig. 26) [94]. The rigid property of this grouping enforces a considerable constraint on the central NiF_6^{3-} octahedron, presumably via an enhanced K_ε force constant. Already a strain-induced decrease of the first order Jahn–Teller contribution to the quartet-doublet separation $2(\delta_1 - \delta_2) = 2800\,cm^{-1}$ of less than 20% (Eq. (64)) would suffice to stabilise the alternative $_a{}^4A_{1g}$ ground state. The d-d spectrum of Cs_2NaNiF_6 gives also hints for the partial presence of high-spin Ni^{III}. It is less structured than that of Cs_2KNiF_6 (Fig. 35), caused – as one might suppose – by broad-band intensity contributions due to $_a{}^4A_{2g}(_a{}^4T_{1g}) \rightarrow {}^4B_{2g}, {}_b{}^4E_g(^4T_{2g})$ and $\rightarrow {}_b{}^4E_g$, $_b{}^4A_{2g}(_b{}^4T_{1g})$ transitions. The latter should appear at 11.2, 12.3 and 21.8, $23.8 \times 10^3\,cm^{-1}$, and might have obscured the sharp minimum at $\approx 10{,}000\,cm^{-1}$, enhanced the intensity of the $_a{}^2A_{1g} \rightarrow {}_a{}^2E_g$ band, and, in particular, filled the deep minimum gap between 22 and $24 \times 10^3\,cm^{-1}$, respectively, in the spectrum of Cs_2KNiF_6. The given band positions are calculated with the parameter set of Fig. 35, but with the δ_1 and δ_2 energies for high-spin Ni^{III} (0.57 and $0.17 \times 10^3\,cm^{-1}$, respectively; Table 18b).

From the EPR data and low-temperature structural powder investigations it was concluded that Cs_2KNiF_6 and Rb_2KNiF_6 undergo second order phase transitions at $\cong$145 K and $\cong$260 K, respectively [1] – these temperatures characterising a change from dynamic to static local JT distortions. The low-temperature structure is tetragonal, with $c/a > 1$, according to a ferrodistortive order of elongated NiF_6^{3-} octahedra (Fig. 39). For the Cs_2K-elpasolite a local distortion of $\rho_\varepsilon^{em} \cong 0.14$ Å [97] was roughly estimated at $T < 77$ K from X-ray data, not too far from the DFT value $\rho_\varepsilon^{eff} \cong 0.18$ Å (Table 18a). Elpasolitic solids with Mn^{III} exhibit analogous unit cell distortions according to a ferrodistortive order, but already at 298 K [1,69]. The ground state splitting and the distortion parameter are considerably smaller in the low-spin Ni^{III} case, as compared to Mn^{III}, mainly caused by – if one believes theory and DFT – a considerably increased force constant K_ε (Tables 13 and 18a).

10.2. The high-spin/low-spin equilibrium

We consider now the influence of temperature on the obviously existing low-spin/high-spin equilibrium in greater detail. The orbital admixtures to the anisotropic g-values at 4 K, due to the $_a{}^2A_{1g}$–$_a{}^4A_{2g}$, $_a{}^4E_g$ interaction [94], increase with temperature, as does the magnetic susceptibility, measured by Alter and Hoppe [93] – without doubt caused by the presence of high-spin Ni^{III} on the octahedral sites and thermal averaging processes. This effect explains the positive deviation of $\chi \cdot T$ from the low-spin value at higher temperatures (Fig. 38) via a specific energy barrier $\Delta E_{2.4}$. On the other hand, the effect of a drastic decrease of χT below the limit given by the low-spin curves, occurring at low temperatures, is without doubt due to antiferromagnetic interactions according to a negative paramagnetic Curie temperature θ_p. The existence of such wide-distance interactions in elpasolites is indeed documented for the analogous solids A'_2AMnF_6 with tetragonally elongated $Mn^{III}F_6^{3-}$ polyhedra in ferrodistortive order and a $(d_{z^2})^1$ configuration on each paramagnetic centre (Fig. 39; top left); deduced θ_p

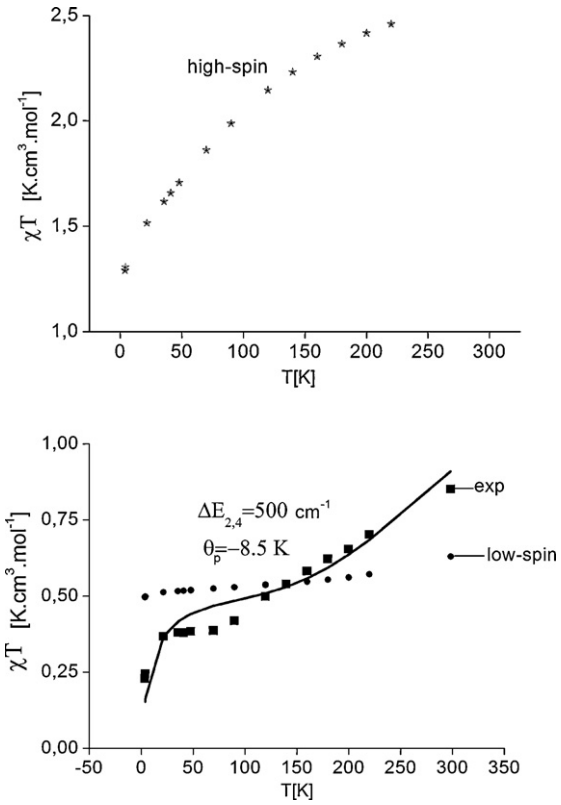

Fig. 38. The calculated magnetic susceptibility (χ) in dependence on temperature, for low-spin and high-spin NiF_6^{3-} polyhedra (parameter set of Fig. 35, and with reduced energies for δ_1 and δ_2 – 0.57 and 0.17×10^3 cm^{-1} – bottom and top, respectively), in comparison with experimental results for Cs_2KNiF_6. The data fit was achieved by the assumption of a thermal admixture of quartet to doublet Ni^{III} species via the energy barrier $\Delta E_{2,4}$, and assuming the presence of weak antiferromagnetic coupling between the low-spin Ni^{III} centres (for the fit quality between 50 and 110 K, see text).

values are here also around −8 K [29]. The correlation between the spins of the d_{z^2} electrons via the interconnecting (A^IF_6) polyhedra within the ferrodistortive order demands antiferromagnetism.

With the sketched model, a rather good fit to the experimental data is achieved (Fig. 38) – though there are deviations in the temperature region between 50 and 100 K. We think, that domains with antiferrodistortive elastic coupling, present in the vicinity of the temperature of the phase transition, are responsible for the discrepancy. Evidence for the existence of antiferrodistortive pairs gives EPR, where a weak signal at $g'_\perp = 1/2(g_{||} + g_\perp)$ appears (Fig. 37). It very probably results from the averaging of a molecular $g_{||}$ and a $g_\perp$ tensor component – oriented parallel to a long ($a_{||}$) and a short ($a_\perp$) Ni^{III}–F bond length, respectively – due to the mentioned clusters with parallel spin orientation within neighboured tetragonally elongated $Ni^{III}F_6^{3-}$ polyhedra. Fig. 39 displays the two alternative patterns of elastic ordering in the elpasolite lattice (top and bottom left). In large domains with antiferrodistortive elastic coupling the planar ferromagnetism is expected to give way to a three-dimensional antiferromagnetic arrangement, caused by antiparallel spin-orientation between the planes. A similar complex structural situation has been analysed for the Cu^{2+} centre with a hole in the $d_{x^2-y^2}$ orbital, via EPR and magnetic investigations on compounds $Ba(Sr)_2{}^{II}Cu^{II}W(Te)^{VI}O_6$ and corresponding mixed crystals with Zn^{2+} on the Cu^{2+} positions [98]. While in the former solids a ferrodistortive order of elongated CuO_6 polyhedra (Fig. 39, top right) is stabilised, with first-order transitions to the cubic phase at very high temperatures, on dilution with Zn^{2+} the alternative antiferrodistortive order (with short-range character) becomes energetically more favourable; here, the phase transition to the cubic elpasolite structure is of continuous nature. To summarize: for Cu^{II}, as for low-spin Ni^{III}, the ferrodistortive order demands antiferromagnetism, while the antiferrodistortive alternative generates ferromagnetic planes, which might be weakly antiferromagnetically coupled in the *c*-direction. A plausible explanation for the mentioned mismatch between calculated and experimental susceptibility data (Fig. 38) is, as we think, that the disorder, introduced by the presence of high-spin Ni^{III} on the octahedral sites of elpasolites A'_2ANiF_6, favours the formation of antiferrodistortive domains with short-range order – in a similar way as initiated by the non-JT cation Zn^{2+}, when substituted into the Cu^{2+} sites of Ba_2CuWO_6.

The potential energy diagram in Fig. 40 is a model description of the energetic situation in the competing $_a{}^2A_{1g}$, $_a{}^4A_{2g}$ ground state manifold. For the construction of the potential curves the force constants for low-spin and high-spin NiF_6^{3-} ($K_\varepsilon^{ls} = 12.7$, $K_\varepsilon^{hs} = 8.6\,\text{eV Å}^{-2}$) as well as the corresponding effective ρ_ε values ($\rho_\varepsilon^{eff}(ls) = 0.183$, $\rho_\varepsilon^{eff}(hs) = 0.060$ Å) were used (Table 18a), and in addition the effective doublet–quartet separation energy $\delta_{2,4}^{eff} \cong 900\,\text{cm}^{-1}$ (including contributions from LS coupling), which is rather precisely known from experiment (see Fig. 36). Because the location of the high-spin potential energy curve with respect to the position of the curve for low-spin Ni^{III} involves not only a change of ρ_ε but also an expansion of the average Ni–F bond length $\delta a = 0.034$ Å, we adopt the Bersuker concept [16] of a single interacting displacement mode *q*. The respective coordinate δq, which comprises changes of both, ε_g- and α_{1g}-type stretching dislocations – when moving from the minimum position of the low-spin state, as the reference, toward the minimum of the potential energy curve of the high-spin state – is defined in our model as follows:

$$\tfrac{1}{2}K_\varepsilon^{hs}(\delta\rho_\varepsilon^{eff})^2 + \tfrac{1}{2}K_\alpha(\sqrt{6}\delta a)^2 \equiv \tfrac{1}{2}K_\varepsilon^{hs}(\delta q)^2 \tag{66a}$$

$$\delta q \equiv \left\{(\delta\rho_\varepsilon^{eff})^2 + \frac{K_\alpha}{K_\varepsilon^{hs}}(\sqrt{6}\delta a)^2\right\}^{1/2} \tag{66b}$$

Here $\delta\rho_\varepsilon^{eff} = 0.183 - 0.060 = 0.123$ Å is the decrease of the radial distortion when switching from low- to high-spin Ni^{III} (Table 18a), while $\sqrt{6}\delta a$ refers to the average bond length increase according to the α_{1g} motion. Explicitly, Eqs. (66a) and (66b) visualize the displacement of the adiabatic potential energy surface of high-spin Ni^{III} in respect to the low-spin potential curve, along the q coordinate. With the tentative choice of $K_\alpha/K_\varepsilon = 1.2$ – suggested by DFT and by reported energies of the two α_{1g} and ε_g vibrational modes (see the data for FeF_6^{3-} in [26]) – a displacement $\delta q = 0.153$ Å results. The potential energy diagram in Fig. 40 is now easily constructed via the following expressions:

$$\begin{aligned} &E(ls) = \tfrac{1}{2}K_\varepsilon^{ls}(\delta q)^2, \text{ at } \delta q = 0.153\,\text{Å} \Rightarrow \delta_{4,2}^{eff} + \Delta_{2,4} \\ &E(hs) = \tfrac{1}{2}K_\varepsilon^{hs}(0.153 - \delta q)^2 + \Delta_{2,4}, \text{ at } \delta q = 0 \Rightarrow \delta_{2,4}^{eff} \end{aligned} \tag{67}$$

The quantity of major interest is $\Delta_{2,4}$, the energy difference between the minimum positions of the high-spin and low-spin potential curves, and comes out to be about 100 cm^{-1}. The energy $\Delta E'_{2,4}$ (≈300 cm^{-1}) characterises the point of intersection between the two potential curves at $\delta q \approx 0.08$ Å and is loosely correlated with the barrier height $\Delta E_{2,4}$ in Fig. 38, which steers the occupation of formerly low-spin sites by high-spin Ni^{III}; indeed, the two quantities are of comparable magnitude ($400 \pm 100\,\text{cm}^{-1}$). The quartet-doublet separation energy $\delta_{4,2}^{eff}$, resulting from Fig. 40, is $\cong 1100\,\text{cm}^{-1}$, indeed near to the $_a{}^4A_{2g}$–$_a{}^2A_{1g}$ energy difference of 1200 cm^{-1}, which results from a ligand field calculation – performed on the basis of available experimental data (Table 18b, footnote a). If, on a finer scale, K_ε^{ls} is adjusted by taking second

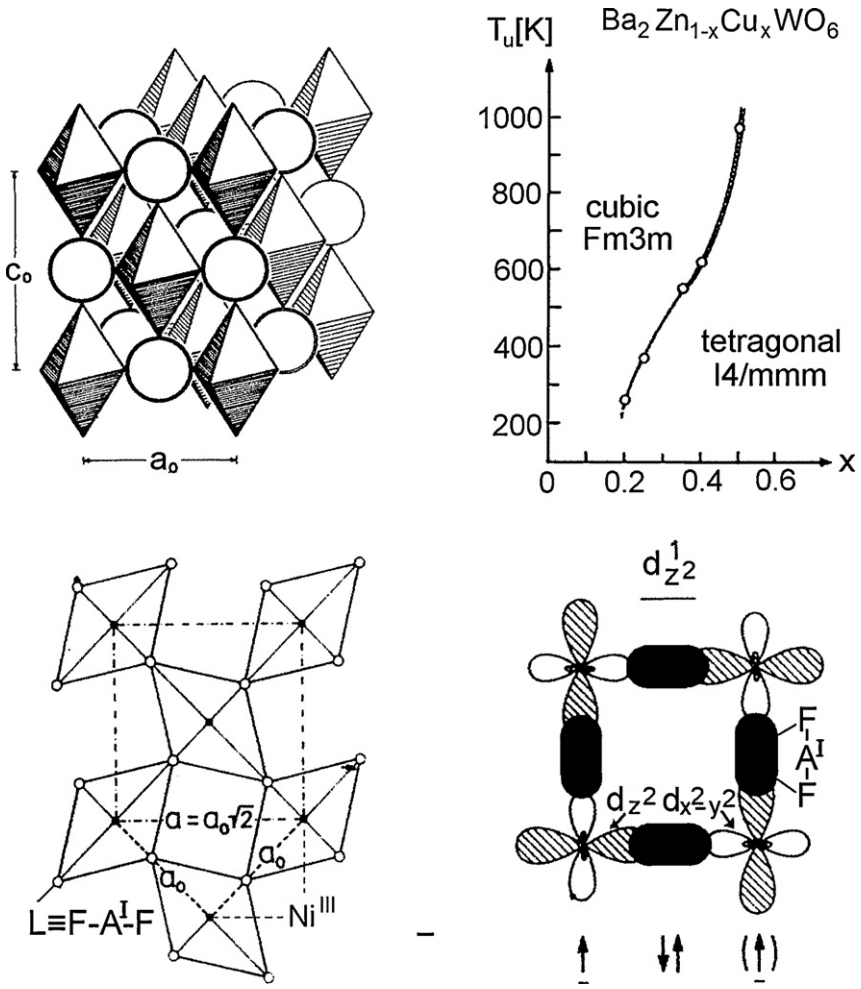

Fig. 39. The ferrodistortive order of tetragonally elongated $Ni^{III}F_6^{3-}$ octahedra in elpasolites $A_2'ANiF_6$ (top, left; the open circles stand for the intervening A^IF_6 polyhedra) and the phase diagram of $Ba_2Zn_{1-x}Cu_xWO_6$ mixed crystals (top, right; for details see text). The bottom figures illustrate the alternative antiferrodistortive order between the NiF_6^{3-} polyhedra with a view into the planes, perpendicular to [0 0 1], and the induced ferromagnetic spin correlation (the black ellipsoids stand for the intervening F–A^I–F bridges and their overlap with the $3d_{z^2}$ and $d_{x^2-y^2}$ orbitals; the orbitals, due to Ni^{III} in the square-centre, are not shown) – adopted from [1].

order vibronic coupling into account ($\Rightarrow K_\varepsilon^{ls} - 2A_2 = 10.9\,eV/Å^2$), significant changes of the above reported energies do not emerge.

We now comment on the DFT results for $\delta_{2,4}^{eff}$ and $\delta_{4,2}^{eff}$ in Table 18b. Due to the underestimation of interelectronic repulsion, and because of an, in one case, overrated Δ value, $\delta_{2,4}^{eff}$ energies result, which are by far too large; for the same reason, the $\delta_{4,2}^{eff}$ separation energies come out to be strongly negative. Considering the splitting parameters only, the following analytical expression for the sum of $\delta_{2,4}$ and $\delta_{4,2}$ (diagonal energies; see Eq. (64)) can be formulated. It refers to the alternative $^2A_{1g}(e_g^4b_{2g}^2a_{1g}^1)$ and $^4A_{2g}(e_g^4b_{2g}^1a_{1g}^1b_{1g}^1)$ ground states if Δ, B, C are equal in the low- and high-spin case:

$$\delta_{2,4} + \delta_{4,2} = 2\{(\delta_1 - \delta_2)^{ls} - (\delta_1 - \delta_2)^{hs}\} \quad (64a)$$

and is consistently $(1.7 \pm 0.2_5) \times 10^3\,cm^{-1}$, if the splitting parameters in footnote a of Table 18b, or the results of the DFT calculations are used. After all, the DFT results for the octahedral (with the exception of the Δ-value near to 15,000 cm^{-1}) and tetragonal ligand field parameters, turn out to be rather reliable quantities, while interelectronic repulsion comes out too small; the increase of B toward the realistic value of 780 cm^{-1} would reduce $\delta_{2,4}^{eff}$ and shift the $\delta_{4,2}^{eff}$ energy to much less negative or even positive magnitudes.

We summarize, that it is preferentially the strong $^2E_g \otimes \varepsilon_g$ coupling ($\delta_1^{ls} = 1.7 \times 10^3\,cm^{-1}$), which stabilises a low-spin ground state (Eq. (64a)) [1,94]. Furthermore, the detailed analysis, underlying Fig. 40, indicates, that *the potential minima of the two competing Ni^{III} species lie very close in energy* [99].

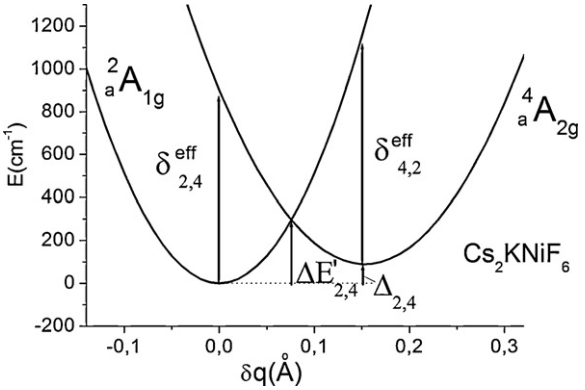

Fig. 40. Potential energy diagram for the NiF_6^{3-} polyhedra in elpasolites (as in [99]). The δq coordinate is defined in reference to the absolute energy minimum of low-spin Ni^{III} at ρ_ε^{em} (eff) = 0.183 Å; the minimum for high-spin Ni^{III} at ρ_ε^{em} (eff) = 0.060 and δa = 0.034 Å (δq = 0.153 Å) is located at a by ≅100 cm^{-1} higher energy. For further details see the text.

Table 19
Structural and energy DFT results for the CuF_6^{3-} octahedron in the excited $t_{2g}^5e_g^3$ configuration – optimised data and Franck–Condon transitions, calculated according to Appendix A.3 – and the derived coupling parameters (above). The E_{FC} transitions, originating from the $^4A_{2g}$ ($t_{2g}^6e_g^2$) ground state in O_h (diagonal energies; in 10^3 cm^{-1}), are listed below, together with the ligand field parameters deduced.

ρ_ε^m (Å)[a]	$e_g^2b_{1g}^1$ (a_{av})	$e_g^2a_{1g}^1$ (a_{av})	$e_g^1b_{2g}^1b_{1g}^1$ (a_{av})	$e_g^1b_{2g}^1a_{1g}^1$ (a_{av})
	0.129[c] (1.962)	0.322[e] (1.970)	0.208[c] (1.970)	0.301[e] (1.972)
	$E_{FC}^{(a)}$ (eV)	$E_{FC}^{(b)}$ (eV)	$A_1\ V_\varepsilon$	$A_2\ K_\varepsilon$'
	0.882[c]	0.315[e]	1.2 ≅0.2 eV Å^{-1}	≅0.7 ≅5.5 eV Å^{-2}
E_{FC}	$^4A_{2g} \rightarrow {}^4T_{2g}$ ($t_{2g}^5e_g^3$)	$\rightarrow {}^4T_{1g}$ ($t_{2g}^5e_g^3$)	$\rightarrow {}^4T_{1g}$ ($t_{2g}^4e_g^4$)	a (Å)
(O_h)	14.34[b] (=Δ)	18.98[b] (=Δ + 12B)	29.59[b] (=2Δ + 3B)	1.909

[a] A half-filled shell $e_g^2b_{2g}^1b_{1g}^1a_{1g}^1$ has to be added; c, e refers to D_{4h} elongated, and compressed, respectively. For the nomenclature (a), (b), see Appendix A.3.
[b] See the d^3 matrices in Eq. (52); the derived B_{te} parameter is 0.39(1) in comparison to the spectroscopic value of 0.70(5) × 10^3 cm^{-1}; the experimental Δ value is 14.3(2) × 10^3 cm^{-1}.

11. The $Cu^{III}F_6^{3-}$ polyhedron

In Table 19 we have listed the DFT results for the CuF_6^{3-} octahedron. Having in mind, that the addition of a half-field d-shell ($t_{2g}^3e_g^2$) does not change the energy matrices, if only the highest-multiplicity terms are considered (see Eq. (52)), we followed the procedure described in Appendix A.3 for Cr^{III} for the evaluation of the coupling and force constants. Surprisingly, the coupling constants A_1 and V_ε (the latter has – as well as K'_ε and A_2 – a larger margin of error) come out very small in comparison to the parameters derived for the cations, preceding Cu^{III}. The thus indicated discontinuously increased bond covalency is also detected, when analysing the charge-transfer and d–d spectra (see below). We have furthermore calculated the Franck–Condon transitions in O_h by DFT – here using the D_{4h}-MOs, however, in order to avoid falsifications due to self-interaction in the case of orbital degeneracy. While the calculated Δ parameter nicely matches with the experimental value (Fig. 41), the Racah parameter is more than 40% smaller than that, derived from the d–d spectra, which is an even larger mismatch than that found for Cr^{III} (Table 10).

There is only one d–d spectrum – for the elpasolite Cs_2KCuF_6 – reported in literature [49]. Fig. 41 shows a second example [31], with band positions near to those of the Cs solid. The $^3A_{2g} \rightarrow {}_a{}^3T_{1g}$ transition is rather broad and hence the B_{te} parameter

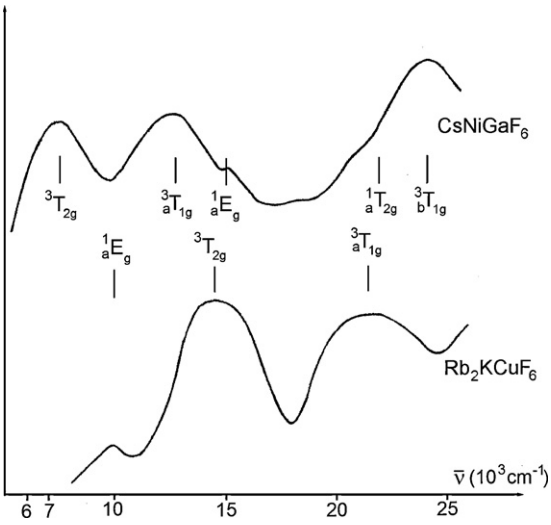

Fig. 41. The d–d spectrum (T = 298K) of the hexafluoro-Ni^{II}-complex ($^3A_{2g}(t_{2g}^6e_g^2)$ ground state)) in a pyrochlore-type structure (top); the assignment and band fitting is accomplished with: Δ = 7.5, a single parameter B = 0.95 × 10^3 cm^{-1} (B/B_0 = 0.92) and a ratio C/B = 4.2. The spectrum of the isoelectronic $Cu^{III}F_6^{3-}$ octahedron (T = 298K) in the cubic elpasolite structure is shown below; band fitting was achieved with the same C/B-ratio and Δ = 14.5; B_{ee} = 0.62, $B_{te} \approx 0.75 \times 10^3$ cm^{-1}.

subject to larger errors (≈0.75 × 10^3 cm^{-1}). The nephelauxetic ratio (with $B_0 \cong 1200$ cm^{-1} [49]) is, with $\beta \approx 0.6$, considerably lower than those for V^{III}, Cr^{III} and Co^{III} (≅0.75) – indicating also via the interelectronic repulsion a pronounced increase of the bond covalency. In the spectra of the isoelectronic Ni^{2+} ion in fluoride solids (Fig. 41) particularly two of the three lowest energy triplet–singlet transitions are usually observed in addition to the spin-allowed bands, namely: $_a{}^3A_g$ ($t_{2g}^6e_g^2$) $\rightarrow {}_a{}^1E_g$ (≅$t_{2g}^6e_g^2$) and $\rightarrow {}_a{}^1T_{2g}$ (≅$t_{2g}^5e_g^3$). The three absorptions are expected (see the respective Tanabe–Sugano energy matrices) – for Δ/B ratios around 20, as for $Cu^{III}F_6^{3-}$ – to occur at:

$$E(_a{}^3A_{2g} \rightarrow {}_a{}^1E_g) \cong 0.01_5\Delta + 7.4B_{ee} + 2C_{ee} \quad (68a)$$

$$E(_a{}^3A_{2g} \rightarrow {}_a{}^1A_{1g}) \cong 0.16_5\Delta + 8.1B_{ee} + 4C_{ee} \quad (68b)$$

$$E(_a{}^3A_{2g} \rightarrow {}_a{}^1T_{2g}) \cong 1.02_5\Delta + 7.0B_{te} + 2C_{te} \quad (68c)$$

Adopting the C/B ratio from Ni^{2+}, one derives from the position of the observed transition within the ground state electron configuration at 10,000 cm^{-1} in the spectra of $Cs(Rb)_2KCuF_6$ a B_{ee} parameter of 620 cm^{-1} (Eq. (68a)); because only σ-antibonding e_g electrons are involved, a further covalency reduction with respect to B_{te} is expected. In the case of the $Ni^{II}F_6^{4-}$ octahedron (Fig. 41, top), due to the only weakly pronounced covalency of the divalent cation toward F^-, one single B parameter and a C/B value of 4.2 suffices for the parameterisation. The transitions to $_b{}^3T_{1g}$ and $_a{}^1T_{2g}$ – the latter is revealed as a shoulder on the low-energy slope of the $_a{}^3A_{2g} \rightarrow {}_b{}^3T_{1g}$ main transition in the case of Ni^{2+} – are calculated to appear at ≅33.5 and 26.5 × 10^3 cm^{-1} for Cu^{III}, already in the charge-transfer region. The $_a{}^3A_{2g} \rightarrow {}_a{}^1A_{1g}$ transition (Eq. (68b)) is reported to appear as a very weak peak in the spectrum of Cs_2KCuF_6 at 16,400 cm^{-1} [49], about 1000 cm^{-1} lower than predicted in our parameterisation.

The trend of increasing covalency has been substantiated for the hexachloro-complexes of the series of cations from Ti^{III} to Fe^{III} in Section 8, where the optical electronegativity of the M^{III} centres steadily moves toward that of Cl^- (Table 16a). In the fluoride case, a rather drastic decrease of the vibronic coupling parameters and of the nephelauxetic ratio is observed, when passing over from Ni^{III} to Cu^{III}. This effect is reflected by the optical electronegativity (Eq. (62)) as well. From the reported [49] lowest-energy $t_{1u}^n \rightarrow e_g^*$ ligand-to-metal charge-transfer band of the NiF_6^{3-} and CuF_6^{3-} octahedra – after having applied the correction arising from changes in the interelectronic repulsion, and here also with respect to the ligand field parameter Δ because of the filled t_{2g} subshell – a dramatic enhancement of χ_{opt} from Ni^{III} to Cu^{III} results (Table 16b). It documents the instability of the (+III) oxidation state of copper even in the field of fluoride, the ligand with the largest electronegativity. Accordingly, a $Zn^{III}F_6^{3-}$ octahedron cannot be stable, for the obvious reason of charge transfer bands, which would cover even

the low-energy spectroscopic region [87]. For similar arguments, chlorocomplexes of $3d^n$-M^{III} cations are not expected to exist as stable species, if $n > 6$ ($\chi_{opt}(Ni^{III}) \approx \chi_{opt}(Cl^{-I})$; Tables 16a and 16b).

The (+III) oxidation state of copper is still reasonably stable in ligand fields of oxygen ligator atoms – in spite of the smaller electronegativity in comparison to fluoride. Usually the Cu^{III} – centres are low-spin in this environment, however, and adopt a square-planar coordination. These energetic and structural properties originate from the pseudo-JT coupling between the ^1E_g- and $^1A_{1g}$-excited states within the $t_{2g}^6e_g^2$ ground state configuration (see Eqs. (68a) and (68b)), which eventually stabilises a low-spin ($e_g^4b_{2g}^2a_{1g}^2$) ground state in D_{4h}. The symmetry aspects and energetic implications are considered in detail elsewhere [99].

12. DFT calculations and further details

12.1. Vibronic coupling calculations

One main goal of this work has been to explore the ground state potential energy surface of hexafluoro- and hexachloro-complexes of 3d metals in their T_{2g} (d^1, high-spin d^6) and T_{1g} (d^2, high-spin d^7) ground sates and to rationalize on this basis their spectra and structures. Because the ground state energy splitting and the finer structural details of these complexes are not known from experiment, we used DFT results as a data base to deduce these quantities from first principles. An analysis of the DFT data in terms of the $T_g \otimes (\varepsilon_g + \tau_{2g})$ vibronic coupling model then allows one to deduce the otherwise inaccessible vibronic coupling parameters.

The general procedure of obtaining the vibronic coupling and force constants from DFT via the relevant distortion parameters and Franck–Condon transition energies is outlined in Sections 2.2–2.4 for the $T_g \otimes \tau_{2g}$, $T_g \otimes \varepsilon_g$ and $T_g \otimes (\varepsilon_g + \tau_{2g})$ vibronic interactions and is related to the one in [100]. It is extended to the $E_g \otimes \varepsilon_g$ coupling case in Section 2.5. The derived equations refer to the $^{2(5)}T_{2g}$, $^{2(5)}E_g$ ground and excited states, respectively, of d^1 (high-spin d^6) cations – Sections 3 and 9.1 – and to the d^2 (high-spin d^7) configurations with $^{3(4)}T_g$-type ground and excited states, which are treated in Sections 5.1–5.3 and 10.1. A critical discussion, concerning the discrimination of certain DFT data with respect to their usability in the vibronic coupling and ligand field calculations is given in Section 3.1. Besides the mentioned electron configurations the excited T_g states of octahedral Cr^{3+} and Cu^{3+} were analysed. Because the ground states are orbital singlets in these cases, the coupling and force constants had to be deduced from DFT data on carefully selected excited state configurations (Sections 6.1, 6.2 and 11). Neglecting higher-order coupling contributions, the following relations between the linear coupling and force constants ($T_g \otimes \varepsilon_g$ interaction), and the DFT-deduced radial distortion parameters and Franck–Condon transition energies within the T_g ground state splitting exist [100] at the absolute minima of the adiabatic $B_{2g}(T_{2g})$ and $A_{2g}(T_{1g})$ potential energy surface for d^1,d^6 (high-spin)and d^2,d^7 (high-spin), with $\rho_\varepsilon^m \equiv \rho_\varepsilon^{cm}$ and ρ_ε^{em}, respectively:

$$V_\varepsilon = \frac{2}{3}\frac{E_{FC}(D_{4h})}{\rho_\varepsilon^m}; \qquad K_\varepsilon = \frac{2}{3}\frac{E_{FC}(D_{4h})}{(\rho_\varepsilon^m)^2} \tag{69}$$

and, similarly, in the $T_g \otimes \tau_{2g}$ coupling case for an $A_{1g}(T_{2g})$ or $A_{2g}(T_{1g})$ ground state, with $\rho_\tau^m \equiv \rho_\tau^{cm}$ and ρ_τ^{em}, respectively:

$$V_\tau = \frac{2}{3}\frac{E_{FC}(D_{3d})}{\rho_\tau^m}; \qquad K_\tau = \frac{2}{9}\frac{E_{FC}(D_{3d})}{(\rho_\tau^m)^2} \tag{70}$$

While Eq. (69) turns out to be exact in the considered cases ($L_\varepsilon \cong 0$), expression (70) is only approximate, because here the second-order coupling constant X_τ is of significant magnitude (see Table 2, for instance). If the $D_{2h}{}^*$ stationary points are considered, the same equations (69) and (70) are valid – again for vanishing higher-order contributions, here from L_τ and W. The, additive, distortion parameter components in the respective case of $T_g \otimes (\varepsilon_g + \tau_{2g})$ vibronic coupling are: $\rho_\varepsilon^m \equiv \rho_\varepsilon^{em}$ (D_{4h}) (d^1) or ρ_ε^{cm} (D_{4h}) (d^2) and ρ_τ^{*m} ($D_{2h}{}^*$) in both cases; the transition energy increments in $D_{2h}{}^*$ (see Fig. 4d), to be substituted into Eqs. (69) and (70), are as follows (d^1-nomenclature):

$$\begin{aligned} E_{FC}(\Delta_{4h}) &\equiv E_{FC}(B_{3g} \rightarrow A_g) - \tfrac{1}{2}E_{FC}(B_{3g} \rightarrow B_{2g}) \\ E_{FC}(D_{3d}) &\equiv E_{FC}(B_{3g} \rightarrow B_{2g}) \end{aligned} \tag{71}$$

The DFT calculations show indeed, that, according to the premise, the higher-order coupling is weak or even vanishing; W – which couples the τ_{2g} and ε_g modes in their interaction with an electronic T_g ground state – is nearly zero and L_τ is small. *The general conclusion is, that, from the stationary points of the adiabatic potential energy surface, those resulting for a pure $T_g \otimes \varepsilon_g$ vibronic interaction are clearly the absolute minima in the case of the analysed fluoro- and chloro-complexes of the 3d-M^{III} cations from Ti to Cu.*

For the furthermore considered vibronic $E_g \otimes \varepsilon_g$ interaction in the $t_{2g}^3e_g^1$ and $t_{2g}^6e_g^1$ ground state configurations of octahedral Mn^{3+} and low-spin Ni^{3+} (and in the excited E_g states of d^1 and d^6(high-spin) as well) the approximation of linear vibronic coupling yields (Section 2.5):

$$A_1(+A_2\rho_\varepsilon^{em}) = \frac{(1/2)E_{FC}(D_{4h}{}^e)}{\rho_\varepsilon^{em}} \tag{72}$$

$$K_\varepsilon(-A_2) = \frac{(1/2)E_{FC}(D_{4h}{}^e)}{(\rho_\varepsilon^{em})^2}$$

The higher-order addition is given in parentheses; it stabilises, via the $3d_{z^2}$–4s interaction, the tetragonal elongation in respect to the compression. In distinction to Eq. (69) the higher-order interaction can by no means be neglected; the energy contributions from A_2 may have magnitudes up to nearly 25% of those, stemming from A_1.

In Section 3.1 we have summarized significant criteria, which – as we think – are crucial for the selection of reliable DFT data. One point of irritation is, that Kohn–Sham DFT in its present implementations is not able to calculate the energies of electronic states in the case of orbital degeneracy (T_{2g} or T_{1g}). For example in the case of octahedrally coordinated Ti^{III} (d^1) one electron is evenly distributed between the d_{xz}, d_{yz} and d_{xy} orbitals. Such a distribution usually leads to a lower energy than the one electron/one orbital occupancy, if no correction for, what is called electron self-interaction, is applied. Similarly, in complexes with D_{4h} or D_{3d} symmetry, electronic transitions within the T_g ground state involve a doubly degenerate excited split state (e_g^1 in the given example). For the energy calculation one has of course to employ the relevant structural properties in D_{4h} or D_{3d}, but may use *an electron distribution according to the lower D_{2h} or C_s symmetry*, where e_g splits into b_{2g} and b_{3g} or a′ and a″, respectively. Thus, one creates a one-electron/one-orbital occupancy by artificially lowering the symmetry. From this consideration also follows, that the stabilisation energy of a distorted polyhedron, with the regular octahedron as the reference ($E_{JT}(D_{4h}$ or $D_{3d})$), is not directly accessible to DFT, as presumed in a previous paper [101]; here again – in order to avoid errors due to self-interaction – *the calculation of E_{JT} should be based on the solutions of the potential energy matrix at the energy minimum of an orbital singlet state*.

We have used the total energies E_t from DFT-COSMO for the derivation of the vibronic coupling parameters and force constants throughout this contribution. A more correct procedure would have been to utilise $E_t'(\equiv E_t - E_{solv})$ energies, because the electrostatic solute–solvent interaction (E_{solv}) is not associ-

ated with the *local* properties of the $M^{III}X_6^{3-}$ centres, which we are interested in d–d spectroscopy [44]. However, because the solvent energies are frequently subject of casual fluctuations, as here – due to the rather large negative charge on the solute – we chose the total energies in our calculations. Since, in the consideration of vertical Franck–Condon transitions, the assumption is met, that E_{solv} does not change essentially during the excitation, the introduced inaccuracy is only small. As one may infer from Tables 6a and 6b, for example, the coupling parameters, derived from the DFT data base, are possibly slightly overrated.

12.2. DFT and interelectronic correlations

The deficiency of DFT to reproduce the parameters of interelectronic repulsion, as they emerge from experimental d–d spectra via the application of ligand field theory, will be critically analysed now. d-Electrons in transition metal complexes are localized und subject to strong correlations in their motion. In the dynamic correlation, electrons avoid each other instantaneously, occupying to maximum extent different regions in space. This kind of correlation is well accounted for by utilising the exchange-correlation hole, intrinsic for the Kohn–Sham formulation of DFT. The static correlation is either completely neglected in a single determinant DFT approach, or considered in an effective way by an appropriate choice of the exchange-correlation functional. In ligand field theory, the mixing of Slater determinants via interelectronic repulsion accounts for this type of d–d correlation. The DFT-based ligand field model (LFDFT) [96] takes advantages of both, DFT and ligand field theory. LFDFT uses the complete set of Slater determinants, thereby comprising the various distributions of the d-electrons over the available molecular orbitals. The energies are derived utilising a common set of such orbitals, obtained in an average-of-configuration DFT calculation (AOC-DFT [102]). These energies and the explicit use of the composition of the 3d orbitals, expressed in terms of corresponding standard basis functions (d_{xy}, d_{yz}, d_{xz}, d_{z^2}, $d_{x^2-y^2}$), yields both, the Racah parameters of interelectronic repulsion (B and C) and the (5×5) matrix of the ligand field [96]. In difference to common other parameterizations, as in the angular overlap model (AOM), the crystal field theory (CFT) or combinations of these, the AOC-DFT approach, yields all parameters from first principles without additional approximations (such as parameter additivity and transferability in AOM); it also allows to describe low-symmetry complexes and avoids overparameterization. While values of the ligand field matrix elements are obtained in a quality comparable with experiment, the parameters B and C are drastically underestimated with current DFT exchange-correlation functionals. This is no severe draw-back in the context of this contribution, because B and C are usually available from the d-d spectra or can be rather well estimated from Jørgensens rules in respect to the nephelauxetic effect and its factorisation. We have applied LFDFT and critically evaluated the method in the case of the NiF_6^{3-} polyhedron in the low- and high-spin state, performing calculations with the complete set of Slater determinants and with a small set of these, restricted to only weakly excited electron configurations besides the ground state (Section 10; Table 18b). The nephelauxetic effect, as formulated by Jørgensen [10], is of sophisticated nature and utilises the spectroscopic experiment and ligand field theory. It comprises two components – the central field covalency, which is a "cloud-expanding" effect, based on the participation of *all electrons* of the central cation, and the *symmetry-restricted covalency*, which involves *d-electrons exclusively*. The latter implies a larger reduction of B and C in magnitude, if interelectronic repulsion between the somewhat delocalised $e_g(\sigma)$ electrons than between the rather localised $t_{2g}(\pi)$ electrons is involved – an effect born out from spectroscopic experiments. *This concept of a differential covalency effect does not necessarily match with DFT, where the electron density originates from all electrons,* and more importantly, *where electrons in the occupied 3d-MO's are taken as frozen (without SCF) when calculating the energies of various Slater determinants.* Aside from the discussed implications in respect to interelectronic repulsion – which are not yet fully understood, as we think – it should be emphasized, that *Kohn–Sham DFT is an orbital-based method as is ligand field theory*.

12.3. Computational comments

The DFT computations were performed with the Amsterdam Density Functional program (ADF) [103]. Large Slater-type orbital basis sets (STO, triple-ζ) with one d-type polarization function for fluorine and chloride, and the frozen core approximation up to 3p for metal ions and with 1 s for fluorine and chloride were used. A series of test geometry optimizations on MnF_6^{3-} in its ground state configuration $e_g^2 b_{2g}^1 a_{1g}^1$ in $D_{4h}{}^e$, using various exchange-correlation functionals, has been carried out. As follows from the comparison between calculated and experimental Mn–F bond lengths (Table B1 in the supplementary material), both, average Mn–F bond lengths (a_{av}) and Jahn–Teller distortions (ρ_ε^m), are best reproduced with the LDA-VWN and BP86 functionals. Other gradient-corrected functionals lead to Mn–F bond lengths and polyhedron distortions, which are distinctly larger than the experimental ones. In difference to the structural quantities, the energy splitting of, for example, T_g ground states turns out to be less sensitive with respect to the choice of a specific functional; the variation of these energies for TiF_6^{3-} and VF_6^{3-}, using various functionals – pure DFT ones (VWN to BLYP) and hybrid – type ones with various degrees of Hartree–Fock exchange (B3LYP* to X3LYP) – illustrates this for D_{4h}, D_{3d} and $D_{2h}{}^*$ molecular structures (Table B2). Also because of the low computational costs (Table B1) we have chosen the LDA-VWN functional for both, polyhedron structures and energy splitting.

For the rather highly charged (MX_6^{3-}) anions a charge-compensating polarizable solvent continuum has been introduced, by applying the conductor-like screening model (COSMO) as implemented in ADF [103]. The dielectric constant of water ($\varepsilon = 78.4$) and the solvent radii, specified in Table B3 in the supplemetary material, have been used. The solute-solvent energy makes an essential contribution to the total energy (about 40% in the V^{III} case; Tables 6a and 6b), while it largely cancels in the Franck–Condon energies (see Section 12.1). The neglect of a charge-compensating polarizing solvent drastically lowers the restoring force constant K_ε, which outweighs by far the opposite effect of the solvent on the vibronic coupling constant V_ε (Table B4). Both observations mirror the softer properties of the polyhedra in the absence of a solvent, with a more covalent M^{III}–F bond due to ligands without the imposed contrapolarising influence by counter cations and hence with reduced electronegativity. Pronounced is the effect on the radial distortion parameters and moderate on the average bond lengths, which increase by 1/3 and 3%, respectively. The resulting polyhedron structures are far from reality; the necessity to include a charge-compensation into the DFT calculations is hence obvious, if reliable data for the structure, but also for the energies and vibronic parameters are desired – as has been noticed before ([9] and Section 3.1).

We have emphasized the failure of DFT, when analysing interelectronic repulsion phenomena – and this deficiency becomes also apparent, if spin-pairing phenomena are considered. In the case of NiF_6^{3-} the vertical high-spin/low-spin separation energy $\delta_{2,4}^{eff}$ is nearly vanishing (see Section 10.1 and Table 18b), which cannot be even approximately reproduced by the calculational procedure applied here($\geq$2500 cm^{-1}). We have tested various functionals in respect to their usefulness for reliably mirroring the

Table 20
Coupling parameters and force constants K_ε – excited state values K_ε' in italics – for the $T_g \otimes \varepsilon_g$ and $E_g \otimes \varepsilon_g$ vibronic coupling in $M^{III}X_6^{3-}$ octahedra (X = F^-; for Cl^- in brackets); the radial distortion and the JT stabilisation energy in the given ground states are also listed (see text). Data for Cr^{III} and Co^{III} originate from excited states, and for Ni^{III} also the high-spin alternative was analysed.

M^{III}	Ti^{III}	V^{III}[a]	Cr^{III}	Mn^{III}	Co^{III}	Ni^{III}[a]	Cu^{III}
V_ε [eV Å^{-1}]	0.82[0.27]	0.89[0.33]	0.7[0.2$_5$]	≅0.7$_5$	0.65	0.68	≈0.2
A_1 [eV Å^{-1}]	2.25[1.80]	2.0[1.1]	1.8[1.0]	2.00[1.3$_5$]	2.00	2.05	1.2
A_2 [eV Å^{-2}]	1.1 [1.2]	0.9[0.5]	0.8[0.4]	0.70[0.5]	0.8	0.90	≈0.7
K_ε [eV Å^{-2}]	9.9[5.4]	11.9[6.2]	(12[6])[b]	9.1[5.0]	8.1	12.7[c]	(7)[d]
	7.8[5.0]	*≈7.6[≈3.7]*	*7.5[3.5]*	*7.5*	*7.7*	*10.8*	*≅5.5*
E_{JT} [eV]	0.034[0.006]	0.033[0.008]	–[b]	0.26[0.23]	0.026	0.194	–[d]
ρ_ε^m [Å]	0.083[0.050]	0.075[0.053]	–[b]	0.26[0.34]	0.081	0.189	–[d]
Ground state	$^2T_{2g}$	$^3T_{1g}$	$^4A_{2g}$	^5E_g	$^5T_{2g}$	^2E_g	$^3A_{2g}$

[a] Without configurational mixing.
[b] Magnitudes, utilizing the estimated ground state force constant $K_\varepsilon \cong 12[6]$ eV Å^{-2}, are: $E_{JT} \cong 0.02\ [0.00_5]$ and 0.16 [0.10] eV; $\rho_\varepsilon^m \cong 0.06[0.04]$ and 0.17[0.19] Å – for $T_g \otimes \varepsilon_g$ and $E_g \otimes \varepsilon_g$ vibronic interactions, respectively.
[c] K_ε for NiF_6^{3-} in the hypothetical $^4T_{1g}$ high-spin ground state is 8.6 eV Å^{-2}, yielding $E_{JT} \cong 0.027$ eV and $\rho_\varepsilon^m \cong 0.079$ Å.
[d] Magnitudes, utilising the estimated ground state force constant $K_\varepsilon \cong 7$ eV Å^{-2}, are: $E_{JT} \cong 0.00_3$ and 0.13 eV, $\rho_\varepsilon \cong 0.03$ and 0.21 Å – for the $T_g \otimes \varepsilon_g$ and $E_g \otimes \varepsilon_g$ interaction, respectively.

change in the interelectronic correlation and repulsion during a spin-flip, and found the hybrid functional B1LYP to be a good choice (Supplementary material B3, Table B5). This is, however, a rather fortuitous result – and not of essential help.

12.4. d–d spectroscopy and experimental

Finally, some critical remarks in respect to the determination of the band positions in the d–d spectra are necessary. Because all used and quoted spectra are from powder reflexion data (between 298 and 77 K, exceptionally at 4 K) and hence absolute intensities were not available, the optical transitions were located according to the absorption envelope. This procedure is surely subject to errors in the case of energetically closely neighboured split bands, but should not touch the gross results too much. Wherever the energies were controlled by DFT, there was agreement within a rather narrow error limit. Exceptions are clearly the broad-band spectra of solids $A^ITi^{III}F_4$, where the excited state splitting can only be roughly estimated, even at 77 K (Fig. 18).

Concerning the preparation of the solids, dealt with in this contribution, we refer to the given literature (see for instance [59]) – but generally remark, that the experimental effort is mostly large, and furthermore, that the handling of the mostly air- and moisture-sensitive solids for the structural and optical studies affords considerable care.

13. Final discussion and summary

13.1. The vibronic JT coupling

Table 20 summarises the JT stabilisation energies and radial distortion parameters for the halide complexes of this study in their ground states. They were derived, and the listed vibronic coupling and force constants as well, by utilising carefully selected DFT results (vide infra), supplemented by available experimental data. In order to get the complete list of coupling constants, also potential energy surfaces of singly excited states were analysed – in particular in the d^3 and d^8 cases. In such a way, E_{JT} energies and ρ_ε values are obtained for each d^n configuration and for both, $T_g \otimes \varepsilon_g$ and $E_g \otimes \varepsilon_g$ vibronic interactions. According to the presupposition of presenting structural and energy quantities, which refer to ε_g vibrations in the respective ground states and which are hence comparable within the considered range of d^n configurations, we used always the ground state force constant K_ε in these calculations (see Fig. 42). For Cr^{III} and Cu^{III}, K_ε was estimated in respect to the parameters of V^{III} and Ni^{III} (high-spin), the neighbours in the periodic table, and in consistence with the DFT-deduced K_ε'-values (Table 20). In Fig. 42 the dependence of ρ_ε^m and E_{JT} on the respective d^n configurations for each type of vibronic coupling is displayed.

In the series from Ti^{III} to Ni^{III}(high-spin) and considering $T_g \otimes \varepsilon_g$ coupling first, one observes the expected dependence of ρ_ε and

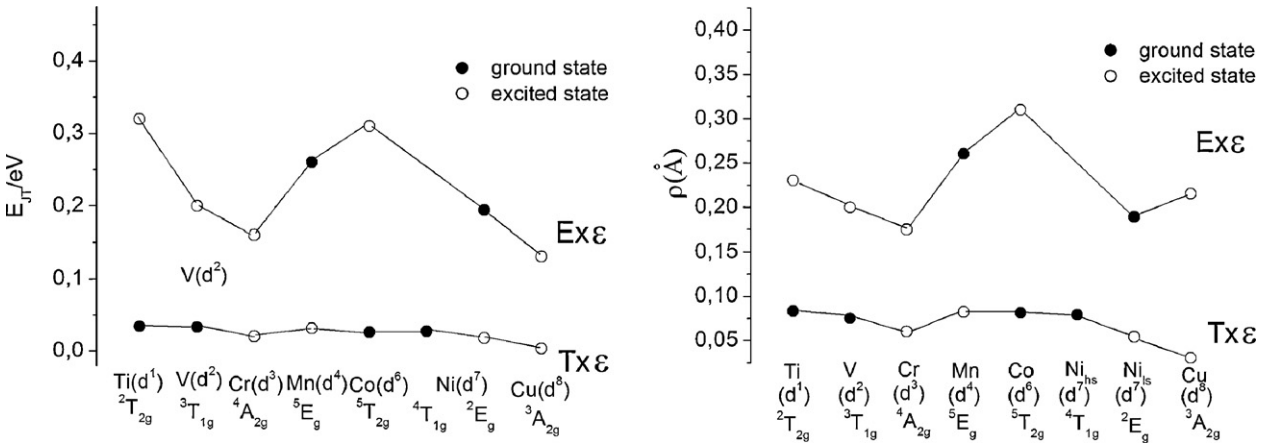

Fig. 42. The dependence of the JT stabilisation energy E_{JT} (in eV) and of the extent of the radial distortion ρ_ε^m (in Å) on the occupation number n of the $3d^n$ cation in $M^{III}F_6^{3-}$ octahedra – for $T_g \otimes \varepsilon_g$ and $E_g \otimes \varepsilon_g$ vibronic coupling, respectively. Also for the evaluation of those data, which refer to excited states, always the ground state force constant K_ε was employed (see text).

E_{JT} on the number of d-electrons – a decrease from the occupation t_{2g}^1 toward t_{2g}^3, an increase when adding e_g electrons and a decrease again, if further t_{2g} electrons are added; the enhancements in the step from d^3 to d^4 obviously mirror the more pronounced antibonding character of the e_g electrons, while the reverse effect is seen, when moving from high-spin to low-spin Ni^{III}. The main reason for the phenomenon seems to be a pronounced reduction of the force constant, if an e_g electron is added ($d^3 \rightarrow d^4$: $K_\varepsilon \approx 12 \rightarrow 9\,eV\,Å^{-2}$; low-spin to high-spin d^7: $12.7 \rightarrow 8.6\,eV\,Å^{-2}$ – see Table 20). Accordingly, the dependencies in Fig. 42 are similar to those obtained, if the M^{III} ionic radii are looked at (Tables 16a and 16b), and well-known to experimental chemists. The linear coupling parameters V_ε, reported here for the first time, decrease steadily from Ti^{III} to Ni^{III} and indicate an enhancement of the bond covalency, which nicely correlates with the increase of the M^{III} electronegativity in the same sequence – this phenomenon was thoroughly discussed in Section 8. Analogous, though much more pronounced ρ_ε and E_{JT} effects are observed in Fig. 42 for the case of $E_g \otimes \varepsilon_g$ coupling. However, the numerical values of A_1 do not vary perceptibly in dependence on the finer covalency effects just discussed, possibly because the A_2 parameters are rather approximate, due to the inability of DFT to reproduce the $3d_{z^2}$–4s interaction exactly. Very striking is the enhancement of the bond covalency, when proceeding from Ni^{III} to Cu^{III} (Section 8); in particular, V_ε decreases dramatically, but also A_1 is reduced by 30%. The large A_1/V_ε ratio for the $M^{III}F_6^{3-}$ octahedra (M^{III}: Ti–Ni) of 3.2(5) indicates, that the vibronic interaction between the ε_g mode and a σ-antibonding E_g state is considerably stronger than the one with an only π-antibonding T_{2g} state. The ratio between the corresponding JT-energies is, with about 10, the square of this number.

Also interesting is the analysis of the coupling constants, if chloro- are compared with the fluoro-complexes. While the $A_1(Cl^-)/A_1(F^-)$-ratio is 0.68(12), the $V_\varepsilon(Cl^-)/V_\varepsilon(F^-)$-ratio is, with 0.35(2), only half in magnitude. Both values indicate the expected ionicity decrease of the metal–halide bond, if F^- is substituted by the softer Cl^-; on a finer scale, the π-antibonding properties are affected to a considerably larger extent – π-overlap becomes comparatively more effective in the longer bonds of the polarisable Cl^- ligand. Due to the distinctly smaller force constants in the $M^{III}Cl_6^{3-}$ octahedra, however, the radial distortion parameters and also the ground state stabilisation energies are near to the values in the fluoride case, if $E_g \otimes \varepsilon_g$ coupling is considered. In contrast, the JT-energies are – for $T_g \otimes \varepsilon_g$ coupling – much smaller for the chloride complexes. This observation moreover explains the easy formation of $M^{III}Cl_5^{2-}$ complexes, where an enhanced ground state splitting is achieved via the loss of one soft axial ligand – which is observed for Mn^{III}.

The absolute minima of the adiabatic potential surfaces for $T_g \otimes (\varepsilon_g + \tau_{2g})$-type vibronic interactions are those, which characterise purely tetragonal polyhedron distortions ($T_g \otimes \varepsilon_g$ coupling). D_{3d} minima, originating from $T_g \otimes \tau_{2g}$ coupling solely, are saddlepoints, and this holds also for the extremum points of $D_{2h}{}^*$ symmetry; here, the higher-order vibronic coupling term W, which results from the interaction of coupled $(\varepsilon_g + \tau_{2g})$-type motions with the electronic T_g parent ground state, is vanishing. This is most probably so, because the coupling to the ε_g- dominates by far the interaction with the τ_{2g}-mode. The given general statement is valid for both, the fluoride and – even more pronounced – the chloride complexes of the 3d-M^{III} metals. A recent investigation [100] on pseudo-octahedral cyanide complexes of Ti^{III}, V^{III} and low-spin Mn^{III}, Fe^{III} shows, that this is not necessarily so. Here, only for Ti^{III} $E_{JT}(D_{4h})$ is largest, while for the other polyhedra $E_{JT}(D_{3d})$ is reported to dominate in energy. However, the JT stabilisation energies are very small in these cases, with magnitudes around 100(40) cm^{-1}, as one might indeed suppose in view of the pronounced covalent character of the M^{III}–CN^- bond with back-donating π-properties.

Fascinating compounds are elpasolites with NiF_6^{3-} polyhedra, first prepared by Klemm and Hoppe [104], in which Ni^{III} appears in the low-spin state. The application of DFT allowed here to construct the adiabatic potential energy curve of also high-spin Ni^{III} [99], whose minimum is calculated to be located about 100 cm^{-1} above the one for the low-spin ground state (Section 10). Generally, DFT is of only restricted help in the analysis of high-spin/low-spin equilibria – unless reliable information about the magnitude of interelectronic replusion and correlation effects is available from experiment, as in this case.

The formalism, used in this contribution [6], differs from the one, frequently adopted in literature [105]. The latter is based on vibronic parameters A_1, V_ε, A_2, K_ε, which have the dimension of an energy, and on dimensionless vibrational coordinates Q_i ($i = \theta$, ε), in the $T_g \otimes \varepsilon_g$ and $E_g \otimes \varepsilon_g$ coupling cases. However, because in this study ρ_ε is a significant observable and also reliably obtainable from DFT, we prefer the here applied approach.

13.2. The influence of strain and cooperavity

The investigated model solids $A'_2AM^{III}F_6$ were assumed to contain isolated $M^{III}(F_t)_6^{3-}$ octahedra, which possess, with regard to their individual JT distortions, a widely unrestricted geometrical freedom in respect to each other in the elpasolite lattice; the large and polarisable A', A alkaline cations embody only small disturbances and thus mediate merely very weak elastic interactions between the JT-distorted complex anions. The mentioned (here absent) intermolecular interactions represent, what is usually called the cooperative Jahn–Teller effect [106]. In a mechanistic, molecular-type description [1,6], these interactions lower the force constant K_ε by favourably adjusting the individual polyhedron distortions toward each other. Accordingly, the radial distortion and the JT stabilisation energy increase, if compared with a single, vibronically isolated JT-unstable entity, which is embedded in the higher-sphere environment of $M^{III}(F_t)_6^{3-}$ octahedra with orbital singlet ground states (M^{III} = Cr^{III} and Fe^{III}, Cu^{III}(both high-spin) or In^{III}, Ga^{III} for example). Fig. 11 substantiates by the d-d spectra of mixed crystals $Cs_2Na(In_{1-x}Ti_x)F_6$, that the premise of very weak elastic coupling between the TiF_6^{3-} polyhedra is satisfied: the splitting of the excited E_g state comes out to be independent on x.

If one proceeds to compounds $AM^{III}F_4$ with structures based on $M^{III}(F_b)_4(F_t)_2^-$ octahedra, *which possess common bridging ligands (F_b) in the equatorial plane* (Fig. 16) – or in one molecular trans-arrangement and two cis-oriented directions (Fig. 28) – the elastic coupling is of a different quality. The modification of K_ε with respect to the reference situation with (in fair approximation) terminal ligands exclusively was taken into account in a strain model in Section 4, by the introduction of an additional parameter K_s – modeling the *different elastic properties of F_b- in comparison to F_t-ligands*. However, the structural pecularities of these types of solids demand the further consideration of the *different binding qualities* of the two kinds of ligands. This difference becomes immediately apparent, if the structural and spectroscopic properties of compounds $M^{III}F_3$ with $M^{III}(F_b)_6$ octahedra are contrasted with those of the elpasolites (Fig. 15). We have transposed this binding diversity into a strain concept via the definition of additional first-order vibronic coupling V_ε^s and A_1^s increments, supplementing V_ε and A_1, valid for the $M^{III}(F_t)_6^{3-}$ parent complex (see Section 4). The results of a strain analysis along these lines confirm qualitative conclusions from chemical intuition. As may be taken from Table 5, for solids $A^IM^{III}F_4$ containing Ti^{III} and high-spin Co^{III} with T_{2g} ground states, the K_s/K_ε ratio is rather large with 0.39(2) and indicates a pronounced soft mode behaviour of the $\alpha_{1g}(\varepsilon_g)$ vibration toward a tetragonal compression. The binding strain contributions via V_ε^s

and A_1^s, on the other hand, if four equatorial F_t ligands are replaced by F_b, amount to 24(8)% and ≈28(5)% (derived from excited states), respectively. These numbers yield – if transposed into corresponding E_{JT} ratios – an enhancement of about 59%, which is larger than the increase by the elastic strain. Though both types of strain-increments (V_ε^s, A_1^s and K_s) indicate a considerable perturbation of particularly the $T_g \otimes \varepsilon_g$ vibronic coupling landscape, they are still perceptibly smaller in respect to the situation, characterised by V_ε, A_1, A_2 and K_ε solely. Accordingly our approach, to consider the first-order JT effect as the basic phenomenon for the ground state stabilisation, is surely justified. Nevertheless, in the $T_g \otimes \varepsilon_g$ coupling case, the total strain effect more than doubles the JT-energy. An interesting result for V^{III} is, that possibly an orthorhombic deformation of the trans-configured $V(F_t)_2(F_b)_4^-$ octahedra in solids $AV^{III}F_4$ occurs (Tables 4 and 5; Fig. 22), because here – in contrast to the situation for Ti^{III} and Co^{III} – strain and JT coupling act in sterically different directions. Furthermore, though the error limit is considerable, we could even derive vibronic coupling increments A_1^s and V_ε^s for the trans-, and also for the cis-$Cr^{III}(F_t)_2(F_b)_4^-$ octahedra in solids $ACr^{III}F_4$, with magnitudes not far from those, just discussed (Table 5). In the case of the trans-$Mn^{III}(F_t)_2(F_b)_4^-$ entities in compounds $AMn^{III}F_4$ finally, sufficient experimental data are available for exact calculations within the splitting of the $^5B_{1g}$ ground state in Fig. 31. The deduced K_s/K_ε and A_1^s/A_1 ratios of 0.34 and 0.18, though smaller, still lie acceptably close to the values for the complexes with T_g ground states (Section 7, Table 13); the φ-dependence of the ^5B_g ground state potential surface (in D_{2h}) is displayed in Fig. 31. We refrained from performing DFT calculations, using sections of the $AM^{III}F_4$-structure centred around the basic $M^{III}(F_t)_2(F_b)_4^-$ octahedron, because the choice of such clusters is rather arbitrary, unless the translational symmetry is properly accounted for – affording more sophisticated calculational procedures (see the following subsection).

The advantage of the proposed strain model is, that the newly defined vibronic parameter increments bear direct significance in respect to observables, such as the polyhedron structures and JT stabilisation energies – a draw-back is, that more unknowns, originating from the elastic and binding strain have to be fitted, instead of one global constant in Hams approach [41]. We add, that the novel strain concept is flexible enough, to account – via K_s – not only for the modification of the elastic properties, induced by local rearrangements within the basic polyhedron (for example by the substitution of F_t- by F_b-ligands), but also for changes, introduced into the lattice via the cooperative-elastic coupling between the JT-distortions of the single polyhedra – giving rise to long-range ferro- or antiferrodistortive order phenomena.

13.3. Recent theoretical and computational approaches

This contribution is sited in solid-state coordination chemistry, with the aim to use DFT results as a data base, wherever these turned out to be reliable. Also, only stoichiometric (not doped) compounds were considered, always close to the chemical reality – restricting to halide compounds of the $M^{III}(3d)$ series and host structures, which are suited to serve as model systems. Though not directly related to this thematic, we shortly focus our attention on some novel trends in the field of JT-coupling with a closer reference to theoretical and solid-state physics. We shortly comment on Cu^{2+}-doped fluoride hosts, because the formal treatment on a molecular level is identical with that in Sections 7.1 and 7.2 for high-spin Mn^{3+}, possessing a d^4 configuration (a spherical d^5 shell is the difference). Interesting indeed are here the results of cluster computations [107], performed on Cu^{2+}-doped $K_2Zn(Mg)F_4$, for example. The respective layer structure resembles closely that of $TlAlF_4$ in Fig. 16 – with pseudo-octahedral $Zn(F_t)_2(F_b)_4$ host sites, subject to elastic and binding strain increments due to the presence of bridging ligands in the molecular *xy*-plane. These sites are tetragonally compressed at very low doping levels, possessing a d_{z^2} ground state, but with a distinct delocalisation toward $d_{x^2-y^2}$ [108,109,105]; the energy barrier of the ground state potential curve at 180° (see Fig. 31) is tiny or even vanishing. The calculations, with the choice of sections from the structure of varying size, reproduce the compressed coordination for Cu^{2+} – but the computed energy gap toward the elongated $Cu(F_t)_2(F_b)_4$ conformation is far from reality, with at least 0.2 eV [110]. A better approach to reality than the sketched cluster calculations – which undoubtedly have their merits – are computations, which use the full symmetry of the lattice and its periodicity, with *the unit cell* as the basic structural entity [111]. Calculations of this kind on Cs_2CuCl_4 and related compounds, and on the Co^{2+}-analogues, for example, show, that the structural properties of the $Cu(Co)Cl_4^{2-}$ tetrahedra can be reproduced within rather narrow limits [44]. An interesting feature of the structural behaviour of the $Cu(F_t)_2(F_b)_2$ octahedra in the K_2ZnF_4-, but also in the Ba_2ZnF_6-host [112] – where the elastic strain component is enhanced in respect to the former lattice – is, that the local distortion changes from compressed to elongated, when increasing the Cu^{2+} concentration [108,112]. It is here the presence of cooperative-elastic forces between the JT species, which stabilise the elongated conformation as compared to the situation at very low doping levels. These experimental observations might be challenging to theorists. We particularly note the progress in the treatment of the cubic anisotropy, if Jahn–Teller cations are incorporated into host structures, which offer sites of perfect O_h symmetry – as Cu^{2+} in MgO [113]. The phenomena, if Cu^{2+} occupies octahedral sites, however, where the volume of the substituted cation exceeds by far that of the dopants, are still less well understood (Cu^{2+}/CaO, SrO) [114].

Acknowledgements

This contribution is dedicated to C.K. Jørgensen, O. Schmitz-DuMont and others, who developed an intuitive sense for what d–d spectroscopy and ligand field theory are able to accomplish, in theory and application. The typing and setting work for the manuscript by Mrs. D. Kloss (Marburg) is gratefully appreciated.

Appendix A.

A.1. The $T \otimes (\varepsilon + \tau_2)$ coupling matrix

The general vibronic Hamiltonian is, up to second order:

$$
\begin{aligned}
H = {} & \left[\frac{1}{2}K_\varepsilon(Q_\theta^2 + Q_{\bar\theta}^2) + \frac{1}{2}K_\tau(Q_\xi^2 + Q_\eta^2 + Q_\zeta^2)\right] I \\
& + \left[V_\varepsilon Q_\theta + \frac{1}{2}L_\varepsilon(Q_\varepsilon^2 - Q_{\bar\theta}^2) - \frac{1}{4}L_\tau(2Q_\zeta^2 - Q_\xi^2 - Q_\eta^2)\right] C_\theta \\
& + \left[V_\varepsilon Q_\varepsilon + L_\varepsilon Q_\theta Q_\varepsilon - \frac{\sqrt{3}}{4}L_\tau(Q_\xi^2 - Q_\eta^2)\right] C_\varepsilon \\
& + \left[V_\tau Q_\xi + X_\tau Q_\eta Q_\zeta + W\left(-\frac{1}{2}Q_\theta + \frac{\sqrt{3}}{2}Q_\varepsilon\right) Q_\xi\right] C_\xi \\
& + \left[V_\tau Q_\eta + X_\tau Q_\xi Q_\zeta + W\left(-\frac{1}{2}Q_\theta - \frac{\sqrt{3}}{2}Q_\varepsilon\right) Q_\eta\right] C_\eta \\
& + [V_\tau Q_\zeta + X_\tau Q_\xi Q_\eta + W Q_\zeta Q_\theta] C_\zeta
\end{aligned}
$$

The basis of the matrix representation is $T_{1\alpha}$, $T_{1\beta}$, $T_{1\gamma}$ or $T_{2\xi}$, $T_{2\eta}$, $T_{2\zeta}$, using Griffith's standard notations. I is the (3×3) unit matrix, and the C_j ($j = \theta, \varepsilon; \xi, \eta, \zeta$) matrices, containing the appropriate

coupling coefficients, are defined as:

$$C_\theta = \begin{vmatrix} \frac{1}{2} & 0 & 0 \\ 0 & \frac{1}{2} & 0 \\ 0 & 0 & -1 \end{vmatrix} \quad C_\varepsilon = \begin{vmatrix} -\frac{\sqrt{3}}{2} & 0 & 0 \\ 0 & \frac{\sqrt{3}}{2} & 0 \\ 0 & 0 & 0 \end{vmatrix}$$

$$C_\xi = \begin{vmatrix} 0 & 0 & 0 \\ 0 & 0 & -\frac{1}{2} \\ 0 & -\frac{1}{2} & 0 \end{vmatrix} \quad C_\eta = \begin{vmatrix} 0 & 0 & -\frac{1}{2} \\ 0 & 0 & 0 \\ -\frac{1}{2} & 0 & 0 \end{vmatrix} \quad C_\zeta = \begin{vmatrix} 0 & -\frac{1}{2} & 0 \\ -\frac{1}{2} & 0 & 0 \\ 0 & 0 & 0 \end{vmatrix}$$

K_ε and K_τ are the harmonic force constants, V_ε and V_τ the linear JT vibronic constants for the $T\otimes\varepsilon$ and $T\otimes\tau_2$ direct products, respectively. W is the quadratic constant arising from the coupling between τ_2 and ε vibrations, and L_ε, L_τ refer to quadratic coupling constants resulting from the non-totally symmetric part of the $\varepsilon\otimes\varepsilon$ and $\tau_2\otimes\tau_2$ symmetrized direct products. The second order coupling constant X_τ is non-diagonal within the $\tau_{2g}\otimes\tau_{2g}$ direct product and couples different components of the active vibration. All constants are obtained from the corresponding many electron wavefunctions.

We have, contrary to the usual convention – for the sake of a better overview of the coupling constants in the various interaction mechanism – reduced the C_ξ, C_η, C_ζ matrices by a factor of 1/2. Here, for example in the $T\otimes\tau_2$ ($D_{3h}{}^c$) and $T\otimes\varepsilon$ ($D_{4h}{}^c$) coupling cases of a d^1 cation, a direct comparison of the π-antibonding effects is possible when inspecting the first-order relations (Fig. 4):

$$E_{JT} = \frac{1}{2} V_\tau \rho_\tau \equiv \delta_2{}^\tau \text{ and } E_{JT} = \frac{1}{2} V_\varepsilon \rho_\varepsilon \equiv \delta_2$$

A.2. $V^{IV}OX_5{}^{3-}$ impurity centres

The presence of $V^{IV}OX_5{}^{3-}$ centres (X = F^-, Cl^-) in elpasolites $A_2'AVX_6$ (Fig. A1) depicts the d–d spectrum of the elpasolitic mixed crystal $K_2NaTi_{0.9}{}^{IV}V_{0.1}{}^{IV}OF_5$. The tetragonally compressed d^1-polyhedron of C_{4v} symmetry gives rise to a pronounced Jahn–Teller splitting of the parent $^2T_{2g}$ ground state. We assign the high-intensity band at 9500 cm^{-1} to the $^2B_2 \rightarrow {}^2E$ transition (=$3\delta_2$); it appears in the spectra of the vanadium(III) fluoride-elpasolites at nearly the same energy, obviously due to the presence of a $VOF_5{}^{3-}$ impurity centre (see below) (Fig. 20).The much weaker band at 15,800 cm^{-1} is accordingly the $^2B_2 \rightarrow {}^2B_1$ excitation (ΔE), which vanishes under the $_a{}^3T_{1g} \rightarrow {}^3T_{2g}$ band-envelope of V(III). The $^2B_2 \rightarrow {}^2A_1$ transition is expected at $>40 \times 10^3$ cm^{-1}.

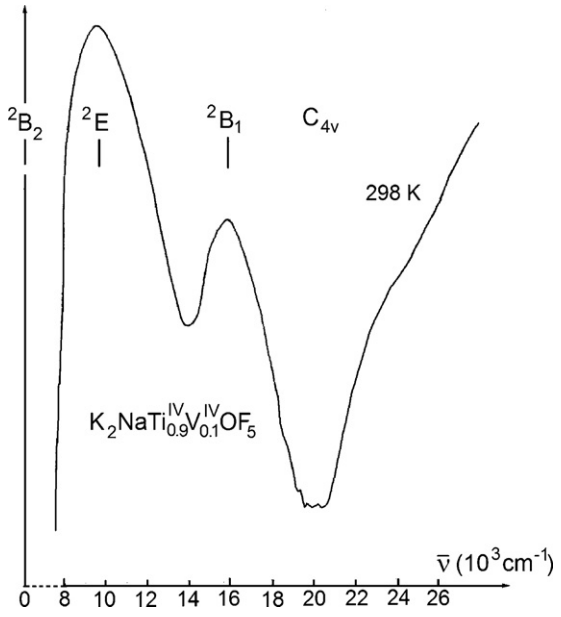

Fig. A1. The d–d spectrum, referring to the colour centre.

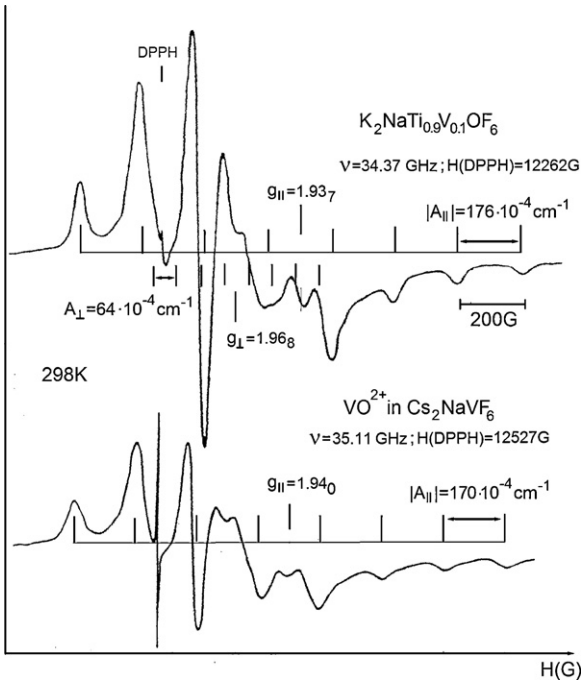

Fig. A2. Q–band EPR spectra of the solid in Fig. A1 and of $V^{IV}OF_5{}^{3-}$ as an impurity centre.

The master equations, transposing the g- and hyperfine-tensor components for a d^1 cation in the b_{2g} MO into binding parameters [115], and further parameter choices [43] are given below.

$V^{IV}O^{2+}$ centre – d_{xy} ground state: $\psi = \alpha\ d_{xy} - \beta\ L_{xy}$

$\delta g_{||} = 2.00_2 - g_{||} = 8k_{||}{}^2\zeta_0/\Delta E \quad \delta g_\perp = 2.00_2 - g_\perp = 2k_\perp{}^2\zeta_0/3\delta_2 \quad (\zeta_o = 250\ cm^{-1})$

$A_{||} = P\ \{-(\kappa + \frac{4}{7})\alpha^2 - \frac{3}{7}\delta g_\perp - \delta g_{||}\} \quad A_\perp = P\ \{-(\kappa - \frac{2}{7})\alpha^2 - \frac{11}{14}\delta g_\perp\}$

Meaningful results are only obtained with negative hyperfine tensor components:

$P = 170\cdot10^{-4}$ cm^{-1}	$K_2NaTi_{0.9}{}^{IV}V_{0.1}{}^{IV}OF_5 \Rightarrow k_{||} = 0.7_1$, $k_\perp \cong 0.8_0$;
$\kappa = 0.78$	$A_{||} = -176$, $A_\perp = -64 \cdot 10^{-4}$ cm^{-1} and $\alpha = 0.84$

The large mixing coefficient α, which refers to the equatorial V^{IV}–ligand bonds, is in accord with the pronounced ionic fluoride coordination in the xy-plane, as is the covalency parameters $k_\perp$.

Interestingly enough, the EPR spectra of the chloride elpasolites also provide evidence for the presence of $V^{IV}O^{2+}$ impurities (Fig. A3). From the well resolved $A_{||}$ hyperfine structure and the g-values a MO coefficient $\alpha \cong 0.80$ is calculated. This indicates the

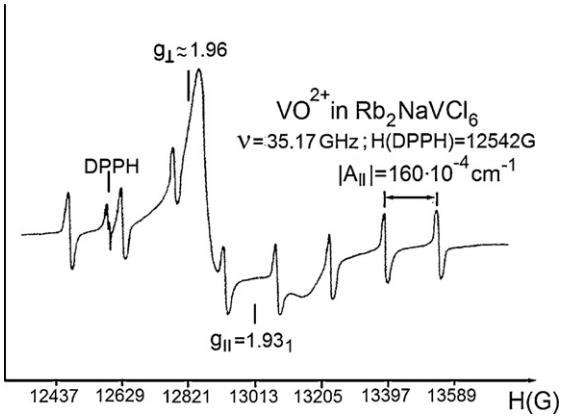

Fig. A3. Q–band EPR spectrum of impurity centres in V^{III}-chloride-elpasolites.

expected larger π-electron delocalisation in the VCl_4-plane. $A_\perp$ is about $-60\times10^{-4}\,cm^{-1}$ and responsible for the weak additional spectroscopic features between the second and fifth $A_{||}$-hyperfine lines.

VOX_5^{3-} impurity centres are also indicated in the IR spectra of V^{III} elpasolites; here, a sharp band at ≅940 cm^{-1} appears, which is tentatively assigned to the V^{IV}–O vibration. This band is also seen in the IR spectra of fluoride and chloride alpasolites of Ti^{III} (at ≅910 cm^{-1}), where the $Ti^{IV}OX_5$ centre is otherwise silent in EPR and the d–d spectra.

A.3. Vibronic coupling in the $Cr(X_t)_6^{3-}$(X = Cl^-, F^-) octahedra, as derived by DFT

1. Energies and ρ-values for the minimum positions of the excited state adiabatic potential energy curves for the following MO configurations in D_{4h} (parent configuration in O_h:$t_{2g}^2e_g^1$):

$^4B_{2g}(e_g^2b_{1g}^1) - D_{4h}{}^c$:

$$E_1{}^c = \frac{1}{2}K'_\varepsilon\rho_\varepsilon^2 + \Delta + V_\varepsilon\rho_\varepsilon - (A_1 - A_2\rho_\varepsilon)\rho_\varepsilon$$
$$\rho_\varepsilon^{cm} = \frac{A_1 - V_\varepsilon}{K'_\varepsilon + 2A_2}$$

$^4A_{2g}(e_g^2a_{1g}^1) - D_{4h}{}^e$:

$$E_2{}^e = \frac{1}{2}K'_\varepsilon\rho_\varepsilon^2 + \Delta + 12B - V_\varepsilon\rho_\varepsilon - (A_1 + A_2\rho_\varepsilon)\rho_\varepsilon$$
$$\rho_\varepsilon^{em} = \frac{A_1 + V_\varepsilon}{K'_\varepsilon - 2A_2}$$

$^4E_g(e_g^1b_{2g}^1a_{1g}^1) - D_{4h}{}^e$:

$$E_3{}^e = \frac{1}{2}K'_\varepsilon\rho_\varepsilon^2 + \Delta + 3B + \frac{1}{2}V_\varepsilon\rho_\varepsilon - (A_1 + A_2\rho_\varepsilon)\rho_\varepsilon$$
$$\rho_\varepsilon^{em} = \frac{A_1 - 1/2V_\varepsilon}{K'_\varepsilon - 2A_2}$$

$^4E_g(e_g^1b_{2g}^1b_{1g}^1) - D_{4h}{}^c$:

$$E_4{}^c = \frac{1}{2}K'_\varepsilon\rho_\varepsilon^2 + \Delta + 9B - \frac{1}{2}V_\varepsilon\rho_\varepsilon - (A_1 - A_2\rho_\varepsilon)\rho_\varepsilon$$
$$\rho_\varepsilon^{cm} = \frac{A_1 + 1/2V_\varepsilon}{K'_\varepsilon + 2A_2}$$

2. Franck–Condon transitions between:

$^4B_{2g}$ and $^4A_{2g}$:

$$E_{FC}{}^{(a)} = E_2{}^c - E_1{}^c(\text{at }\rho_\varepsilon^{cm}) = 12B + 2(A_1 - A_2\rho_\varepsilon^{cm})\rho_\varepsilon^{cm}$$

$^4A_{2g}$ and $^4B_{2g}$:

$$E_{FC}{}^{(b)} = E_1{}^e - E_2{}^e\,(\text{at }\rho_\varepsilon^{em}) = -12B + 2(A_1 + A_2\rho_\varepsilon^{em})\rho_\varepsilon^{em}$$

The four energy equations under 1. are diagonal energies of the matrices (52), with the substitutions:

$$2\delta_2 = V_\varepsilon\rho_\varepsilon(L_\varepsilon \cong 0)$$

$$2\delta_1(\delta'_1) = (A_1 + (-)A_2\rho_\varepsilon)\rho_\varepsilon$$

where $(\delta_1; \rho_\varepsilon^e)$ and $(\delta_1'; \rho_\varepsilon^c)$ refer to elongated and compressed octahedra, respectively. Note also the sign change in the expressions for the splitting parameters when switching from a tetragonal elongation to a D_{4h} compression. The results of the DFT calculations are summarised in Table 10. Because we had to use one energy connected with an $a_{1g}{}^1$ configuration, the parameter A_2 might be slightly erroneous, due to a not necessarily correct consideration of the $3d_{z^2}$–4s interaction (vide supra) by DFT, particularly in the case of the chloride polyhedron.

A.4. Analysis of the $^2E_g(d^7)$ ground state splitting in D_{4h}

In the following we list the MO configurations in D_{4h} and their ligand field energies, with the octahedral ^2E_g ground state as the reference, which we have used to derive the equations for four distortion parameters and four Franck–Condon energies. The latter refer to the diagonal energies of the lowest states in the $^2A_{1g}$ and $^2B_{1g}$ matrices, and to the energies of the lowest two B_{2g} states, *after diagonalisation with respect to the tetragonal ligand field component*. For the optimisation with respect to the radial distortion parameter, the restoring energy ($(1/2)K_\varepsilon\rho_\varepsilon^2$ and $(1/2)K'_\varepsilon\rho'^2_\varepsilon$ for the $t_{2g}{}^6e_g$ ground and the $t_{2g}{}^5e_g{}^2$ excited state configuration, respectively) has to be added to the listed ligand field energies:

$$D_{4h}{}^e{:}^2A_{1g}(e_g{}^4b_{2g}{}^2a_{1g}{}^1) \Rightarrow E = -(A_1 + A_2\rho_\varepsilon{}^e)\rho_\varepsilon{}^e;\ \rho_\varepsilon{}^{em} = \frac{A_1}{K_\varepsilon - 2A_2}$$

$$D_{4h}{}^c{:}^2B_{1g}(b_{2g}{}^2e_g{}^4b_{1g}{}^1) \Rightarrow E = -(A_1 - A_2\rho_\varepsilon{}^c)\rho_\varepsilon{}^c;\ \rho_\varepsilon{}^{cm} = \frac{A_1}{K_\varepsilon + 2A_2}$$

$$D_{4h}{}^e : E_{FC}(^2A_{1g}\rightarrow{}^2B_{1g}) = 2(A_1 + A_2\rho_\varepsilon{}^{em})\rho_\varepsilon{}^{em} = 4\delta_1$$

$$D_{4h}{}^c : E_{FC}(^2B_{1g}\rightarrow{}^2A_{1g}) = 2(A_1 - A_2\rho_\varepsilon{}^{cm})\rho_\varepsilon{}^{cm} = 4\delta'_1$$

$$D_{4h}{}^e{:}^2B_{2g}(e_g{}^4b_{2g}{}^1a_{1g}{}^2) \Rightarrow$$

$$E = \Delta - V_\varepsilon\rho'_\varepsilon{}^e - 2(A_1 + A_2\rho'_\varepsilon{}^e)\rho'_\varepsilon{}^e + 20B;\ \rho'_\varepsilon{}^{em} = \frac{2A_1 + V_\varepsilon}{K'_\varepsilon - 4A_2}$$

$$D_{4h}{}^c{:}^2B_{2g}(b_{2g}{}^1e_g{}^4b_{1g}{}^2) \Rightarrow$$

$$E = \Delta + V_\varepsilon\rho'_\varepsilon{}^c - 2(A_1 - A_2\rho'_\varepsilon{}^c)\rho'_\varepsilon{}^c;\ \rho'_\varepsilon{}^{cm} = \frac{2A_1 - V_\varepsilon}{K'_\varepsilon + 4A_2}$$

$$D_{4h}{}^e : E_{FC}{}^e(^2A_{1g}\rightarrow{}^2B_{2g}[e_g{}^4b_{2g}{}^1a_{1g}{}^2]) = \Delta - 2\delta_1 - 2\delta_2 + 20B$$

$$E_{FC}{}^e(^2A_{1g}\rightarrow{}^2B_{2g}[e_g{}^4b_{2g}{}^1b_{1g}{}^2]) = \Delta + 6\delta_1 - 2\delta_2$$

We are aware, that the utilized Franck–Condon energies involve excitations with the participation of the a_{1g} orbital and may give rise to small numerical errors in the magnitude of A_2 (see text).

Appendix B. Supplementary data

Supplementary data associated with this article can be found, in the online version, at doi:10.1016/j.ccr.2010.04.015.

References

[1] D. Reinen, C. Friebel, Struct. Bonding 37 (1979) 1.
[2] M.L. Halcrow, Dalton Trans. (2003) 4375.
[3] B. Murphy, B. Hathaway, Coord. Chem. Rev. 243 (2003) 237, classical approach.
[4] M.D. Kaplan, Physica C 180 (1991) 351.
[5] D. Reinen, J. Wegwerth, Physica C 183 (1991) 261.
[6] D. Reinen, M. Atanasov, Magn. Reson. Rev. 15 (1991) 167.
[7] D. Reinen, M. Atanasov, P. Köhler, J. Mol. Struct. 838 (2007) 151.
[8] A. Agresti, J.H. Ammeter, M. Bacci, J. Chem. Phys. 81 (1984) 1861; A. Agresti, J.H. Ammeter, M. Bacci, J. Chem. Phys. 82 (1985) 5299.
[9] D. Reinen, M. Atanasov, W. Massa, Z. Anorg. Allg. Chem. 632 (2006) 1375.
[10] C.K. Jørgensen, Oxidation Numbers and Oxidation States, Springer, 1969; C.K. Jørgensen, Struct. Bonding 1 (1966) 3.
[11] P. Köhl, D. Reinen, G. Decher, B. Wanklyn, Zeitschr. Kristallogr. 153 (1980) 211.
[12] J. Pebler, K. Schmidt, F. Steffens, D. Reinen, J. Solid State Chem. 25 (1978) 107.
[13] A.B.P. Lever, Comprehensive Coordination Chemistry, Elsevier, 2003, II, Notes on Time Frames, Vol. 2, 2.34, p. 435.
[14] H. Brokopf, D. Reinen, O. Schmitz-Du Mont, Z. Physik. Chem. NF 68 (1969) 228; G.D. Jones, Phys. Rev. 155 (1967) 259.
[15] J.T. Hoff, J.A. Konigstein, Chem. Phys. 1 (1972) 232.
[16] I.B. Bersuker:, The Jahn–Teller Effect and Vibronic Interactions in Modern Chemistry, Plenum Press, New York, 1984 (with supplementing reference volume: The Jahn–Teller Effect—A Bibliographic Review).
[17] D. Reinen, M. Atanasov, S.-L. Lee, Coord. Chem. Rev 175 (1998) 91; M. Atanasov, D. Reinen, in: A.B.P. Lever (Ed.), Comprehensive Coordination Chemistry II, vol. I, Fundamentals, Elsevier, 2003, 1.36, 669.
[18] U. Öpik, M.H.L. Pryce, F. R. S. Proc. R. Soc. Lond. Ser. A 238 (1957) 425.
[19] A. Ceulemans, D. Beyens, L.G. Vanquickenborne, J. Am. Chem. Soc. 106 (1984) 5824.
[20] P. Murray-Rust, H.-B. Bürgi, J.D. Dunitz, Acta Crystallogr. A35 (1979) 703.
[21] P. Curie, Ouvres de Pierre Curie, Gauthiers-Villars, Paris, 1908, p. 118.
[22] F.J. Weißenhorn, Doctoral thesis, Tübingen, Germany, 1972.
[23] R. Hoppe, E. Alter, Z. Anorg. Allg. Chem. 403 (1974) 127.
[24] R. Ameis, S. Kremer, D. Reinen, Inorg. Chem. 24 (1985) 2751.
[25] (a) I.B. Bersuker, J. Comput. Chem. 18 (1997) 260; (b) M. Atanasov, C.A. Daul, Chimia 59 (2005) 504.
[26] K. Nakamoto, Infrared and Raman Spectroscopy of Inorganic and Coordination Compounds, Part A, Wiley-Interscience, 1997.
[27] T.M. Dunn, Trans. Faraday Soc. 57 (1961) 1441.
[28] R. Hoppe, S. Becker, Z. Anorg. Allg. Chem. 568 (1989) 126.
[29] P. Köhler, W. Massa, D. Reinen, B. Hofman, R. Hoppe, Z. Anorg. Allg. Chem. 446 (1978) 131.
[30] B.N. Figgis, M.A. Hitchman, Ligand Field Theory and its Applications, Wiley-VCH, 2000.
[31] A. Hartung, Doctoral thesis, Marburg, Germany, 1978.
[32] P. Köhler, Diploma and doctoral thesis, Marburg, Germany, 1974 and 1976.
[33] J. Omaly, P. Batail, D. Grandjean, D. Avignant, J.C. Cousseins, Acta Crystallogr. B32 (1976) 2106.
[34] R. Sabatier, G. Charroin, D. Avignant, J.C. Cousseins, R. Chevalier, Acta Crystallogr. B35 (1979) 1333.
[35] R. Sabatier, A.M. Vasson, P. Lethuiller, J.L. Soubeyrous, R. Chaevalier, J. Cousseins, Mater. Res. Bull. 17 (1982) 369.
[36] W. Massa, D. Babel, M. Epple, W. Rüdorff, Rev. Chim. Miner. 23 (1986) 508.
[37] M. Leblanc, J. Pannetier, G. Ferey, R. de Pape, Rev. Chim. Miner. 22 (1985) 107.
[38] G. Heger, R. Geller, D. Babel, Solid State Commun. 9 (1971) 335; J. Lapasset, P. Sciau, J. Moret, N. Gros, Acta Crystallogr. B42 (1986) 258.
[39] A. Tressaud, J. Galy, J. Portier, Bull. Soc. Fr. Minér. Crystallogr. 92 (1969) 335; M.C. Moron, A. Bulou, C. Pique, J.L. Fourquet, J. Phys. Condens. Mat. 2 (1990) 8269.
[40] D. Babel, F. Wall, G. Heger, Z. Naturforsch. B29 (1974) 139.
[41] F.S. Ham, Phys. Rev. A138 (1965) 1727, and in: Electron Paramagnetic Resonance, Plenum Press, New York (1972).
[42] M.J. Riley, M.A. Hitchman, D. Reinen, G. Steffen, Inorg. Chem. 27 (1988) 1924; D. Reinen, M. Hitchman, Z. Physik. Chem. 200 (1997) 11.
[43] H. Werner, T. Ngo-Khac, C. Friebel, P. Köhler, D. Reinen, Z. Naturforsch. 36b (1981) 322.
[44] M. Atanasov, B. Delley, D. Reinen, Z. Anorg. Allg. Chem., in press.
[45] J.R. Perumareddi, J. Phys. Chem. 71 (10) (1967) 3144.
[46] D. Reinen, Z. Naturforsch. 23a (1968) 521.
[47] R. Hoppe, E. Alter, Z. Anorg. Allg. Chem. 412 (1975) 110.
[48] C.J. Ballhausen, F. Winther, Acta Chem. Scand. 13 (1959) 1729.
[49] G.C. Allen, K.D. Warren, Struct. Bonding 9 (1971) 67.
[50] C. Reber, H.U. Güdel, G. Meyer, Th. Schleid, C.A. Daul, Inorg. Chem. 28 (1989) 3249.
[51] P. Daniel, A. Bulou, M. Leblanc, M. Rousseau, J. Nóuet, Mater. Res. Bull. 25 (1990) 413.
[52] J.R. Perumareddi, J. Phys. Chem. 76 (1972) 3401.
[53] D. Babel, R. Haegele, J. Solid State Chem. 18 (1976) 39.
[54] D. Reinen, Struct. Bonding 6 (1969) 30.
[55] O.S. Wenger, H.U. Güdel, J. Chem. Phys. 114 (2001) 5832.
[56] J. Ferguson, D.L. Wood, K. Knox, J. Chem. Phys. 39 (1963) 890.
[57] H.L. Schläfer, Inorg. Chem. 6 (1967) 1528.
[58] Kozhina, Shapkin, Russ. J. Inorg. Chem. 12 (1967) 1161; G. Brand, L. Baraduc, C. R. Acad. Ser. C: Sci. Chim. 272/2 (1971) 1328.
[59] W. Massa, D. Babel, Chem. Rev. 88 (1988) 275; D. Babel, A. Tressaud, in: P. Hagenmüller (Ed.), Inorganic Solid Fluorides, Acad. Press, 1985.
[60] S. Becker, R. Hoppe, Z. Anorg. Allg. Chem. 579 (1989) 16.
[61] J.-E. Jørgensen, W.G. Marshall, R.I. Smith, Acta Crystallogr. B60 (2004) 669.
[62] (a) St. Andersson, J. Galy, Acta Crystallogr. B25 (1969) 847; (b) R. Peschel, D. Babel, Z. Anorg. Allg. Chem. 623 (1997) 1614; (c) G. Knoke, W. Verscharen, D. Babel, J. Research Chem. (S) (1979) 213; (d) J.M. Dance, A. Tressaud, W. Massa, D. Babel, J. Chem. Res. (S) (1981) 202.
[63] D. Babel, G. Knoke, Z. Anorg. Allg. Chem. 442 (1978) 151.
[64] J.C. Devan, A.J. Edwards, J.J. Guy, J. Chem. Soc., Dalton Trans. (1986) 2623.
[65] M. Shustorovich, A. Porai-Koshits, Y.A. Buslaev, Coord. Chem. Rev. 17 (1975) 1.
[66] F. Schrötter, B.G. Müller, Z. Anorg. Allg. Chem. 619 (1993) 1426.
[67] (a) W. Massa, Rev. Inorg. Chem. 19 (1999) 117; (b) U. Englich, W. Massa, Acta Crystallogr. C48 (1992) 6.
[68] P.R. Perumareddi, J. Phys. Chem. 78 (26) (1974) 2678.
[69] (a) D.W. Smith, Inorg. Chim. Acta 22 (1977) 107; (b) J.K. Burdett, Inorg. Chem. 20 (1981) 1959.
[70] M. Molinier, W. Massa, S. Khairoun, A. Tressaud, J.L. Soubeyroux, Z. Naturforsch. 46b (1991) 1669.
[71] R. Haegele, D. Babel, D. Reinen, Z. Naturforsch. 31b (1976) 60.
[72] (a) M. Molinier, W. Massa, Z. Naturforsch. 47b (1992) 783; (b) W. Massa, M. Steiner, J. Solid State Chem. 32 (1980) 137.
[73] D. Oelkrug, Struct. Bonding, 9, Springer, 1971, p. 1.
[74] F. Rodriguez, P. Nuñez, M.C. Marco de Lucas, J. Solid State Chem. 110 (1994) 170.
[75] W.E. Hatfield, R.C. Fay, C.E. Pfluger, T.S. Piper, J. Am. Chem. Soc. 85 (1963) 265; T.S. Davis, J.P. Fackler, M.J. Weeks, Inorg. Chem. 1 (1968) 1994.
[76] H.A. Goodwin, R.N. Sylva, Aust. J. Chem. 18 (1965) 1743; W. Levason, C.A. McAuliffe, J. Chem. Soc., Dalton (1973) 455.
[77] C. Bellitto, A.A. Tomlinson, C. Furlani, J. Chem. Soc. (A) (1971) 3267.
[78] I. Bernal, N. Elliot, R. Lalancette, Chem. Commun. (1971) 803.
[79] R.J. Deeth, Faraday Discuss. 124 (2003) 379.
[80] D. Reinen, M. Atanasov, Chem. Phys. 136 (1989) 27.
[81] P. Köhler, G. Amthauer, J. Solid State Chem. 28 (1979) 329.
[82] K. Neuenschwander, H.U. Güdel, J.C. Collingwood, P.N. Schatz, Inorg. Chem. 22 (1983) 1712.
[83] A.B.P. Lever, Inorganic Electronic Spectroscopy, Elsevier, 1984.
[84] C.K. Jørgensen, Progr. Inorg. Chem. 12 (1970) 101.
[85] J.A. Duffy, Bonding, Energy Levels and Bands in Inorganic Solids, Longman, 1990, Chapter 5.
[86] R.D. Shannon, C.T. Prewitt, Acta Crystallogr. B25 (1969) 925; R.D. Shannon, Acta Crystallogr. A32 (1976) 751.
[87] D. Reinen, We here recall a remark of C.K. Jørgensen in one of his lectures: "This compound is so black that it does not exist," Struct. Bonding, Honorary 106 (2004) 246.
[88] O. Schmitz-DuMont, H. Brokopf, K. Burkhardt, Z. Anorg. Allg. Chem. 295 (1958) 7; O. Schmitz-DuMont, D. Reinen, Ber. Bunsenges. Phys. Chem. 355 (1967) 280; O. Schmitz-DuMont, D. Grimm, Z. Anorg. Allg. Chem. 355 (1967) 280.
[89] F.A. Cotton, M.D. Meyers, J. Am. Chem. Soc. 82 (1960) 5023.
[90] (a) A.L. Hector, E.G. Hope, W. Levason, M.T. Weller, Z. Anorg. Allg. Chem. 624 (1998) 1982; (b) E. Alter, R. Hoppe, Z. Anorg. Allg. Chem. 407 (1974) 313.
[91] P. Lacorre, J. Pannetier, T. Fleischer, R. Hoppe, G. Ferey, J. Solid State Chem. 93 (1991) 37.
[92] P. Lacorre, J. Pannetier, F. Averdunk, R. Hoppe, G. Ferey, J. Solid State Chem. 79 (1989) 1.
[93] E. Alter, R. Hoppe, Z. Anorg. Allg. Chem. 405 (1974) 167.
[94] D. Reinen, C. Friebel, V. Propach, Z. Anorg. Allg. Chem. 408 (1974) 187.
[95] J.R. Perumareddi, Coord. Chem. Rev. 4 (1969) 73.
[96] M. Atanasov, C.A. Daul, C. Rauzy, Chem. Phys. Lett. 367 (2002) 737, and Struct. Bonding 106 (2004) 97.
[97] J. Grannec, Ph. Sorbe, B. Chevalier, J. Etourneau, J. Portier, C. R. Acad. Sci. Paris 282C (1976) 815.
[98] D. Reinen, H.O. Wellern, J. Wegwerth, Z. Phys. B104 (1997) 595; B.L. Ramakrishna, D. Reinen, M. Atanasov, J. Solid State Chem. 129 (1997) 117.
[99] D. Reinen, M. Atanasov, in: H. Köppel, D. Yarkony, H. Barentzen (Eds), The Jahn–Teller Effect—Advances and Perspectives, Springer Series in Chem. Phys. 97 (2009) 451.

[100] M. Atanasov, P. Comba, C.A. Daul, A. Hauser, J. Phys. Chem. A 111 (2007) 9145, here, a different definition of the vibronic coupling constants for the trigonal modes ($T_g \otimes \tau_{2g}$ problem) is used, emerging from a factor (1/2) in the matrices of the Clebsh–Gordon coefficients C_ξ, C_η and C_ς (Appendix A) and for the Q_τ displacements. The relations in respect to those, used in the foregoing reference (primed notations), are: $Q_\tau = (1/2)Q'_\tau$; $V_\tau = 4V'_\tau$; $K_\tau = 4K'_\tau$; $L_\tau = 4L'_\tau$; $W = 4W'$; $X_\tau = 8X'_\tau$.
[101] R. Bruyndonck, C. Daul, P.T. Manoharan, E. Deiss, Inorg. Chem. 36 (1997) 4251.
[102] E.J. Baerends, V. Branchadell, M. Sodupe, Chem. Phys. Lett. 265 (1997) 481; C. Anthon, C.E. Schäffer, Coord. Chem. Rev. 226 (2002) 17.
[103] A. Bérces, C. Bo, P.M. Boerrigter, L. Cavallo, D.P. Chong, L. Deng, R.M. Dickson, D.E. Ellis, L. Fan, T.H. Fischer, C. Fonseca Guerra, S.J.A. van Gisbergen, J.A. Groeneveld, O.V. Gritsenko, M. Grüning, F.E. Harris, P. van den Hoek, H. Jacobsen, G. van Kessel, F. Kootstra, E. van Lenthe, D.A. McCormack, V.P. Osinga, S. Patchkovskii, P.H.T. Philipsen, D. Post, C.C. Pye, W. Ravenek, P. Ros, P.R.T. Schipper, G. Schreckenbach, J.G. Snijders, M. Sola, M. Swart, D. Swerhone, G. te Velde, P. Vernooijs, L. Versluis, O. Visser, E. van Wezenbeek, G. Wiesenekker, S.K. Wolff, T.K. Woo, E.J. Baerends, J. Autschbach, T. Ziegler, ADF2006.01 SCM, Theoretical Chemistry, Vrije Universiteit, Amsterdam, The Netherlands, 2006.
[104] W. Klemm, B. Brandt, R. Hoppe, Z. Anorg. Allg. Chem. 308 (1961) 179.
[105] M.J. Riley, M.A. Hitchman, D. Reinen, Chem. Phys. 102 (1986) 11.
[106] V. Polinger, in [99] 97 (2009) 685.
[107] M. Moreno, M.T. Barriuso, J.A. Aramburu, P. Garcia-Fernández, J.M. Garcia Lastra, J. Phys.: Condens. Mat. 18 (2006) R315.
[108] D. Reinen, S. Krause, Inorg. Chem 20 (1981) 2750 (there is an incorrect Journal citation in ref. [107]).
[109] O.A. Anikeenok, R.M. Gurnerov, M.V. Eremin, T.A. Ivanova, Yu.Y. Yablokov, Phys. Solid State 26 (1984) 1365.
[110] J.M. Garcia-Lastra, J.A. Aramburu, M.T. Barriuso, M. Moreno, Chem. Phys. Lett. 385 (2004) 286.
[111] B. Delley, J. Chem. Phys. 113 (2000) 7756.
[112] G. Steffen, D. Reinen, H. Stratemeier, M.J. Riley, M.A. Hitchman, H.E. Matthies, K. Recker, F. Wallrafen, J.R. Niklas, Inorg. Chem. 29 (1990) 2123; C. Friebel, V. Propach, D. Reinen, Z. Naturforsch. 31b (1976) 1574.
[113] M.J. Riley, C.J. Noble, P.L.W. Tregenna-Piggott, J. Chem. Phys. 130 (2009) 104708.
[114] P.L.W. Tregenna-Piggott, Adv. Quant. Chem. 44 (2003) 462.
[115] B.R. McGarvey, in: R.L. Carlin (Ed.), Trans. Metal Chem., vol. 3, Marcel Dekker, New York, 1966, p. 90.